DNA G-QUADRUPLEXES: FROM NUCLEIC ACIDS INVOLVED IN GENE CONTROL EXPRESSION TO HIGHLY ORDERED SUPRAMOLECULAR STRUCTURES.

Maria Marzano

Dottorato in Biotecnologie – 32 °ciclo
Università degli Studi di Napoli Federico II

Dottorato in Biotecnologie – 32 ° ciclo
Università degli Studi di Napoli Federico II

DNA G-QUADRUPLEXES: FROM NUCLEIC ACIDS INVOLVED IN GENE CONTROL EXPRESSION TO HIGHLY ORDERED SUPRAMOLECULAR STRUCTURES.

Maria Marzano

Dottorando: Maria Marzano

Relatore: Gennaro Piccialli

Coordinatore: Prof. Marco Moracci

Settore Scientifico Disciplinare CHIM 06

C'è una forza motrice
più forte del vapore, dell'elettricità
e dell'energia atomica: la volontà.

- Albert Einstein -

Index

Short Abstract

Synthetic nucleosides, nucleotides and nucleic acids are extremely versatile molecules, all from a biological, biotechnological and therapeutic point of view. In fact, by virtue of their remarkable properties, such as: higher bioavailability, affinity with target, biostability and higher resistance against nucleases degradation, they can be used as diagnostic tools, nanoprobes, biosensors, vaccines, aptamers, but also for the development of new materials in nanotechnology fields.

In this contest resides my research activity dedicated to the synthesis and study of analogues ODN, with potential application properties ranging from the development of new strategies for gene regulation and recognition of specific proteins, until the construction of new scaffolds based on higher ordered supramolecular structures.

Specifically, my research work has been focused on:

- Study of the topology, stability and molecularity of G-quadruplexes linked to a “double-end-linker”.
- Implementation of anti-HIV activity aptamers based on G-quadruplexes linked to a “tetra-end-linker”.
- Evaluation of an analogue ε-Poly(L-Lysine) or ε-PLL as ligand for G-quadruplex structures.
- Realization of a new supramolecular structures formed by G-rich oligonucleotide sequences containing an inversion of polarity site for the development of long G-wires.
- Chemical synthesis and structural and biological characterization of Peptide Nucleic Acid-functionalized Adenoviral vectors for the modulation of Bcl-2 proto-oncogene.

Long Abstract

Grazie alla straordinaria flessibilità e selettività, il DNA può assumere diverse conformazioni o strutture secondarie. Tra queste, abbiamo le G-quadruplex, osservate 50 anni prima della scoperta della doppia elica di DNA ma determinate solo nel 1962 attraverso metodi cristallografici. A differenza del DNA, le G-quadruplex sono caratterizzate dall'impilamento di due o più tetradi di guanine. Ogni tetrade è composta da quattro basi guaniniche che si auto-assemblano in una conformazione planare ben ordinata, stabilizzata dalla presenza di cationi monovalenti quali K^+ o Na^+. Queste strutture sono rimaste in gran parte una curiosità di laboratorio fino a quando non si è scoperto il loro attivo coinvolgimento in regioni importanti del genoma umano, come le estremità cromosomiche dei telomeri, nei promotori di geni ed oncogeni. Da qui la possibilità di utilizzare le G-quadruplex nella regolazione dei processi replicativi e trascrizionali oltre che nell'inibizione dello sviluppo o della proliferazione cellulare nelle cellule neoplastiche. Al di là dell'interesse prettamente biologico, tali strutture stanno riscuotendo ampi consensi anche nell'ambito delle nanotecnologie e della chimica supramolecolare, per la loro capacità di formare, in maniera ordinata e controllata, strutture di ordine superiore, conosciute come G-wires, tramite processi di auto-assemblaggio o self-assembly. Grazie alle loro proprietà fisiche, come: struttura 3D ben definita, proprietà ottiche, conducibilità, basso potenziale ossidativo, flessibilità, abilità nella funzionalizzazione e biocompatibilità, le G-quadruplex possono trovare nuove e diverse applicazioni, tra cui biocatalisi, nanodispositivi, drug delivery, nanomateriali e biosensori.

Un'altra interessante scoperta per quanto riguarda la regolazione del DNA o RNA è rappresentata dal PNA o acido peptido nucleico, mimico sintetico del DNA. La sua struttura consiste essenzialmente nella ripetizione di unità di N-(2-amminoetil) -glicina unite attraverso legami ammidici. Le basi azotate puriniche (A e G) e pirimidiniche (C e T) sono unite al backbone mediante legami metilencarbonilici. Proprio come il DNA, l'appaiamento e la distanza tra le basi azotate segue fedelmente la regola di Watson e Crick (A-T e G-C), ma a differenza della sua controparte naturale, non contiene né zuccheri pentosi né gruppi fosfato. Oltre alle ovvie differenze strutturali, i PNA presentano un backbone aciclico, achirale e neutro, infatti data la loro chimica neutralità risultano essere meno solubili e tendono ad aggregare, in aggiunta, presentano un'elevata stabilità biologica, infatti sono resistenti all'attacco di proteasi e nucleasi, sia nel siero umano

che in estratti cellulari e sono resistenti e stabili in ambienti fortemente acidi. In virtù delle loro proprietà chimico-fisiche, i PNA sono i candidati ideali per la modulazione artificiale dell'espressione genica.

È in questo ampio contesto che si colloca il mio progetto di tesi, focalizzato sulla:

- Sintesi e caratterizzazione di G-quadruplex monomolecolari coniugate ad un linker bifunzionale.
- Sintesi e caratterizzazione di aptameri tetraramificati (TEL-ODNs) ad attività anti-HIV.
- Valutazione di un analogo ε-Poly(L-Lisinico) or ε-PLL come ligando di G-quadruplex.
- Realizzazione di strutture supramolecolari provviste nel tratto G-rich di in un'inversione di polarità 3'-3'.
- Modulazione del proto-oncogene Bcl-2 attraverso l'utilizzo di PNA funzionalizzati con vettori Adenovirali.

CHAPTER 1

Oligonucleotides and analogues: synthetic strategies and applications

1.1 Introduction

Oligonucleotides (ONs) are short (13-25 nucleotides) single stranded DNA or RNA molecules which are able to hybridize a unique sequence in the total pool of targets occurring in a cell. In contrast, certain unfavourable properties, such as the degradation of nucleases, the poor uptake through cellular membranes, and the presence of unfavourable biodistribution and pharmacokinetic properties [1][2], can represent a limit for diagnostic and therapeutic applications. To overcome these limitations, it is possible to chemically modify the phosphodiester bond [3], the ribose spine [4] or the nucleobases [5][6][7][8] in order to obtain analogue ONs of the first, second and third generation. The first generation of ONs, in particular that of the Phosphorothioates (PS), is characterized by the replacement of a phosphodiester oxygen with a sulphur atom [9]. This modification confers on the ONs a higher resistance against nuclease degradation, leading to a higher bioavailability. However, this modification can slightly reduce the affinity of the ONs towards their mRNA targets [10]. To further improve the nuclease resistance and increase the binding affinity for the target mRNA, the second generation of ONs comes to the rescue. The ribose can be modified through the replacement of the 2'-hydroxyl by different groups. The most commonly used are 2'-O-Methyl (2'-OMe) and 2'-OMethoxyethyl(2'-MOE) (4). The 2'-modifications increase the thermal stability during hybridization and increase the stability with respect to digestion by nucleases. Instead, to enhance the target affinity, biostability, pharmacokinetics and resistance against the nucleases, the employment of ONs of the third generation is possible. They mainly modify the furanose ring of the nucleotide [11]. The first suggestion about the use of ONs as therapeutic agents was made in 1978 by Zamecnik and Stephenson [12][13]. Although 41 years have passed since this event, ONs and their analogues still represent a valid pharmaceutical and nanotechnological tool. In fact, they can be used: i) in gene therapy to correct genetic disorders or to silence gene expression (antisense and antigene), ii) in

biosensing, iii) as nanodevices, iv) as DNA vaccines and v) as aptamers [14][15][16][17] (Figure 1).

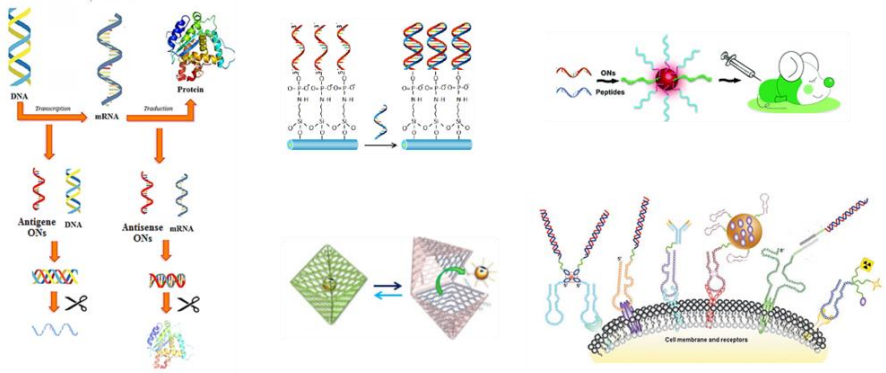

Figure 1. Schematic representation of some applications of oligonucleotides and their analogues.

1.2 Oligonucleotides and analogues in the antisense strategy

An antisense oligonucleotide (ASO) is a short (12-20 nucleotides) synthetic strand of DNA complementary to the mRNA target. Hybridization of an ASO to its target mRNA via Watson-Crick base pairing leads to the formation of a heteroduplex capable of causing a specific inhibition of gene expression through various mechanisms depending on the chemical composition of the ASO and the location of hybridization [18]. The mechanisms by which an ASO may induce biological effects are numerous and complex. For example, the inhibition of translation from a mRNA into a protein may occur in three different ways [19]:

i) activation of RNase H. This leads to a splitting of the RNA-DNA heteroduplex and the degradation of the target mRNA and leaves the ASO intact,

ii) translational arrest by the steric hindrance of ribosomal activity, or

iii) destabilization of the pre-mRNA in the nucleus.

Antisense technology can offer not only an important opportunity for the manipulation of gene expression within the cells, but also represents a powerful tool for the study of the gene function in specific diseases. This

approach has been successfully used for the treatment of cancer, HIV and other mutating viral diseases. Currently, different ASOs are undergoing clinical trials in relation to many neurodegenerative diseases, such as Huntington's disease, Parkinson's disease, Alzheimer's disease, amyotrophiclateral sclerosis and several other cancer states [20][21]. Although many are being tested in clinical trials (Table 1), to date only two ASOs have been approved by the US FDA to be used on humans, including, Formivirsen (Vitravene), for the treatment of human retinitis induced by cytomegalovirus (CMV).

Study id; year; country of conduct of study	*Sponsor*	*Disease conditions*	*Phase of clinical trial; target mRNA*
NCT02947893; 2017; USA	Georgetown University	Moderate Alzheimer's Disease	Phase 2; anti-*tau*
NCT01563302; 2012; USA	Isis Pharmaceuticals	Lymphoma	Phase 1/2; STAT-3
NCT02294851; 2016; USA	Biogen	Parkinson's disease	Phase 1; Tau

Table1. Recorded clinical trials which use ASOs

1.3 Oligonucleotides and analogues in the antigene strategy

In the antigene strategy the ONs can recognize and bind selectively double-helical DNA, forming through hydrogen bonds (Hoogsteen and reverse-Hoogsteen) triplex oligodeoxynucleotides (TFO). TFOs were first described in 1957 by Felsenfeld and Rich [22] and in 1986 it was demonstrated that a short (15-mer) mixed-sequence TFO had formed a stable and specific triplex DNA complex [23]. In particular, the third strand of the DNA triplex followed a path through the major groove of the duplex DNA. According to the base composition and binding-direction against the duplex DNA, TFOs can be classified into two types: intramolecular and intermolecular. Intermolecular triplexes (Figure 2A) are formed of two or three DNA strands, usually between a DNA duplex and a single stranded DNA. Instead, in intramolecular triplexes (Figure 2B) the third strand is physically tethered to the DNA

duplex. The most studied intermolecular triplex is H-DNA. In H-DNA the homopurine and homopyrimidine sequences must contain a specular repetition. In this way, half of the pyrimidine tract rotates on the purine strand of the duplex. The orientation of the strands can be parallel or antiparallel.

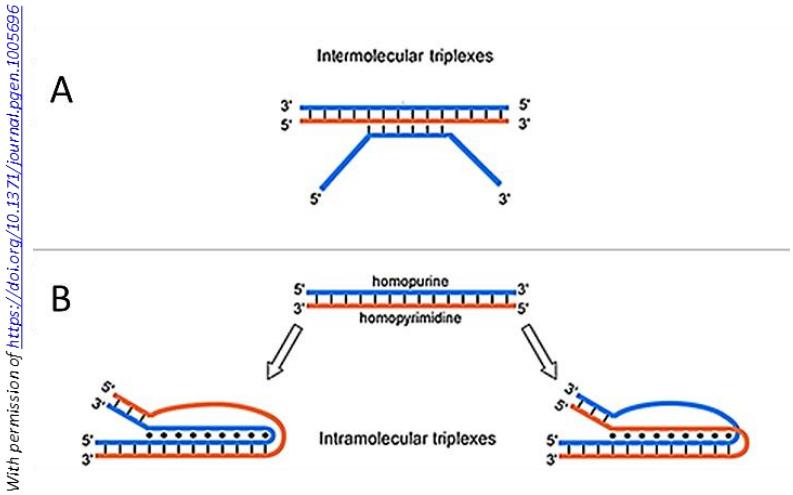

With permission of https://doi.org/10.1371/journal.pgen.1005696

Figure 2. Schematic representation of an intermolecular triplex with an antiparallel strand orientation (**A**). Examples of intramolecular H-DNA structures with parallel and antiparallel strand orientations (**B**).

1.4 Oligonucleotides and analogues as aptamers

In the past two decades, the use of biomolecules, called aptamers, has attracted the attention of the scientific community due to their applicability in the diagnosis and treatment of various diseases. Aptamers are short single-stranded DNA or RNA molecules (25-50 nucleotides), equipped with an affinity and selectivity towards their molecular targets, mainly proteins [26]. The major applications of aptamers include their use in diagnostics and therapeutics, as biomaterials or nanomaterials and in nanomedicine. They can bind an intracellular or extracellular target and can function as agonists or antagonists. Aptamers are selected by an in vitro process described by Tuerk and Gold (1990) and Ellington and Szostak (1990), called SELEX (Systematic Evolution of Binding by Exponential Enrichment). The SELEX method (Figure 3) involves the progressive selection of aptamers, by the repetition of binding cycles and the elution and amplification of ligands from a random nucleic acid library (DNA and RNA) to the selection of sequences with a higher binding affinity for the target is achieved [27][28]. The differences in the majority of RNA SELEX (Figure 3A) protocols, compared to DNA SELEX, (Figure 3B)

include: i) the protection of RNA from RNAases through modifications of their ends 5 'or 3', ii) amplification by T7 RNA polymerase and iii) reversed transcription step before PCR. After this iterative process, the resulting nucleic acid molecules can be chemically modified, in order to provide them additional properties and, above all, to extend their half-life in biological fluids [29].The characteristics of the selected ONs are identified by using various physical, chemical and biological assays [30].

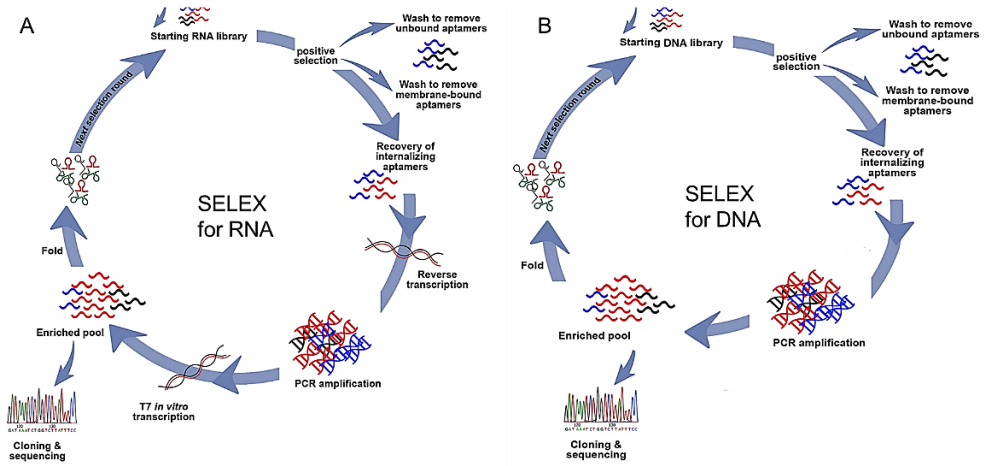

Figure 3. Graphical representation of the SELEX (Systematic Evolution of Binding by Exponential Enrichment) strategy starts with random (**A**) ssDNA or (**B**) ssRNA libraries

Analogically to monoclonal antibodies, aptamers can specifically recognize and bind their targets, but unlike antibodies, they have a number of advantages, described in Table 2. Due to their abilities, a number of aptamers have entered clinical trials, such as in the treatment of ocular diseases [31], hematologic diseases [32], cancer [33], immune disorders, inflammatory processes [34], neurodegenerative diseases, and bacterial infections [34][35]. Some of the most extensively studied aptamers present Guanine rich (G-rich) consensus sequences that allow them to fold into stable four-stranded structures, known as G-quadruplexes [36]. G-rich aptamers that form G-quadruplexes have several advantages compared with unstructured sequences [36]. They are thermodynamically and chemically stable, show no immunogenicity and are resistant to numerous serum nucleases. A few years ago, a number of G-rich aptamers were developed, which can now be used as anticoagulant agents [37], therapeutic agents for cancer treatment [38][39], nano-devices [40] and APT-sensors [41].

	Aptamers	*Antibodies*
Stability	Withstand repeated rounds of denaturation/renaturation. Stable at room temperature. Long shelf life (several years). Can be lyophilized. Degradable by nucleases. Resistant to proteases.	Easily denatured. Limited shelf life. Must be refrigerated for storage and transport. Degradable by proteases. Resistant to nucleases.
Synthesis	In vitro SELEX takes only 2-8 weeks. No batch-to-batch variation. Cheap to synthesize.	Produced in vivo. More than 6 months. Batch-to-batch variations. Laborious and expensive.
Target potential	From ions and small molecules to whole cells and live animals.	Targets must cause a strong immune response for antibodies to be produced.
Size	Small molecules (~12 – 30 kDa).	Relatively large by comparison (~150 – 170 kDa).
Modifiability	Aptamers can readily and easily be modified without affinity loss.	Modifications often lead to reduced activity.
Affinity	High and increased in multivalent aptamers.	Dependent on the number of epitopes on the antigene.
Specificity	Single point mutations identifiable.	Different antibodies might bind the same antigen.
Tissue uptake/kidney filtration	Fast.	Slow.

Table 2. Comparison of aptamers and monoclonal antibodies.

1.5 References

[1] R. L. Juliano, “The delivery of therapeutic oligonucleotides,” *Nucleic Acids Res.*, vol. 44, no. 14, pp. 6518–6548, 2016.

[2] S. T. Crooke, S. Wang, T. A. Vickers, W. Shen, and X. H. Liang, “Cellular uptake and trafficking of antisense oligonucleotides,” *Nat. Biotechnol.*, vol. 35, no. 3, pp. 230–237, 2017.

[3] Z. G. Dikmen, T. Ozgurtas, S. M. Gryaznov, and B. S. Herbert, “Targeting critical steps of cancer metastasis and recurrence using telomerase template antagonists,” *Biochim. Biophys. Acta - Mol. Basis Dis.*, vol. 1792, no. 4, pp. 240–247, 2009.

[4] M. Manoharan, “2’-Carbohydrate modifications in antisense oligonucleotide therapy: Importance of conformation, configuration and conjugation,” *Biochim. Biophys. Acta - Gene Struct. Expr.*, vol. 1489, no. 1, pp. 117–130, 1999.

[5] J. Wengel *et al.*, “LNA (Locked Nucleic Acid),” *Nucleosides and Nucleotides*, vol. 18, no. 6–7, pp. 1365–1370, 1999.

[6] S. Obika *et al.*, “Stability and structural features of the duplexes containing nucleoside analogues with a fixed N-type conformation, 2’-O,4’-C- methyleneribonucleosides,” *Tetrahedron Lett.*, vol. 39, no. 30, pp. 5401–5404, 1998.

[7] D. A. Braasch and D. R. Corey, “Locked nucleic acid (LNA): Fine-tuning the recognition of DNA and RNA,” *Chem. Biol.*, vol. 8, no. 1, pp. 1–7, 2001.

[8] P. P. Seth *et al.*, “Synthesis and biophysical evaluation of 2′,4′-Constrained 2′O-Methoxyethyl and 2′,4′-Constrained 2′O-Ethyl nucleic acid analogues,” *J. Org. Chem.*, vol. 75, no. 5, pp. 1569–1581, 2010.

[9] F. Eckstein, “What Is Their Origin and What Is Unique About Them ? Phosphorothi oate,” *Antisense Nucleic Acid Drug Dev.*, vol. 10, pp. 117–121, 2000.

[10] S. T. Crooke, “Progress in antisense technology: The end of the beginning,” *Methods Enzymol.*, vol. 313, no. 1991, pp. 3–45, 2000.

[11] M. E. Gleave and B. P. Monia, “Antisense therapy for cancer,” *Nat. Rev. Cancer*, vol. 5, no. 6, pp. 468–479, 2005.

[12] P. C. Zamecnik and M. L. Stephenson, “Inhibition of Rous sarcoma virus replication and cell transformation by a specific oligodeoxynucleotide,” *Proc. Natl. Acad. Sci. U. S. A.*, vol. 75, no. 1, pp. 280–284, 1978.

[13] M. L. Stephenson and P. C. Zamecnik, “Inhibition of Rous sarcoma viral RNA translation by a specific oligodeoxyribonucleotide,” *Proc. Natl. Acad. Sci. U. S. A.*, vol. 75, no. 1, pp. 285–288, 1978.

[14] D. D. F. Ma, T. Rede, N. A. Naqvi, and P. D. Cook, “Synthetic oligonucleotides as therapeutics: The coming of age,” *Biotechnol. Annu. Rev.*, vol. 5, pp. 155–196, 2000.
[15] D. Y. Wang, “A general approach for the use of oligonucleotide effectors to regulate the catalysis of RNA-cleaving ribozymes and DNAzymes,” *Nucleic Acids Res.*, vol. 30, no. 8, pp. 1735–1742, 2002.
[16] J. J. Donnelly, J. B. Ulmer, and M. A. Liu, “DNA vaccines.,” *Dev. Biol. Stand.*, vol. 95, pp. 43–53, 1998.
[17] H. Sun, X. Zhu, P. Y. Lu, R. R. Rosato, W. Tan, and Y. Zu, “Oligonucleotide aptamers: New tools for targeted cancer therapy,” *Mol. Ther. - Nucleic Acids*, vol. 3, no. May, 2014.
[18] S. T. Crooke, “Progress in Antisense Technology,” *Annu. Rev. Med.*, vol. 55, no. 1, pp. 61–95, 2004.
[19] N. Dias and C. A. Stein, “Antisense oligonucleotides: Basic concepts and mechanisms,” *Mol. Cancer Ther.*, vol. 1, no. 5, pp. 347–355, 2002.
[20] K. P. Anderson, M. C. Fox, V. Brown-Driver, M. J. Martin, and R. F. Azad, “Inhibition of human cytomegalovirus immediate-early gene expression by an antisense oligonucleotide complementary to immediate-early RNA,” *Antimicrob. Agents Chemother.*, vol. 40, no. 9, pp. 2004–2011, 1996.
[21] G. Monteleone *et al.*, “Phase i clinical trial of smad7 knockdown using antisense oligonucleotide in patients with active crohn’s disease,” *Mol. Ther.*, vol. 20, no. 4, pp. 870–876, 2012.
[22] G. Felsenfeld and A. Rich, “Studies on the formation of two- and three-stranded polyribonucleotides,” *BBA - Biochim. Biophys. Acta*, vol. 26, no. 3, pp. 457–468, 1957.
[23] P. B. Dervan, “DNA-Binding Molecules of,” 1968.
[24] “Ó 2005 Oxford University Press Nucleic Acids Symposium Series No. 49 335–336,” *Nucleic Acids Symp. Ser.*, no. 49, pp. 335–336, 2005.
[25] A. Bacolla, G. Wang, and K. M. Vasquez, “New Perspectives on DNA and RNA Triplexes As Effectors of Biological Activity,” *PLoS Genet.*, vol. 11, no. 12, pp. 1–12, 2015.
[26] D. Proske, M. Blank, R. Buhmann, and A. Resch, “Aptamers - Basic research, drug development, and clinical applications,” *Appl. Microbiol. Biotechnol.*, vol. 69, no. 4, pp. 367–374, 2005.
[27] C. Tuerk and L. Gold, “Systematic evolution of ligands by exponential enrichment: RNA ligands to bacteriophage T4 DNA polymerase,” *Science (80-.).*, vol. 249, no. 4968, pp. 505–510, 1990.
[28] A. D. Ellington and J. W. Szostak, “In vitro selection of RNA molecules that bind specific ligands,” *Nature*, vol. 346, no. 6287, pp. 818–822, 1990.
[29] S. C. B. Gopinath, “Methods developed for SELEX,” *Anal. Bioanal. Chem.*, vol. 387, no. 1, pp. 171–182, 2007.

[30] K. M. Song, S. Lee, and C. Ban, “Aptamers and their biological applications,” *Sensors*, vol. 12, no. 1, pp. 612–631, 2012.
[31] D. Maberley, “Pegaptanib for neovascular age-related macular degeneration.,” *Issues Emerg. Health Technol.*, no. 76, pp. 1–4, 2005.
[32] C. P. Rusconi *et al.*, “RNA aptamers as reversible antagonists of coagulation factor IXa,” *Nature*, vol. 419, no. 6902, pp. 90–94, 2002.
[33] P. J. Bates, D. a Laber, D. M. Miller, S. D. Thomas, and J. O. Trent, “as a Novel Treatment for Cancer,” *Exp. Mol. Pathol.*, vol. 86, no. 3, pp. 151–164, 2010.
[34] S. I. Ismail and W. Alshaer, “Therapeutic aptamers in discovery, preclinical and clinical stages,” *Adv. Drug Deliv. Rev.*, vol. 134, pp. 51–64, 2018.
[35] Q. Pan, J. Yan, Q. Liu, C. Yuan, and X. L. Zhang, “A single-stranded DNA aptamer against mannose-capped lipoarabinomannan enhances anti-tuberculosis activity of macrophages through downregulation of lipid-sensing nuclear receptor peroxisome proliferator-activated receptor γ expression,” *Microbiol. Immunol.*, vol. 61, no. 2, pp. 92–102, 2017.
[36] B. Gatto, M. Palumbo, and C. Sissi, “Nucleic Acid Aptamers Based on the G-Quadruplex Structure: Therapeutic and Diagnostic Potential,” *Curr. Med. Chem.*, vol. 16, no. 10, pp. 1248–1265, 2009.
[37] D. M. Tasset, M. F. Kubik, and W. Steiner, “Oligonucleotide inhibitors of human thrombin that bind distinct epitopes,” *J. Mol. Biol.*, vol. 272, no. 5, pp. 688–698, 1997.
[38] P. Daei *et al.*, “Aptamer-based targeted delivery of miRNA let-7d to gastric cancer cells as a novel anti-tumor therapeutic agent,” *Iran. J. Pharm. Res.*, vol. 17, no. 4, pp. 1537–1549, 2018.
[39] B. Wilbanks, J. Smestad, R. M. Heider, A. E. Warrington, M. Rodriguez, and L. James Maher, “Optimization of a 40-mer Antimyelin DNA Aptamer Identifies a 20-mer with Enhanced Properties for Potential Multiple Sclerosis Therapy,” *Nucleic Acid Ther.*, vol. 29, no. 3, pp. 126–135, 2019.
[40] D. W. Hwang *et al.*, “A nucleolin-targeted multimodal nanoparticle imaging probe for tracking cancer cells using an aptamer,” *J. Nucl. Med.*, vol. 51, no. 1, pp. 98–105, 2010.
[41] Y. Wu, B. Midinov, and R. J. White, “Electrochemical aptamer-based sensor for real-Time monitoring of insulin,” *ACS Sensors*, vol. 4, no. 2, pp. 498–503, 2019.

CHAPTER 2

DNA G-Quadruplexes: from nucleic acids involved in gene control expression to highly ordered supramolecular structures

2.1 Introduction

DNA or deoxyribonucleic acid is a fascinating model of self-assembling material. In fact, through a cooperative balance of hydrogen bonds, π-π stacking interactions and other non-covalent forces, a single DNA fragment can find with extraordinary selectivity its complement in solution. Nevertheless, the rotational freedom of the six single bonds of the DNA backbone gives rise to various possible conformations for the polymeric chain, depending first on the DNA sequence on the amount and the direction of the bases with respect to the sugar moiety and then on the hydration level [1]. During the last few years, more than ten different DNA conformations have been discovered. These are often referred to as secondary structures of DNA or non-B-DNA and include the left-handed DNA (Z-DNA) [2], triplex (H-DNA) [3], Holliday junction [4], G-Quadruplex [5] and i-motif [6] (Figure 1). These secondary structures form spontaneously on tracts of repeat sequences in genomes and, besides having a range of biological functions such as immune response activation [7], gene regulation [8] and telomere maintenance [9], can also induce genetic instability with a predisposition to disease. For these reasons, in recent years a new pharmacological approach has been developed, that predicts the use of these non-canonical structures as potential targets for cancer therapy, in order to affect gene expression and telomerase activation, respectively [10][11].

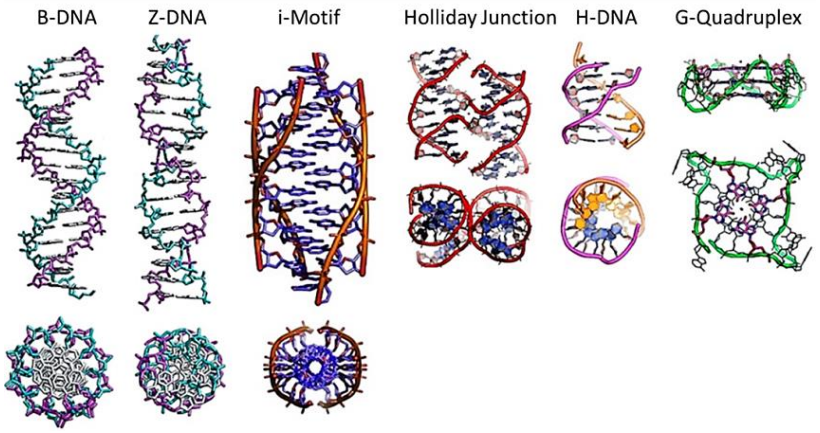

Figure 1. Schematic illustration of Non-B-DNA structures.

2.2 Background Information on DNA G-Quadruplexes

The self-association of guanosines was observed in 1910 by German chemist Ivan Bang [12], but only in 1962 did Gellert and co-workers determine for the first time, by crystallographic methods, the ability of guanosines to form tetrameric structures by the self-association of guanine bases [13]. The basic unit of a G-quadruplex is the G-quartet or G-tetrad, which is composed of a planar arrangement of four guanine bases stabilised by Hoogsteen hydrogen bondings. More precisely, the cyclic arrangement involves N1, N7, O6 and N2 of each guanine base. This produces a central cavity with a specific geometry in which only one pair of electrons of the four O6 is able to coordinate a monovalent cation of the correct size. The different behaviour of these cations within the cavity depends on their dimensions. For example, among the smaller cations, Na^+ can reside in a plane with the G-quartet, whereas K^+ cations can coordinate between two tetrads (Figure 2).

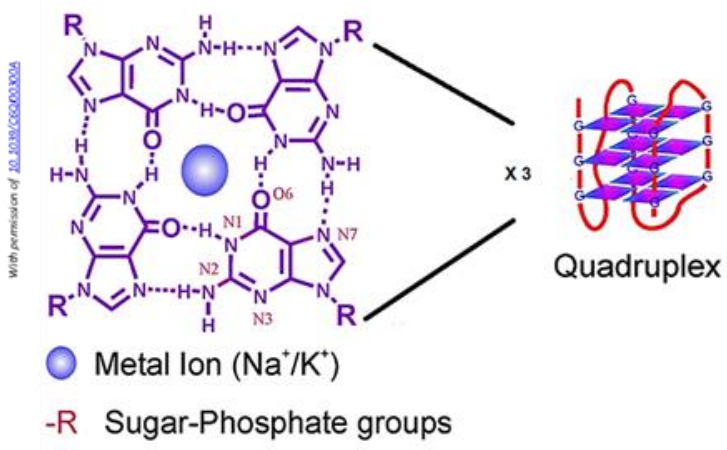

Figure 2. The planar arrangement of four guanine bases bound by eight Hoogsteen hydrogen bonds and between three quartets.

The ions are also able to contribute to charge screening, by reducing the strong negative electrostatic potential generated by the guanine O6 atoms. Furthermore, the O6 atoms form a square planar arrangement for each tetrad, with a twist of 30° and a distance of 3.3 Angstrom between each tetrad. The stacking of the guanine planes contributes to further stabilize the quadruplex structure by the π-π stacking interaction [14] (Figure 2). The formation of any type of G-quadruplex structure is driven by the enthalpy per quartet, from -15 to -25 kcal mol^{-1}, which is more negative than the enthalpy per base pair helix.

2.2.1 *Structural Polymorphism of DNA G-Quadruplexes*

The family of G-Quadruplexes is characterized by a great structural polymorphism that results in a wide variety of topologies. In part this is a consequence of the number of possible combinations, such as the presence of a monovalent cation, the conformation of the glycosidic bond, the number of molecules of the nucleic acid involved in their formation, the orientation of the leading strands [15][16][17], the base composition of the loops (when it occurs) and the number of stacking G-quartets [18][19][20]. G-quadruplex structures can be found in many different multimeric forms including one, two or four separate chains [21]. Therefore, they can be classified, in terms of stoichiometry, as intramolecular (unimolecular-Figure 3A) or intermolecular (bimolecular-Figure 3B and tetramolecular-Figure 3C).

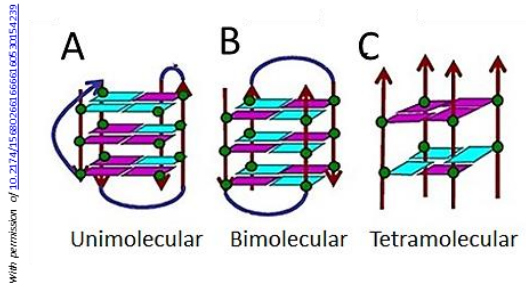

Figure 3. Different topological forms of unimolecular, bimolecular and tetramolecular G-quadruplex structures.

Depending on the DNA strand orientation, a G-quadruplex can be described as parallel, antiparallel or mixed. A parallel G-quadruplex is formed when all four strands are oriented in the same direction, and as a consequence, all the residues found in the G-tetrad have the same glycosidic bond conformation (*anti-anti-anti-*anti or *syn-syn-syn-syn*) (Figure 4A). Antiparallel G-quadruplexes are formed by one or more DNA strands that run in an orientation opposite to the other strands. In particular, we can observe two types of orientation. In the first type, two strands run in the opposite orientation to the other two, and the G-tetrads comprise two guanosines with *syn*-conformations and two with *anti*-conformations (*syn-syn-anti-anti* and *syn-anti-syn-anti*) (Figure 4C and D). Instead, in the second type, known as a mixed-type-hybrid (3+1), three strands are parallel to each other, while the fourth strand runs in the opposite direction.

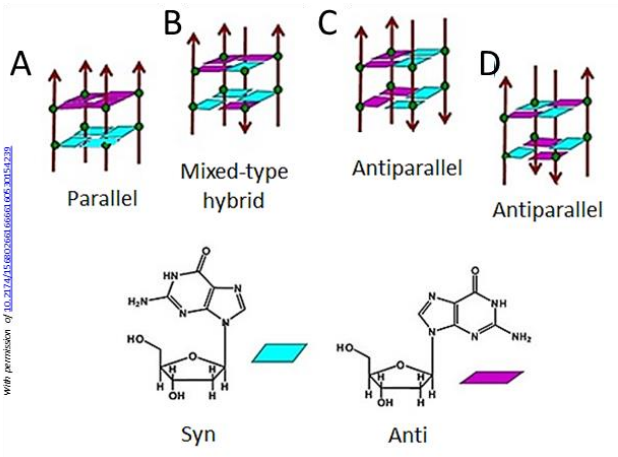

Figure 4. Strand polarities in parallel (**A**), antiparallel (**C** and **D**) and hybrid-type antiparallel (**B**) G-quadruplexes together with a corresponding *syn-anti* orientation of the guanosine residues.

In the (3+1) G-quadruplex, three guanosines adopt the same glycosidic bond conformation, while the fourth residue exhibits an opposite conformation (*syn-anti-anti-anti or anti-syn-syn-syn)* (Figure 4B). Within the G-quadruplex structure, the G-tetrads can be connected by loops of a variable size and sequence. Based on their arrangement within the structure, it is possible to distinguish three loop types: i) a double chain reversal loop (also known as a propeller) which connects the adjacent parallel strands (Figure 5C), ii) a diagonal loop connecting two opposite antiparallel strands (Figure 5B), and iii) an edgewise loop (also known as a lateral loop) in which two adjacent antiparallel strands are connected (Figure 5A).

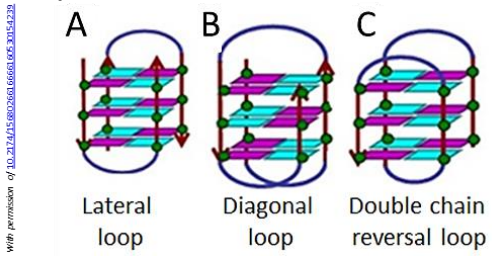

Figure 5. Arrangements of the loop in inter- and intramolecular G-quadruplexes. The loops are marked in blue.

The formation and stability of a G-quadruplex are guaranteed by the presence of monovalent cations. As described previously, the presence of the strong negative electrostatic potential created by the guanine O6 atoms forms a central channel in the G-tetrad, allowing the cation to

position itself inside [22][23][24]. In 1992, Hardin *et al*. provided a classification of cations as a function of their G-quadruplex stabilization properties: $K^+ > Ca^{2+} > Na^+ > Mg^{2+} > Li^+$ and $K^+ > Rb^+ > Cs^+$. However, due to their physiological relevance, the most extensively studied ions are K^+ and Na^+ [25]. Several studies have shown that the concentration of these ions can stabilize or inhibit the interconversion of G-quadruplex DNA structures. In particular, it has been demonstrated that K^+ ions preferably stabilize linear four-stranded parallel quadruplexes, whereas Na^+ ions stabilize folded forms [26].

2.2.2 *Biological Implications of DNA G-Quadruplexes*

As is well known, nucleic acid structures are fundamental to cellular function and the regulation of several biological events. Recently, several studies have reported the involvement of G-quadruplex structures in fundamental regulatory regions critical for biological processes such as DNA replication, transcription and translation, providing new and important mechanisms for controlling gene expression and genome stability. Bioinformatic analysis of the human genome has identified about 375,000 possible guanine-rich (G-rich) regions that could form G-quadruplex structures [27][28], including the telomeric regions, immunoglobulin switch regions, and promoter regions of different genes and oncogenes, such as c-MYC, VEGF, KRAS, c-kit, PDGF-A and c-Myb [29][13][30][31]. The most studied G-quadruplex sequence is the human telomeric sequence, well organized in a specialized nucleoprotein structure, known as a telomere, located at the end of a eukaryotic chromosome. In human somatic cells, the telomerase consists of 500 to 3,000 tandem repetitions of the hexanucleotide $d(T_2AG_3)_n$. During each round of chromosome replication, the telomerase loses about 50-200 base pairs and gradually becomes shorter until it reaches a critical length below which there is cell senescence or apoptosis [32]. For this reason, the protection of its terminal ends from fusion and nuclease degradation represents an important checkpoint in telomere structure and function. In human cells, telomerase activity is detected at around 90-95%. Instead, for cancer cells, the telomerase enzyme is overexpressed in more than 85% of tumours, leading in this way to an uncontrolled cellular proliferation [33]. Therefore, the possibility of inhibiting the telomerase activity in tumour cells has drawn the attention and interest of the scientific community. Another notable feature of G-quadruplexes derives from the fact that they constitute the scaffold of several aptamers [34]. Aptamers are short DNA or RNA fragments, which consist of supporting sections immobilized on solid substrates. This characteristic allows them to

recognize with a specific interaction proteins and enzymes (Table 1) [35]. Due to their well-known properties, namely there: i) resistance to serum nucleases, ii) thermodynamic and chemical stability, iii) low immunogenicity and iv) good cellular uptake, aptamers are used in biosensing, bioimaging and therapeutics, as described below [36][37].

G4-containing aptamer	*Targets*	*Aptamer sequences*
3R02	VEGF	d(TGTGGGGGTGGACTGGGTGGGTACC)
ISIS 5320	HIV gp120	d(T*T*G*G*G*G*T*T)
93del	HIV integrase	d(GGGGTGGGAGGAGGT)
TBA	Thrombin	d(GGTTGGTGTGGTTGG)

Table 1. Representative list of G-quadruplex containing aptamers.

One well-known G-quadruplex-based aptamer is the thrombin-binding aptamer (TBA), discovered in 1992 by Bock *et al*. and characterized [38][39] as comprising two G-quartets connected by one TGT and two TT loops (Figure 6) [40].

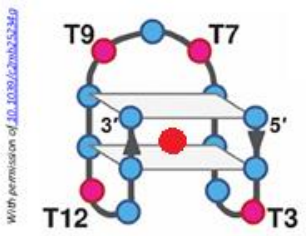

Figure 6. G-quadruplex of the thrombin binding aptamer (TBA). The K^+ ion is marked in red.

In particular, the TBA sequence d($G_2T_2G_2TGTG_2T_2G_2$) is able to bind the fibrinogen binding site of thrombin, responsible for the cleavage of the fibrinogen and the subsequent formation of fibrin clots in the blood. The binding of TBA to α-thrombin prevents the pathological process of thrombosis. Recent studies on TBA aptamers suggest that they can be used in biosensing, with a nanomolar affinity to thrombin. A similar

approach has also been used for the preparation of aptamers against the HIV-integrase and the vascular endothelial growth factor (VEGF), thus demonstrating the establishment of a promising new class of pharmacological molecules. Among the techniques used to monitor the distribution and tracking of the intracellular biomolecules involved in various biochemical reactions and cellular metabolic processes, fluorescence imaging has been found to be very effective in identifying the expression and understanding the cellular location of biomolecules. A particular example of such an aptamer is reported by Jaffrey *et al.*, who established a strategy for the identification of the cellular metabolites in E. coli using fluorogenic Rnas [41]. Since the structural stability of G-quadruplex-forming aptamers is closely related to the biological activity of the aptamer, different synthetic approaches have been proposed to improve the chemical-physical characteristics of the G-quadruplex structures, including the introduction of large aromatic substituents at the 3'- and/or 5'-end [42] and the anchoring of the filaments to an alkyl tetra-end-linker (TEL) [43] able to direct the structuring of the G-quadruplex, as suggested by Oliviero *et al*. in 2010 (Figure 7) [44].

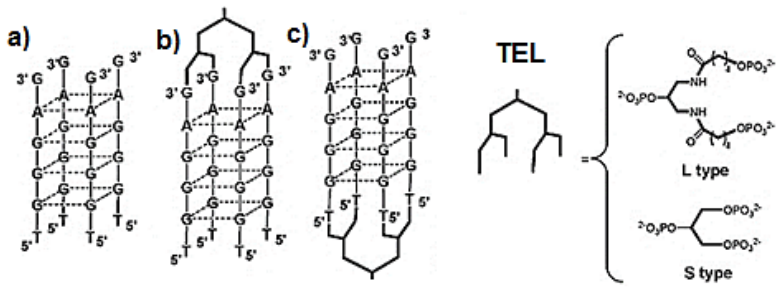

Figure 7. Schematic structures of the ODNs investigated. a) Hotoda's sequence; b) TEL-$^{3'}$-Hotoda sequence-$^{5'}$; c) TEL-$^{5'}$-Hotoda sequence-$^{3'}$; where TEL= tetra-end-linker (long or short)

2.2.3 *Small Molecules that Recognize and Stabilize DNA G-Quadruplexes*

The development of small molecules (**G4-ligands**) able to recognize and bind to G-quadruplex structures with a high affinity plays a crucial and important role in the treatment of certain diseases with anticancer, antiparasitic and antimicrobial agents. On account of their high degree of polymorphism, G-quadruplexes can be bound in different ways (Figure 8), namely by means of i) intercalation between base pairs [45], ii) minor groove binding [46], iii) major groove binding [47] and iv) end-stacking. In particular, ligands containing amino groups and/or side

chains can interact with the grooves, loops and the negatively charged backbone of the G-quadruplex.

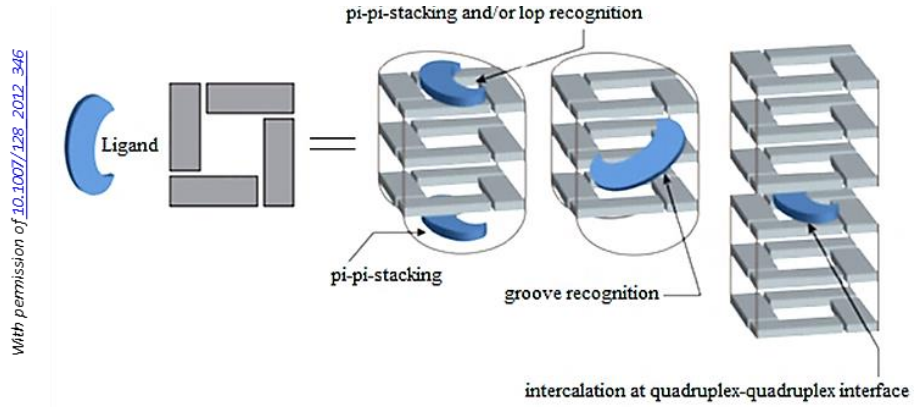

Figure 8. Binding modes of ligands to G-quadruplexes.

With respect to their effects, these compounds have been divided into three classes: i) “light-up” probes, compounds that display a strongly enhanced fluorescence upon binding, ii) “light-off” probes compounds that show a strongly decreased fluorescence upon binding and iii) “permanent” probes, compounds whose fluorescence is not modified by binding. Some of these ligands are designed as fluorescent or imaging probes to verify the G-quadruplex formation or to structurally stabilize the G-quadruplex and others as libraries to detect and identify particular topologies of G-quadruplexes.

2.2.4 *Use of DNA G-Quadruplex Building Blocks in Nanotechnology and Biotechnology*

A cooperative action of hydrogen-bonding, π-stacking, electrostatic and hydrophobic interactions leads to the assembly of G-rich sequences into G-quadruplex structures according to precise rules of base pairing. In particular, by exploiting certain structural features, such as their electronic conductivity, optical properties, well-defined 3D structures, high specificity of assembly, conformational flexibility, biocompatibility and ability for functionalization, it is possible to explore new and different applications, including biocatalysis, nanorobotics, drug delivery, and the design of sensors and nanomaterials. In fact, in recent years, G-quadruplexes have drawn particular interest in relation to nanotechnology and biotechnology applications [48] due to the fact that they can be used as building blocks to create supramolecular structures (Figure 9).

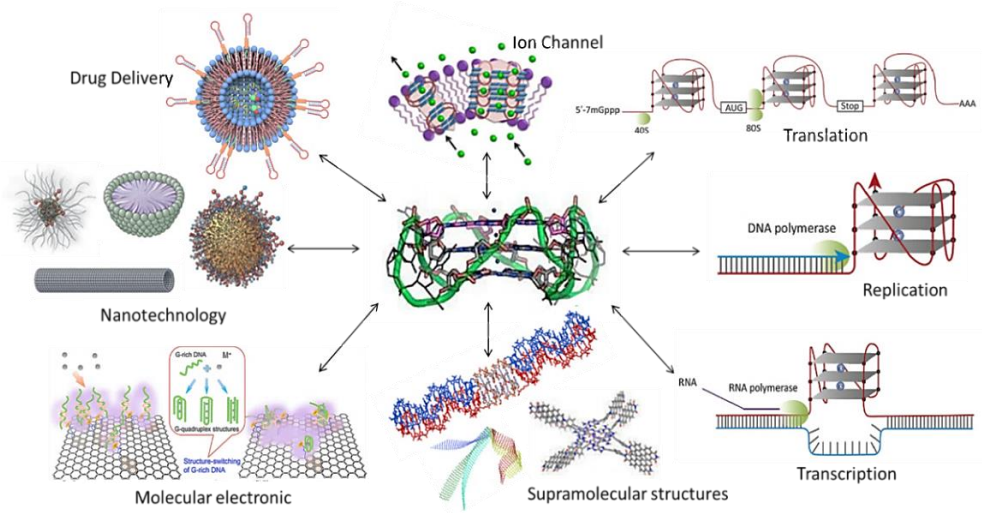

Figure 9. Several applications obtaining an advantage from building blocks of G-quadruplexes.

Despite their various applications, the use of supramolecular assemblies in the real world encounters a series of obstacles, such as the cost of synthetic DNA, the small production scales, the low yields and the sensitivity of DNA to ionic strength and temperature. For these reasons, many studies have been devoted to the optimization and strengthening of their chemico-physical properties.

2.2.5 *Nanostructures based on DNA G-Quadruplexes*

In 2003 Seeman *et al*. designed for the first time a stable four-stranded DNA junction, in which each strand was fitted with a “sticky-end” [49]. These assemblies are called “DNA origami” and “DNA super origami” [50]. It is well known that G-rich strands can self-assemble into highly ordered assemblies by multimerization between the several units that compose the G-quadruplex structure[48]. In the literature three major types of supramolecular structures are reported: i) G-wires [51], ii) frayed G-wires [52] and iii) G-Legos (Figure 10). In 1990, Henderson and Sheardy established, for the first time, the capacity for the sequence d($G_4T_4G_4$), corresponding to the telomeric repetition of *Tetrahymena Thermophila*, to form in the presence of K^+ buffer a nanometre assembly known as a “G-wire”. G-wires form when the 5’-end of one duplex with G-G pairs associates with the 3’-end of a similar duplex (Figure 10A). MacGregor and co-workers identified in the sequence d($A_{15}G_{15}$) the formation of another type of structure, called a “frayed G-wire”, distinguished from a G-wire in terms of the flexible A_{15}

strands that radiate from the guanine core (Figure 10B). Instead, Nishigaki and Biyani proposed another model, called a “G-Lego” formed by the sequence d(G_{11}T). In this model, the G-rich strands form a parallel or antiparallel monomeric building block, and the terminal thymidine residue of each monomeric unit interacts with the next one, leading to the formation of an ultra-stable aggregate (Figure 10C).

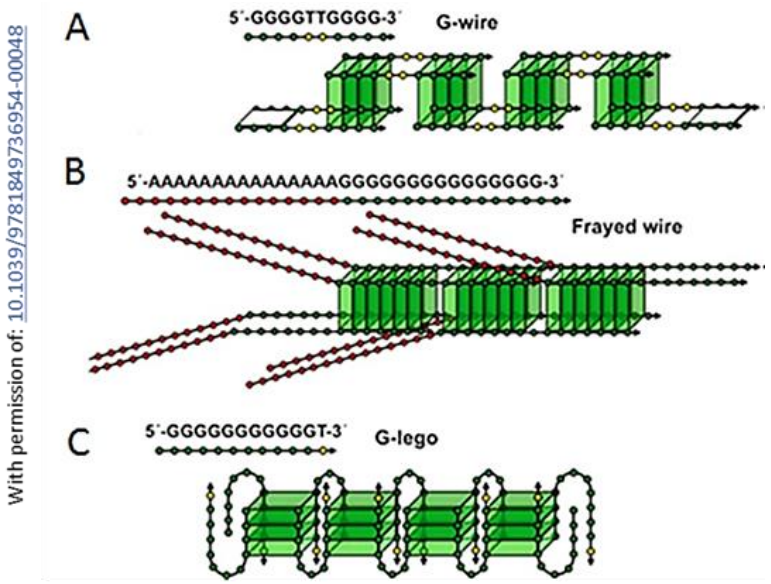

Figure 10. Models proposed for G-quadruplex supramolecular structures: (**A**) G-wires, (**B**) Frayed G-wires and (**C**) G-Legos.

2.2.6 *Hydrogels Utilizing DNA G-Quadruplexes*

The first observation of hydrogel on a G-quadruplex base was reported more than 100 years ago. Most hydrogels and their derivatives have been employed in the development of platforms for biomedical and bioengineering purposes. Hydrogels are characterized by crosslinked 3D networks of hydrophilic polymer chains able to retain a large amount of water due to their structure [53][54][55][56]. Compared with other types of biomaterials, hydrogels have a series of advantages, such as their biocompatibility and biodegradability. However, due to their low mechanical strength and fragile nature, the use of hydrogels is still limited. With the development of various synthetic strategies, it is now possible to design hydrogels with the required chemical composition and mechanical strength. For many years, hydrogels were prepared by following long and complex procedures, but instead, nowadays they

can be produced from completely artificial components, showing a remarkable stability under hard conditions such as high temperatures, acidic or basic environments and chemical agents. Some of the major growth areas include the use of injectable fillers in orthopaedic applications to guide the growth of osteoblasts and to improve vascular infiltration or in cell therapies such as immunomodulation [57][58][59][60]. Major advances in this field have resulted from the development of nanocomposite or hybrid hydrogels. In general, nanocomposite hydrogels are made by combining natural or synthetic nanomaterials with the hydrated polymer network [61][62]. These systems could represent a valid springboard for the use of multifunctional materials.

2.2.7 *Dynamic DNA G-Quadruplex Biosensors*

A biosensor is an analytical tool formed of an electrode combined with a DNA probe immobilized on its surface. As a result of the recognition of DNA-binding molecules (analytes) there is a signal transduction. Research in the field of oligonucleotide-based biosensors has become very prevalent in the last few decades. In fact, electrochemical biosensors based on oligonucleotides have attracted remarkable attention with respect to the tasks of monitoring and controlling specific DNA sequences related to microorganisms, viruses and inherited diseases and, also, of detecting the presence of infectious agents in various environmental matrices [63]. In literature two important types of electrochemical biosensors have been reported, G4 electrochemical aptasensors and hemin/G4 DNAzyme electrochemical biosensors.

The first type uses a MB-labelled TBA sequence, hybridised on gold electrodes, necessary for the electrochemical transduction. In the absence of any target, the immobilized TBA remains in part unfolded, allowing the electron transfer on the surface (Figure 11A). After the binding with thrombin, the formation of a TBA-quadruplex inhibits the electron transfer (Figure 11B). In this case, the biosensor proves very selective, being in fact able to identify thrombin directly in blood serum.

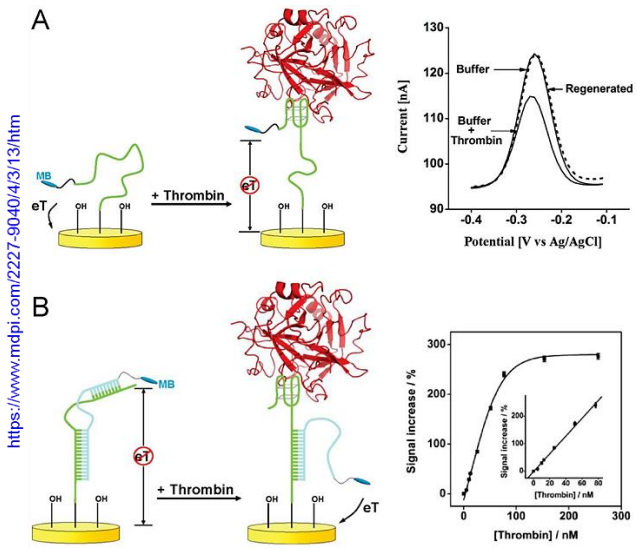

Figure 11. A structure-switching G-quadruplex electrochemical aptasensor for thrombin. A) signal off: thrombin binding reduces the current from the MB redox tag; and B) signal on: thrombin binding increases the current from the MB redox tag.

The second type of biosensor has proved to be the most popular and is characterized by an artificial DNA molecule (DNAzyme) composed of a harpin G-quadruplex DNA with intercalated hemin molecules. Hemin is a porphyrin containing iron, whose peroxidase activity increases in the presence of DNA. The strategy consists in the modification of the electrode by a harpin oligonucleotide that contains three segments.

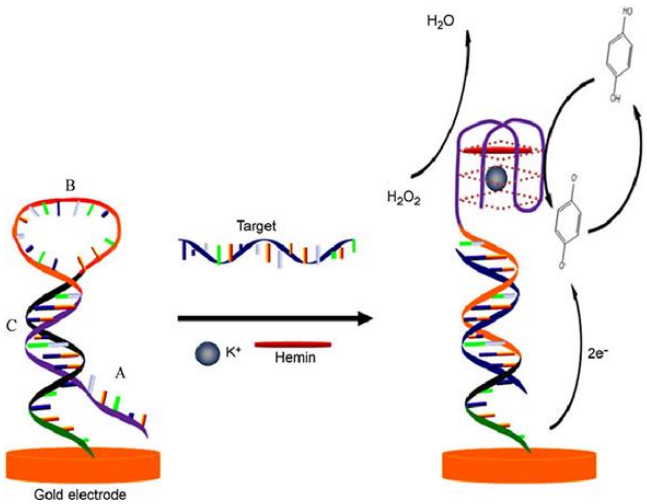

Figure 12. A hemin/G-quadruplex peroxidase-DNAzyme electrochemical biosensor.

Segment A is able to form a G-quadruplex structure that receives the hemin, used as an amplifier. Segment B is complementary to the target DNA, while segment C is complementary to the 5'-end of segment A. In the absence of any target, segment A remains hybridized with segment C, while, during the hybridization with the target, the harpin opens and releases segment A. This action produces with hemin the G-quadruplex-based DNAzyne that induces the oxidation and provides a quantitative measure for the detection of the target DNA [64][65] (Figure 12).

2.3 The aim of the work

G-Quadruplexes, characterized by a great structural polymorphism, can be recognized as critical in several fundamental regulatory regions for many biological processes, including DNA replication, transcription and translation. In fact, bioinformatics analysis of the human genome has confirmed their presence in telomeric regions, regulatory regions of viral genomes, immunoglobulin switch regions and promoter regions of different genes and oncogenes, such as c-MYC, VEGF, KRAS, c-kit, PDGF-A and c-Myb [29][13][66]. In this context, the use of G-Quadruplex-based aptamers represents a valid chemical structural alternative for the development of new biosensors or drugs which are able to control gene expression and genome stability. In particular, my research activity has been focused on: i) the synthesis and characterization of a new modified ODN called a *"double-end-linker"* (DEL-ODNs, 1, Scheme 1) capable of forming a stable monomolecular G-quadruplex in comparison with its tetramolecular counterpart; ii) the synthesis and characterization of a new modified ODN called a *"tetra-end-linker"* (TEL-ODNs, 1, Scheme 2) useful for the development of anti-HIV aptamers; iii) the study of an analogue of the Poly(ε-Lysine) peptide as a ligand of G-quadruplexes; and iv) the synthesis and characterization of a new supramolecular structure characterized by self-assemblies of G-rich sequences.

Objective 1. Study of the topology, stability and molecularity of a G-quadruplex linked to a "double-end-linker"

As is well known, G-quadruplexes can be versatile scaffolds for the construction of supramolecular structures and new biomaterials. Unfortunately, the formation of G-quadruplex scaffolds and their structuring in a linear or reticular topology is a complicated process to

control [66]. For these reasons, much effort has been devoted to the design of structural modifications in order to obtain polymeric or multimeric structures [67]. Several studies have shown that the presence of a tetra-branched-linker (TEL) can positively influence the stability of a G-quadruplex structure. In a previous work, the research group formed by Piccialli, Borbone and Oliviero has proposed the synthesis of a new class of monomolecular quadruplexes in which four d(TG$_4$T) strands are linked by the 3'-and 5'-ends of a *"tetra-end-linker"* (TEL-ODN) (Figure 13). Moreover, in a later paper, the influence of the linker size at the 3'- and 5'-ends has been studied (Figure 14) [68][69][70][43].

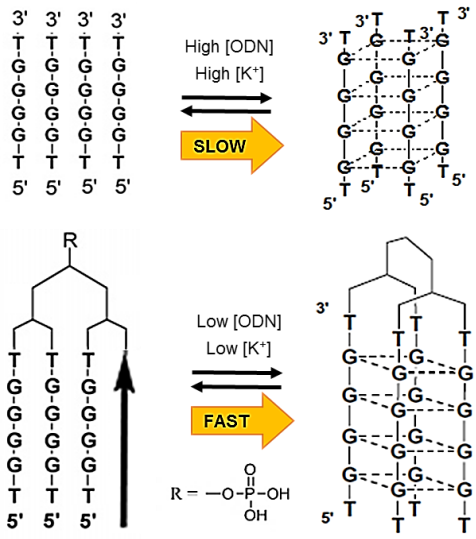

Figure 13. Schematic representations of four d(TG$_4$T) strands attached to a tetra-branched-linker at the 3'-ends.

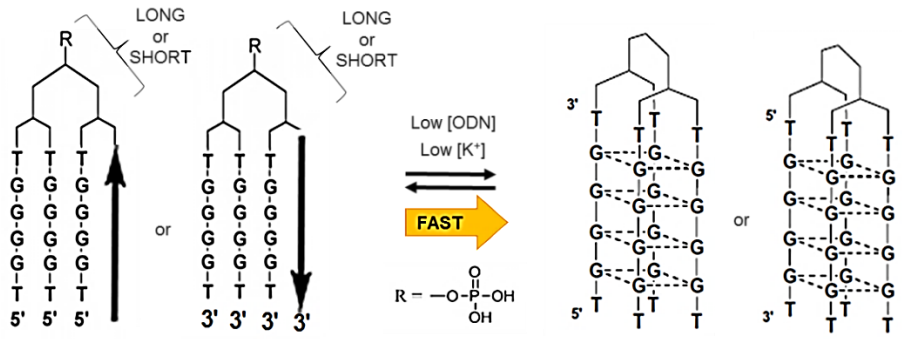

Figure 14. Schematic representations of four d(TG$_4$T) strands attached to a tetra-branched-linker with different sizes at the 3' and 5'-ends.

In this context my PhD research has been focused on the synthesis of a new analogue of TEL-$(TG_4T)_4$, here named a *"double-end-linker"* (DEL-ODN) characterised by the presence of two G-rich strands attached to symmetric bifunctional linkers of two different lengths by their 3'- and 5'-ends. Modulating the lengths of the linker has been performed for two reasons: i) to generate quadruplexes with a higher thermal and kinetic stability, and ii) to hinder the folding of the linker around the G-quadruplex structure, thus forcing the G-quadruplex strand polarity.

Synthesis and Purification of DEL-ONs. The syntheses of DEL-$(TG_4T)_2$ were performed on an automated synthesizer through standard solid-phase phoshoramidite chemistry. 50 mg of Controlled Pore Glass (CPG)-sulphone-resin support **1** (0.18 mmol/g) were used for each synthesis in the automated DNA synthesizer following standard phosphoramidite chemistry. 45 mg/mL solutions of phosphoramidites **4** and **5** (both in anhydrous CH_3CN) were used for the synthesis of **2L** and **2S**, respectively. This step was followed by reactions with 3'-phosphoramidite (for **D1L** and **D1S**) or 5'-phosphoramidite (for **D2L** and **D2S**) nucleotide building blocks (six cycles, 45 mg/mL in anhydrous CH_3CN). The coupling yields were consistently higher than 98% (by DMT spectrophotometric measurements). The solid support was then treated with concentrated aqueous ammonia solution for 7 h at 55 °C. The filtered solution and washings were concentrated under reduced pressure and purified by HPLC with an anion exchange column (Macherey–Nagel, 1000-8/46, 4.4 × 295 50 mm, 5 μm) eluted with a linear gradient from 0 to 100% B in 30 min; buffer A: 20 mM NaH_2PO_4, pH 7.0 containing 20% CH_3CN; buffer B: 1M NaCl, 20 mM NaH_2PO_4, pH 7.0, containing 20% CH_3CN; flow rate 1 mL/min. The collected products were desalted by gel filtration on a BioGel P2 column eluted with H_2O/ethanol (9:1, v/v) to obtain, after lyophilisation, pure **D1L,S** and **D2L,S** (92, 85 and 80, 88 OD_{260} units, respectively).The ON concentrations were determined spectrophotometrically in water at λ = 260 nm and 90 °C, using the molar extinction coefficient ε = 28,900 cm^{-1} M^{-1}calculated for the unstacked oligonucleotide by the nearest-neighbour method.

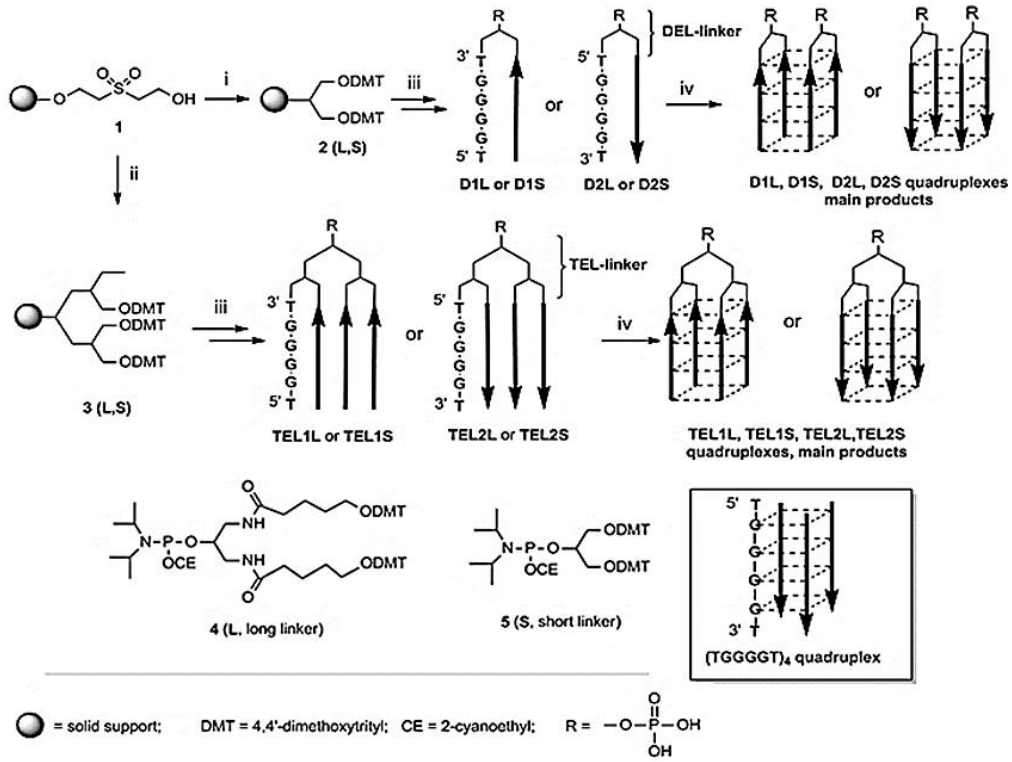

Scheme 1. i, coupling with the phosphoramidite linker **4** or **5**; **ii,** two sequential couplings with the phosphoramidite linker **4** or **5**; **iii,** solid-phase DNA synthesis by phosphoramidite chemistry; **iv,** annealing procedure in Na^+ or K^+ buffers.

CD and CD Thermal Analyses. As reported in the literature, the CD spectrum of a parallel G-quadruplex is characterized by a positive band at 264 nm and a negative band at 240 nm, whereas the CD spectrum of an antiparallel G-quadruplex shows a positive maximum at 295 nm and a negative minimum at 265 nm [71][72]. In order to demonstrate that **D1L,S** and **D2L,S** can adopt stable G-Quadruplex structures, circular dichroism (CD) studies and CD thermal denaturation experiments were performed, in comparison with the tetramolecular G-quadruplex $(TG_4T)_4$ and TEL-$(TG_4T)_4$. CD spectra were recorded at 5 °C at a 20 μM ON concentration in 100 mM K^+ and Na^+ buffers. We observed that **D1L,S** and **D2L,S** showed, in the K^+ buffer, CD profiles characterized by a positive and a negative Cotton effect at 264 and 249 nm, respectively, diagnostic of parallel-oriented G-quadruplex structures, independently of the orientation of the ON strands and the length of the linker (Figure 15). This behaviour had already been observed for TEL-$(TG_4T)_4$ G-quadruplexes which showed CD profiles

almost superimposable with those reported in Figure 15 [73][43].The CD spectra of **D1L,S** and **D2L,S,** recorded at 5 °C in 100 mM Na^+ buffer (Figure 15), essentially matched those obtained in the K^+ buffer.

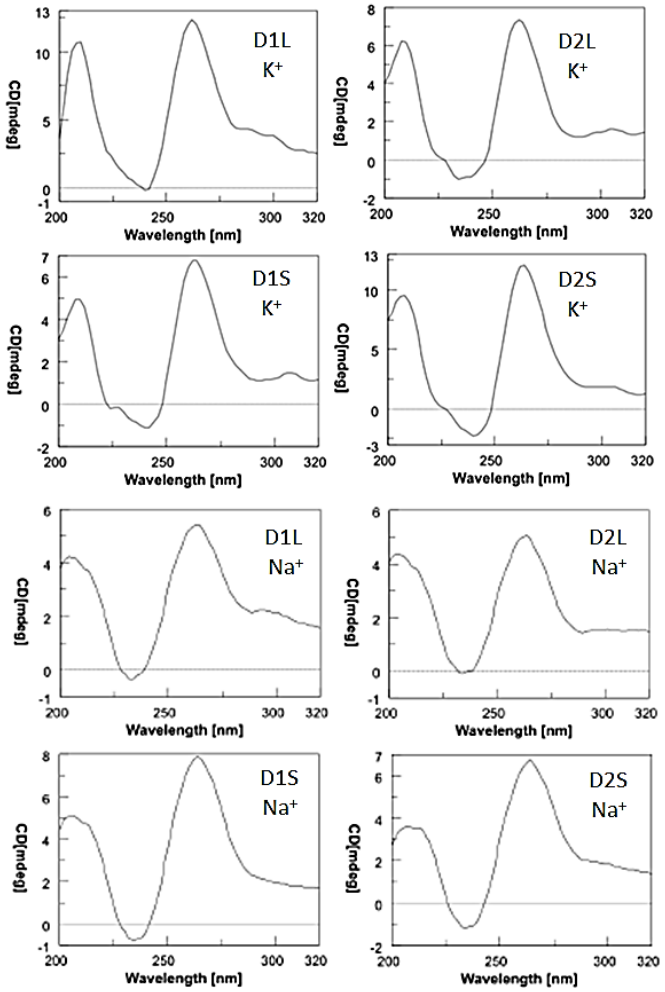

Figure 15. CD profiles of DELs formed by DEL-$(TG_4T)_2$: **D1L,S; D2L,S** in 100 mM K^+ and Na^+ buffer at 5 °C.

CD thermal denaturation experiments were performed monitoring the CD value (mdeg) at 263 nm within the range 5-80 °C with a 0.5 °C min^{-1} heating rate. In 100 mM K^+ buffer, all DEL-$(TG_4T)_2$ structures proved to be stable up to 80 °C, as indicated by the insignificant variation of the CD values up to this temperature. On the contrary, in the presence of 100 mM Na^+ buffer, the increase in temperature led to a significant reduction of the CD value and reliable half-transition temperature T½

(Table 2) were calculated from the resulting sigmoidal melting curves. These data indicated that DEL-$(TG_4T)_2$ structures formed by **D1L** and **D1S** have almost the same T½ values (55 and 54 °C, respectively) as the tetramolecular counterpart $(TG_4T)_4$ (58 °C) recorded in the same conditions. However, the T½ values of DEL-$(TG_4T)_2$ formed by **D2L** and **D2S** (64 °C for both) proved to be about 10 °C higher than those of **D1L** and **D1S**, indicating that the attachment of the DEL moiety at the 5' end of the TG_4T strand results in a DEL-$(TG_4T)_2$ structure provided with a higher thermal stability. Furthermore, the invariance of the T½ values between DEL-$(TG_4T)_2$ structures ncorporating either the long or short DEL reveals that the length of the DEL arms does not affect the thermal stability of the resulting DEL-$(TG_4T)_2$.

ODN	$T_{½}$ (K^+)	$T_{½}$ (Na^+)
D1L	> 80	55
D1S	> 80	54
D2L	> 80	64
D2S	> 80	64
TG_4T	> 80	58

Table 2. Melting temperatures (T½ values in °C) of **D1L,S; D2L,S** and $(TG_4T)_4$ annealed in 100 mM K^+ and Na^+ containing buffer (ƛ = 263 nm, 0.5 °C min^{-1} heating rate).

^{1}H-NMR Studies. The formation of a G-quadruplex structure is usually confirmed by the observation in the region (10–13 ppm) of N-1 imino protons of guanosines involved in the formation of G-tetrads. When guanosines are involved in the formation of a G-tetrad, their N-1 imino proton is engaged in the formation of a Hoogsteen-type hydrogen bond with the O-6 oxygen atom of the flanking guanosine and does not exchange with the protons of bulk water [74][75][76][77][78] (Figure 16a). ^{1}H NMR spectra (500 MHz) on DEL-$(TG_4T)_2$ were recorded in 100 mM K^+ buffer at 25,45 and 85 °C (Figure 17). The presence of strong imino proton signals (10.7–11.8 ppm) in all the recorded spectra confirmed that the four new DEL-$(TG_4T)_2$ structures fold into G-quadruplexes when annealed in K^+ buffer. Their NMR spectra were very similar to that of the tetramolecular parallel $(TG_4T)_4$ (Figure 16b) and that of the corresponding TEL$(TG_4T)_4$ [43]. In particular, imino proton signals were detectable up to 85 °C, in agreement with the CD thermal denaturation results reported in Table 2. Only in the case of **D1L** at 25

and 45 °C did we not observe any well-resolved imino proton signals, but only very broad signals resonating at the expected frequencies.

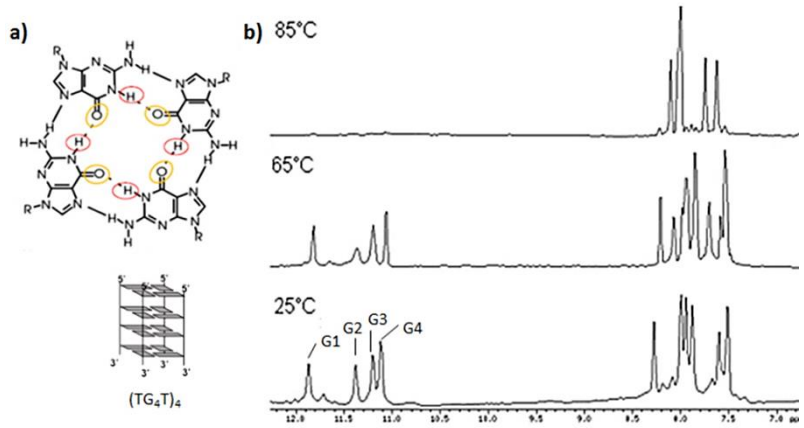

Figure 16. ^{1}H-NMR (500 MHz) spectrum of $(TG_4T)_4$ in K^+ buffer recorded at 25, 45 and 85 °C in H_2O/D_2O (9:1, v/v). Image taken from ref. 83 in the main text.

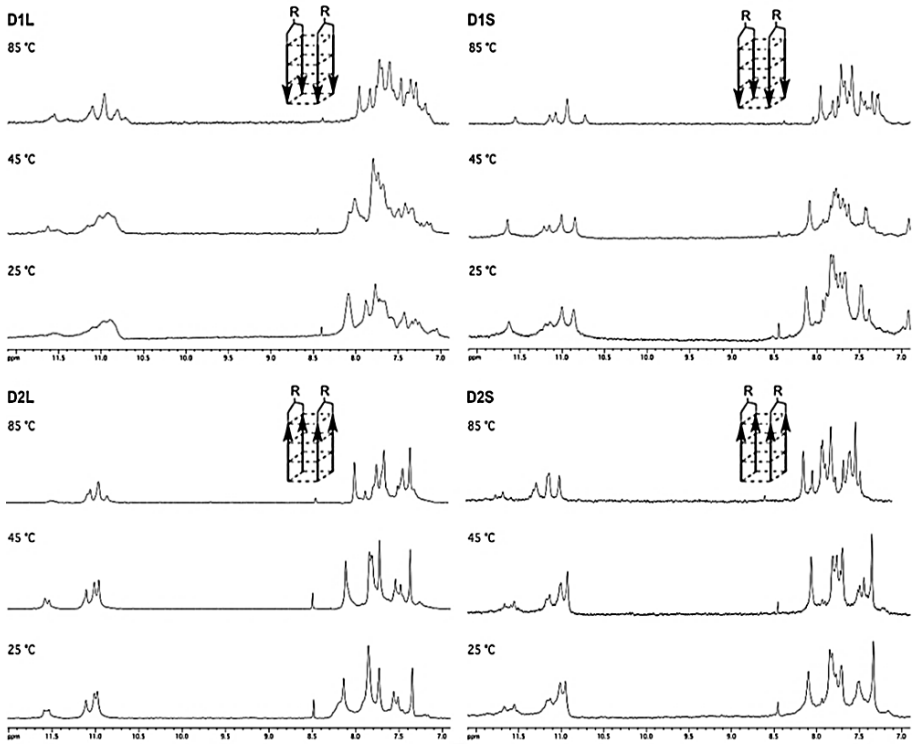

Figure 17. NMR spectra of **D1L,S; D2L,S** annealed in 100 mM K^+ buffer and recorded at 25, 45 and 85 °C.

Electrophoretic gel mobility studies. In order to obtain information about the propentisty of DEL-ODNs to fold into G-quadruplex structures and their molecularity, we performed a non-denaturing polyacrylamide gel Electrophoresis (PAGE) analysis. The final ON concentration of the samples was of 100 µM, and the electrophoretic analysis was carried out using a 12% polyacrylamide gel in 1x TBE buffer at pH 7.0.The PAGE bands of **D1L**, **D1S**, **D2L**, **D1S** migrated a little more slowly than those of the tetramolecular quadruplex $(TG_4T)_4$ (Figure 18a).This behaviour suggests that all DEL-ODNs principally form the bimolecular G-quadruplex complexes depicted in Scheme 1 but that the presence of traces of higher MW complexes cannot be ruled out.

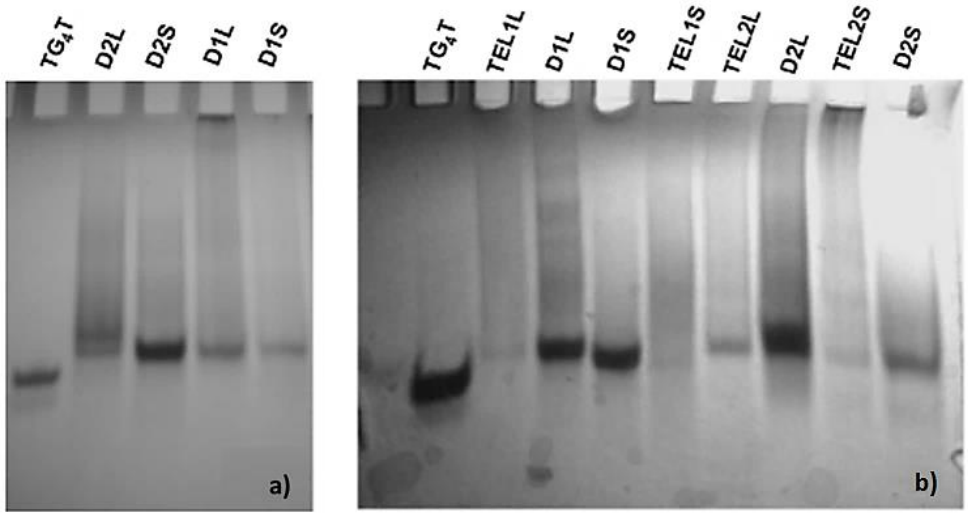

Figure 18. PAGE analysis of the complexes formed by the DEL-$(TG_4T)_2$ ODNs in comparison with $(TG_4T)_4$ and with the complexes formed by TEL-$(TG_4T)_4$ ODNs. All samples were annealed in 100 mM K^+ buffer.

In particular, for **D1L** and **D2L** (the long linkers), we observed a significant smearing, which suggests the presence of G-quadruplex aggregates or polymeric species, whereas for **D1S** and **D2S** (the short linkers), we observed a reduced smearing and better-defined bands (Figure 18b).

Size exclusion chromatography studies. All DEL-ODNs were analyzed by Size Exclusion Chromatography (SEC-2000 Column) at room temperature (Figure 19) with the aim of further investigating the molecularity of the resulting complexes. For this purpose, the tetramolecular G-quadruplex formed by $(TG_4T)_4$ and the G-quadruplex

multimers formed by the $(^{5'}\text{-CGG}^{3'\text{-}3'}\text{TGGC}^{\text{-}5'})_{2\text{-n}}$ sequence [79], were used as size markers for the monomeric (**Q_1**) and multimeric G-quadruplex building blocks (**Q_{2-n}**), respectively. (Figure 19). All species formed by DEL-ONs showed a similar retention time (t_R) of around 14 min. whereas, compared to the tetramolecular quadruplex $(TG_4T)_4$, the t_R is slightly lower.

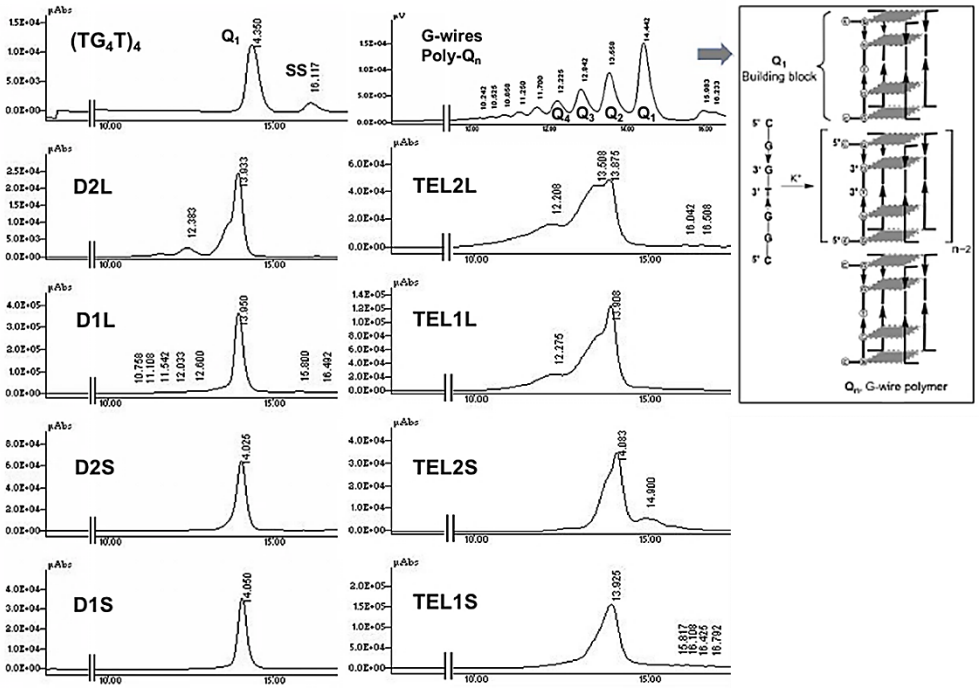

Figure 19. HPLC-SEC profiles of the complexes DEL-$(TG_4T)_2$ and TEL-$(TG_4T)_4$ in comparison with those of $(TG_4T)_4$ (**Q_1**) and **$Q_{2\text{-n}}$** G-wires.

In particular, **D1L** and **D2L** show small numbers of complexes having a higher molecular weight (Figure 19, right column). For the species corresponding to the TEL-ODNs, the t_R were almost superimposable with those of the corresponding peaks obtained from the DEL-ODNs. These results suggest that the size of the linkers and the polarity of the linkages have a negligible effect on the t_R for both complexes, thus implying a similar 3D conformation. However, the comparison of the HPLC-SEC profiles indicate a higher propensiity of all TEL-ODNs to form higher molecular weight complexes, in particular for **TEL1L** and **TEL2L**.

Isolation and analysis of higher molecular weight species produced by D2L. To obtain further structural information on the higher molecular weight complexes, we decided to isolate in a single fraction the peaks at a higher t_R of the HPLC-SEC fractionation of **D2L** (Figure 20a) and reinject them on the same column 24 hours after storage at 4 °C. The resulting HPLC profile (Figure 20b) presented four partially resolved peaks, which we attributed to the bimolecular DEL-ODNs (**Q_1**, t_R = 13.7 min) and to the DEL-G-quadruplex multimers incorporating two (**Q_2**, t_R = 12.9 min), three (**Q_3**, t_R = 12.1 min) and four (**Q_4**, t_R = 11.4 min) G-quadruplex scaffolds, respectively. (Figure 20b).

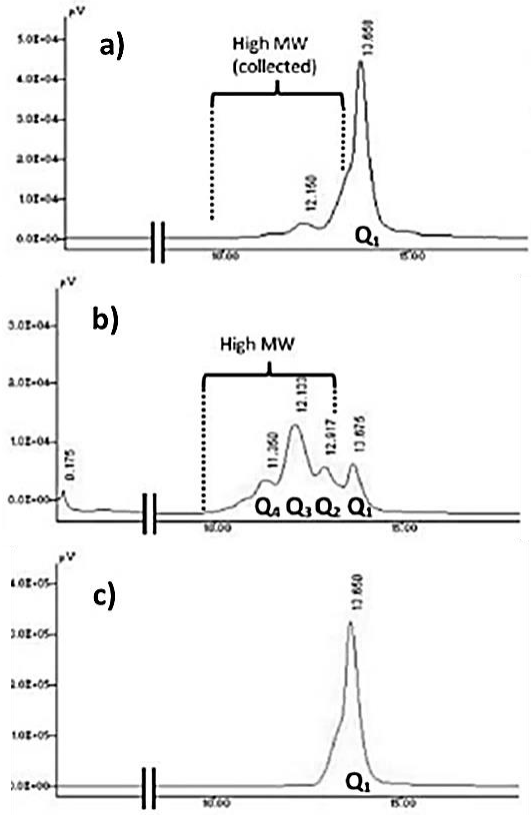

Figure 20. HPLC-SEC profiles of: (**a**) the complexes formed by **D2L**; (**b**) after reinjection of the higher molecular weight species formed by **D2L** collected as shown in panel (**a**); and (**c**) after reinjection of the purified **DEL-Q_1** complex formed by **D2L** collected as shown in panel (**a**).

To establish the conformation of the higher molecular weight complex CD analysis was performed. The CD spectrum obtained, was almost superimposable on that of the isolated **Q_1** species (Figure 21). We

attributed the small amount of **Q_1** detected in Figure 20b to the partial recovery of this species during the first HPLC-SEC fractionation and not to the dissociation of the higher molecular weight DEL-G-quadruplex multimers. This hypothesis was corroborated by the HPLC-SEC profile shown in Figure 20c (obtained by injecting the **Q_1** peak isolated from the first HPLC fractionation of **D2L**), which did not show any trace of the higher molecular weight complexes. These data confirmed the stability of **Q_1** and the multimeric species isolated by **D2L**.

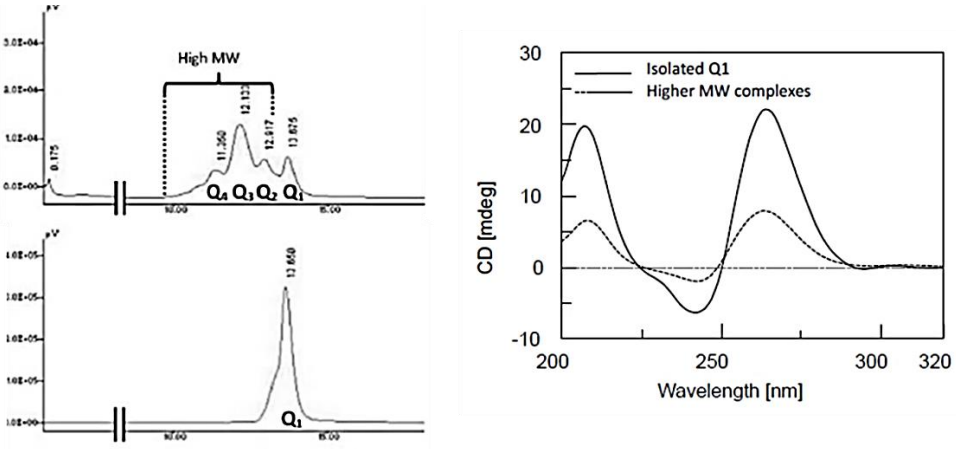

Figure 21. CD profiles of **DEL-Q_1** and the higher molecular weight species obtained by HPLC-SEC fractionation of **D2L** (100 mM K^+ containing buffer, 5 °C).

The results described in this paper confirm the potential of a new kind of G-quadruplex, named DEL-ODN to fold into a stable intramolecular G-quadruplex ($T_{½}$ > 80 °C in 100 mM K^+ buffer, pH 7.0) independently of the linker size and the polarity of the strands that compose it. In particular, for **D2L**, which was obtained by linking the 5'-end of two d(TG_4T) strands to the long linker, we have demonstrated the formation of G-quadruplex multimers based on reticulated G-quadruplex building blocks (like those shown in Figure 22), rather than end-to-end stacked G-quadruplex building blocks (like the **Q_n** species reported in Figure 19).

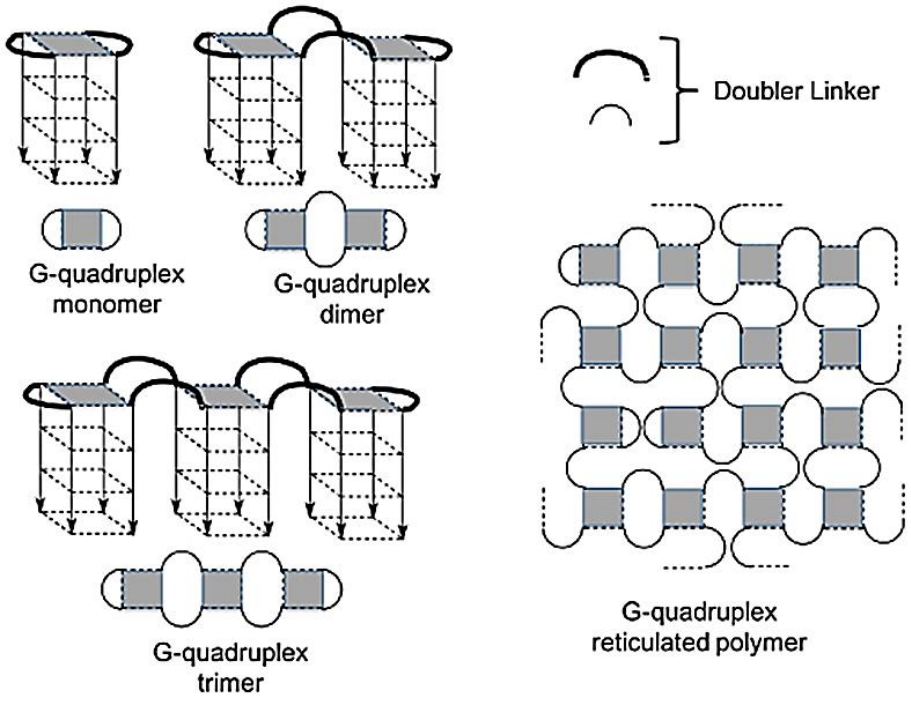

Figure 22. Schematic representation of the parallel G-quadruplex obtainable from the self-assembly of DEL-ODNs. The first three complexes having the lowest molecular weight are shown on the left. The hypothetical topology of the G-quadruplex supramolecular nanostructure based on the reticulated parallel DEL-G-quadruplex is shown on the right.

EXPERIMENTAL SECTION

Reagents and equipment

The chemicals and solvents were purchased from Sigma-Aldrich (Milan, Italy). The reagents and phosphoramidites for the DNA syntheses were purchased from Glen Research (Sterling, VA, USA). The DEL linker **2**, the TEL linker **3** and all the ODNs were assembled on a PerSeptive Biosystems (Framingham, MA, USA) Expedite DNA synthesizer using standard phosphoramidite chemistry. The HPLC analyses and purifications were performed with a Jasco (Jasco Europe Srl, Cremella, LC, Italy) The PU2089 pump system equipped with an UV detector model 2075 Plus. CPG-resin **1** and the linkers **4** and **5** were purchased from Glen Research. The UV spectra were recorded using a Jasco V-530 spectrophotometer. The thermal denaturation experiments were performed and the CD spectra obtained with a Jasco715 CD spectrophotometer equipped with a Jasco PTC-348-WI temperature controller unit. The NMR spectra were recorded either on a Varian (Palo Alto, CA, USA) Unity Inova 500 MHz spectrometer equipped with a broadband inverse probe with a z-field gradient or on a Varian Unity INOVA 700 MHz spectrometer equipped with a triple resonance cryoprobe and processed using the VarianVNMR and iNMR (http://www.inmr.net) software packages. The PAGE bands were visualised on a Bio-Rad Laboratories (Segrate, MI, Italy) Gel Doc™ XR+ image system.

Syntheses and purifications of DEL-ODNs (D1L,S and D2L,S)

50 mg of Controlled Pore Glass (CPG) support **1** (0.18 mmol/g) were used for each synthesis in the automated DNA synthesizer following standard phosphoramidite chemistry. 45 mg/mL solutions of phosphoramidite **4** or **5** (both in anhydrous CH_3CN) were used for the synthesis of **2L** or **2S**, respectively. This step was followed by reactions with 3'-phosphoramidite (for **D1L** and **D1S**) or 5'-phosphoramidite (for **D2L** and **D2S**) nucleotide building blocks (six cycles, 45 mg/mL in anhydrous CH_3CN). The coupling yields were consistently higher than 98% (by DMT spectrophotometric measurements). The solid support was then treated with conc. aq. ammonia solution for 7 h at 55 °C. The filtered solution and washings were concentrated under reduced pressure and purified by HPLC with an anion exchange column (Macherey–Nagel, 1000-8/46, 4.4 × 50 mm, 5 µm) eluted with a linear gradient from 0 to 100% B in 30 min; buffer A: 20 mM NaH_2PO_4, pH 7.0 containing 20% CH_3CN; buffer B: 1M NaCl, 20 mM NaH_2PO_4, pH 7.0, containing 20% CH_3CN; flow rate 1 mL/min. The collected products were desalted by gel filtration on a BioGel P2 column eluted with H2O/ethanol (9:1, v/v) to obtain, after lyophilisation, pure **D1L,S** and **D2L,S** (92, 85 and 80, 88 OD_{260} units, respectively). The ON concentrations were determined spectrophotometrically in water at λ = 260 nm and 90 °C, using the molar extinction coefficient ε = 28,900 cm^{-1} M^{-1} for DEL-$(TG_4T)_2$ and ε = 57,800 cm^{-1} M^{-1} for TEL-$(TG_4T)_4$ calculated for the unstacked ODNs by the nearest-neighbour method.

Preparation of the G-quadruplexes (annealing)

All the G-quadruplexes were formed by dissolving the DEL-ODNs, TEL-ODNs or TG_4T in the K^+ buffer 90 mM KCl, 10 mM KH_2PO_4, pH 7.0) or Na^+ buffer (90 mM NaCl, 10 mM NaH_2PO_4, pH 7.0) and heating to 95 °C for 5 min and then cooling at 4 °C rapidly (annealing). All samples were stored at 4 °C for 24 hours before the analyses. The solutions were equilibrated at 25 °C for 2 hours before the experiments were performed.

PAGE experiments

The native gel electrophoresis experiments were performed on 12% polyacrylamide gels containing 1× TBE buffer, pH 7.0 with 30 mM KCl, at 4 °C, 120 V for 2 hours. The samples were loaded at a final ON concentration of 100 μM; glycerol was added (10% final) to facilitate sample loading in the wells. The bands were finally visualized by UV-shadowing or by SYBR Green staining.

CD experiments

The CD spectra and CD thermal profiles were recorded in 0.1 cm optical path quartz cuvettes (100 nm/min scanning speed, 1s response time). The spectra were recorded in triplicate at 5 °C from 200 to 320 nm. The CD samples were prepared in the above reported 0.1 M K^+ or Na^+ buffer at the final single strand concentration of 20 μM. The buffer baseline was subtracted from each spectrum. The CD thermal experiments were performed monitoring the CD value (mdeg) at 263 nm in the temperature range 5–95 °C at 0.5 °C min^{-1} heating rate.

HPLC-SEC analyses

The HPLC-SEC analyses and purifications were performed using a Phenomenex (Bologna, Italy) Yarra SEC-2000 column (300 × 7.8 mm, 3 μm) eluted with 90 mM KCl and 10 mM KH_2PO_4/CH_3CN (80:20, v/v), flow rate 0.6 mL/min, UV-detector at 260 nm. The analyses were performed at room temperature.

NMR experiments

The NMR samples were prepared at a 1.8 mM single strand concentration in 200 mL of 100 mM K^+ solution (90 mM KCl, 10 mM KH_2PO_4, pH 7.0, 9:1 H_2O/D_2O). The water suppression was achieved by including a double pulsed-field gradient spin-echo (DPFGSE) module in the pulse sequence prior to acquisition. The NMR spectra were acquired as 16 data points with a recycle delay of 1.0 s at 25, 45, and 85 °C and the spectra were apodized with a shifted sine bell squared window function.

Objective 2. Anti-HIV aptamer based on a G-quadruplex linked to a tetra-end-linker

The human immunodeficiency virus (HIV) is an RNA lentivirus, a subgroup of retroviruses, able to attack the immune system, progressively destroy certain white blood cells and thereby cause the acquired immunodeficiency syndrome (AIDS).The outer shell of the virus is called an "*envelope"* and this is covered by *"glycoproteins"* gp120 and gp41, which allow HIV to lock onto the CD4 receptor of the CD4 T cells (monocytes, macrophages, T-lymphocytes and dendritic cells) and enter into the cell. The process of producing new viruses happens in two stages, attachment and fusion (Figure 23). When HIV makes contact with a CD4 cell, the gp120 locks onto the CD4 receptor and another co-receptor, CCR5 or CXCR4, and the gp41 protein fuses the HIV envelope with the cell wall.

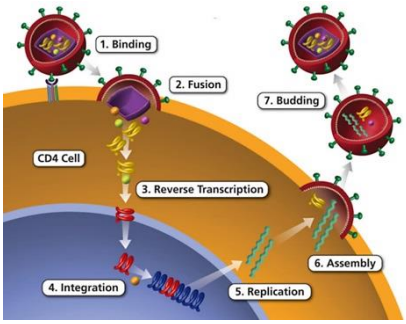

Figure 23. The life-cycle of HIV replication.

This process of fusion allows the HIV capsid (a cone-shaped structure that contains the nucleus) to enter the CD4 cell. After fusion, the virus releases RNA, its genetic material, into the host cell and an HIV enzyme called a reverse transcriptase converts the single-stranded HIV RNA into double-stranded HIV DNA. The newly formed HIV DNA enters the host cell nucleus, where an HIV enzyme called an integrase "hides" the HIV DNA within the host cell's own DNA. The integrated HIV DNA is called a provirus and this provirus may remain inactive for several years, producing few or no new copies of HIV. When the host cell receives a signal to activate, the provirus uses a host enzyme called the RNA polymerase to create copies of the HIV genomic material, ie shorter strands of RNA called messenger RNA (mRNA) used as a template to make long chains of HIV proteins. Subsequently an HIV enzyme called a protease cuts the long chains of the HIV proteins into smaller individual proteins that will come together with copies of the HIV's RNA genetic material forming new assemblies. The assembled

virus pushes out from the host cells and the new copies of HIV can now move on to infect other cells.
In the last two decades, many drugs based on G-rich aptamers have been identified as promising antiviral agents, because they are able to block: i) the binding of the virus and its entry into the target cell; ii) the activity of the HIV reverse transcriptase; and iii) the integration of virus. In 1994 Hotoda [80] reported the first anti-HIV aptamers against the V3 loop of gp120. The sequence $^{5'}$-TGGGAG-$^{3'}$ ODN (known as ‘‘Hotoda’s sequence’’) was chemically modified to improve its resistance against nucleases by capping the 5’-end with dimethoxytrityl (DMT) or 3,4-dibenzyloxybenzyl groups, and the 3’-end with a 2-hydroxy-ethyl-phosphate group [81]. Biophysical studies have established that the presence of aromatic groups at the 5’-end and/or the 3’-end of the Hotoda’s sequence dramatically enhances the rate of formation of the G-quadruplex complexes. In 2010, with the aim of overcoming the unfavourable entropic factor and of stabilizing Hotoda’s analogues, Oliviero *et al.* proposed the *“tetra-end-linker”* (TEL) strategy [44]. Compared to the Hotoda’s sequence, the new modified aptamers showed an improvement in their thermodynamic parameters and biological activity, especially when the 5’-end of the TEL-ODN was conjugated with a lipophilic group (TBDPS) (Figure 24A, EC_{50} = 82 nM). In 2012 D’Atri *et al.* reported the chemico-physical and biological characterization of a mini-library of Hotoda analogues based on the TEL G-quadruplex structure [82]. The study confirmed that all new TEL-(TGGG**X**G)$_4$ (with **X** = A, G, T or C) aptamers retained a potent anti-HIV-1 activity in the nanomolar range. In particular, the replacement of adenosine by cytosine results in an improvement of the anti-HIV activity (Figure 24B, EC_{50} = 39 nM). Considering these result and literature reports about bioactive higher order aptamers [83], we decided to synthesize three new TEL-ODNs (**1-3**) based on the ODN sequence $^{5'}$-CGGAGG-$^{3'}$ (Figure 25, above). This sequence was chosen with the aim of studying the effect of dimerization on the anti-HIV activity. In fact, the 6-mer sequence is endowed with the following properties i) it contains two GG repeats required for the formation of stable G-quadruplex species and ii) it includes the $^{5'}$-CGGA-$^{3'}$sequence allowing for 5’-5’ end-stacking dimerization [84]. In **1-3** each arm of the TEL moiety was linked to the 3’-end on the ODN sequence, whereas the 5’-end maintained the hydroxyl group unprotected (**1**) or received a capping with a dimethoxy-trityl (DMT) group (**2**) or a glucosyl-4-phosphate group (pGlc) (**3**) (Figure 25, below).

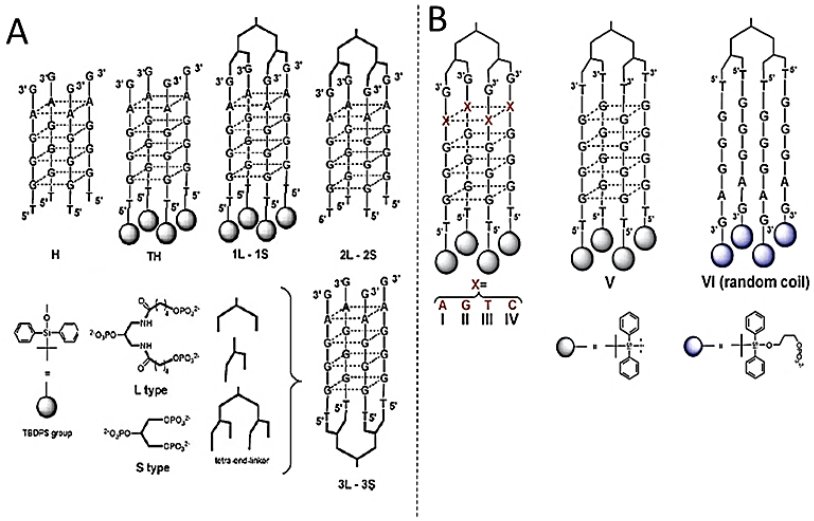

Figure 24. (**A**) Schematic representation of the investigated TEL-ODNs; (**B**) Mini-library of TEL-Hotoda analogues.

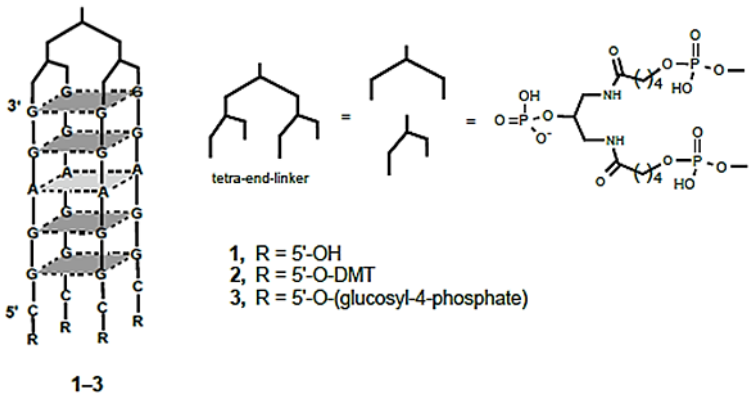

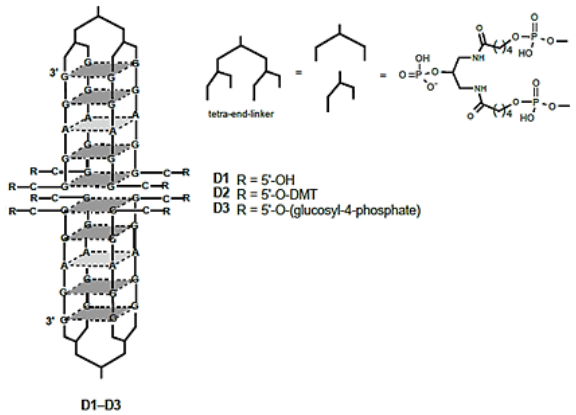

Figure 25. Schematic representation of the TEL-G-quadruplex monomers (**1–3**) and dimers (**D1–D3**).

Synthesis and Purification of the DEL-ONs. The syntheses of the TEL-ODNs **1-3** were performed on an automated synthesizer through standard solid-phase phoshoramidite chemistry. To obtain the final product TEL-ODN **2**, the final DMT deblocking step was excluded from the synthesis protocol. However, in the case of TEL-ODN **3**, an additional coupling step was inserted at the completion of the synthesis, using an obtained DMT-protected glucose phosphoramidite derivative. After the automated synthesis, the ODNs were detached from the support and deprotected by treatment with concentrated aqueous ammonia solution for 7 h at 55 °C. The filtered solution and washings were concentrated under reduced pressure and purified by HPLC with an anion exchange column (Macherey–Nagel, 1000-8/46, 4.4 × 295 50 mm, 5 μm) eluted with a linear gradient from 0 to 100% B in 30 min; buffer A: 20 mM NaH_2PO_4, pH 7.0 containing 20% CH_3CN; buffer B: 1M NaCl, 20 mM NaH_2PO_4, pH 7.0, containing 20% CH_3CN; flow rate 0.3 mL/min. The collected products were desalted by gel filtration on a BioGel P2 column eluted with H_2O/ethanol (9:1, v/v) to obtain, after lyophilisation, pure TEL-ODNs **1-3**. The ON concentrations were quantified spectrophotometrically in water at λ = 260 nm and 90 °C, using the molar extinction coefficient of $^{5'}$-CGGAGGG-$^{3'}$ (ε = 61,500 cm^{-1} M^{-1}) as calculated with the nearest-neighbour model multiplied by 4 (the number of strands in each TEL-ODN complex, ε = 246,000 cm^{-1} M^{-1}) .

CD and CD Thermal Analyses. The different interactions between guanosines within parallel or antiparallel G-quadruplex conformations and the circularly polarized light generated by different CD profiles create distinctive signatures of the different G-quadruplex topologies. In order to demonstrate that TEL-ODNs **1-3** can adopt a stable G-quadruplex structure, circular dichroism (CD) studies and CD thermal denaturation experiments were performed. The CD spectra of all the TEL-ODNs recorded at 5 °C at a 10 μM ON concentration in 1.0 M K^+ buffer showed a large positive band at 264 nm and a small negative band al 220 nm, indicative of the presence of head-to-tail stacked G-tetrads, as found in parallel G-quadruplex structures (Figure 26A). To evaluate the thermal stability of the complexes, CD thermal denaturation-renaturation experiments were performed, monitoring the CD value (mdeg) at 264 nm in the range 5-90 °C with a 0.5 °C min^{-1} heating rate. As reported in Figure 26B, due to the incomplete unfolding at 90 °C, the resulting melting curves did not allow the determination of the melting temperature but only the T½, which was 65 °C for all three

TEL-ODNs. The presence of a small hysteresis, in all studied systems, suggests the presence of an aggregation process, attributable to the formation of higher order G-quadruplex structures. It is probable that the TEL prevents the four strands from dissociating completely and speeds up the reannealing process.

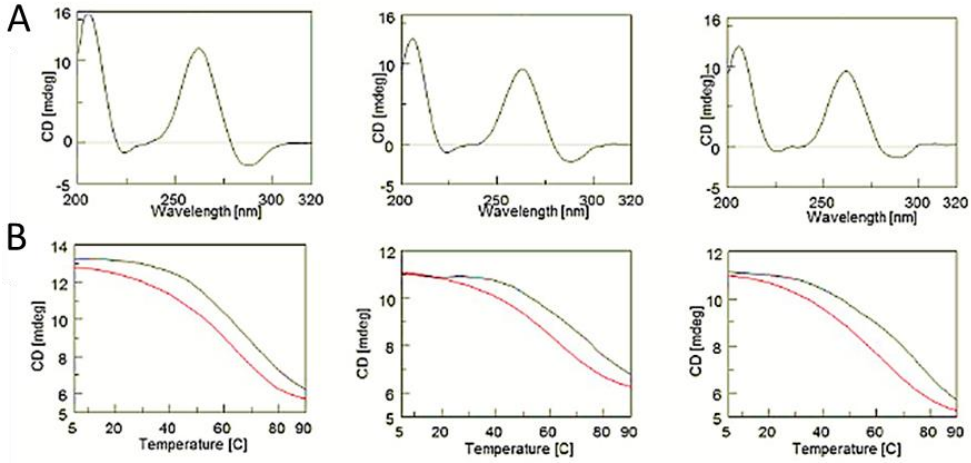

Figure 26. (**A**) CD spectra and (**B**) CD melting (black) and annealing (red) curves of **1–3** recorded in 1 M K^+ buffer.

NMR Analysis. The formation of G-quadruplex assemblies for TEL-ODNs **1-3** in K^+ buffer was confirmed by water-suppressed ^{1}H-NMR spectroscopy. As reported in the literature, we could observe, in the 10.5-11.5 ppm NMR region, the presence of one exchange-protected H1 imino proton signal for each G2, G3 and G5 tetrad and two signals for the G6 tetrad because of the partial loss of symmetry induced by the binding to the TEL arms. (Figure 27). In addition, in the 9.2 ppm region, we could observe the presence of an exchange-protected amino proton signal attributed to the presence of a stable A-tetrad in all the three TEL-ODNs. From the NMR data, it appears that the insertion of a glucose-phosphate group did not significantly alter the size and symmetry of the resulting G-quadruplex structure, whereas the capping with the DMT group promoted a loss of symmetry in the G-quadruplex structure. Unfortunately, due to the almost perfect symmetry of the dimeric complex TEL-ODNs **D1-D3** and to the insufficient signal resolution, it was not possible to obtain information on the relative amounts of the dimeric G4 complexes **D1–D3** relative to the corresponding monomeric G-quadruplexes **1–3**.

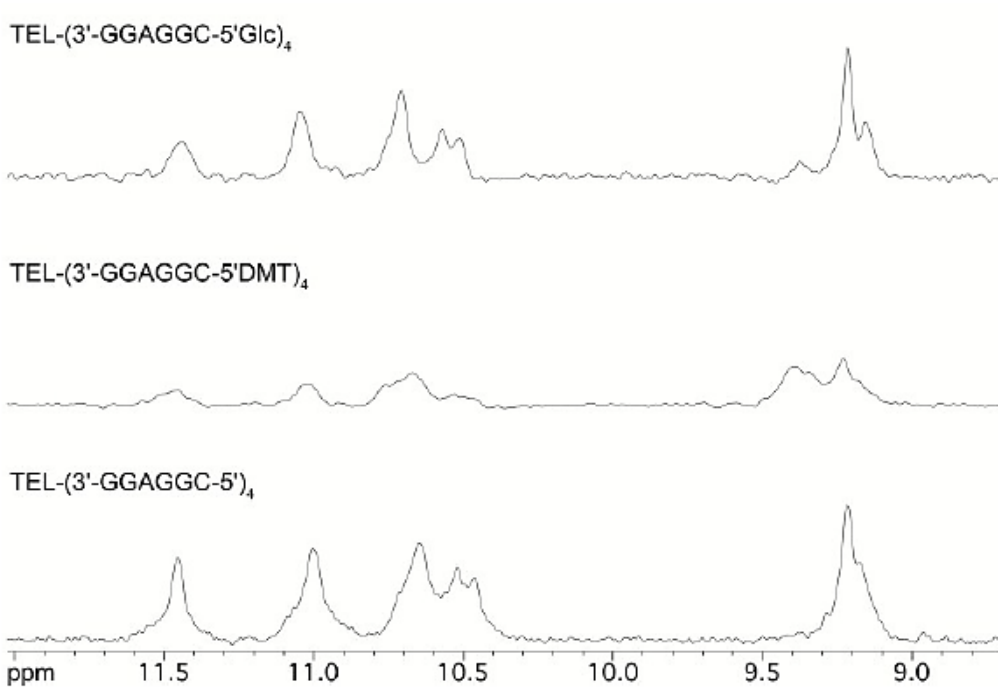

Figure 27. Imino and amino proton regions of the ^{1}H NMR spectra of **1–3** recorded in 1M K^{+} buffer.

HPLC-Size exclusion chromatography (HPLC-SEC). To corroborate the PAGE results and to estimate the number of dimeric TEL-ODNs, we performed HPLC Size Exclusion Chromatography (HPLC-SEC). For this purpose, the monomeric G-quadruplexes formed by $(^{5'}\text{-}TG_4T^{\text{-}3'})_4$ and the dimeric G-quadruplex $(^{5'}\text{-}CGGAGGT^{\text{-}3'})_8$ were used as size markers. The HPLC-SEC profiles confirmed the formation of two distinct main assemblies for all three TEL-ODNs corresponding to the dimeric TEL-ODNs **D1-D3** with a retention time (t_R) of around 19 min and the monomeric TEL-ODNS **1-3** with a retention time (t_R) of around 20 min. The relative number of dimeric TEL-ODNs **D1-D3** vs. the corresponding number of monomeric assembly TEL-ODNS **1-3** was assessed by means of a comparison of the area of the corresponding HPLC peaks (Figure 28).

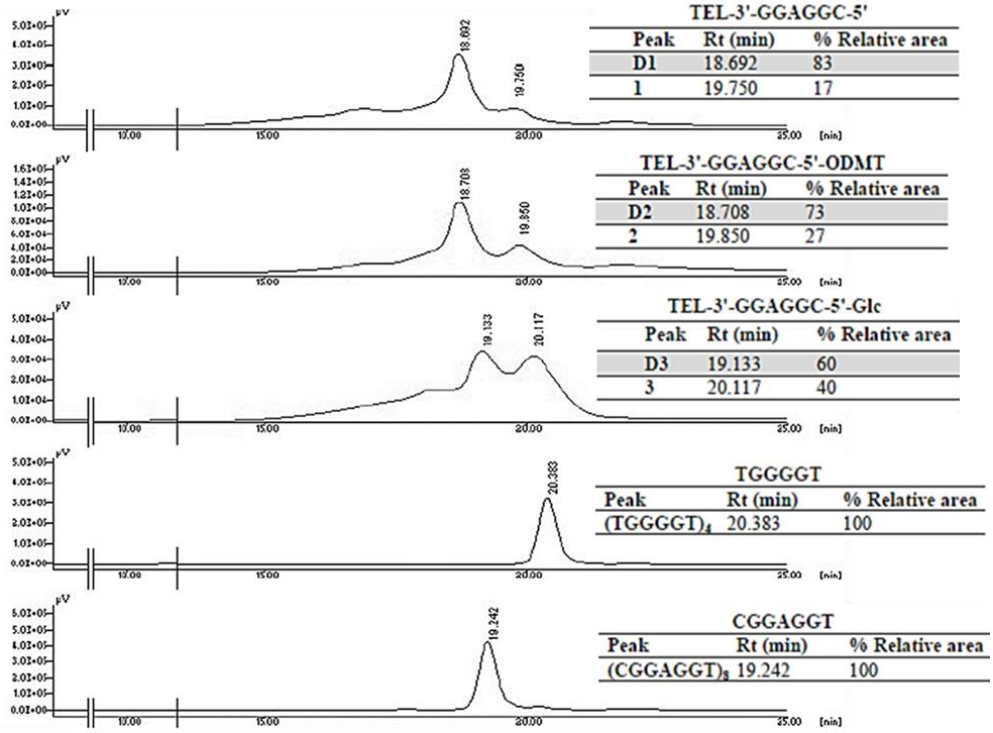

Figure 28. HPLC-SEC profiles of the TEL-ODNs **1–3** and monomeric ($^{5'}$-TG$_4$T-$^{3'}$)$_4$ and dimeric ($^{5'}$-CGGAGGT-$^{3'}$)$_8$ size markers annealed in 1.0 M K^+ buffer and the relative areas.

Electrophoretic gel mobility studies. To obtain information on the molecular size of the TEL-ODN **1-3** complexes, we performed a non-denaturing polyacrylamide gel electrophoresis (PAGE) analysis. For this purpose, we compared the electrophoretic mobility of: i) TEL-($^{3'}$-GGAGGC-$^{5'}$)$_4$ (**1**, lane 4); ii) TEL-($^{3'}$-GGAGGC-$^{5'\text{-DMT}}$)$_4$ (**3**, lane 5) and iii) TEL-($^{3'}$-GGAGGC-$^{5'\text{-pGlc}}$)$_4$ (**2**, lane 6) with that of iv) ($^{5'}$-TG$_4$T-$^{3'}$)$_4$ (lane 2) and v) ($^{5'}$-CGGAGGT-$^{3'}$)$_8$ (lane 3), used as size markers for the monomeric and dimeric G-quadruplexes (Figure 29). The migration of TEL-ODNs **1** and **2** (lanes 4 and 5 respectively), like that of ($^{5'}$-CGGAGGT-$^{3'}$)$_8$ (lane 3), suggest that these sequences can form higher order assemblies On the other hand, the migration profile of TEL-ODN **3** (lane 6) showed the presence in solution of both species, the dimer TEL-ODN **D3** (major band migrating like a dimeric G-quadruplex) and the monomeric TEL-ODN **3** (less sharply defined band, having a mobility similar to the monomeric G-quadruplex). Either of the three modifications at the 5'-end is able to affect the migration properties in the polyacrylamide gel.

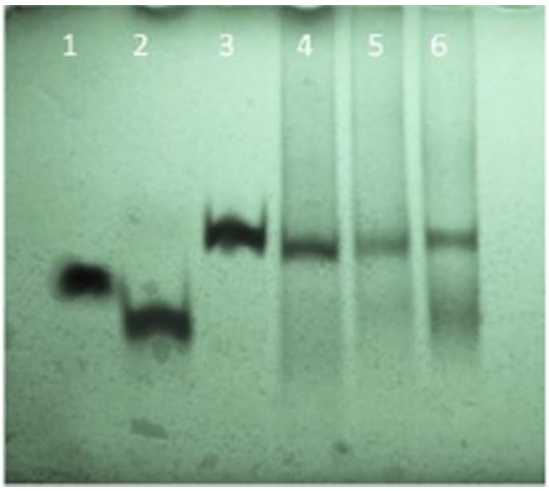

Figure 29. Non-denaturing PAGE analysis for the sequences ($^{5'}$-TG$_4$T-$^{3'}$)$_4$ (lane 2); ($^{5'}$-CGGAGGT-$^{3'}$)$_8$ (lane 3); TEL-($^{3'}$-GGAGGC-$^{5'}$)$_4$ (**1**, lane 4);TEL-($^{3'}$-GGAGGC-$^{5'\text{-DMT}}$)$_4$ (**3**, lane 5); and TEL-($^{3'}$-GGAGGC-$^{5'\text{-pGlc}}$)$_4$ (**2**, lane 6) annealed in 1 M K$^+$ containing buffer. Dye (lane 1).

Anti-HIV activity. To assess the effect of dimerization and 5'-capping with each lipophilic or hydrophilic moiety on the anti-HIV activity, we tested the inhibitory effect of **1-3** on the HIV-1-induced cytopathicity in MT-4 cells. As reported in Table 3, the 5'-DMT capped TEL-ODN **2** was the only compound which is able to block the HIV-induced cytopathogenic effect with EC_{50} of 0.54 μM and CC_{50} of 3.3 μM with a maximum protection between 70 and 76%. Different situations apply for TEL-ODN compounds **1** and **3,** which reached maximum protections of 24% and 33%, respectively, at the highest tested concentration of 5 μM.

Compound	EC_{50} (μM)[a,c]	CC_{50} (μM)[b,c]	Max % Protection
1	>5	>5	4-24%
2	0.54 ± 0.04	3.3 ± 1.3	70-76%
3	>5	>5	8-33%

[a]EC_{50}: compound concentration required to achieve 50% protection of MT-4 cells against HIV-1(III_B)-induced cytopathicity. [b]CC_{50}: compound concentration required to reduce the viability of mock-infected cells by 50%. [c]All data represent mean values (standard deviations for at least two separate experiments).

Table 3. Anti-HIV and cytotoxicity studies on TEL-aptamers **1-3**.

Binding affinity study using SPR. As extensively described in the introductory section, the HIV-infection begins with the attachment of the virus on the glycoprotein gp120 of the host cell. To mimic the viral attachment, a Surface Plasmon Resonance (SPR) based approach was used to measure the binding between the gp120 and glycosaminoglycans immobilized on the chip surface. As a positive control of the interaction and consequently of the "infection", the heparin molecules were biotinylated and captured on a streptavidin sensor chip to mimic the host cell membrane. As described in Figure 30, curve a, the gp120 at 2 μg/mL showed a specific binding on heparin. Subsequently, gp120 was pre-incubated with different G-quadruplex aptamers and injected over the chip. The result indicated that all TEL-ODNs are able to block the gp120-heparin interaction**.** In particular, TEL-ODN **2** characterized by the hydrophobic DMT moiety showed the highest inhibitory activity (Figure 30, curve d). In fact, already at the 50 μM concentration this compound achieved a 50% binding inhibition while at 2 μM the gp120-heparin bond was completely blocked (Figure 31). For TEL-ODN **1** and TEL-ODN **3** a 2-fold and 10-fold reduction of inhibition, respectively, was observed.

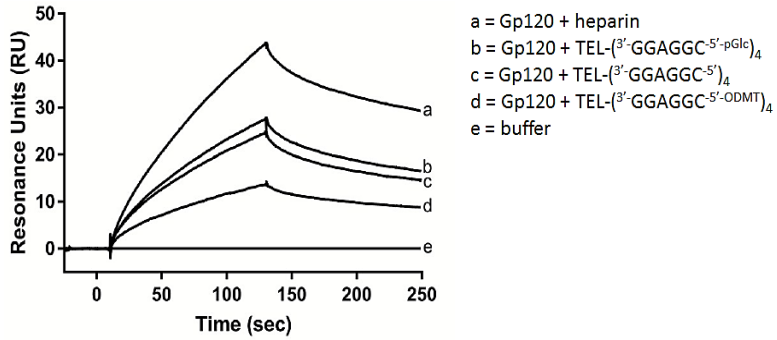

Figure 30. The SPR Sensorgram shows the response (RU) during association (0–120 sec) and dissociation (2 min) of gp120 with TEL-ODNs **1-3**.

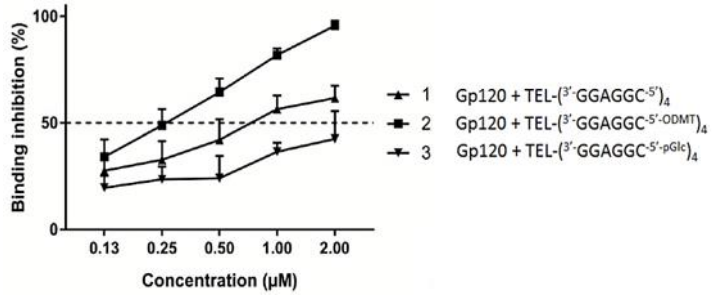

Figure 31. A dose-dependent inhibition of gp120-heparin binding measured by SPR.

In this work we observed that all these new TEL-ODNs are able to fold into dimeric G-quadruplex complexes and only TEL-ODN **2**, conjugated with the lipophilic aromatic DMT groups, showed significant anti-HIV activity at sub-micromolar concentrations.

EXPERIMENTAL SECTION

Reagents and equipment

The chemicals and solvents were purchased from Sigma-Aldrich (Milan, Italy). The reagents, phosphoramidites, linkers and CPG support used for the DNA syntheses were purchased from Glen Research (Sterling, VA, USA). The HPLC analyses and purifications were performed with a Jasco (Jasco Europe Srl, Cremella, LC, Italy) PU2089 pump system equipped with an UV detector model 2075 Plus, using an anion-exchange Macherey-Nagel column. The ODNs were assembled with a PerSeptive Biosystems Expedite DNA synthesizer using standard phosphoramidite chemistry. The UV spectra were recorded using a Jasco V-530 spectrophotometer. The thermal denaturation experiments were performed and CD spectra obtained with a Jasco715 CD spectropolarimeter equipped with a Jasco 505T temperature controller unit. The NMR spectra were recorded either on a Varian Unity Inova 500 MHz spectrometer equipped with a broadband inverse probe with z-field gradient or on a Varian Unity INOVA 700 MHz spectrometer equipped with a triple resonance cryoprobe and processed using the Varian VNMR and iNMR (http://www.inmr.net) software packages.

Syntheses and purifications of TEL-ODNs 1-3

The syntheses of TEL-ODNs **1–3** were performed using a solid-phase automated DNA synthesizer according to the previously described procedure.To obtain the final products **2** and **3**, a DMT-on protocol, not including the final DMT deblocking step, was adopted. In the case of TEL-ODN **3**, the DMT-protected glucose phosphoramidite derivative, obtained through the previously reported protocol, was used at a concentration of 50 mg/mL in an anhydrous acetonitrile solution in the last coupling step. After the automated synthesis, the DMT-ODNs were detached from the support and deprotected by treatment with concentrated aqueous ammonia at 55 °C for 17 h. The combined filtrates and washings were dried, redissolved in water, analyzed and purified by HPLC on an anion exchange column (Macherey-Nagel, 1000-8/46, 4.4×50mm, 5 µm) using a linear gradient from 0 to 100% B in 30 min, flow rate = 0.3 mL/min and detection at 260 nm (buffer A: 20 mM NaH_2PO_4 aq. solution pH 7.0, containing 20% (v/v) CH_3CN; buffer B: 20 mM NaH_2PO_4 aq. solution pH 7.0, containing 1 M NaCl and 20% (v/v) CH_3CN). After HPLC purification, the ODN samples were desalted on a Biogel column (BIORAD) eluted withH_2O/CH_3CH_2OH (9:1, v/v). After drying, the desalted **2** and the DMT-protected precursor of **3** (DMT-**3**) were further purified by HPLC on a RP-18 column (Purosphere STAR, 5 µm, 250 x 10mm, Merck) eluted with a linear gradient from 0 to 100% B 30 min, flow rate 0.7 mL/min and detection at 260 nm (eluent A: triethyl ammonium bicarbonate buffer (TEAB) 0.1 µM; eluent B:CH_3CN).The retention time of **2** (23.1 min) and DMT-**3** (23.4 min) corresponded to that of the most highly retained peak in each HPLC profile due to the presence of the terminal DMT lipophilic groups. The collected peaks were dried under reduced pressure and lyophilised twice after solubilization in water. The purified **2** and DMT-**3** were quantified by UV

spectroscopic analyses in pure water by measuring the absorbance at 260 nm at 90 °C using the molar extinction coefficient of $^{5'}$-CGGAGG-$^{3'}$ as calculated by the nearest-neighbour model4 multiplied by 4 (the number of strands in each TEL-ODN complex).The calculated ε = 246,000 cm^{-1} M^{-1} was augmented by 1% due to the contribution of the DMT groups. The DMT deprotected **1** and **3** were obtained by treating the corresponding precursors with a mixture of acetic acid and water (8:2, v/v, 3 mL) for 40 min at room temperature. After the addition of water (5 mL) the solutions were extracted with diethyl ether (4 x 10 mL) in a separating funnel. The acqueous layer was dried under reduced pressure (max 40 °C) and co-evaporated with water three times to remove the residual acetic acid. Finally, the fully deprotected TEL-ODNs **1** and **3** were dissolved in water, lyophilised and quantified by UV.

Characterization of TEL-ODNs 1–3 by quantification of the DMT cations released from 2 and DMT-3

0.1 μmol of **2** or DMT-**3** was treated with a solution of 70% $HClO_4$/Ethanol (3:2, v/v) and the red solution was analysed by spectroscopic measurements at 498 nm (ε = 71,700 cm^{-1} M^{-1}). 0.1 μmol of **2** and DMT-**3** furnished 0.39 and 0.42 μmol of DMT, respectively, thus confirming the assigned structures and the purity of both products.

Preparation of G-quadruplexes (annealing)

The G-quadruplexes were formed by dissolving the TEL-ODNs **1–3** in 1 M K^+ containing aqueous buffer (900 mM KCl, 100 mM KH_2PO_4, pH 7) and annealed by heating at 90 °C for 5 min followed by quick cooling at 4 °C (kinetic annealing procedure). Stock solutions of 6 mM strand concentrations of **1** and **2** and 3 mM of **3** were prepared. The samples were stored at 4 °C for 24 h before the measurements.

Native gel electrophoreses. Native gel electrophoresis experiments were run on 20% non-denaturing polyacrylamide gels in 1x TBE buffer, pH × 7.0, supplemented with 30 mM NaCl. 600 μM single strand ODN samples, obtained by diluting the annealed stock solutions just before the experiment, were loaded on the gel and 10% glycerol was added to each sample just before loading. The gels were run at room temperature at a constant voltage (120 V) for 1 h. The bands were visualized by UV shadowing.

CD experiments. The CD spectra of the annealed **1–3** were recorded in a 0.1 cm path length cuvette at 5 °C at a 10 μM G4 concentration. The spectra were recorded in the 360–200 nm wavelength range as an average of 3 scans (100 nm/min, 1 s response time, 1 nm bandwidth) and normalized by subtraction of the background scan containing only the buffer. CD melting experiments were performed, monitoring the CD value (mdeg) at 264 nm in the temperature range 5–90 °C with 0.5 °C min^{-1} heating rate.

HPLC-SEC experiments. The HPLC-SEC analyses were performed on a Yarra 2000 SEC Column (Phenomenex, 300 x 7.8 mm, 3 um) equipped with a Phenomenex Security Guard pre-column eluted with 90 mM KCl and 10 mM

KH_2PO_4/CH_3CN (80/20, v/v), flow rate 0.6 mL/min, detector at 260nm. The analyses were performed at room temperature.

NMR experiments. The NMR samples were prepared at a 1.6 mM concentration by dissolving **1–3** in 250 µL of 1 M K^+ containing annealing buffer (900 mM KCl, 100 mM KH_2PO_4, pH = 7 in H_2O/D_2O 9:1v/v). One-dimensional NMR spectra were acquired as 16,384 data points with a recycle delay of 1.0s at 25 °C. The data sets were zero-filled to 32,768 points prior to Fourier transformation and apodized with a shifted sine bell squared window function. Water suppression was achieved by including a double pulsed-field gradient spin-echo (DPFGSE) module in the pulse sequence prior to acquisition.

Anti-HIV activity assay. The anti-HIV activity and cytotoxicity of the ODNs were evaluated against wild-type (WT) HIV-1 strain IIIB in MT-4 cell cultures using the 3-(4,5-dimethylthiazol-2-yl)-2,5-diphenyltetrazolium bromide (MTT) method. Briefly, stock solutions (10 × final concentration) of the tested compounds were added in 25 µL volumes to two series of triplicate wells so as to allow a simultaneous evaluation of their effects on mock-and HIV-infected cells at the beginning of each experiment. Serial 5-fold dilutions of the test compounds were made directly in flat-bottomed 96-well microtiter trays using a Biomek 3000 robot (Beckman instruments, Fullerton, CA). Untreated control HIV-and mock-infected cell samples were included for each sample. Virus stock (50 µL) at 100-300 $CCID_{50}$ (50% cell culture infectious dose) or culture medium was added to either the virus-infected or mock-infected wells of the microtiter tray. Mock-infected cells were used to evaluate the effect of the test compounds on the uninfected cells in order to assess the cytotoxicity of the tested compounds. Exponentially growing MT-4 cells were centrifuged for 5 min at 220 g and the supernatant was discarded. The MT-4 cells were resuspended at 6 x 105 cells/mL and 50µL volumes were transferred to the microtiter tray wells. Five days after the infection, the viability of the mock- and HIV-infected cells was examined spectrophotometrically by MTT assay. The MTT assay is based on the reduction of yellow coloured 3-(4,5-dimethylthiazol-2-yl)-2,5-diphenyltetrazolium bromide (MTT) (Acros Organics) by mitochondrial dehydrogenase activity in metabolically active cells to a blue-purple formazan that can be spectrophotometrically measured. The absorbances were read in an eight-channel computer-controlled photometer (Infinite M1000, Tecan), at two wavelengths (540 and 690 nm). All data were calculated using the median absorbance value of three wells. The 50% cytotoxic concentration (CC_{50}) was defined as the concentration of the tested compound that reduced the absorbance (OD_{540}) of the mock-infected control sample by 50%. The concentration achieving 50% protection against the cytopathic effect of the virus in infected cells was defined as the 50% inhibitory concentration (IC_{50}).

Surface Plasmon Resonance (SPR) experiments. The binding of gp120 on immobilized heparin was measured using Surface Plasmon Resonance (SPR). The experiments were performed at 25 °C on a Biacore T200 (GE Healthcare, Uppsala, Sweden) in HBS-EP (10 mM HEPES, 150 mM NaCl,3 mM EDTA and 0.05% (v/v) Tween20; pH 7.4). Heparin (Iduron) was minimally biotinylated at the reducing end using biotinamidohexanoic acid hydrazide (Sigma-Aldrich). Biotinylated-heparin was extensively dialyzed to remove unreacted biotin and 400 Resonance Units (RU) were captured on a Streptavidin Sensor Chip. Recombinant gp120 HIV-1 (III_B) (ImmunoDiagnostics Inc., Woburn, MA), alone (2 µg/ml) or premixed with a concentration range of the G-quadruplex aptamers, was injected for 2 minutes at a flow rate of 30 µl min^{-1}, followed by a dissociation phase of 2 minutes. The Sensorchip was regenerated by treatment with 1M NaCl in 10 mM NaOH. A reference flow was used as a control for non-specific binding. Several buffer blanks were used for double referencing.

Objective 3. Study and evaluation of an analogue ε-Poly(L-Lysine) peptide as ligand of G-quadruplexes

ε-Poly(L-Lysine) or ε-PLL peptide is a cationic biopolymer isolated from the marine bacterium *Bacillus subtilis* with antibacterial and anticancer activity [85]. The same peptide and his analogues, can be also used in many biomedical applications, including the enhancement of some anticancer agents [86], the suppression of the production of the prion protein in neurodegenerative disorders [87], the use in contrast agent probes for Magnetic Resonance Imaging [88] and the enhancement of gene delivery efficiency [89]. In particular, α- and ε-PLL peptides are well soluble in aqueous media, biodegradable and environmental-friendly [90], and both are good candidates as drug delivery agents due to their polycationic nature [90][91]. The interest in poly-L-lysine structures containing both α- and ε- peptide bonds is justified: i) by their superior gene delivery properties [92]; ii) by their resistant to proteolytic action [93]; iii) by their ability to bind structural specific nucleic acids and iv) by their capacity to resist degradation after 24 h of incubation in human serum at 37 ˚C [94]. In this work, we reported a synthetic approach for linear PLLs characterized by sequential α and ε peptides bonds (α, ε-PLL, Figure 32) and we described the effect of α, ε-PLL to bind different G-quadruplex structures.

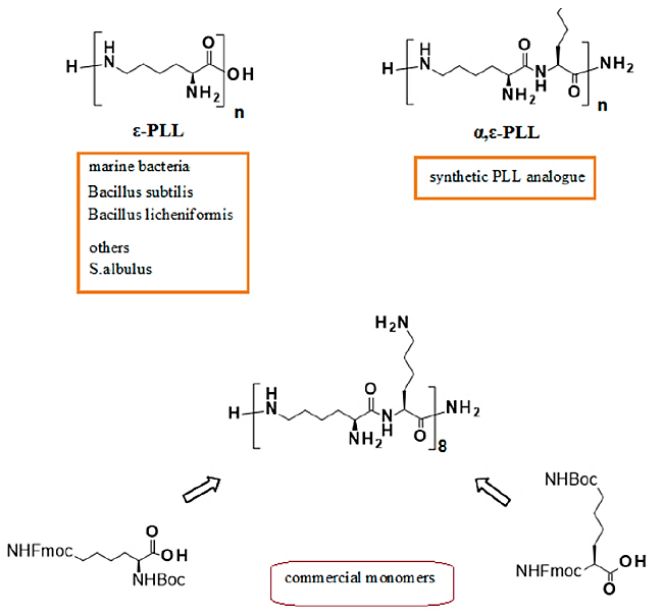

Figure 32. Schematic representation of the natural ε-peptide (ε-PLL) and of our synthetic analogue studied in G-quadruplex-DNA binding.

Specifically, we have chosen the Tel22 telomeric sequence d(AGGGTTAGGGTTAGGGTTAGGG) and the Pu22 sequence d(TGAGGGTGGGTAGGGTGGGTAA) able to form a hybrid-type and a parallel G-quadruplex respectively.

Results and Discussions. The CD spectra of Tel22, showed the characteristic CD bands (~290 nm maximum, ~250–260 nm shoulder, ~240 nm minimum) previously attributed to an equimolar mixture of the hybrid 1 and hybrid 2 G-quadruplexes [95][96][97][98]. After the addition of α, ε-PLL we observed no change in the CD spectrum, reaching the conclusion that α, ε-PLL did not induce any significant structural change on the G-quadruplex secondary structure of Tel22 (Figure 33, left). The same study was repeated using Pu22 DNA sequence that showed a negative signal at 240 nm and a positive signal at 265 nm (Figure 33, right) typically to a parallel G-quadruplexes [99][100]. Immediately after the addition of α, ε-PLL, we observed a we observed a substantial enhancement and broadening of the positive CD band at 260 nm, which indicated that the interaction of α, ε-PLL with Pu22 induced significant changes into the parallel G4 secondary structure.

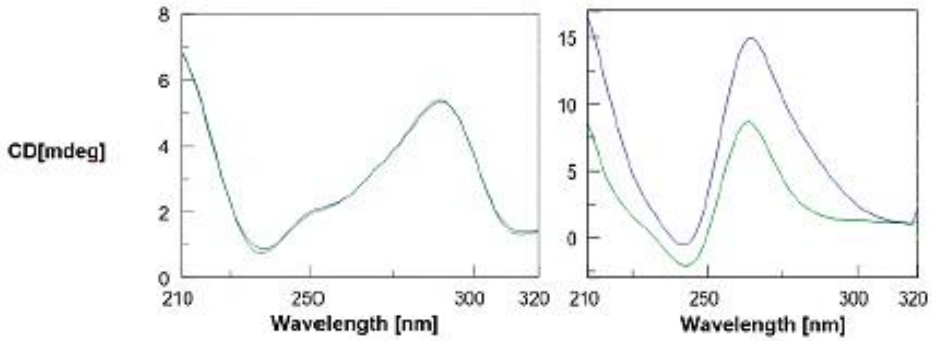

Figure 33. CD spectra of 2.5 μM G-quadruplex DNA (Tel22, left; Pu22 right) + 1.7 μM α, ε-PLL in 10 mM TRIS HCl buffer, 100 mM KCl, pH 7.4 at 15 °C. Arithmetic sum (-); α, ε-PLL/G-quadruplex complex (-).

By repeating the acquisition of CD (Figure 34) and UV (Figure 35) spectra at different time points from the addition of α, ε-PLL to the preformed Pu22 G-quadruplex, we observed a continuous variation of the signals (Figure 34a and 35a) which was particularly evident by plotting the CD value recorded at 261 nm or 281 nm (Figure 34b), as well as the UV value at 261 nm Figure 35b) vs. time.

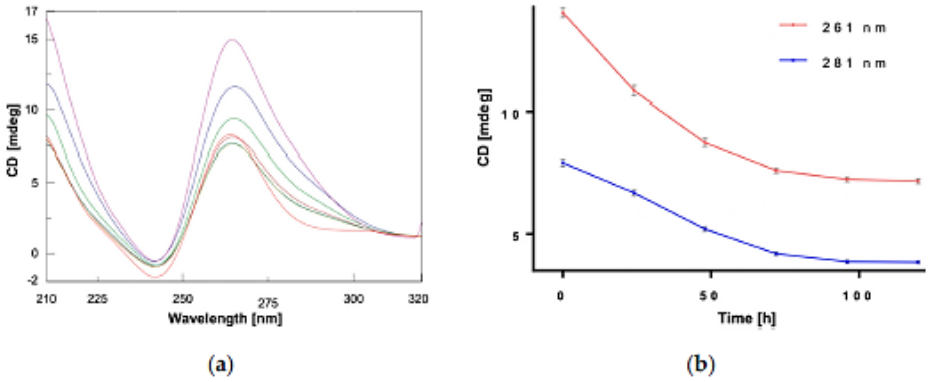

Figure 34. (**a**) CD spectra of Pu22 (2.5 µM) recorded before (-) and 0 (-), 24 (-), 48 (-), 72 (-), 96 (-) and 120 (-) h after mixing with α, ε-PLL (1.7 µM) in 10 mM TRIS HCl buffer, 100 mM KCl, pH 7.4 at 15 °C.(**b**) Plots of CD values vs. time at 261 nm and 281 nm.

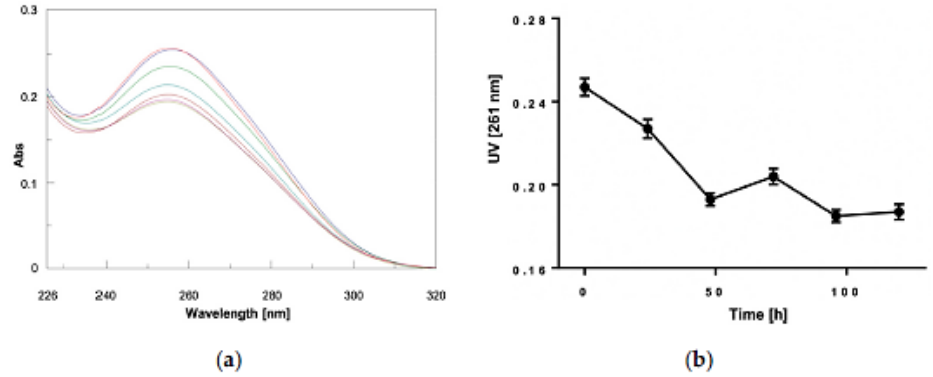

Figure 35. (**a**) UV spectra relative to Pu22 (2.5 µM) in 10 mM TRIS HCl buffer, 100 mM Cl, pH 7.4, b = 0.4375 cm, at 15 °C recorded before (-) and 0 (-), 24 (-), 48 (-), 72 (-), 96 (-) and 120 (-) h after mixing with α, ε-PLL (1.7 µM) in 10 mM TRIS HCl buffer, 100 mM KCl, pH 7.4 at 15 °C.(**b**) Plots of CD values vs. time at 261 nm and 281 nm.

From this kinetic study, we concluded that the interaction of α, ε-PLL with the Pu22 G-quadruplex leads to the formation of complexes that evolve during the first 96 h after mixing and eventually reach the most stable one when the stabilization of CD signal was achieved (Figure 34). Similarly, to CD, also the fluorescence spectra confirmed a higher structural perturbation for Pu22 G-quadruplex DNA with respect to the telomeric one after binding with α, ε-PLL. We observed a slight blue-shift effect associated with increased fluorescence emission in the former case, whereas we did not see any significant effect in the latter

case (Figure 36). We also investigated the effects induced by α, ε-PLL on the apparent melting temperature of the two G-quadruplex models.

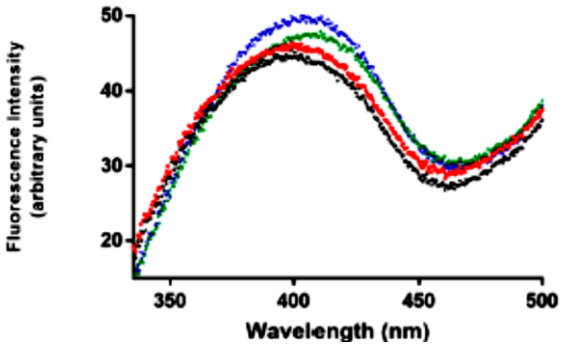

Figure 36. Fluorescence emission spectra of Pu22 (-), Tel22 (-), Pu22 + α, ε-PLL (-) and Tel22 + α, ε-PLL (-): 2.5 μM DNA, α, ε-PLL (1.7 μM) in 10 mM TRIS TRIS HCl buffer, 100 mM KCl, pH 7.4 at 15 °C.

The CD melting curves of the α, ε-PLL/G-quadruplex complexes (Figure 37) disclosed a slight thermal stabilization ($\Delta T_m \sim 2$ °C) in the case of Pu22, whereas no significant difference was found between the T_m of Tel22 and that of its complex with α, ε-PLL.

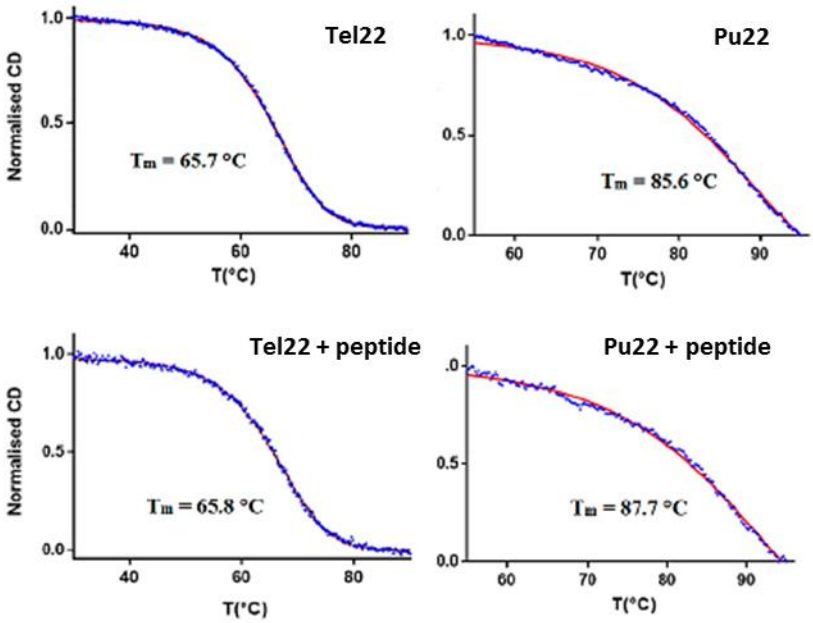

Figure 37. CD melting curves relative to G4 DNA (Tel22, **top left**; Pu22, **top right**; 2.5 μM) and their complexes with 1.7μ_M α, ε-PLL (Tel22 + α, ε-PLL, **bottom left**; Pu22 + α, ε-PLL, **bottom right**) in 10 mM TRIS HCl buffer, 100 mM KCl, pH 7.4.

To quantitatively evaluate the binding affinity of α, ε-PLL for both the studied G-quadruplex topologies, we used the surface plasmon resonance (SPR) technique. SPR binding profiles (Figure 38) confirmed that α, ε-PLL was actually capable of binding, in a concentration-depending manner, to both G-quadruplex models, and the fitting of the binding isotherms allowed us to estimate the dissociation constants for the two complexes, even though a higher affinity for Pu22 was observed, in interval time of analysis. Strikingly, the affinity of α, ε-PLL for Pu22 and Tel22 G-quadruplexes is similar or higher than that found for other previously reported basic peptides acting as G-quadruplex DNA ligands (K_D 1–8 μM) [101].

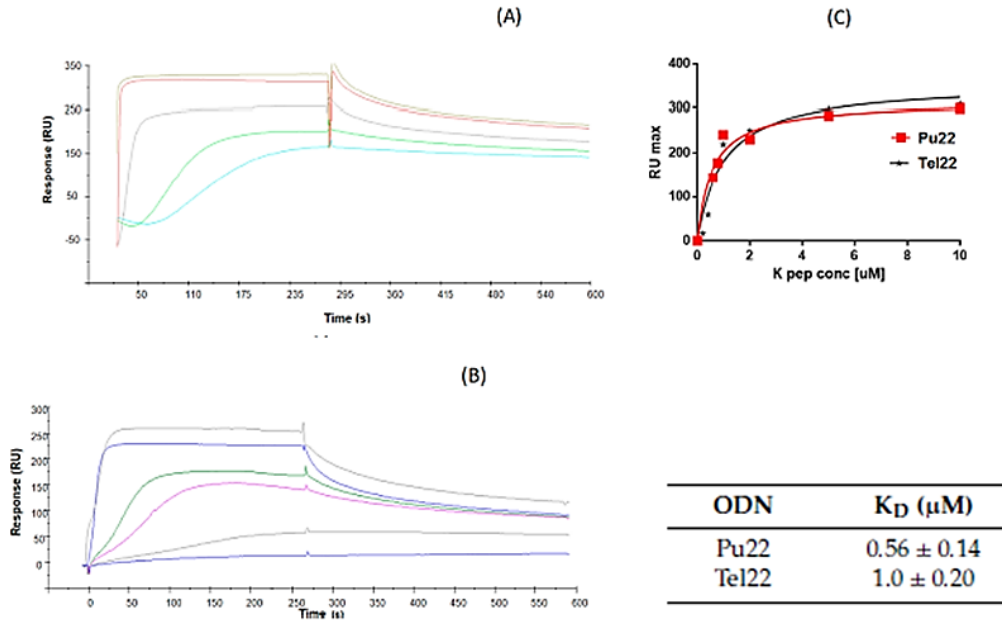

ODN	K_D (μM)
Pu22	0.56 ± 0.14
Tel22	1.0 ± 0.20

Figure 38. Overlay of surface plasmon resonance (SPR) sensorgrams for the binding of α, ε-PLL to immobilized (**A**) Biot-Pu22 or (**B**) Biot-Tel22. (**C**) Overlay of the corresponding binding isotherms of RU_{max} values vs. α, ε-PLL concentration (0–10μM concentration range).

Aiming at further confirming the binding of α, ε-PLL with the two G-quadruplex models and also at investigating the effect of the addition of α, ε-PLL on the molecularity of Tel22 and Pu22 G-quadruplexes, we used the HPLC Size Exclusion Chromatography (HPLC-SEC) technique. The analysis of Tel22 and P22 was performed before and 96 h after their incubation with α, ε-PLL (Figure 39). As expected, the HPLC-SEC profile of Tel22 alone was populated by a single peak attributable to the mixture of monomeric hybrid 1 and hybrid 2 G-quadruplexes, which was eluted at min 14.733. After incubation with α,

ε-PLL, the appearance of a new less-retained peak eluted at min 13.767 suggested the formation of a higher molecular weight complex in agreement with the SPR data which indicated a concentration-dependent binding between α, ε-PLL and Tel22. Differently from what was observed for Tel22, the HPLC-SEC profile obtained by injecting of Pu22 alone was populated by two main peaks, that we assigned to the monomeric parallel G-quadruplex (t_R= 14.525 min) and its dimer (t_R= 13.950 min) based on literature reports [102]. On the other hand, the HPLC-SEC profile of Pu22 did not change significantly after the addition of α, ε-PLL, suggesting that the α, ε-PLL/Pu22 binding confirmed by CD, fluorescence and SPR data, did not affect the relative abundance of the monomeric and dimeric G-quadruplex forms.

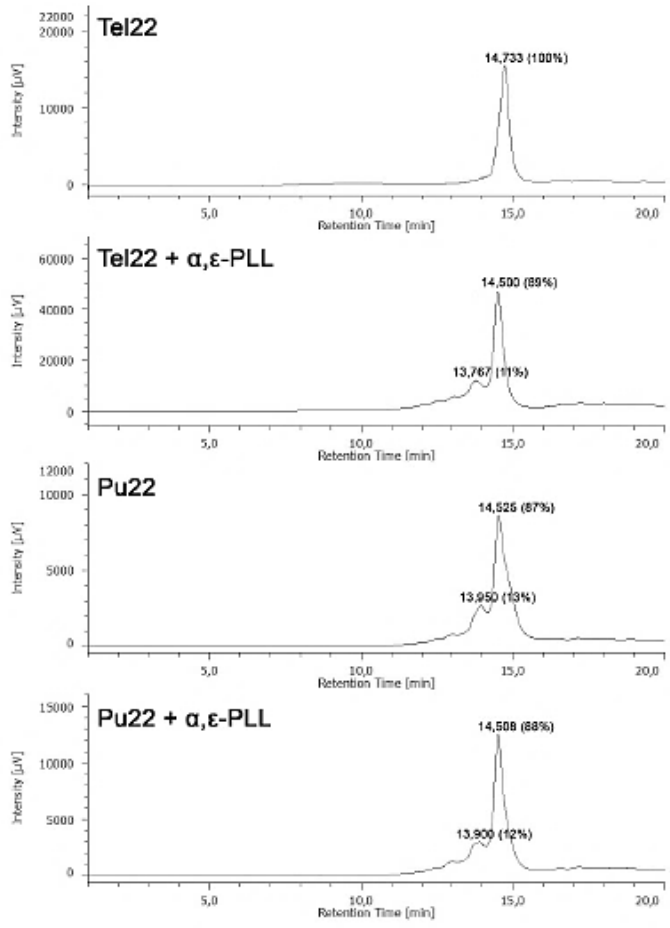

Figure 39. HPLC-size exclusion chromatography (SEC) profiles of Tel22 and Pu22 G4s before and after the addition of α, ε-PLL.

The results reported, showed that α, ε-PLL binds the two herein investigated DNA G-quadruplexes with good affinity (as demonstrated by SPR), though clues of changes of the secondary structure and slight thermal stabilization were seen only for the interaction with the Pu22 parallel G-quadruplex. The study reported here provides an interesting insight into G-quadruplex binding of α, ε-PLL, a serum stable [14], marine-inspired peptide that, in spite of its cationic nature, recognizes the structural properties of its targets and uses different binding modes according to their topology.

EXPERIMENTAL SECTION

Sinthesis of α, ε-PLL and DNA.

The hexadecapeptide α,ε-PLL (Figure 1) was prepared accordingly to the procedure previously reported by Moccia et al. Pu22 d(TGAGGGTGGGTAGGGTGGGTAA) and Tel22 d(AGGGTTAGGGTTAGGGTTAGGG) G4-forming DNAs werepurchased from Eurofins Genomics.

CD and UV Experiments

We obtained the CD spectra in a 210–320 nm wavelength range, on a Jasco J-810 spectropolarimeter equipped with a Jasco PTC-423S/15 Peltier temperature controller (Jasco Europe Srl, Cremella, Italy) in a dual-chamber quartz cell (b = 2 × 0.4375, Hellma 238-QS, Hellma® Analytics, Hellma GmbH & Co. KG, Müllheim, Germany). UV spectra were recorded on a Jasco V-550 spectrophotometer equipped with a Jasco ETC-505T Peltier temperature controller. All spectroscopic experiments were run in duplicate and were repeated three times. Standard deviation values for CD and UV Abs were ≤ 2%. CD meltings of telomeric and Pu22 G4 DNAs were obtained by recording CD values at 295 and 263 nm, respectively, as function of temperature. All nucleic acids were annealed by heating the solutions at 95 °C for 5 min and letting them cool overnight at room temperature. Melting temperature values were determined as the temperatures relative to minima of the 1st derivative plots of denaturation curves.

Fluorescence Studies

The experiments were performed at 15 °C using the intrinsic fluorescence of G4 DNAs, using an excitation wavelength of 270 nm and a fluorescence emission wavelength ranging from 330 to 500 nm on a Jasco FP 8300 spectrofluorometer using a 10 mm path-length quartz cuvette. The acquisition parameters were set as follows: excitation and emission slits at 5 nm; 200 nm/min scan rate; 0.5 nm data interval averaging time at 0.050 s, PMT voltage at “medium”.

Surface Plasmon Resonance (SPR) Experiments

SPR assays were performed at 25 °C on a Biacore 3000 instrument (GE Healthcare, Chicago, IL, US). For immobilization, 5’-biotinylated Tel22 and Pu22 ODNs were injected for 7 min (at 20 μM) on a SA-chip until an immobilization of ~700 RU was achieved, as previously reported [47,48]. The α,ε-PLL analyte was serially diluted in the 10 μM TRIS HCl buffer supplemented with 100 μM KCl (pH 7.4) running buffer, covering a concentration range between 50 and 1000 nM. 90 μL analyte samples were injected at a flow rate of 20 μL min^{-1} and the dissociation was followed for 300 s. The reference chip sensorgrams were properly subtracted to sample sensorgrams. After each cycle, the sensor chip surface was regenerated with a 1.0 M NaCl solution for 30 s followed by multiple buffer injections to yield a stable baseline for the following cycles. Experiments were carried out in duplicates. Kinetic parameters were estimated assuming a 1:1 binding model and using version 4.1 Evaluation Software (GE Healthcare).

HPLC-Size Exclusion Chromatography (SEC) Analyses

HPLC-SEC was performed using a Phenomenex (Bologna, Italy) Yarra SEC-2000 column (300 × 7.8 mm, 3 µm) eluted with 90 mM KCl and 10 mM KH_2PO_4/CH_3CN (80:20, v/v), flow rate 0.6 mL/min, UV-detector at 260 nm. The analyses were performed at room temperature.

Objective 4. A new supramolecular structure formed by G-rich oligonucleotide sequences

The construction of switchable and controllable molecular devices plays an important role in the development of new nanomaterials and nanomachines. DNA molecules and their secondary structures, in particular G-wires, represent a valid alternative for the design of nanodevices because, in addition to having unique optical and electrochemical characteristics [103][104][105], they can be easily designed, basing on their complementary bindings. G-wires, nanostructures based on a four-stranded DNA helix called a G-quadruplex, have recently been used to generate nanocircuits, DNA computers and nanotechnological materials [106][107][108].

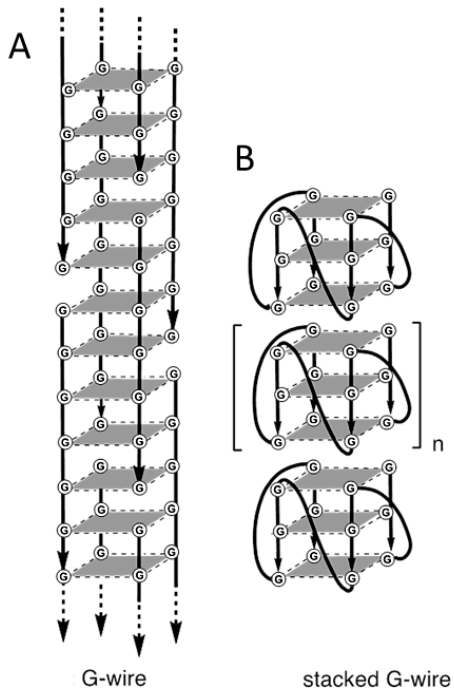

Figure 40. Schematic representation of two types of multimeric G-wires: (**A**) interlocked and (**B**) stacked.

These supramolecular structures can be obtained by the multimerization of the G-rich strands in a self-assembling process that combines two different modes: i) interlocked G-wires, characterized by the cooperative assembly of interlocked slipped strands (Figure 40A) and ii) stacked G-wires, in which the G-quadruplex building blocks are piled one upon the other by end-to-end stacking (Figure 40B).The

factors that influence this multimerization process are: i) the molecularity of the G-quadruplex, ii) the base composition of the loops, iii) the presence of overhanging nucleotides at the 5' or 3' end of the G-rich strand, iv) the number of G-tetrads in the G-quadruplex monomer and v) the kind of π-π stacking among the monomeric building blocks. Starting from these data, in a previous paper published in NAR in 2011, the research group formed by Piccialli, Borbone and Oliviero identified a novel dimerization pathway. In particular they observed that the sequence $^{5'}$-CGGTGGT-$^{3'}$ (**1**, Figure 41) is able to fold in a dimeric structure (**2Q**) (**2**, Figure 41), via 5'-5' π-π stacking of two unusual G(:C): G(:C): G(:C): G(:C) planar octads belonging to two identical tetramolecular parallel G-Quadruplexes [109] (Figure 41).

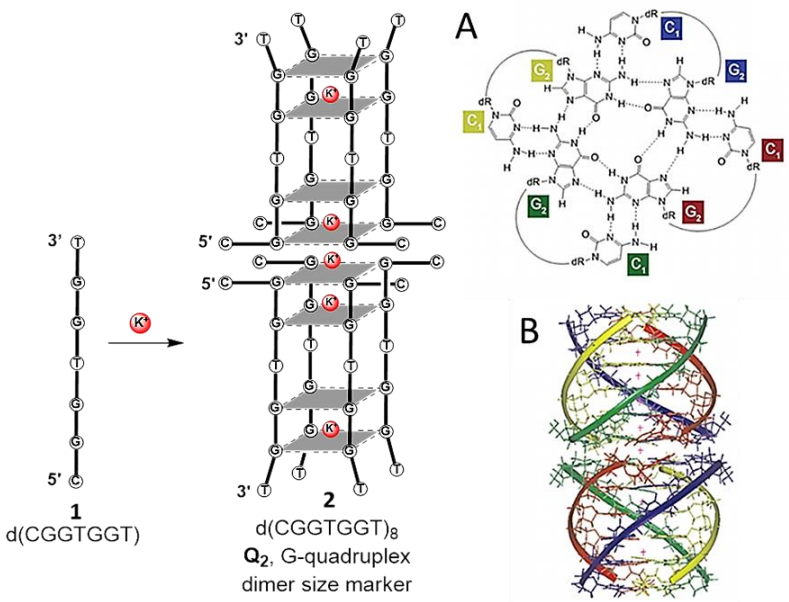

Figure 41. Schematic representations of single stranded ODN (**1**) and its dimeric tetramolecular quadruplex assembly (**2**). Structural model for the $d(CGGTGGT)_8$ octamer (**A**). Proposed structure of the G2(:C1):G2(:C1):G2(:C1):G2(:C1) octad (**B**).

In 2014, D'Atri *et al*., reported a small library of G-rich oligonucleotide strands having the sequence $^{5'}$-**X**GG**Y**GGT-$^{3'}$ (where **X** and **Y** stand for A, C, G, or T) (Figure 42). They demonstrated that the dimerization process was not peculiar to $^{5'}$-**C**GG**T**GGT-$^{3'}$, but was possible for all the remaining $^{5'}$-**C**GG**Y**GGT-$^{3'}$ sequences (with **Y**= A, C or G). Furthermore, they found that the $^{5'}$-**T**GG**A**GGT-$^{3'}$ sequence, despite the absence of the 5'-ending C, was capable of forming a **2Q**-like higher order quadruplex by using a slightly different dimerization interface [84].

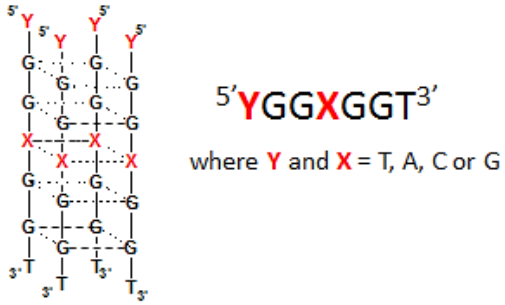

Figure 42. Monomeric G-quadruplex building block containing in the sequence $^{5'}$-**X**GG**Y**GGT$^{-3'}$ a double substitution (where **X** and **Y** stand for A, C, G, or T).

With the goal of obtaining polymers very similar to G-wires, we decided, considering the dimerization induced by the octad (**2Q**) (Figure 41), to introduce into the sequence $^{5'}$-CGG$^{-3'-3'-}$TGGC$^{-5'}$(called **InvT**) a 3'-3' inversion of polarity site, so as to obtain at the 5'-ends cytosine-guanine-guanine residues, which can act as hydrophobic glue between the monomeric units of the G-quadruplex [79] (Figure 43).

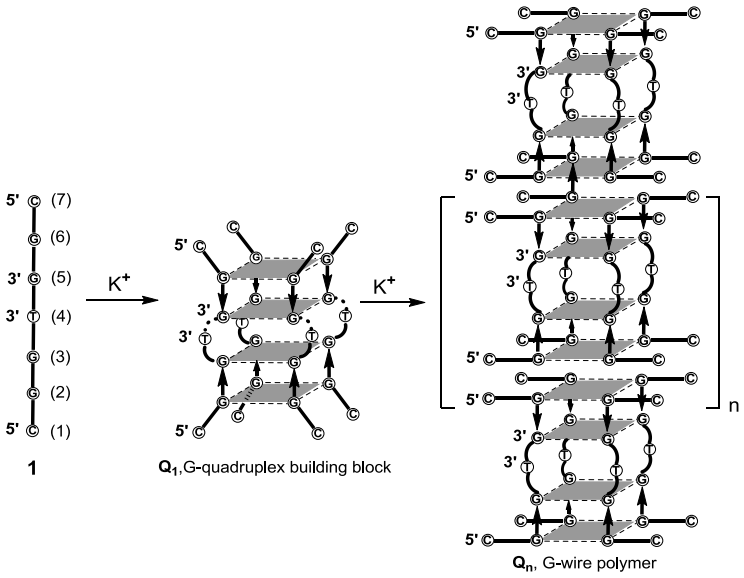

Figure 43. Formation of the G-quadruplex building block $\mathbf{Q_1}$ and its multimerization into $\mathbf{Q_n}$ G-wire polymers starting from ODN **1** $^{5'}$-CGG$^{-3'-3'-}$TGGC$^{-5'}$.

Through structural studies the disposition of the thymidine residue towards the outside for **InvT** emerged. Hence, the idea of synthesizing a sequence characterized by a greater symmetry obtained by the

absence of a thymidine residue in the middle of the base sequence (Figure 44).

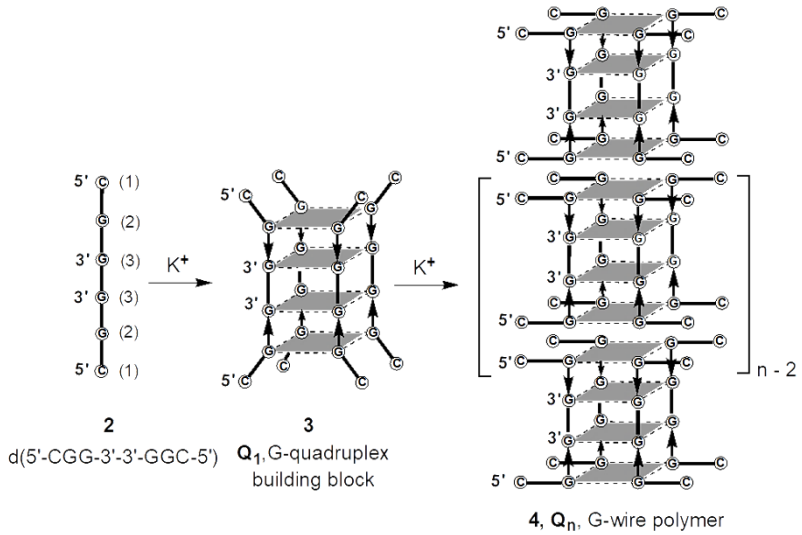

Figure 44. Formation of the G-quadruplex building block Q_1 and its multimerization into $\mathbf{Q_n}$ G-wire polymers starting from ODN **2** $^{5'}$-CGG-$^{3'-3'}$-GGC-^{5}.

Synthesis and Purification of d($^{5'}$-CGG-$^{3'-3'}$-GGC-$^{5'}$).

The synthesis of d($^{5'}$-CGG-$^{3'-3'}$-GGC-$^{5'}$) was performed on an automated synthesizer through standard solid-phase phoshoramidite chemistry. The 3'-3' phosphodiester bond was achieved by performing the first three coupling cycles using 5'-phosphoramidites and the remaining three using standard 3'-phosphoramidates. After the automated synthesis, the ODN **2** was detached from the support and deprotected by treatment with concentrated aqueous ammonia solution for 7 h at 55 °C. The filtered solution and washings were concentrated under reduced pressure and purified by HPLC with an anion exchange column (Macherey–Nagel, 1000-8/46, 4.4 × 295 50 mm, 5 µm) eluted with a linear gradient from 0 to 100% B in 30 min; buffer A: 20 mM NaH_2PO_4, pH 7.0 containing 20% CH_3CN; buffer B: 1M NaCl, 20 mM NaH_2PO_4, pH 7.0, containing 20% CH_3CN; flow rate 0.3 mL/min. The collected product was desalted by gel filtration on a BioGel P2 column eluted with H_2O/ethanol (9:1, v/v) to obtain, after lyophilisation, pure ODN **2**. The ON concentration was quantified spectrophotometrically in water at λ = 260 nm and 90 °C, using the molar extinction coefficient of $^{5'}$-CGG-$^{3'-3'}$-GGC-$^{5'}$ (ε = 54,400 cm^{-1} M^{-1}) as calculated with the nearest-neighbour model.

Polyacrylamide Gel Electrophoresis (PAGE) studies. Non-denaturing Polyacrylamide Gel Electrophoresis (PAGE) is a simple method to demostrate the formation of a G-quadruplex structure For this purpose, we compared the electrophoretic mobility of ($^{5'}$-CGG-$^{3'}$-$^{3'}$-GGC-$^{5'}$)$_{2\text{-}n}$ (lanes 3 and 4, Figure 45A) with that of the corresponding monomeric quadruplex ($^{5'}$-TGGGGT-$^{3'}$)$_4$ (lane 1) and of the dimeric quadruplex ($^{5'}$-CGGTGGT-$^{3'}$)$_8$ (lane 2) used as size markers for the G-quadruplex monomeric building block **Q_1** and G-quadruplex dimeric building block **Q_2**, respectively. The ($^{5'}$-CGG-$^{3'}$-$^{3'}$-GGC-$^{5'}$)$_{2\text{-}n}$ annealed at a 1.0 mM ODN concentration migrated as a well-defined band (lane 3, Figure 45A) in which the short bands **$Q_{1\text{-}4}$** of the **Q_n** polymer could be identified. The faster band of ($^{5'}$-CGG-$^{3'}$-$^{3'}$-GGC-$^{5'}$)$_{2\text{-}n}$ (lane 3) migrated with almost the same mobility as the monomeric G-quadruplex ($^{5'}$-TGGGGT-$^{3'}$)$_4$ and for this reason, also considering the DNA ladder reference (lane 5, Figure 45A) it was attributed to the **Q_1** species. As expected, the **Q_2** species corresponded to about 48 nucleotides, migrating a little faster that the dimeric ($^{5'}$-CGGTGGT-$^{3'}$)$_8$ (lane 2, Figure 45A) corresponding to 58 nucleotides.

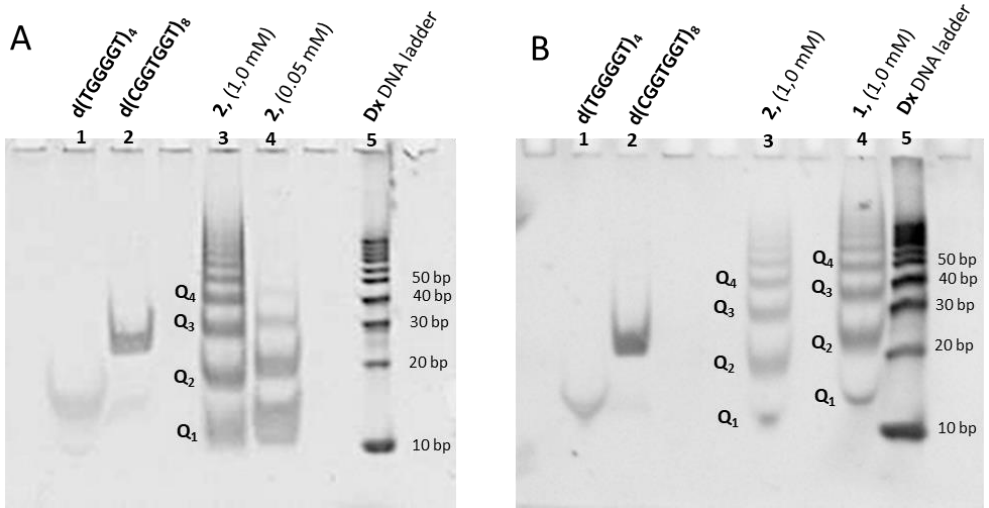

Figure 45. Electrophoretic mobility of the ODNs annealed in 100 mM K^+ buffer after 24h at 4 °C.

Furthermore, through the PAGE analysis, we observed that the progression of the polymerization process of ($^{5'}$-CGG-$^{3'}$-$^{3'}$-GGC-$^{5'}$)$_{2\text{-}n}$ depends on its concentration. In fact, when ($^{5'}$-CGG-$^{3'}$-$^{3'}$-GGC-$^{5'}$)$_{2\text{-}n}$ was annealed at a different ODN concentration (0.05 mM), in the distrubution of the multimers it was possible to identify only the first three bands **$Q_{1\text{-}3}$** (lane 4, Figure 45). The PAGE in Figure 45B, reports

the comparison between the electrophoretic mobility of ($^{5'}$-CGG-$^{3'-3'}$-GGC-$^{5'}$)$_{2-n}$ (lane2) and ($^{5'}$-CGG-$^{3'-3'}$-TGGC-$^{5'}$)$_{2-n}$ (lane 4). The bands formed by ($^{5'}$-CGG-$^{3'-3'}$-TGGC-$^{5'}$)$_{2-n}$ had a lower mobility compared to the corresponding bands formed by ($^{5'}$-CGG-$^{3'-3'}$-GGC-$^{5'}$)$_{2-n}$ probably attributed to the presence of the thymidine residue.

Size Exclusion Chromatography (HPLC-SEC) studies. The ($^{5'}$-CGG-$^{3'-3'}$-GGC-$^{5'}$)$_{2-n}$ annealed in 1.0 mM K^+ buffer was analyzed by Size Exclusion Chromatography (HPLC-SEC). The HPLC-SEC profile reported in Figure 46 showed a distribution of peaks in which low molecular weight species had longer retention times. To obtain information about the molecular weight of the analyzed species, we used as size markers ($^{5'}$-T_6-$^{3'}$), ($^{5'}$-TGGGGT-$^{3'}$)$_4$ and ($^{5'}$-CGGTGGT-$^{3'}$)$_8$ respectively for a single stranded (ODN 6-mer), a monomeric G-quadruplex **Q_1** (ODN 24-mer) and a dimeric G-quadruplex **Q_2** (ODN 54-mer) (Figure 46A, left panel). On the basis of the retention times (t_R) and in agreement with the PAGE data, we could observe for ($^{5'}$-CGG-$^{3'-3'}$-GGC-$^{5'}$)$_{2-n}$ annealed at a 0.05 mM ODN concentration the presence of only three peaks (**Q_{1-3}**) confirming that the polymerization process is slower at a lower ODN concentration (Figure 46C, left panel). Instead, when the ODN concentration was increased (3.6 mM) and the annealing time is extended (48h and 72h - data not shown) a distribution of multimers with a higher molecular weight (**Q_n**, with n < 6 for Figure 46D, left panel) were observed. Further to this information, SEC analysis revealed a strong dependence between the annealing times and the polymerization (Figure 46, right panel). Analyzing the ($^{5'}$-CGG-$^{3'-3'}$-GGC-$^{5'}$)$_{2-n}$ sample 30 min after heating and equilibration at 25, 45, 65 and 85 °C (Figure 46, right panel), we can observed, unlike the previous work [79], where in the same condition the depolymerization process was much faster, the presence at 85 °C, of alone two species **Q_1** and **Q_2** (in the ratio 5:1) and the total absence of the single stranded. These data indicated that the G-quadruplex **Q_1** formed by ODN **2** (Figure 44) is more stable of the **Q_1** formed by ODN **1** (Figure 43)**.** Taking advantage of the good resolution of the peaks on the HPLC-SEC column, the species attributed to **Q_1** was isolated, stored at 4 °C and re-injected 30 min after its isolation. The chromatographic analysis of the **Q1** peak confirmed almost total purity with very low contamination from the peaks of the adjacent products (Figure 47).

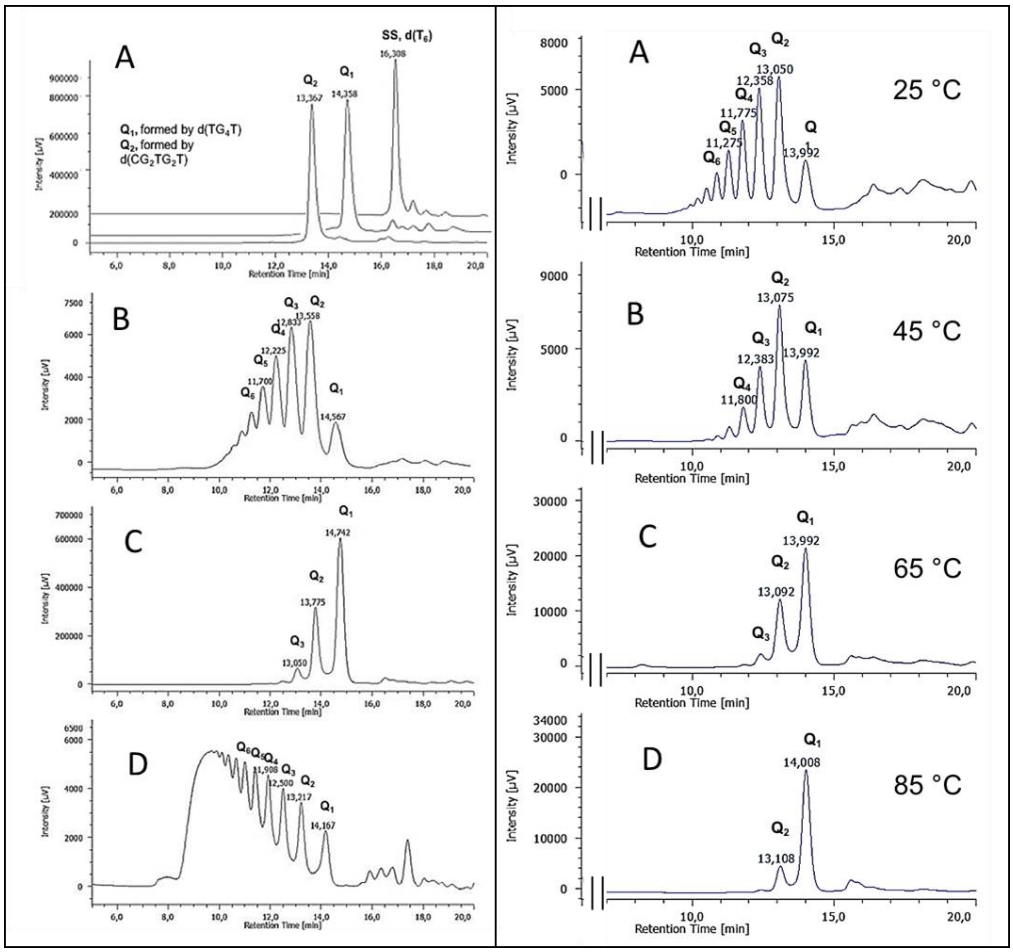

Figure 46. HPLC-SEC profiles of (**A**) molecular weight markers; (**B**) ODN annealed at 1.0 mM conc.; (**C**) ODN annealed at 0.05 mM conc.; (**D**) ODN annealed at 3.6 mM conc.; (left panel). HPLC-SEC profiles of ODN 1.0 mM conc. injected 30 min after heating at 25 (**A**), 45 (**B**), 65 (**C**) and 85 °C (**D**) (right panel).

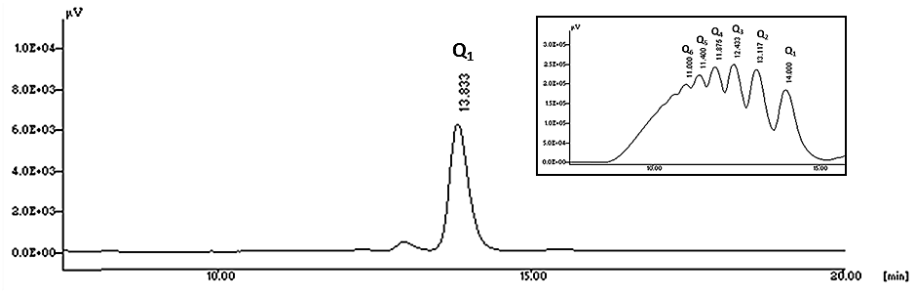

Figure 47. HPLC-SEC profile of product peak **Q_1** isolated from profile **C**, Figure 46.

Circular Dichroism (CD). Circular dichroism (CD) is a widespread technique for studying the polymorphism of G-quadruplexes. Generally, the CD profile of a parallel G-quadruplex in solution is characterized by a positive signal at 265 nm and a negative signal at 240 nm; whereas an antiparallel G-quadruplex is characterized by a negative signal at 260 nm and a positive signal at 295 nm [71]. The CD spectrum obtained for the ODN **2** is very similar to antiparallel G-quadruplex with aternating *syn-anti* glycosidic bonds along the stems. In fact, the dichroic profile is characterized by two positive signal at 250 nm and 300 nm and one negative signal at 276 nm (Figure 48). On the other hand, the CD spectra of **Q_1** isolated from ODN **2** showed a positive signal at 294 nm and a negative signal at 270 nm, probably attributed to the loss of symmetry (Figure 49).

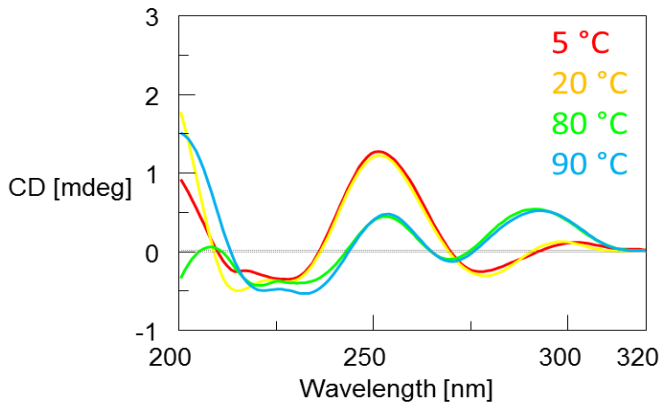

Figure 48. CD spectra of ODN **2** 40 µM, recorded at 5 °C (red line), 20 °C (orange line), 80 °C (neon green line) and 90 °C (light blue line).

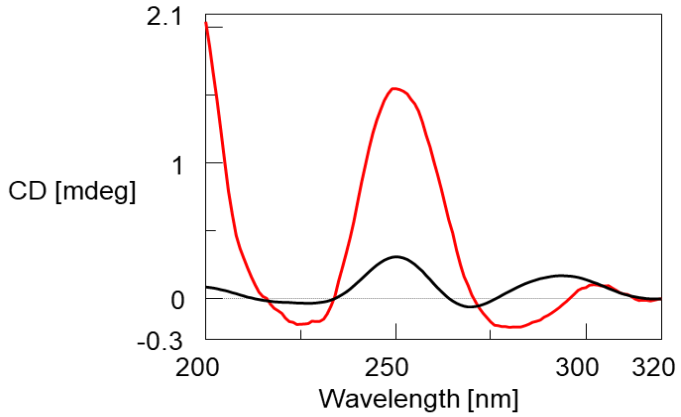

Figure 49. CD spectra of **Q_1** (black line) isolated from ODN **2** (red line).

In order to estimate the thermal stability, ODN **2** was subjected to melting and annealing CD experiment. The CD spectra at different temperatures, recorded during the melting experiment indicated for the ODN **2** a lower thermal stability also confirmed by CD melting curve (Figure 50).

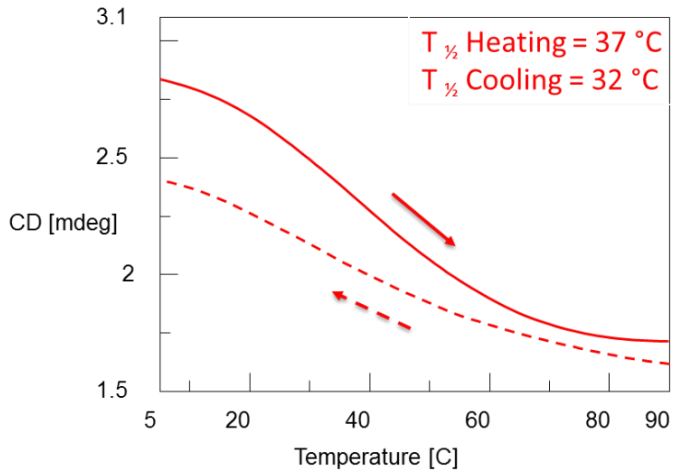

Figure 50. CD melting curves of ODN **2**. The melting experiment was performed with a temperature range of 5 °C to 90 °C at 0.5 °C min^{-1}. The CD absorbance was measured at a single wavelength (240 nm).

Atomic Force Microscope (AFM). The morphology of the ODN **2** has been investigated by AFM. The AFM images of the G-quadruplexes spontaneouly adsorbed from 3.6mM ODN freshly prepared solutions revealed more than 300 structure formations (Figure 51). It is very evident the repetition of a kind elementary units that arranges in formation of linear shape with several length, but about the same highness (1,8±0,2nm) and a mean wideness of (21±7nm). Statistical analysis has been illustrated and reported in Table 3, where the distribution of highness, wideness and length are plotted.

	Length (nm)	*Wideness (nm)*	*Highness (nm)*
Mean	80	21	1.8
Std.	60	7	0.2

Table 3. Statistical analysis where the distribution of highness, wideness and length are plotted.

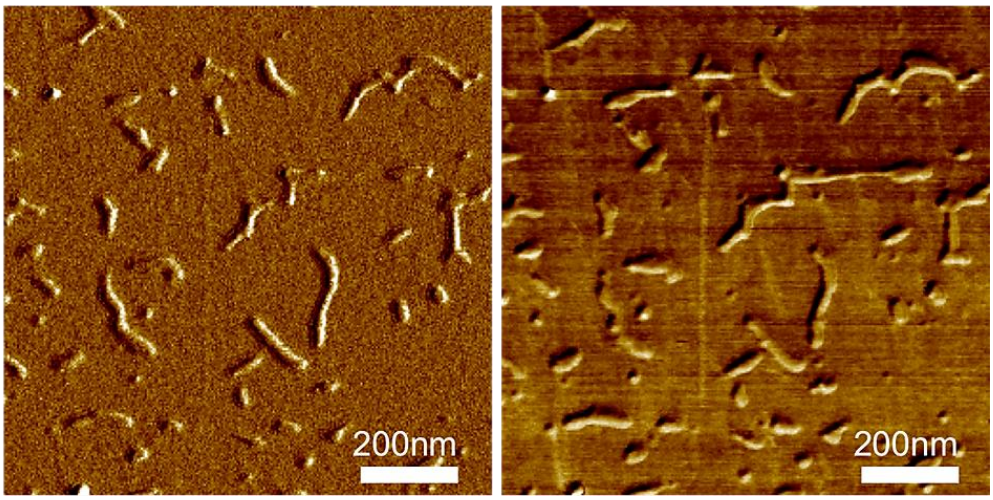

Figure 51. AFM imaging: Non-contact mode (NCM) amplitude (left) and phase (right) of symmetric sample.

The present study demonstrated the formation of a DNA based nanostructure consisting of a polymer of G-quadruplex. By means of PAGE, HPLC, CD, NMR and AFM analyses it is possible to demonstrate and characterize the formation of self-assembling into higher-order nanostructures, in the presence of K+ ion concertation and/or long incubation times. In summary, we believe that the discovery of new rules that address the process of multimerization of G-quadruplexes may be a useful achievement to project and obtain DNA based superstructures. All of this could allow the construction of G-quadruplex and their polymers with predictable dimension and shapes thus enlarging the field of their uses and, more generally, extending the DNA toolboxes for the construction of self-assembled supramolecular entities.

EXPERIMENTAL SECTION

DNA sinthesis and purifications.
DNA sequences d(TGGGGT) and d(CGGTGGT), were chemically synthesized on an Expedite 8909 DNA synthesizer (PerSeptive Biosystems, USA) using a universal CPG support purchased from Glen Research. The syntheses were performed adopting the standard β-cyanoethyl phosphoramidite chemistry at 10-15 μM scale and the products were purified as previously described. The synthesis of d($^{5'}$-CGG-$^{3'}$-$^{3'}$-GGC-$^{5'}$) (ODN **2**) was performed on the same DNA synthesizer. The inversion of polarity site within the sequence was achieved by initially assembling the $^{5'}$-CGG-$^{3'}$ tract using 5'-phorphoramidites and then the $^{3'}$-GGC-$^{5'}$ tract using standard 3'-phosphoramidites. After completion of the ODN sequence, the support was treated with concentrated aqueous ammonia at 55 °C for 15 hours. The combined filtrates and washings were concentrated under reduced pressure and purified through HPLC (JASCO PU2089 pumps equipped with the JASCO 2075 UV detector) on an anion exchange column (Macherey-Nagel, 1000-8/46, 4.4x50 mm, 5 μm) using a linear gradient from 0 to 100% B in 30 min, flow rate = 1 mL/min and detection at 260 nm (buffer A: 20 mM NaH_2PO_4 aq. solution pH 7.0, containing 20% (v/v) CH3CN; buffer B: 20 mM NaH_2PO_4 aq. solution pH 7.0, containing 1 M NaCl and 20% (v/v) CH_3CN.

Annealing procedue.
The ODN concentration was determined spectrophotometrically at λ = 260 nm at 90 °C, using molar extinction coefficient ε = 54400 M^{-1} cm^{-1} for $^{5'}$-CGGGGC-$^{3'}$, as determined using the Sigma-Aldrich OligoEvaluatorTM web tool (www.oligoevaluator.com). The 0.5-3.6 mM solutions of 2 were obtained by dissolving the lyophilized sample in 900 mM KCl and 100 mM KH_2PO_4. The samples were annealed by heating at 90 °C for 10 minutes and then quickly cooling at 4 °C. After the annealing procedure, the samples were stored at 4 °C before measurements.

(PAGE). Native gel electrophoresis experiments were performed on 15% polyacrylamide gels containing TBE 1 x (8.9 mM Tris, 8.9 mM Borate, 0.2 mM EDTA, from BIORAD) and 30 mM KCl, pH 7.0 at constant voltage of 130 V for 2 h at a temperature close to 5 °C. The ODN samples, annealed at 3.6 and 0.05 mM single strand concentration in 1.0 M K^+ buffer, were diluted at 0.6 mM loading concentration just before PAGE runs. Glycerol was added (10% final) to facilitate sample loading in the wells. The gels were finally visualized with SYBR Green (Sigma-Aldrich) and visualized using the Bio-Rad Laboratories Gel DocTM XR apparatus.

HPLC (SEC) analyses. HPLC-SEC analyses and purifications were performed on a Phenomenex (Bologna, Italy) Yarra SEC-2000 column operating in the MW range of 1,000-300,000 Dalton (300 × 7.8 mm, 3 μm)

eluted with 90 mM KCl and 10 mM KH2PO4/CH3CN (80:20, v/v), flow rate 0.6 mL min-1, detector at 260 nm. The analyses were performed at room temperature using a JASCO PU-2089 Plus quaternary gradient pump equipped with a Jasco UV-2075 Plus UV/vis detector.

(CD). CD spectra and CD melting profiles were recorded on a Jasco 1500 spectropolarimeter (Jasco, Tokyo, Japan) equipped with a Jasco PTC-348-WI temperature controller in the 200-320 nm range, using 0.1 cm path-length cuvette in potassium buffer (90 mM KCl and 10 mM KH_2PO_4/CH_3CN) at 20 μM final single strand concentration. The spectra were averaged over 3 scans at 5 °C, which recorded at 200 nm min-1 scanning speed, 4 s response time, 2 nm bandwidth. CD samples were prepared in potassium buffer (90 mM KCl and 10 mM KH_2PO_4/CH_3CN) at 20 μM final single strand concentration. The buffer baseline was subtracted from each spectrum and the spectra were normalized to have zero at 320 nm. CD melting curves were registered at 268 nm, 0.5 °C min^{-1} heating rate, temperature range 5–90 °C.

Atomic Force Microscopy (AFM). A XE-100 Park Systems instrument was used for the AFM imaging of $\mathbf{Q_n}$ G-wires. Surface imaging was obtained in non-contact mode by using 125 μm long silicon/aluminium-coated cantilevers (PPP-NCHR 10 m; Park Systems; tip radius lower than 10 nm), with a resonance frequency of 200 to 400 kHz and nominal force constant of 42 N m^{-1}. The scan frequency was typically 0.5 Hz per line. When necessary, the AFM images were processed by flattening to remove the background slope, and the contrast and brightness were adjusted. Muscovite mica of about 1 cm^2 surface was used as the substrate in the AFM study. Muscovite mica surfaces are typically used as AFM substrates owing to their perfect cleavage along a <001> plane, yielding large atomically flat areas. Mica consists of layers of an aluminium phyllosilicate lattice ionically bonded through interstitial K^+ ions. Upon cleavage, the K^+ ions are highly mobile and are readily exchanged with divalent cation species at the solid–liquid interface. This exchange results in a positive overcharging of the mica surface, which enables the deposition of molecules that hold a net negative charge, such as DNA. Moreover, the positive charge distribution after cleavage enables a super-hydrophilic surface that guarantees a lower interaction between suspended biomolecules during the evaporation of aqueous solvent. Mica was freshly cleaved by using adhesive tape prior to each deposition to establish its cleanliness. Aliquots (2 μL) of the DNA/imaging buffer were directly deposited by casting onto freshly cleaved muscovite mica. After 2 min, every sample was gently washed with deionized water and then dried by evaporation at room temperature under a ventilated fume hood.

2.4 Referencces

[1] H. S. Basu, B. G. Feuerstein, D. A. Zarling, R. H. Shafer, and L. J. Marton, “Recognition of z-rna and z-dna determinants by polyamines in solution: Experimental and theoretical studies,” *J. Biomol. Struct. Dyn.*, vol. 6, no. 2, pp. 299–309, 1988.

[2] R. V. Gessner, C. A. Frederick, G. J. Quigley, A. Rich, and A. H. J. Wang, “The molecular structure of the left-handed Z-DNA double helix at 1.0-Å atomic resolution. Geometry, conformation, and ionic interactions of d(CGCGCG),” *J. Biol. Chem.*, vol. 264, no. 14, pp. 7921–7935, 1989.

[3] A. Manuscript, “potential,” vol. 90, no. 8, pp. 1117–1130, 2009.

[4] E. Palecek, “Local Supercoil-Stabilized DNA Structures,” vol. 26, no. 2, 1991.

[5] D. Svozil, J. Kalina, M. Omelka, and B. Schneider, “DNA conformations and their sequence preferences,” *Nucleic Acids Res.*, vol. 36, no. 11, pp. 3690–3706, 2008.

[6] H. A. Day, P. Pavlou, and Z. A. E. Waller, “I-Motif DNA: Structure, stability and targeting with ligands,” *Bioorganic Med. Chem.*, vol. 22, no. 16, pp. 4407–4418, 2014.

[7] B. Kidd, “of Triple-X,” pp. 90–95, 1963.

[8] B. P. Belotserkovskii, R. Liu, S. Tornaletti, M. M. Krasilnikova, S. M. Mirkin, and P. C. Hanawalt, “Mechanisms and implications of transcription blockage by guanine-rich DNA sequences,” *Proc. Natl. Acad. Sci. U. S. A.*, vol. 107, no. 29, pp. 12816–12821, 2010.

[9] S. Neidle and G. N. Parkinson, “The structure of telomeric DNA,” *Curr. Opin. Struct. Biol.*, vol. 13, no. 3, pp. 275–283, 2003.

[10] S. Sharma, K. M. Doherty, and R. M. Brosh, “DNA helicases as targets for anti-cancer drugs,” *Curr. Med. Chem. - Anti-Cancer Agents*, vol. 5, no. 3, pp. 183–199, 2005.

[11] L. A. Christensen, R. A. Finch, A. J. Booker, and K. M. Vasquez, “Targeting oncogenes to improve breast cancer chemotherapy,” *Cancer Res.*, vol. 66, no. 8, pp. 4089–4094, 2006.

[12] T. M. Bryan and P. Baumann, “G-quadruplexes: From guanine gels to chemotherapeutics,” *Mol. Biotechnol.*, vol. 49, no. 2, pp. 198–208, 2011.

[13] M. GELLERT, M. N. LIPSETT, and D. R. DAVIES, “Helix formation by guanylic acid,” *Proc. Natl. Acad. Sci. U. S. A.*, vol. 48, pp. 2013–2018, 1962.

[14] S. B. Zimmerman, “X-ray study by fiber diffraction methods of a self-aggregate of guanosine-5′-phosphate with the same helical parameters as poly(rG),” *J. Mol. Biol.*, vol. 106, no. 3, pp. 663–672, 1976.

[15] Y. Wang and D. J. Patel, “Solution structure of the oxytricha telomeric repeat d[G4(T4G4)3] G-tetraplex,” *J. Mol. Biol.*, vol. 251, no. 1, pp. 76–94, 1995.
[16] W. I. Sundquist and A. Klug, “Tetrads Between Hairpin Loops,” vol. 342, no. December, pp. 825–829, 1989.
[17] D. Sen and W. Gilbert, “Formation of parallel four-stranded complexes by guanine-rich motifs in DNA and its implications for meiosis,” *Nature*, vol. 334, no. 6180, pp. 364–366, 1988.
[18] A. Risitano and K. R. Fox, “Influence of loop size on the stability of intramolecular DNA quadruplexes,” *Nucleic Acids Res.*, vol. 32, no. 8, pp. 2598–2606, 2004.
[19] P. A. Rachwal, I. S. Findlow, J. M. Werner, T. Brown, and K. R. Fox, “Intramolecular DNA quadruplexes with different arrangements of short and long loops,” *Nucleic Acids Res.*, vol. 35, no. 12, pp. 4214–4222, 2007.
[20] P. Hazel, J. Huppert, S. Balasubramanian, and S. Neidle, “Loop-length-dependent folding of G-quadruplexes,” *J. Am. Chem. Soc.*, vol. 126, no. 50, pp. 16405–16415, 2004.
[21] Woalder, “乳鼠心肌提取 HHS Public Access,” *Physiol. Behav.*, vol. 176, no. 1, pp. 139–148, 2017.
[22] S. Burge, G. N. Parkinson, P. Hazel, A. K. Todd, and S. Neidle, “Quadruplex DNA: Sequence, topology and structure,” *Nucleic Acids Res.*, vol. 34, no. 19, pp. 5402–5415, 2006.
[23] T. Van Mourik and A. J. Dingley, “Characterization of the monovalent ion position and hydrogen-bond network in guanine quartets by DFT calculations of NMR parameters,” *Chem. - A Eur. J.*, vol. 11, no. 20, pp. 6064–6079, 2005.
[24] A. J. Dingley, R. D. Peterson, S. Grzesiek, and J. Feigon, “Characterization of the cation and temperature dependence of DNA quadruplex hydrogen bond properties using high-resolution NMR,” *J. Am. Chem. Soc.*, vol. 127, no. 41, pp. 14466–14472, 2005.
[25] C. C. Hardin, T. Watson, M. Corregan, and C. Bailey, “Cation-Dependent Transition between the Quadruplex and Watson-Crick Hairpin Forms of d(CGCG3GCG),” *Biochemistry*, vol. 31, no. 3, pp. 833–841, 1992.
[26] V. M. Marathias and P. H. Bolton, “Determinants of DNA quadruplex structural type: Sequence and potassium binding,” *Biochemistry*, vol. 38, no. 14, pp. 4355–4364, 1999.
[27] J. L. Huppert and S. Balasubramanian, “Prevalence of quadruplexes in the human genome,” *Nucleic Acids Res.*, vol. 33, no. 9, pp. 2908–2916, 2005.
[28] A. K. Todd, M. Johnston, and S. Neidle, “Highly prevalent putative

quadruplex sequence motifs in human DNA," *Nucleic Acids Res.*, vol. 33, no. 9, pp. 2901–2907, 2005.
[29] W. Guschlbauer, J. F. Chantot, and D. Thiele, "Four-stranded nucleic acid structures 25 years later: From guanosine gels to telomer dna," *J. Biomol. Struct. Dyn.*, vol. 8, no. 3, pp. 491–511, 1990.
[30] E. Henderson, C. C. Hardin, S. K. Walk, I. Tinoco, and E. H. Blackburn, "Telomeric DNA oligonucleotides form novel intramolecular structures containing guanine·guanine base pairs," *Cell*, vol. 51, no. 6, pp. 899–908, 1987.
[31] J. R. Williamson, M. K. Raghuraman, and T. R. Cech, "Monovalent cation-induced structure of telomeric DNA: The G-quartet model," *Cell*, vol. 59, no. 5, pp. 871–880, 1989.
[32] 2013 John R.Giudicessi, BA.Michael J.Ackerman., "基因的改变NIH Public Access," *Bone*, vol. 23, no. 1, pp. 1–7, 2008.
[33] J. W. Shay and S. Bacchetti, "A survey of telomerase activity in human cancer," *Eur. J. Cancer Part A*, vol. 33, no. 5, pp. 787–791, 1997.
[34] S. C. Zimmerman and P. S. Corbin, "Heteroaromatic Modules for Self-Assembly Using Multiple Hydrogen Bonds," vol. 96, pp. 63–94, 2000.
[35] C. K. Kwok and C. J. Merrick, "G-Quadruplexes: Prediction, Characterization, and Biological Application," *Trends Biotechnol.*, vol. 35, no. 10, pp. 997–1013, 2017.
[36] G. W. Collie and G. N. Parkinson, "The application of DNA and RNA G-quadruplexes to therapeutic medicines," *Chem. Soc. Rev.*, vol. 40, no. 12, pp. 5867–5892, 2011.
[37] C. Platella, C. Riccardi, D. Montesarchio, G. N. Roviello, and D. Musumeci, "G-quadruplex-based aptamers against protein targets in therapy and diagnostics," *Biochim. Biophys. Acta - Gen. Subj.*, vol. 1861, no. 5, pp. 1429–1447, 2017.
[38] I. Russo Krauss, A. Merlino, A. Randazzo, E. Novellino, L. Mazzarella, and F. Sica, "High-resolution structures of two complexes between thrombin and thrombin-binding aptamer shed light on the role of cations in the aptamer inhibitory activity," *Nucleic Acids Res.*, vol. 40, no. 16, pp. 8119–8128, 2012.
[39] J. A. Kelly, J. Feigon, and T. O. Yeates, "Reconciliation of the X-ray and NMR structures of the thrombin-binding aptamer d(GGTTGGTGTGGTTGG)," *J. Mol. Biol.*, vol. 256, no. 3, pp. 417–422, 1996.
[40] K. Y. Wang, P. H. Bolton, S. H. Krawczyk, N. Bischofberger, and S. Swaminathan, "The Tertiary Structure of a DNA Aptamer Which Binds to and Inhibits Thrombin Determines Activity," *Biochemistry*, vol. 32, no. 42, pp. 11285–11292, 1993.
[41] J. S. Paige, T. Nguyen-Duc, W. Song, and S. R. Jaffrey, "Fluorescence

imaging of cellular metabolites with RNA," *Science (80-.).*, vol. 335, no. 6073, p. 1194, 2012.
[42] G. Di Fabio *et al.*, "Discovery of novel anti-HIV active G-quadruplex-forming oligonucleotides," *Chem. Commun.*, vol. 47, no. 8, pp. 2363–2365, 2011.
[43] G. Oliviero *et al.*, "Synthesis of quadruplex-forming tetra-end-linked oligonucleotides: Effects of the linker size on quadruplex topology and stability," *Biopolymers*, vol. 91, no. 6, pp. 466–477, 2009.
[44] G. Oliviero *et al.*, "Tetra-end-linked oligonucleotides forming DNA G-quadruplexes: A new class of aptamers showing anti-HIV activity," *Chem. Commun.*, vol. 46, no. 47, pp. 8971–8973, 2010.
[45] D. Řeha *et al.*, "Intercalators. 1. Nature of stacking interactions between intercalators (ethidium, daunomycin, ellipticine, and 4′,6-diaminide-2-phenylindole) and DNA base pairs. Ab initio quantum chemical, density functional theory, and empirical potential study," *J. Am. Chem. Soc.*, vol. 124, no. 13, pp. 3366–3376, 2002.
[46] B. S. P. Reddy, S. K. Sharma, and J. W. Lown, "Recent Developments In Sequence Selective Minor Groove DNA Effectors," *Curr. Med. Chem.*, vol. 8, no. 5, pp. 475–508, 2012.
[47] T. Niidome *et al.*, "Binding of cationic α-helical peptides to plasmid DNA and their gene transfer abilities into cells," *J. Biol. Chem.*, vol. 272, no. 24, pp. 15307–15312, 1997.
[48] J. T. Davis, "G-Quartets 40 Years Later: From 5′-GMP to Molecular Biology and Supramolecular Chemistry," *Angew. Chemie - Int. Ed.*, vol. 43, no. 6, pp. 668–698, 2004.
[49] N. C. Seeman, "DNA in a material world," *Nature*, vol. 421, no. 6921, pp. 427–431, 2003.
[50] P. W. K. Rothemund, "Folding DNA to create nanoscale shapes and patterns," *Nature*, vol. 440, no. 7082, pp. 297–302, 2006.
[51] T. C. Marsh and E. Henderson, "G-Wires: Self-Assembly of a Telomeric Oligonucleotide, d(GGGGTTGGGG), into Large Superstructures," *Biochemistry*, vol. 33, no. 35, pp. 10718–10724, 1994.
[52] E. Protozanova and R. B. Macgregor, "Frayed wires: A thermally stable form of DNA with two distinct structural domains," *Biochemistry*, vol. 35, no. 51, pp. 16638–16645, 1996.
[53] E. M. Ahmed, "Hydrogel: Preparation, characterization, and applications: A review," *J. Adv. Res.*, vol. 6, no. 2, pp. 105–121, 2015.
[54] Y. Sun *et al.*, "Self-assembly of a 5-fluorouracil-dipeptide hydrogel," *Chem. Commun.*, vol. 52, no. 30, pp. 5254–5257, 2016.
[55] S. H. Kim, Y. Sun, J. A. Kaplan, M. W. Grinstaff, and J. R. Parquette, "Photo-crosslinking of a self-assembled coumarin-dipeptide hydrogel," *New J. Chem.*, vol. 39, no. 5, pp. 3225–3228, 2015.
[56] M. Verhulsel, M. Vignes, S. Descroix, L. Malaquin, D. M. Vignjevic, and

J. L. Viovy, “A review of microfabrication and hydrogel engineering for micro-organs on chips,” *Biomaterials*, vol. 35, no. 6, pp. 1816–1832, 2014.

[57] D. E. Discher, D. J. Mooney, and P. W. Zandstra, “Growth factors, matrices, and forces combine,” *Growth (Lakeland)*, vol. 324, no. 5935, pp. 1673–1677, 2010.

[58] M. E. Gleave and B. P. Monia, “Antisense therapy for cancer,” *Nat. Rev. Cancer*, vol. 5, no. 6, pp. 468–479, 2005.

[59] S. Z. Fu *et al.*, “Injectable and thermo-sensitive PEG-PCL-PEG copolymer/collagen/n-HA hydrogel composite for guided bone regeneration,” *Biomaterials*, vol. 33, no. 19, pp. 4801–4809, 2012.

[60] S. S. Kim, M. Sun Park, O. Jeon, C. Yong Choi, and B. S. Kim, “Poly(lactide-co-glycolide)/hydroxyapatite composite scaffolds for bone tissue engineering,” *Biomaterials*, vol. 27, no. 8, pp. 1399–1409, 2006.

[61] A. Vashist *et al.*, “Nanocomposite Hydrogels: Advances in Nanofillers Used for Nanomedicine,” *Gels*, vol. 4, no. 3, p. 75, 2018.

[62] K. Haraguchi, “Nanocomposite gels: New advanced functional soft materials,” *Macromol. Symp.*, vol. 256, pp. 120–130, 2007.

[63] J. Wang, “SURVEY AND SUMMARY: From DNA biosensors to gene chips,” *Nucleic Acids Res.*, vol. 28, no. 16, pp. 3011–3016, 2000.

[64] H. W. Lee and D. Sen, “Structure-function investigation of a deoxyribozyme with dual chelatase and peroxidase activities,” *Pure Appl. Chem.*, vol. 76, no. 7–8, pp. 1537–1545, 2004.

[65] P. Travascio, Y. Li, and D. Sen, “DNA-enhanced peroxidase activity of a DNA aptamer-hemin complex,” *Chem. Biol.*, vol. 5, no. 9, pp. 505–517, 1998.

[66] P. Murat *et al.*, “Template-Assembled Synthetic G-Quadruplex (TASQ): A Useful System for Investigating the Interactions of Ligands with Constrained Quadruplex Topologies,” *Chem. - A Eur. J.*, vol. 16, no. 20, pp. 6106–6114, 2010.

[67] P. Murat *et al.*, “A novel conformationally constrainedparallel G Quadruplex,” *ChemBioChem*, vol. 9, no. 16, pp. 2588–2591, 2008.

[68] G. Oliviero, N. Borbone, A. Galeone, M. Varra, G. Piccialli, and L. Mayol, “Synthesis and characterization of a bunchy oligonucleotide forming a monomolecular parallel quadruplex structure in solution,” *Tetrahedron Lett.*, vol. 45, no. 25, pp. 4869–4872, 2004.

[69] T. Kobori, S. Iwamoto, K. Takeyasu, and T. Ohtani, “Biopolymers Volume 85 / Number 4 295,” *Biopolymers*, vol. 85, no. 4, pp. 392–406, 2007.

[70] G. Oliviero *et al.*, “Synthesis and characterization of monomolecular DNA G-quadruplexes formed by tetra-end-linked oligonucleotides,” *Bioconjug. Chem.*, vol. 17, no. 4, pp. 889–898, 2006.

[71] J. Cheng and T. J. Deming, “synthesis of polypeptides by ROP of

NCAs," *Pept. Mater.*, vol. 310, pp. 1–26, 2011.
[72] M. Vorlíčková *et al.*, "Circular dichroism and guanine quadruplexes," *Methods*, vol. 57, no. 1, pp. 64–75, 2012.
[73] N. Borbone *et al.*, "Synthesis and characterization of tetra-end linked oligonucleotides capable of forming monomolecular G-quadruplexes," *Nucleosides, Nucleotides and Nucleic Acids*, vol. 26, no. 10–12, pp. 1231–1236, 2007.
[74] R. Jin, B. L. Gaffney, C. Wang, R. A. Jones, and K. J. Breslauer, "Thermodynamics and structure of a DNA tetraplex: A spectroscopic and calorimetric study of the tetramolecular complexes of d(TG3T) and d(TG3T2G3T)," *Proc. Natl. Acad. Sci. U. S. A.*, vol. 89, no. 18, pp. 8832–8836, 1992.
[75] C. C. Hardin, A. G. Perry, and K. White, "Thermodynamic and kinetic characterization of the dissociation and assembly of quadruplex nucleic acids," *Biopolymers*, vol. 56, no. 3, pp. 147–194, 2000.
[76] V. Dapić *et al.*, "Biophysical and biological properties of quadruplex oligodeoxyribonucleotides," *Nucleic Acids Res.*, vol. 31, no. 8, pp. 2097–2107, 2003.
[77] L. Petraccone *et al.*, "Stability and Structure of Telomeric DNA Sequences Forming Quadruplexes Containing Four G-Tetrads with Different Topological Arrangements," *Biochemistry*, vol. 43, no. 16, pp. 4877–4884, 2004.
[78] J. Feigon, K. M. Koshlap, and F. W. Smith, "1H NMR spectroscopy of DNA triplexes and quadruplexes," *Methods Enzymol.*, vol. 261, no. C, pp. 225–255, 1995.
[79] G. Oliviero *et al.*, "Self-assembly of g-rich oligonucleotides incorporating a 3'-3' inversion of polarity site: A new route towards G-Wire DNA nanostructures," *ChemistryOpen*, vol. 6, no. 4, pp. 599–605, 2017.
[80] H. Hotoda *et al.*, "Biologically active oligodeoxyribonucleotides - ii 1 : Structure activity relationships of anti-hiv-1 pentadecadeoxyribonucleotides bearing 5'-end-modifications," *Nucleosides and Nucleotides*, vol. 13, no. 6–7, pp. 1375–1395, 1994.
[81] M. Koizumi *et al.*, "Biologically active oligodeoxyribonucleotides-VII: Anti-HIV-1 activity of hexadeoxyribonucleotides bearing 3'- and 5'-end-modifications," *Nucleosides and Nucleotides*, vol. 16, no. 7–9, pp. 1205–1208, 1997.
[82] V. D'Atri *et al.*, "New anti-HIV aptamers based on tetra-end-linked DNA G-quadruplexes: Effect of the base sequence on anti-HIV activity," *Chem. Commun.*, vol. 48, no. 76, pp. 9516–9518, 2012.
[83] A. D. Keefe, S. Pai, and A. Ellington, "Aptamers as therapeutics," *Nat. Rev. Drug Discov.*, vol. 9, no. 7, pp. 537–550, 2010.
[84] V. D'Atri *et al.*, "DNA-based nanostructures: The effect of the base

sequence on octamer formation from d(XGGYGGT) tetramolecular G-quadruplexes," *Biochimie*, vol. 99, no. 1, pp. 119–128, 2014.

[85] N. A. El-Sersy, A. E. Abdelwahab, S. S. Abouelkhiir, D. M. Abou-Zeid, and S. A. Sabry, "Antibacterial and Anticancer activity of ε -poly-L-lysine (ε -PL) produced by a marine Bacillus subtilis sp.," *J. Basic Microbiol.*, vol. 52, no. 5, pp. 513–522, 2012.

[86] W. Bao *et al.*, "PLGA-PLL-PEG-Tf-based targeted nanoparticles drug delivery system enhance antitumor efficacy via intrinsic apoptosis pathway," *Int. J. Nanomedicine*, vol. 10, pp. 557–566, 2015.

[87] W. B. Titlow *et al.*, "Effect of polylysine on scrapie prion protein propagation in spleen during asymptomatic stage of experimental prion disease in mice," *J. Microbiol. Biotechnol.*, vol. 26, no. 9, pp. 1657–1660, 2016.

[88] G. Zu *et al.*, "Functional Hyperbranched Polylysine as Potential Contrast Agent Probes for Magnetic Resonance Imaging," *Biomacromolecules*, vol. 17, no. 6, pp. 2302–2308, 2016.

[89] J. Du, C. Tian, J. Ling, and Y. Wang, "R8-modified polysarcosine- b -polylysine polypeptide to enhance circulation stability and gene delivery efficiency," *J. Control. Release*, vol. 213, pp. e50–e51, 2015.

[90] I.- Shih, Y.- Van, and M.- Shen, "Biomedical Applications of Chemically and Microbiologically Synthesized Poly(Glutamic Acid) and Poly(Lysine)," *Mini-Reviews Med. Chem.*, vol. 4, no. 2, pp. 179–188, 2005.

[91] J. P. Ayyappan, H. Sami, D. C. Rajalekshmi, S. Sivakumar, and A. Abraham, "Immunocompatibility and toxicity studies of Poly-L-lysine nanocapsules in Sprague-Dawley rats for drug-delivery applications," *Chem. Biol. Drug Des.*, vol. 84, no. 3, pp. 292–299, 2014.

[92] Z. Kadlecova *et al.*, "DNA delivery with hyperbranched polylysine: A comparative study with linear and dendritic polylysine," *J. Control. Release*, vol. 169, no. 3, pp. 276–288, 2013.

[93] Z. Kadlecova, L. Baldi, D. Hacker, F. M. Wurm, and H. A. Klok, "Comparative study on the in vitro cytotoxicity of linear, dendritic, and hyperbranched polylysine analogues," *Biomacromolecules*, vol. 13, no. 10, pp. 3127–3137, 2012.

[94] G. N. Roviello, D. Musumeci, and V. Roviello, "Cationic peptides as RNA compaction agents: A study on the polyA compaction activity of a linear alpha,epsilon-oligo-l-lysine," *Int. J. Pharm.*, vol. 485, no. 1–2, pp. 244–248, 2015.

[95] M. C. Miller, R. Buscaglia, J. B. Chaires, A. N. Lane, and J. O. Trent, "Hydration is a major determinant of the G-quadruplex stability and conformation of the human telomere 3′ sequence of d(AG 3(TTAG3)3)," *J. Am. Chem. Soc.*, vol. 132, no. 48, pp. 17105–17107, 2010.

[96] H. L. Bao, H. S. Liu, and Y. Xu, "Hybrid-type and two-tetrad antiparallel

telomere DNA G-quadruplex structures in living human cells," *Nucleic Acids Res.*, vol. 47, no. 10, pp. 4940–4947, 2019.
[97] A. Ambrus, D. Chen, J. Dai, T. Bialis, R. A. Jones, and D. Yang, "Human telomeric sequence forms a hybrid-type intramolecular G-quadruplex structure with mixed parallel/antiparallel strands in potassium solution," *Nucleic Acids Res.*, vol. 34, no. 9, pp. 2723–2735, 2006.
[98] A. Virgilio, V. Esposito, L. Mayol, C. Giancola, L. Petraccone, and A. Galeone, "The oxidative damage to the human telomere: Effects of 5-hydroxymethyl-2′-deoxyuridine on telomeric G-quadruplex structures," *Org. Biomol. Chem.*, vol. 13, no. 27, pp. 7421–7429, 2015.
[99] A. Ambrus, D. Chen, J. Dai, R. A. Jones, and D. Yang, "Solution structure of the biologically relevant G-quadruplex element in the human c-MYC promoter. Implications for G-quadruplex stabilization," *Biochemistry*, vol. 44, no. 6, pp. 2048–2058, 2005.
[100] J. Kypr, I. Kejnovská, D. Renčiuk, and M. Vorlíčková, "Circular dichroism and conformational polymorphism of DNA," *Nucleic Acids Res.*, vol. 37, no. 6, pp. 1713–1725, 2009.
[101] P. Sengupta, N. Banerjee, T. Roychowdhury, A. Dutta, S. Chattopadhyay, and S. Chatterjee, "Site-specific amino acid substitution in dodecameric peptides determines the stability and unfolding of c-MYC quadruplex promoting apoptosis in cancer cells," *Nucleic Acids Res.*, vol. 46, no. 19, pp. 9932–9950, 2018.
[102] S. Stump, T. C. Mou, S. R. Sprang, N. R. Natale, and H. D. Beall, "Crystal structure of the major quadruplex formed in the promoter region of the human c-MYC oncogene," *PLoS One*, vol. 13, no. 10, pp. 1–15, 2018.
[103] Y. Hua *et al.*, "Cation effect on the electronic excited states of guanine nanostructures studied by time-resolved fluorescence spectroscopy," *J. Phys. Chem. C*, vol. 116, no. 27, pp. 14682–14689, 2012.
[104] G. I. Livshits *et al.*, "Long-range charge transport in single G-quadruplex DNA molecules," *Nat. Nanotechnol.*, vol. 9, no. 12, pp. 1040–1046, 2014.
[105] S. P. Liu, S. H. Weisbrod, Z. Tang, A. Marx, E. Scheer, and A. Erbe, "Direct measurement of electrical transport through G-quadruplex DNA with mechanically controllable break junction electrodes," *Angew. Chemie - Int. Ed.*, vol. 49, no. 19, pp. 3313–3316, 2010.
[106] A. Calzolari, R. Di Felice, E. Molinari, and A. Garbesi, "G-quartet biomolecular nanowires," *Appl. Phys. Lett.*, vol. 80, no. 18, pp. 3331–3333, 2002.
[107] W. Ren, Y. Zhang, H. G. Chen, Z. F. Gao, N. B. Li, and H. Q. Luo, "Ultrasensitive Label-Free Resonance Rayleigh Scattering Aptasensor for Hg2+ Using Hg2+-Triggered Exonuclease III-Assisted Target Recycling and Growth of G-Wires for Signal Amplification," *Anal.*

Chem., vol. 88, no. 2, pp. 1385–1390, 2016.
[108] N. Ma'Ani Hessari, L. Spindler, T. Troha, W. C. Lam, I. Drevenšek-Olenik, and M. Webba Da Silva, "Programmed self-assembly of a quadruplex DNA nanowire," *Chem. - A Eur. J.*, vol. 20, no. 13, pp. 3626–3630, 2014.
[109] N. Borbone *et al.*, "D(CGGTGGT) forms an octameric parallel G-quadruplex via stacking of unusual G(:C):G(:C):G(:C):G(:C) octads," *Nucleic Acids Res.*, vol. 39, no. 17, pp. 7848–7857, 2011.
[110] M. Adrian, B. Heddi, and A. T. Phan, "NMR spectroscopy of G-quadruplexes," *Methods*, vol. 57, no. 1, pp. 11–24, 2012.
[111] V. Esposito, A. Virgilio, A. Randazzo, A. Galeone, and L. Mayol, "A new class of DNA quadruplexes formed by oligodeoxyribonucleotides containing a 3′-3′ or 5′-5′ inversion of polarity site," *Chem. Commun.*, no. 31, pp. 3953–3955, 200

CHAPTER 3
Peptide nucleic acids (PNAs): an important tool for the modulating of gene expression

3.1 Introduction

Peptide Nucleic Acid (PNA) was discovered during the 1990s by groups of biochemist Peter Nielsen and organic chemist Ole Buchardt. PNA is a DNA/RNA mimic characterized by a backbone made from repeating N-(2-aminoethyl) glycine units linked by peptide bonds, with the standard nucleobases (purines and pyrimidines) attached to the backbone through methylene carbonyl linkages. Conventionally PNAs are represented as peptides, with the N-terminus at the first position and the C-terminus at the last position, corresponding to the 5'-end and 3'-end of DNA (Figure 1).

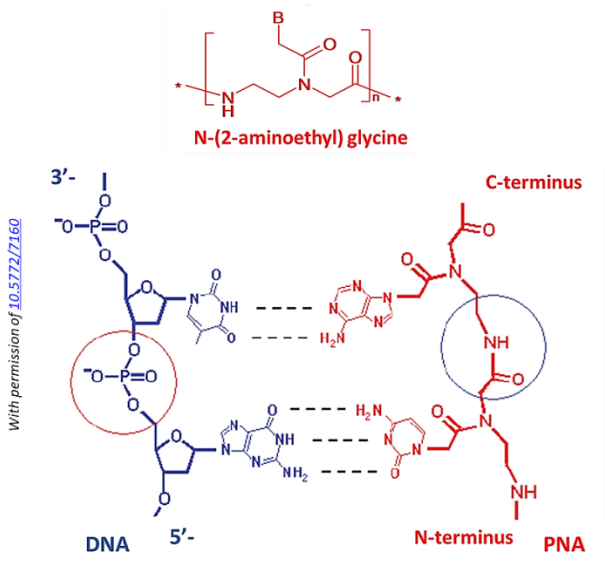

Figure 1. Comparison of the structure of Peptide Nucleic Acid (PNA) and DNA. The deoxyribose-phosphate backbone of DNA (blue) is replaced by N-2(-aminoethyl) glycine units in PNA (red). The nucleobases are shown in blue for DNA and red for PNA.

Unlike DNA or DNA analogues, PNAs do not contain any pentose sugar moieties or phosphate groups. Its backbone is acyclic, achiral and neutral. These features, the neutral character and the low electrostatic repulsion, provide PNAs with several important characteristics, such as: i) the capacity to form very stable and specific complexes with DNA and RNA targets; ii) the thermal stability (T_m) of the PNA/DNA complex

largely independent of the salt concentration [1][2][3]; iii) an increased the rate of hybridization; and iv) resistance again nucleases and proteases. PNAs recognize and hybridize complementary strands in several modes, namely: parallel, antiparallel, triplex and strand invasion (Figure 2). In the parallel type, the N-terminus of the PNA binds the 3'-end of the DNA strand (Figure 2A) [4], whereas in the antiparallel type, the N-terminus of the PNA binds the 5'-end of the DNA strand (Figure 2B). In the PNA-DNA-PNA triplex we can observed a combination of an antiparallel Watson-Crick duplex with a parallel bound Hoogsteen strand (Figure 2C) [5]. In the triplex invasion is require an opening of the DNA double helix and the pairing of only one strand of DNA is required, while the other unbound DNA strand is moved to a D-loop structure (Figure 2D) [1][6][7][8].

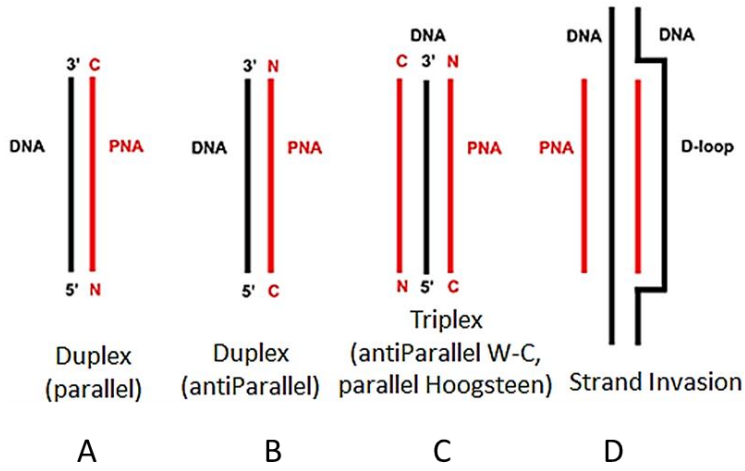

Figure 2. Schematic representation of a: PNA-DNA duplex in the parallel mode (**A**), PNA-DNA duplex in the antiparallel mode (**B**), PNA-DNA-PNA triplex (**C**) and PNA-DNA-PNA triplex-strand invasion (**D**).

3.2 Synthesis of Peptide Nucleic Acid through the Fmoc strategy

PNA can be synthesized using automated procedures (Mayfield and Corey, 1999) [169] or manual procedures (Norton *et al*., 1995). Usually, when large scale PNA synthesis is required (> 2 μmol), the best way is by using the Fmoc-solid phase protocol. The synthesis is accomplished using monomers protected by either t-Boc or Fmoc protecting groups. Generally, Boc monomers produce better yields than Fmoc monomers. The synthetic steps consist in: i) a *swelling* and functionalization of the solid support; ii) *deblocking*; iii) *coupling*; iv) *capping* and v) a detachment of the oligomer from the solid support. Prior to beginning a synthesis, the resin should be *swelling* in the synthesis solvent. Resins

are like a sponge. Swellings allow them to expand minimize the exposure of their functional groups to the incoming reactants. *Deprotection* is the first step in a synthesis cycle. It removes the Fmoc protecting group from the resin-linker (in the case of Rink amide resin) or attached amino acids (in the case of Wang resins, or an existing peptide chain). Fmoc groups are removed by basic treatment with 20% piperidine in DMF for 2 to 20 minutes. For difficult deprotections, a stronger base, 2% DBU in DMF may be used. In order for the carboxylic acid of an amino acid to attach or couple to the amino group of another amino acid, it must first be activated. In order to speed up the coupling reactions, an excess of reactants, such as HBTU, HCTU, Py BOP, HATU, HOBt/DIC or DCC, is added. The bases used during coupling are NMM or DIPEA. In general, the activator/base ratio should be 1:2 to 1:4 and typical amino acid solution concentrations range from 0.1 to 0.5 in DMF. The coupling efficiency determines the final purity of the peptide. For this reason, the reaction times can range from 5 minutes to 2 hours depending on the activator used, the amino acid being coupled and the sequence of the peptide. In fact, some peptide sequences tend to aggregate, or clump together, hiding the reactive sites at the end of the peptide chains. Various methods can be employed to reduce the effects of aggregation including the use of different solvents such as DMS, NMP or chaotropic salts. Between the deprotection and coupling steps it is very important to wash the resin with a primary solvent, e.g. DMF (2 to 6 times for 30 seconds), because, otherwise the residual piperidine could remove the Fmoc group from the amino acid being introduced. Capping is performed to permanently block any unreacted amino groups following a coupling reaction, or to acetylate the N-terminus of a completed peptide. It Is useful during the synthesis of long peptides to minimize any deletion products. Typical capping solution compositions include 1:1:3 acetic anhydride/base/DMF, where pyridine or DIPEA may be used as the base. After the synthesis is complete, the final Fmoc protecting group and side chain protecting groups need to be removed, and the peptide needs to be removed or cleaved from the resin. The final deprotection is performed with 20% piperidine in DMF to remove the final Fmoc group while the peptide is still attached to the resin. Cleavage of the peptide from the resin and the removal of the side chain protecting groups is accomplished with trifluoroacetic acid (TFA). It is common to add additional reagents to the TFA which are used as scavengers of the side chain protecting groups to prevent their reattachment to the peptide. Typical scavengers include EDT, water, thioanisole, TIS and phenol. After the cleavage reaction, the solution is filtered from the resin

and the peptide is obtained by precipitation with ice-cold ether. Peptides should be washed at least 3 times to remove as many of the scavengers as possible. If the peptide does not precipitate, there may be an excess of TFA. In this case, it is necessary to evaporate off the excess TFA and ether and repeat the process. Afterwards, the peptides may be left in a hood to air-dry overnight or may be lyophilized for storage.

3.3 The aim of the work

The favourable biophysical properties of PNAs, together with their high chemical and enzymatic stability and low toxicity, make them one of the most valuable tools for diagnostics [10], biomedical and therapeutics applications, such as anti-gene [11], anti-sense [12] and anti-miRNA strategies [13]. In diagnostics, biosensors represent an ideal platform for the construction of minimally invasive tools able to provide molecular-level information to be used for the implementation of personalised medicine approaches. They are analytical devices that incorporate a biological sensing element and are based on the conversion of molecular recognition events into a measurable signal generated by a transducer. For example, the use of chips properly functionalized with PNA probes makes it possible to detect cancer biomarkers [14] circulating in the blood through a hybridization with complementary ODN sequences in agreement with the Watson-Crick base paring rules. In molecular biology and therapeutics, PNA has enabled the design of new methods for gene regulation by acting on the transcription (anti-gene), splicing and translation (anti-sense) of microRNA (anti-miRNA). These strategies can be useful for the modulation of the expression of cancer-related genes in connection with certain diseases that currently do not have sufficient drug treatments or that use selective anticancer agents with cytotoxic effects. In 2014 Professor Piccialli's research group reported the design of PNAs as inhibitors of a miRNA, miR-509-3p, discovered by Professor Castaldo's research group involved in the pathological progress of Cystic Fibrosis [4][15]. In vitro studies demonstrated that, with the anti-miRNA approach, the PNAs were able to recognize the target within the cells while at the same time producing pleiotropic effects. With the aim of improving the specificity of binding, in accordance with the literature [16], we decided to synthesize two PNAs with different lengths (13 and 7 bases) complementary to a sequence within the promoter of the CFTR gene in order to depress the CFTR expression [17]. Using another approach, we proposed a potential method to regulate the c-kit

protooncogene transcription by using short PNA sequences [12]. Supported by these experimental data we decided to exploit the characteristic properties and higher stability of PNA to downregulate, through the anti-gene approach, the expression of. the human B-cell lymphoma 2 (Bcl-2). The Bcl-2 gene product is a mitochondrial protein (26kDa), which has a key role in the dynamics of apoptosis. Its overexpression, found in a wide range of human malignancies, including breast, cervical, non-small cell lung and prostate cancers [18][19][20], correlates with a prolonged survival of cells, tumour development, a poor prognosis and resistance to anticancer therapies. Based on their structure and function, the Bcl-2 family of proteins is further divided into three groups. Among these, the most characterized proteins are: Bcl-2, Bcl-XL, Bcl-w, Mcl-1 and A1 (anti-apoptosis); BAK, BAX and BOX (pro-apoptosis) and BID, BIM and BAD (pro-apoptosis). Studies conducted on the Bcl-2 gene have identified two promoters, P1 and P2, involved in controlling the start of transcription. The P1 promoter is the largest and is located in the region of 1.3 to 1.5 kbp upstream of the transcription start site. This region lacks the TATA box but is rich in CG sequences, with numerous transcriptions start sites. P2 is located at 1.3 kbp downstream of P1. Recent studies have shown the existence of another promoter, called M, which seems to have a suppressive activity towards promoters P1 and P2. The promoters P2 and M apparently modulate the activity of P1, while P1 seems to be the main regulator of the transcription of Bcl-2 (Figure 3). Researchers have focused their attention on the CG-rich sequence of the promoter P1. By using modified sequences [21], they have shown that the 39-bp long GC-rich region located from -58 to -19 bp upstream of the promoter P1 has the ability to fold into three different G-quadruplex structures in vitro [22].

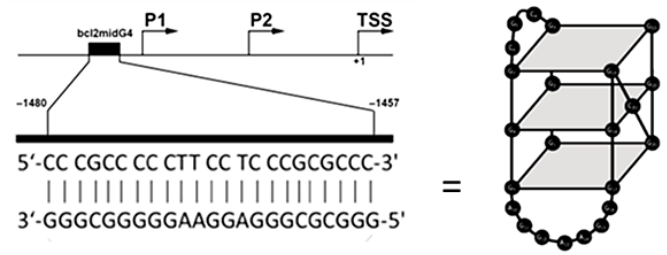

Figure 3. Schematic representations of the Bcl-2 promoter region, the bcl2midG4 sequence and the main G4 formed by the **bcl2midG4** DNA sequence.

Among these, the G-quadruplex formed by the 23-mer sequence, called **bcl2midG4**, (Figure 3) is characterized by a peculiar monomolecular hybrid-type topology involving two lateral loops (three and seven bases

long) and one single base propeller loop [19]. Among molecular approaches designed to target Bcl-2, such as those using peptides, peptidomimetics, small-molecule inhibitors (SMIs), porphyrins and antisense ODNs, a valid alternative consists in the use of PNAs. In this work we have proposed, for the first time, a new anti-gene strategy which uses oncolytic adenoviruses (OAds) as a PNA drug delivery system. In particular, we have synthesized two PNAs, **PNAK** and **PNA6K**, whose seven bases long sequences are fully complementary to the longer lateral loop of the bcl2midG4 G-quadruplex (Table 1). To improve the electrostatic attraction with the negatively charged surface of the oncolytic adenoviruses (OAds), we prolonged the positively charged lysine (K) tail of **PNAK** (required for water solubility) from one to six lysines, thus obtaining **PNA6K**.

Sample	Sequence
G-rich bcl2midG4	d(5'GGGCGCGGGAGGAAGGGGGCGGG3')
C-rich bcl2midG4	d(5'CCCGCGCCCTCCTTCCCCCGCCC3')
PNAK	H-ccttcct-K-NH_2 (N to C)
PNA6K	H-ccttcct-KKKKKK-NH_2 (N to C)

Table 1. Sequences of DNAs and PNAs used in this study.

PNA Synthesis and Purifications. PNAK and **PNA6K** (Table 1) were synthesized using the 9-fluorenylmethoxycarbonyl (Fmoc) solid-phase strategy. Briefly, 50 mg of 4-methylbenzhydrylamine (MBHA) resin (0.5 mmol g^{-1}), after swelling in CH_2Cl_2 for 30 min and washings in dimethylformamide (DMF), was treated with a solution of 20% piperidine in DMF for 10 min. After washings in DMF (5×), one or six couplings with Fmoc-L-Lys(MMt)-OH (MMT=monomethoxytrityl) were performed for **PNAK** and **PNA6K**, respectively. At the end of the synthetic cycle, the PNAs were cleaved from the solid support by treatment with trifluoroacetic acid (TFA)/anisole/ethanedithiol (9:1:1; v/v/v) for 4 h and the products were precipitated with cold diethyl ether. The precipitates were recovered by centrifugation, washed twice with diethyl ether, dissolved in water and finally lyophilized. The crude samples were purified by semi-preparative HPLC analyses, the purifications being carried out on a Jasco (Easton, MD, USA) PU-2089 Plus pump equipped with a Jasco UV-2075 Plus UV detector using a 10 × 250 mm C-18 reverse-phase column (particle size 5 μm) eluted with a linear gradient of CH_3CN containing 0.1% (v/v) trifluoroacetic acid (TFA) in H_2O containing 0.1% (v/v) TFA (from 0 to 100% in 45 min, flow 1.2 mL/min). The collected fractions were lyophilized. The amount of

each PNA sample dissolved in pure water was estimated by quantitative UV with a Jasco V-530 spectrophotometer (λ = 220–310 nm, 400 nm/min scanning speed, 2.0 nm bandwidth) using the molar molar extinction coefficients ε = 52.8 cm^{-1} mM^{-1} for both **PNAK** and **PNA6K**. The final pure products were characterized by ESI-MS.

DNA Synthesis and Purifications. The ON sequence bcl2midG4 and its complementary C-rich sequence (Table 1) were synthesized by solid phase β-cyanoethyl phosphoramidite chemistry using a Perseptive Biosystem Expedite 8909 automated DNA synthesizer. The syntheses were performed on a CPG Universal Support (35 mg, 1.4 μmol) using the 1 μmol scale standard protocol, with the DMT-OFF option. After the syntheses, the oligomers were detached from the support and deprotected by treatment with concentrated aqueous ammonia at 55 °C for 12 h. The combined filtrates and washings were concentrated under reduced pressure, redissolved in H_2O, analyzed and purified by HPLC on a Nucleogen anion exchange column (Macherey-Nagel, 1000-8/46) using: buffer A, 20 mM NaH_2PO_4 aqueous solution, pH 7.0, containing 20% (v/v) CH_3CN; buffer B, 1 M NaCl, 20 mM NaH_2PO_4 aqueous solution, pH 7.0, containing 20% (v/v) CH_3CN. A linear gradient from 0% to 100% B in 30 min and the flow rate of 1.2 mL min^{-1} were used. The ONs were collected and successively desalted by Sep-Pak cartridges (C18). The isolated ONs proved to be >99% pure (NMR). The ON concentration was determined spectrophotometrically at λ = 260 nm and 90 °C, using the molar extinction coefficient ε = 231.3 cm^{-1} mM^{-1} for **G-rich bcl2midG4** and ε = 175.4 cm^{-1} mM^{-1} for **C-rich bcl2midG4**, as determined using the Sigma-Aldrich OligoEvaluatorTM web tool (www.oligoevaluator.com).

Circular Dichroism (CD). As reported in the literature, the CD spectrum of **G-rich bcl2midG4** annealed in K^+ buffer is characterized by two positiwe CD bands at 263 nm and 293 nm and one negative band at 240 nm (Figure 4A, solid lane) diagnostic of 3+1 hybrid-type G-quadruplexes. To confirm the interaction between **PNAK** (Figure 4A, dotted line) and **bcl2midG4**, we compared the CD profile of the **bcl2midG4 G-quadruplex** alone (solid line) with the one obtained after its incubation with **PNAK** (Figure 4A, dashed line). The CD spectrum of the **bclmid2G4 G-quadruplex/PNAK** mixture was clearly different from the arihtmetic sum of the two separate components, thus confirming that the interaction between the **bclmid2G4 G-quadruplex** and **PNAK**

had occurred. In particular, the positive CD hump at 293 nm was shifted by about 2 nm. In parallel, we studied the interaction between **PNAK** and the **bcl2midG4 duplex** (Figure 4B). In this case, the spectrum of **bclmid2G4 duplex/PNAK** (Figure 4B, dashed line) overlapped almost perfectly with the arithmetic sum of the individual components (Figure 4B, dot-dashed line), thus indicating that no hybridization had occurred in this condition.

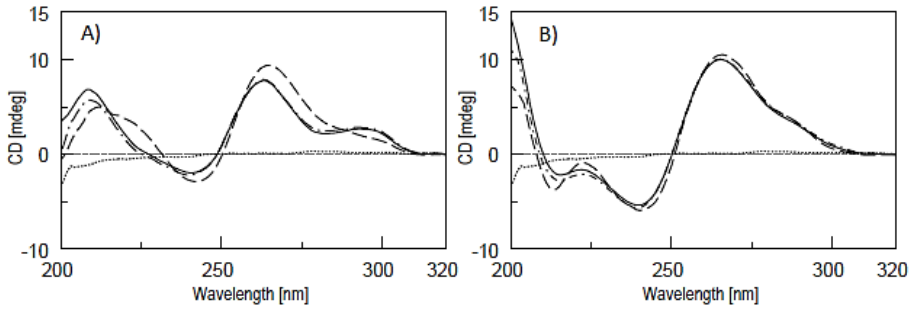

C)

Sample	λ min	λ max
bcl2midG4-G4	240	208, 263, 293
bcl2midG4-G4/**PNAK**	242	212, 265
bcl2midG4-ds	215, 240	265
bcl2midG4-ds/**PNAK**	213, 240	266

Figure 4. (**A**) CD spectra of the **bcl2midG4 G-quadruplex** (solid line) and the **bcl2midG4 G-quadruplex** incubated with **PNAK** (dashed line); (**B**) CD spectra of **bcl2midG4-duplex** (black solid line) and the **bcl2midG4 duplex** incubated with **PNAK** (dashed line).

To obtain further information about the interaction between the **bclmid2G4 G-quadruplex** or **bcl2midG4 duplex** and **PNAK**, we recorded the CD spectra at different temperatures during the melting and annealing procedures (Figure 5). For the CD melting profiles of the **bcl2midG4 duplex** before and after incubation with 5 eq. of **PNAK** (Figure 5C and D) we did not observe any significant spectra. These data confirmed that **PNAK** does not bind to the **bcl2midG4 duplex**. Conversely, two significant differences were observed for the **bcl2midG4 G-quadruplex**. First, the CD spectrum of **bcl2midG4 G-quadruplex/PNAK** recorded at 50 °C during the cooling run (Figure 5B, orange dotted line) was almost superimposable with that of the **bcl2midG4 G-quadruplex** alone recorded at the same temperature (Figure 5A), being characterized by a minimum at 240 nm and two maxima at 263 nm and 293 nm. In contrast, in all other spectra of the

bcl2midG4 G- quadruplex/PNAK acquired at temperatures ≤ 40 °C the hump at 293 nm was not present (Figure 5B). Secondly, the comparison of the CD spectra recorded at 5 °C before the melting and after the cooling procedure (Figure 5B, green solid and dotted lines, respectively) and the comparison of the heating and cooling CD melting curves of the **bcl2midG4 G-quadruplex/PNAK** mixture (Figure 5B) indicated a positive dichroic signal, 265 nm. Taken together, the CD results indicate that **PNAK** is able to form more than one complex with the **bcl2midG4 G-quadruplex** at temperatures lower than 50 °C.

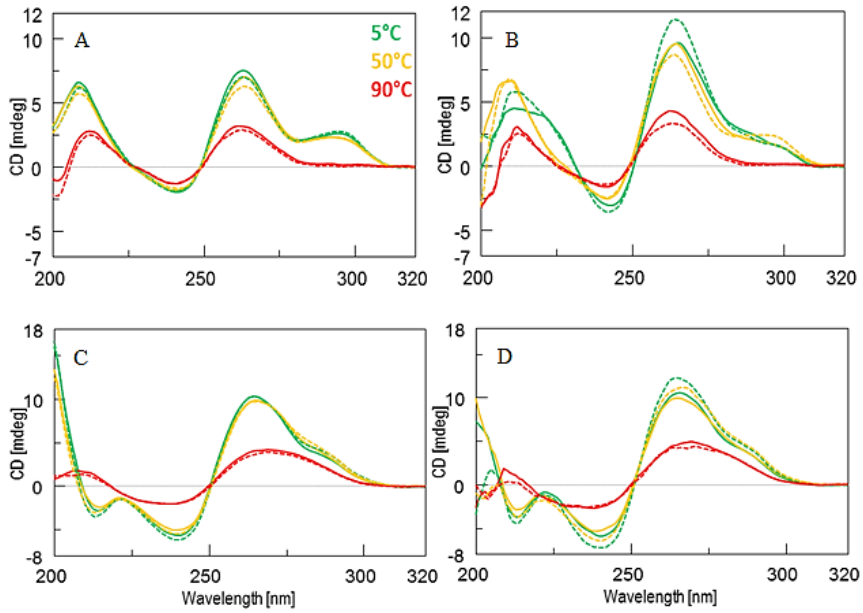

Figure 5. CD profiles of the **bcl2midG4 G-quadruplex** (**A**), **bcl2midG4 G-quadruplex/PNAK** (**B**), **bcl2midG4 duplex** (**C**) and **bcl2midG4 duplex/PNAK** (**D**) recorded at 5 °C (green), 50 °C (yellow) and 90 °C. Heating: solid line; cooling: dashed line.

Polyacrylamide gel electrophoresis (PAGE). The molecular size of the complexes formed in the different conditions was examined by non-denaturing polyacrylamide gel electrophoresis (PAGE). In the case of the **G-rich bcl2mid G-quadruplex** strand alone annealed in 60 mM K^+ buffer, we observed two main bands corresponding to the monomeric and dimeric G-quadruplexes (Figure 6, lane 3) in agreement with the data reported by Lin *et al.* [23] The fastest band migrating like the 10 bp reference of the DNA ladder (Figure 6, lane 7) was assigned to the 3+1 monomeric bcl2midG4 G-quadruplex, whereas the slowest band, migrating like the $(CGGAGGT)_8$ dimeric G-quadruplex size marker

(Figure 6, lane 2) [24], was assigned to a dimeric G4. The PAGE mobility of the sample obtained by incubating the **bcl2midG4 G-quadruplex** with 5 eq. **PNAK** is shown in Figure 6, lane 4. We observed a reduction of the intensity of the monomeric **bcl2midG4 G-quadruplex** band and the appearance of a new intense band attributable to a DNA/**PNAK** complex having a mobility intermediate between 30 and 40 base pairs. We also observed the band attributable to the dimeric G-quadruplex alone and an intense smearing attributable to even higher molecular weight complexes. The comparison of the PAGE mobility of the **bcl2midG4 duplex** before and after its incubation with **PNAK** (shown in Figure 6, lanes 5 and 6, respectively) confirmed the CD data, suggesting the absence of any interaction between **PNAK** and the double stranded **bcl2midG4** sequence. Taken together, the PAGE study confirmed the ability of **PNAK** to bind selectively the **bcl2midG4 G-quadruplex** over the **bcl2midG4 duplex**, and also evidenced that the incubation with **PNAK** triggers the formation of higher order complexes, attributable to multimeric **bcl2midG4 G-quadruplexes** complexed with the short complementary PNA strand.

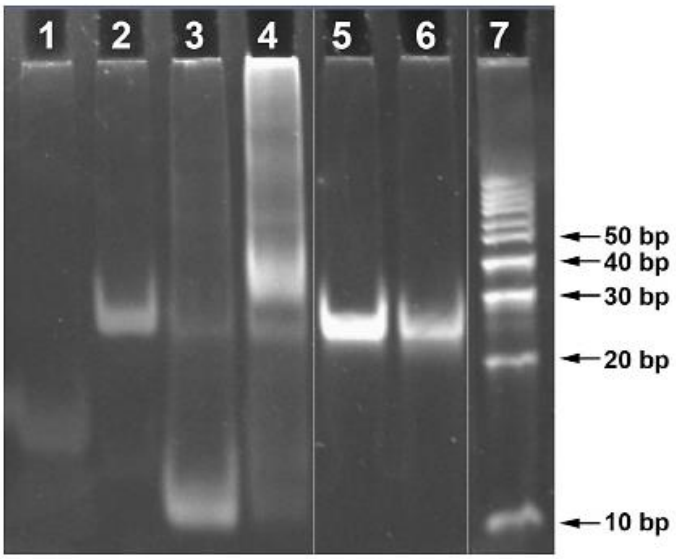

Figure 6. PAGE of the **bcl2midG4** G-quadruplex and duplex incubated with **PNAK** in potassium solution. Lane 1: the $(TGGGGT)_4$ G4 marker; lane 2: the $(CGGAGGT)_8$ dimeric G-quadruplex marker; lane 3: the **bcl2midG4 G-quadruplex** annealed in K^+; lane 4: the **bcl2midG4-G-quadruplex** incubated with **PNAK**; lane 5: the **bcl2midG4 duplex**; lane 6: the **bcl2midG4 duplex** incubated with **PNAK**; lane 7: the DNA duplex ladder (10-100 bp).

Size-exclusion chromatography (SEC). In consideration of the indications obtained by the PAGE studies and in order to shed light on the molecular weight distribution of the complexes formed after the incubation with **PNAK**, we performed an HPLC Size Exclusion Chromatography study (SEC). Generally, HPLC-SEC profiles show a distribution of peaks in which lower MW species have higher retention times. In Figure 7 the HPLC-SEC profiles obtained at room temperature on a ReproSil 2000 SEC column are reported i) the pre-annealed **bcl2midG4 G-quadruplex** (A), and ii) the **bcl2midG4 G-quadruplex** incubated with 5 eq. of **PNAK** (B) and **PNAK** alone (C).Based on SEC principles and considering the PAGE results, the peak at the highest retention time (t_R) in the HPLC-SEC profile of the **bcl2midG4 G-quadruplex** (Figure 7A; t_R = 12.16 min) was assigned to the monomeric G-quadruplex structure, while the preceding peak (t_R = 11.74 min) was attributed to a dimeric G-quadruplex formed by the G-rich **bcl2midG4 G-quadruplex.** For the **bcl2midG4 G-quadruplex/PNAK** 1:5 mixture (Figure 7B), the HPLC-SEC profile showed the peaks of the unbound species (**PNAK** excess at t_R= 19.16; and those of the monomeric and dimeric **bcl2midG4 G-quadruplexes** at t_R = 12.08 and 11.42 min, respectively, together with a sharp intense peak at t_R = 11.25 min attributable to a **PNAK**-bound dimeric **bcl2midG4 G-quadruplex**. The remaining more highly retained peak at t_R = 10.03 min and the envelope peak centred at t_R = 9.13 min confirmed the PAGE indications of the presence in solution of supramolecular assemblies of bcl2midG4, either bound or not to one or more **PNAK** molecules, whose formation was triggered by the incubation with **PNAK**. Conversely, the addition of **PNAK** to the **bcl2midG4 duplex** neither induced a significant variation in the retention time of the **bcl2midG4 duplex** peak (Figure 8B; t_R = 11.78 min), nor determined the appearance of any new peak besides the peak of the unbound **PNAK** (t_R = 19.38 min).

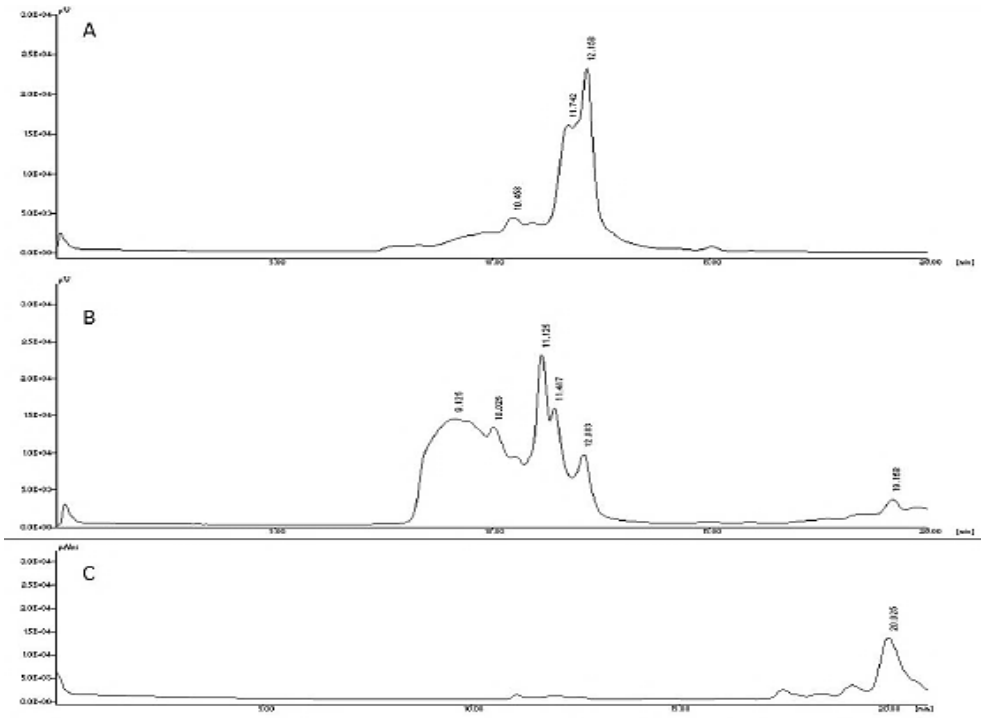

Figure 7. HPLC-SEC profile of the **bcl2midG4 G-quadruplex** (**A**), the **bcl2midG4 G-quadruplex/PNAK** (**B**) and **PNAK** (C).

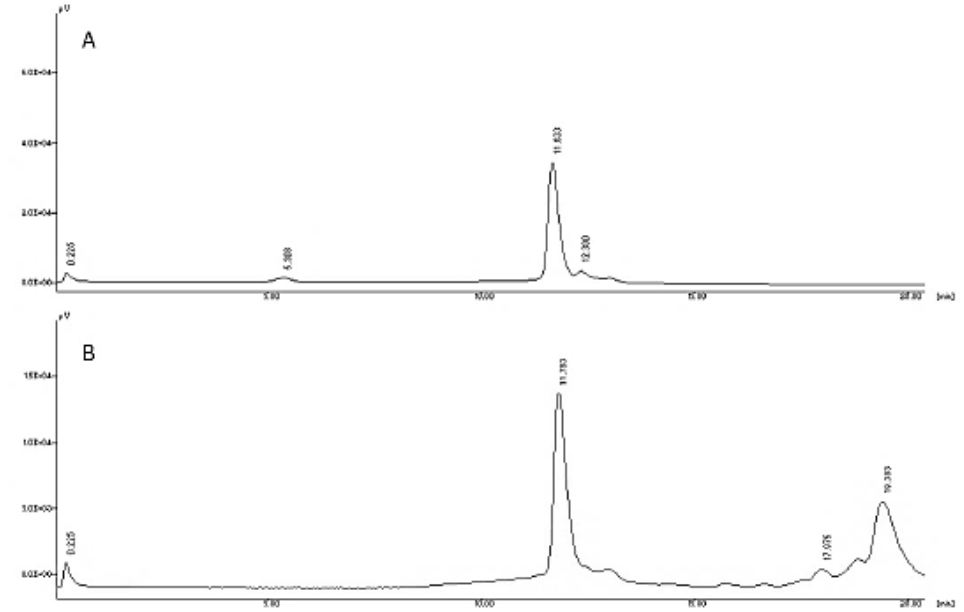

Figure 8. The HPLC-SEC profile of **bcl2midG4 duplex** (**A**) and **bcl2midG4 duplex/PNAK**.

Ad5D24-PNA6K complex formation. After having demonstrated the ability of **PNAK** to selectively bind the G-quadruplexes formed by the **G-rich bcl2midG4** sequence, we developed a novel delivery system for the on-demand administration of PNA-based drugs to tumour cells by exploiting the capability of OAds (Ad5D24 strain) to enter and lyse selectively cancer cells with respect to healthy tissues, as well as to transport into the infected cells any suitable cargo adsorbed on the virus surface. The human adenocarcinomic alveolar basal epithelial A549 and the triple negative breast cancer MDAMB436 cell lines were selected as cellular models because of their high expression of the Bcl-2 gene product. First, A549 and MDA-MB 436 cells were incubated with **PNAK** at several concentrations and their viability was assessed by MTS assay at days 1, 3 and 5 after the incubation (Figure 9). The absence of any effect on the cell viability, even at the highest **PNAK** concentration (100 μM) and at the longest incubation time (day 5), confirmed the requirement for an efficient delivery strategy to transport **PNAK** within the cancer cells. As previously reported, positively charged molecules can be efficiently adsorbed on the negatively charged surface of OAds via electrostatic interactions. In line with previous reports, in order to maximize the amount of **PNAK** on the OAd vectors, we enhanced the positive charge of **PNAK** by prolonging the C-terminal lysine tail from one to six lysines, thus obtaining **PNA6K** with an increased positive net charge. Next, **PNA6K**-coated OAds were prepared following the protocol reported in the Materials and Methods section. The analysis of the CD melting curve of the **bcl2midG4 G-quadruplex** incubated with **PNA6K** in K^+ buffer (Figure 10) confirmed the ability of **PNA6K** to bind the **bcl2midG4-G-quadruplex**, as indicated by the presence of two clear melting transitions at 24 and 76 °C, the first of which corresponding to the dissociation of the **PNA6K** strand from the **bcl2midG4 G-quadruplex** and the second to the melting of the G-quadruplex. We used several OAd/**PNA6K** ratios and monitored the size and charge of the resulting complexes by using dynamic light scattering (DLS) and zeta potential measurements (Figure 11). As summarized in Figure 11 Table B, the net charge of the OAd vectors rose from –32.67 ±0.21 to +26.13 ± 5.51 respectively for the naked OAd and OAd-**PNA6K** [1:500] complexes, whereas the corresponding hydrodynamic diameter rose from 109.03 ± 1.95 to 142.47 ± 4.55 nm. These results suggest that the addition of the positively charged PNA masks the negative charge of the OAds, not

affecting the colloidal stability, except in the case of the 1:10 OAd/PNA ratio at which point significant aggregation phenomena occurred, as evidenced by the higher values of the particle size (515.50 ±34.24 nm) and poly dispersion index (PDI = 0.47). Above the 1:10 ratio, the positive net charge reached a plateau-like kinetics, as indicated by our measurements of the z-potentials of 19.67 ± 0.42, 23.90 ± 2.89, 27.33 ±1.10 and 26.13 ± 5.51, respectively, for the 1:10, 1:50, 1:100 and 1:500 ratios (Figure 10A). On the basis of the DLS and zeta potential calculations, we selected the 1:100 OAd/PNA ratio as optimal for the subsequent cell viability assays.

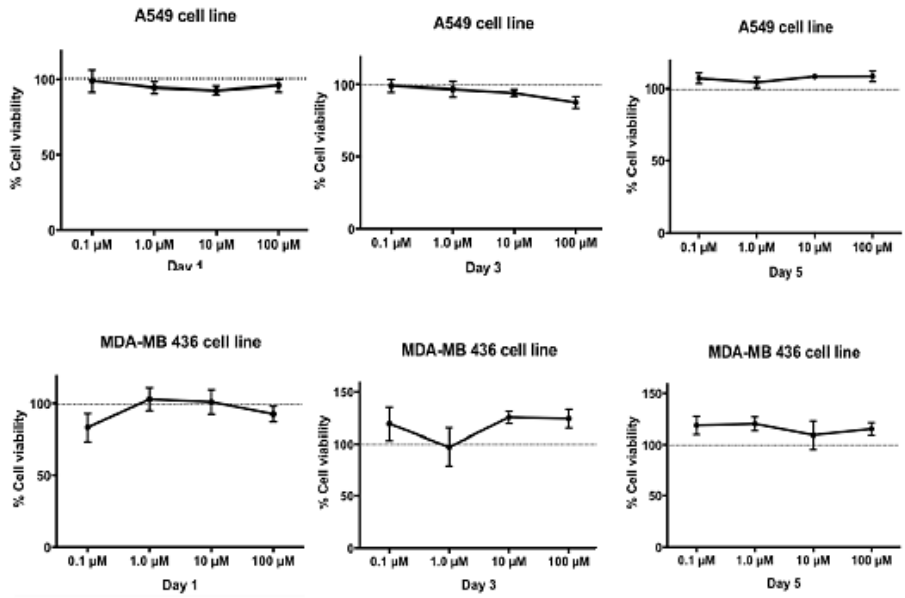

Figure 9. MTS assay on the A549 and MDA-MB-436 human cancer cell lines treated with **PNAK**.

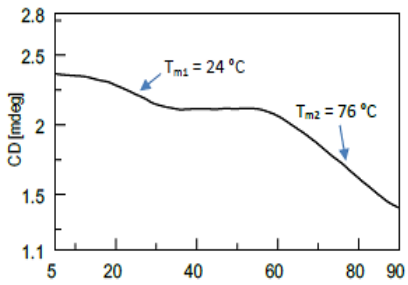

Figure 10. CD melting curve recorded 24 hours after the incubation of the **bcl2midG4 G-quadruplex** with **PNA6K**.

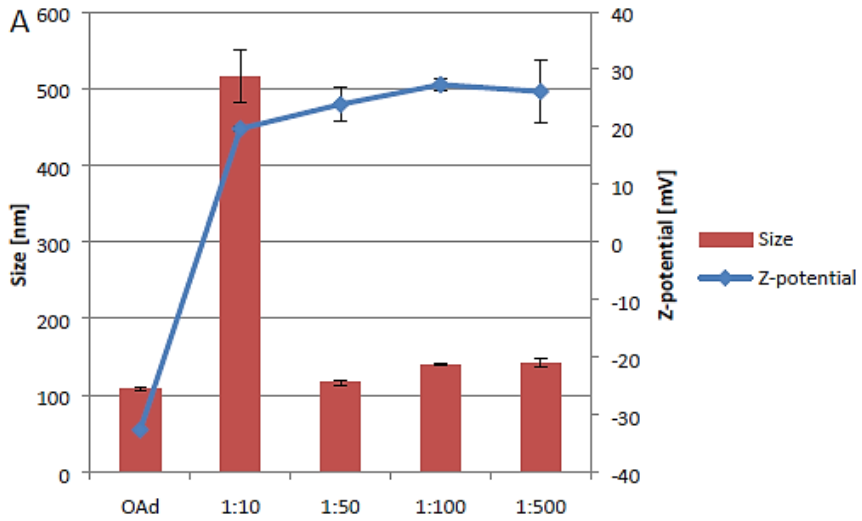

B Preps [OAd-PNA6K]	Size [nm] ± SD	PDI	Z-Potential [mV] ± SD
Ad5D24	109.03 ± 1.95	0.12	-32.67 ± 0.21
Ad5D24-**PNA6K** [1:10]	515.50 ± 34.24	0.47	19.67 ± 0.42
Ad5D24-**PNA6K** [1:50]	116.07 ± 2.32	0.03	23.90 ± 2.89
Ad5D24-**PNA6K** [1:100]	140.23 ± 2.05	0.18	27.33 ± 1.10
Ad5D24-**PNA6K** [1:500]	142.47 ± 4.55	0.20	26.13 ± 5.51

Figure 11. Hydrodynamic diameter (nm ± SD) and zeta potential (mV ± SD) values of the virus-PNA complexes obtained by incubating the Ad5D24 OAds with **PNA6K** at increasing virus/PNA ratios.

Cell viability studies on the A549 and MDA-MB-436 cancer cell lines. To assess the efficiency of the new OAd-based PNA delivery system in transporting PNA6K within tumour cells and inducing cell death, probably by the inhibition of the expression of the anti-apoptotic Bcl2 protein, we determined by *in vitro* MTS assay the cell viability of A549 and MDA-MB-436 cell cultures one, three and five days after their incubation with either Ad5D24 OAd alone – using 0.1, 1, 10 and 100 viral particles (VP) per cell – or with the corresponding Ad5D24-**PNA6K** [1:100] preparations. At each time point and for each VP/cell preparation, we also measured the cell viability of the cells incubated with **PNA6K** alone at concentrations corresponding to those used for the Ad5D24-**PNA6K** preparations (Figure 12). The mitochondrial activity of the treated cells was compared to that of the untreated control

cells and the cell viability was expressed as a percentage relative to the untreated control cells (Figure 12). We did not observe any significant reduction in the cell viability of the cells treated with **PNA6K** alone, even five days after the treatment at the highest concentration for both the tested cell lines. As far as the cells treated with the OAd alone, no significant oncolytic effect was evidenced up to day 3, except for the 100 VP/cell preparations for which an 84% and 61% reduction in cell viability was observed for the A549 and MD-MB-436 cell lines, respectively.

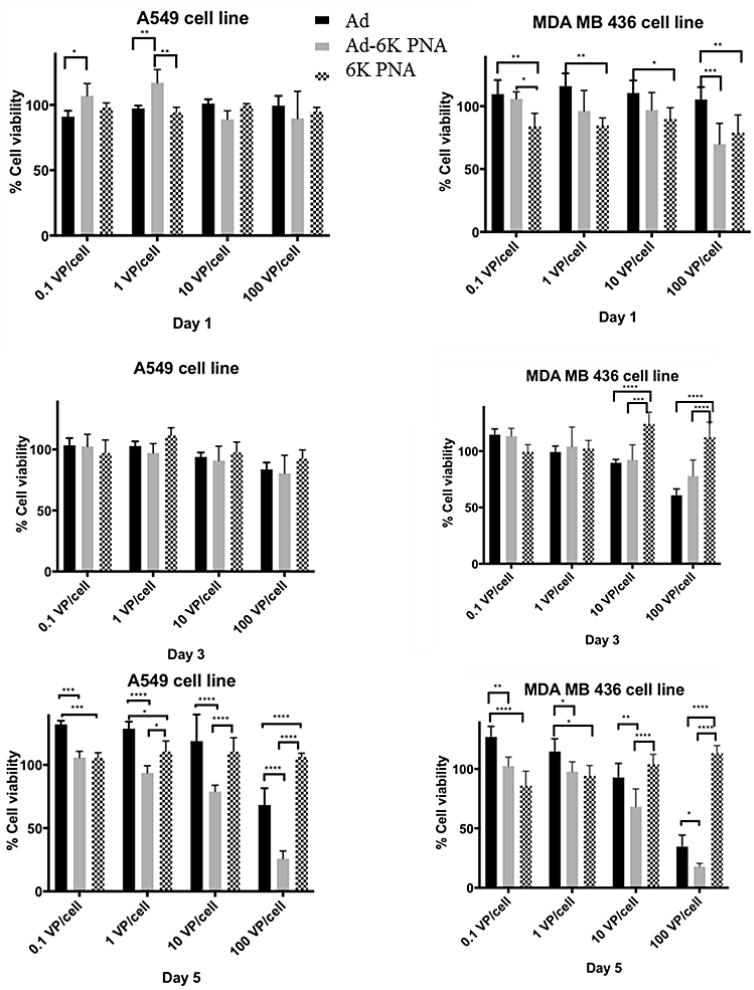

Figure 12. MTS assay on the A549 and MDA-MB 436 cells after 1, 3 and 5 days of incubation with Ad5D24 (black bars) or **PNA6K** alone (dotted bars), or with Ad5D24-**PNA6K** preparations (grey bars). The cell viability is expressed as a percentage with respect to the non-treated control cells. The significance was assessed using the 2-way ANOVA, *P < 0.05, ** P ≤ 0.01, ***P <0.01, ****P = 0.0001.

Up to day 3, in all cases we did not observe any enhancement in the oncolytic activity of the Ad5D24-**PNA6K** preparations relative to the Ad5D24 preparations alone. In contrast, the MTS assays performed at day 5 evidenced a striking enhancement in the oncolytic effect of the Ad5D24-**PNA6K** preparations relative to the OAd alone at all VP/cell ratios and on both cell lines. The enhancement in the cell killing effect was more evident on the A549 cells, which proved more resistant against the oncolytic activity of Ad5D24. The viability of the A549 and MDA-MB-436 cells incubated with Ad5D24-**PNA6K** at 100 VP/cell recorded at day 5 was 26% and 18%, respectively. The cell viability at day 5 of the same cells treated with the PNA-uncoated Ad5D24 at 100 VP/cell rose to 68% and 35%, respectively.

Western blot analyses. To further confirm that the lower cell viability observed at day 5 for the cells treated with the Ad5D24-**PNA6K** preparations compared to those treated with the naked Ad5D24 viruses was actually due to the specific downregulation of the Bcl-2 protein, we performed western blot analyses (Figure 13). A549 and MDA-MB-436 cells were incubated with Ad5D24 viruses alone, **PNA6K** alone or Ad5D24/**PNA6K** preparations, and the expression of the Bcl-2 protein was evaluated at day 5 after the incubation, as described in the experimental section. The western blot analyses confirmed that **PNA6K** is actually able to downregulate the expression of the Bcl-2 protein in both tested cell lines, and that its conjugation with the Ad5D24 oncolytic adenovirus greatly enhances the downregulation of the target gene. Using the ImageJ software tool, we estimated that the incubation of the MDA-MB-436 cells with the naked virus or with **PNA6K** alone reduced the expression of the Bcl-2 protein by 23.7% and 21.4%, respectively, compared to the non-treated control cells. More interestingly, when the same cells were treated with the Ad5D24-**PNA6K** preparation, the expression of the Bcl-2 protein fell drastically to 55.9% (see the chart in Figure 13). Unfortunately, we could not obtain the corresponding data for the western blot analysis of the A549 cells because the image processing gave unreliable results.

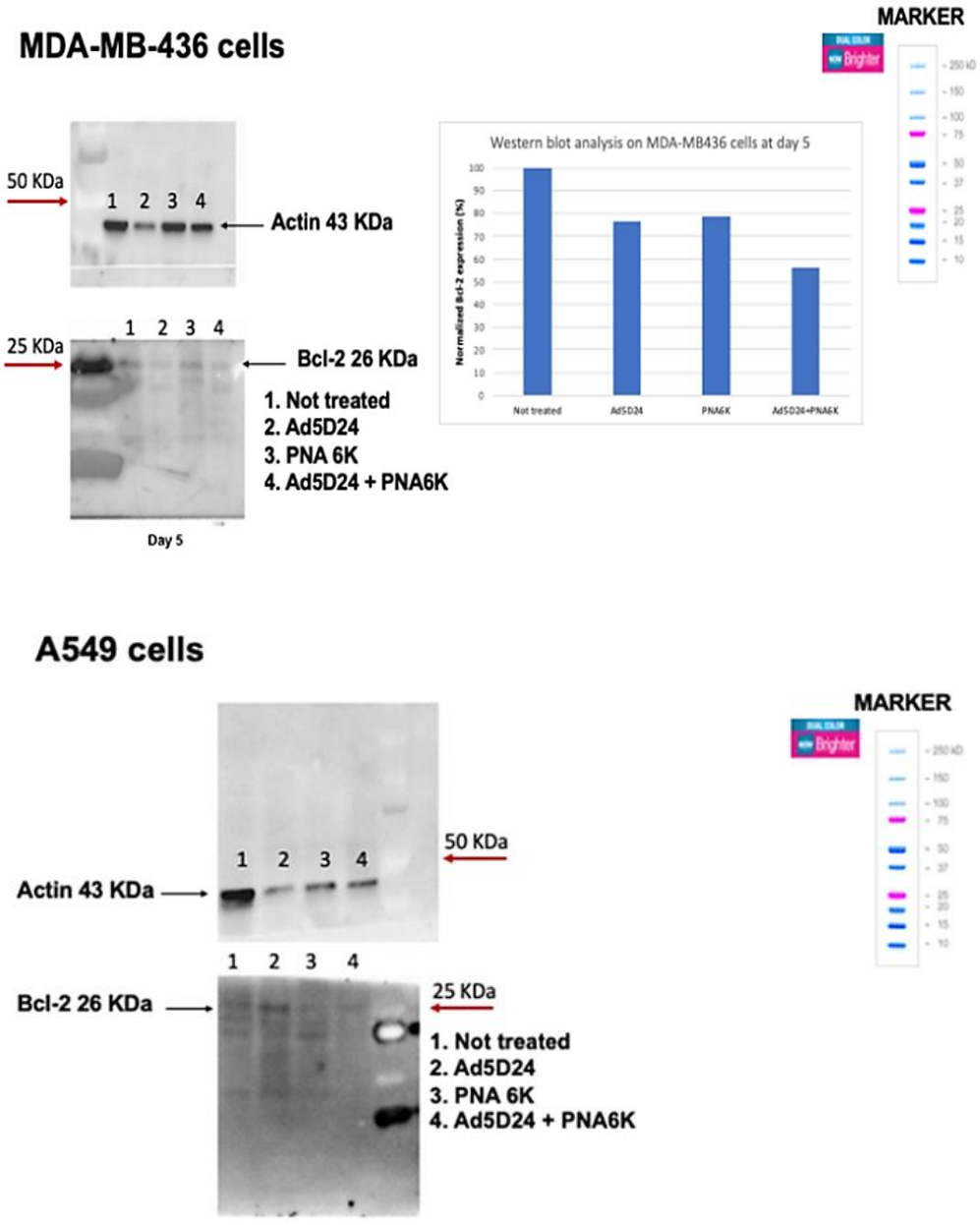

Figure 13. Western blot analysis of the Bcl-2 expression in the MDA-MB-436 (above) and A549 (below) human cancer cell lines performed 5 days after incubation with Ad5D24.

In conclusion, in this work, through physico-chemical and biological investigations, we have demonstrated that i) **PNAK** binds selectively the G4 formed by the **G-rich bcl2midG4** DNA sequence

unlike the corresponding duplex; ii) **PNA6K,** characterized by the presence of a longer six lysines tail, binds the negatively charged capsid of Ad5D24 OAd forming the Ad5D24-**PNA6K** delivery system; iii) Ad5D24 vectors are able to load and transfect **PNA6K** into human A594 and MDA-MB-436 cancel cell lines and to promote the onset of a synergic cytotoxic effect due to the oncolytic activity of the virus and to the downregulation of the anti-apoptotic Bcl-2 gene .We believe that the approach here reported could open the way to the development of site-specific and safer chemotherapy on account of the reduced toxicity to healthy tissues and organs.

Experimental Section

Preparation of the bclmidG4 duplex and quadruplex and their incubation with PNAK. All the DNA samples were prepared at a 20 μM concentration in 60 mM potassium buffer obtained by diluting the 1 M buffered solution (100 mM KH_2PO_4, 900 mM KCl, pH = 7.0). For the **bcl2midG4 G-quadruplex** preparation, 10 nmol of **G-rich bcl2midG4** were lyophilized and dissolved in 0.5 mL of 60 mM potassium buffer to achieve the 20 μM concentration. For the **bcl2midG4 duplex** preparation, a solution of **C-rich bcl2midG4** at 1 mM concentration in 60 mM potassium buffer was used. The **bcl2midG4 duplex** was obtained by dissolving 10 nmol of lyophilized **G-rich bcl2midG4** with 10 μL of the 1mM **C-rich bcl2midG4** stock solution. The resulting solution was finally diluted to 0.5 mL with the 60 mM potassium buffer. The solutions containing either the **bcl2midG4 G-quadruplex** or the **bcl2midG4 duplex** were heated at 90 °C for 5min, then slowly cooled to t_R over 12h (annealing procedure) and equilibrated at 4 °C for at least 4 hours before the **PNAK** addition at a 1:5 DNA/PNA ratio. The mixtures were incubated at 4 °C for 24 h before the data acquisition.

Preparation of the bclmidG4 duplex and quadruplex and their incubation with PNAK. All the DNA samples were prepared at a 20 μM concentration in 60 mM potassium buffer obtained by diluting the 1 M **buffered** solution (100 mM KH_2PO_4, 900 mM KCl, pH = 7.0). For the **bcl2midG4 G-quadruplex** preparation, 10nmol of **G-rich bcl2midG4** were lyophilized and dissolved in 0.5 mL of 60 mM potassium buffer to achieve the 20 μM concentration. For the **bcl2midG4 duplex** preparation, a solution of **C-rich bcl2midG4** at 1 mM concentration in 60 mM potassium buffer was used. The **bcl2midG4 duplex** was obtained by dissolving 10 nmol of lyophilized **G-rich bcl2midG4** with 10 μL of the 1mM **C-rich bcl2midG4** stock solution. The resulting solution was finally diluted to 0.5 mL with the 60 mM potassium buffer. The solutions containing either the **bcl2midG4 G-quadruplex** or the **bcl2midG4 duplex** were heated at 90 °C for 5min, then slowly cooled to t_R over 12h (annealing procedure) and equilibrated at 4 °C for at least 4 hours before the **PNAK** addition at a 1:5 DNA/PNA ratio. The mixtures were incubated at 4 °C for 24 h before the data acquisition.

Circular Dichroism (CD). The CD spectra were recorded on a Jasco 1500 spectropolarimeter equipped with a Jasco PTC-348-WI temperature controller in the 200–320 nm range at 5, 50 and 90 °C, using a 0.1 cm path-length cuvette in 60 mM potassium buffer at a concentration of 20 μM. All CD spectra were averaged over 5 scans, which were recorded at a 200 nm min^{-1} scan rate, 4 s response time, 2 nm bandwidth. The buffer baseline was subtracted from each spectrum and the spectra were normalized to have a zero ellipticity at 360 nm. The thermal denaturation experiments were also carried out in the temperature range 5–90 °C by monitoring the CD values at 263 nm for the

bcl2midG4 G-quadruplex, 265 nm for the **bcl2midG4 G-quadruplex/PNAK** and **the bcl2midG4 G-quadruplex/PNA6K**, 265 nm for the **bcl2midG4 duplex** and 266 nm for the **bcl2midG4 duplex/PNAK** at a heating rate of 0.5 C°min^{-1}.

Non-denaturing Polyacrylamide Gel Electrophoresis (PAGE). The non-denaturing gel electrophoreses were performed using 18% polyacrylamide gels, which were run in 1 × Tris-Borate-EDTA (TBE) buffer supplemented with 30 mM KCl, pH 7.0 for 1 hour at 4 °C. All the samples were loaded at a 20 μM ON concentration. 2 μL of each sample were added to 8 μL of loading buffer (glycerol/1 × TBE + 30 mM KCl 1:9) before gel loading. The electrophoresis was performed at a constant voltage of 120 V at a temperature close to 5° C. The gels were stained with Sybr green (Sigma- Aldrich) and visualized using the Bio-Rad Laboratories Gel Doc™ XR apparatus.

HPLC-Size Exclusion Chromatography (SEC) analyses. The HPLC-SEC analyses were performed using a ReproSil 2000 SEC column operating in the MW range of 2,000–70,000 Dalton (Dr. Maisch GmbH, 300 × 8 mm, 5 μm) eluted with 60 mM potassium buffer, flow rate 0.6 mL min^{-1}, detector at 260 nm. The analyses were performed at t_R using a Jasco PU-2089 Plus quaternary gradient pump equipped with a Jasco UV-2075 Plus UV/vis detector.

OAds preparation and complexation with PNA6K. The Ad5D24 OAds were generated, propagated and characterized using standard protocols. The OAd-**PNA6K** complexes were prepared by mixing the Ad5D24 OAds and **PNA6K** at 1:10, 1:50, 1:100 and 1:500 ratios according to the following protocol: (i) for each μL of viral preparation used, the corresponding number of μg of protein was calculated; (ii) for each μg of viral protein, 10, 50, 100 or 500 μg of **PNA6K** was added adjusting the volume to 100 μL with sterile Milli-Q water (purchased from VWR); and (iii) after vortexing, the mixtures were incubated at room temperature for 15 minutes; and then vortexed again just before being used. New OAd-**PNA6K** complexes were prepared before each experiment using fresh reagents.

Zeta potential and dynamic light scattering (DLS) analysis. The OAd-**PNA6K** complexes were vortexed and diluted to a final volume of 700 mL with sterile Milli-Q water adjusted to pH 7.4 before being transferred to a polystyrene disposable cuvette for the DLS analysis. Next, the samples were recovered from the cuvette and transferred to a DTS1070 disposable capillary cell (Malvern, Worcestershire, UK) for the zeta potential measurements, which were performed at 25 °C using a Malvern Zetasizer Nano ZS system.

Cell culture and viability assay. The human lung carcinoma cell line A549 and human breast cancer cell line MDA-MB-436 were purchased from the American Type Culture Collection (ATCC; Manassas, VA, USA). Both cell lines were grown in adhesion in Dulbecco's modified Eagle's medium (DMEM, Gibco). The medium was supplemented with 10% heat-inactivated foetal

bovine serum FBS (Gibco), penicillin (50 U mL^{-1}), streptomycin (500 μgmL^{-1}), and glutamine (4 mmol L^{-1}) in a humidified atmosphere of 95 % air and 5 % CO_2 at 37 °C. Adherent cells were seeded in 96-multiwell plates at a density of 5 × 103 cells/well. A 1:100 ratio (w/w) of OAd-**PNA6K** was chosen to assess the cell viability. At 24 hours after the seeding, the cells were treated with 50 µL of 0.1, 1, 10 and 100 VP/cell in cell culture medium for 1, 3 and 5 days and then the MTS assay was performed according to the manufacturer's protocol (CellTiter 96 AQueous One Solution Cell Proliferation Assay; Promega, Nacka, Sweden). The spectrophotometric data were acquired with a Varioskan Flash Multimode Reader (Thermo Scientific, Carlsbad, CA, USA). The cytotoxicity was evaluated as the percentage of viability of the treated cells compared to the untreated cells. The experiments were run in quadruplicate.

Western blot analyses. The MDA-MB436 and A549 cells were incubated with Ad5D24, **PNA6K** and Ad5D24-**PNA6K** for 5 days at a 1:100 Ad5D24/**PNA6K** ratio and at a concentration of 100 VP/cell. The extracts of the treated cells were isolated by using RIPA Buffer (SIGMA) supplemented with protease inhibitors (Thermo Fisher Scientific). The concentration of the isolated proteins was determined by using the Bradford Protein Assay Reagent (BioRad). 25 µg of the protein were separated on 4-20% Mini PROTEAN TGX Precast Gels (BioRad) and transferred to PVDF membranes (BioRad). The membranes where then incubated with the primary antibodies against Bcl-2 (Abcam) or β-actin (Santa-Cruz) and the appropriate secondary antibodies. The Bcl-2 protein (26 KDa) was analyzed and β-actin (43 KDa) was used as a loading marker. The ImageJ54 tool was used to measure the mean gray value of the bands. The mean gray value of each sample was normalized with the corresponding actin control. Finally, each result was normalized with the non-treated control. The percentages of the normalized mean gray values were plotted on the graph.

Statistical analyses and correlation models. The statistical analysis was performed using the GraphPad Prism 6 software (GraphPad Software, Inc., La Jolla, CA, USA). The data were expressed as the mean ± the standard deviation (SD). Any result repeats were compared by means of a 2-way analysis of variance (ANOVA), with a P-value < 0.05 being considered as statistically significant.

3.4 References

[1] F. G. Dev *et al.*, “oligonucleotides obeying the Watson-Crick hydrogen-bonding rules,” vol. 365, no. October, pp. 566–568, 1993.

[2] K. Kilså Jensen, H. Ørum, P. E. Nielsen, and B. Nordén, “Kinetics for hybridization of peptide nucleic acids (PNA) with DNA and RNA studied with the BIAcore technique,” *Biochemistry*, vol. 36, no. 16, pp. 5072–5077, 1997.

[3] S. Tomac *et al.*, “Ionic effects on the stability and conformation of peptide nucleic acid complexes,” *J. Am. Chem. Soc.*, vol. 118, no. 24, pp. 5544–5552, 1996.

[4] F. Amato *et al.*, “Design, synthesis and biochemical investigation, by in vitro luciferase reporter system, of peptide nucleic acids as new inhibitors of miR-509-3p involved in the regulation of cystic fibrosis disease-gene expression,” *Medchemcomm*, vol. 5, no. 1, pp. 68–71, 2014.

[5] N. J. Peffer *et al.*, “Strand-invasion of duplex DNA by peptide nucleic acid oligomers,” *Proc. Natl. Acad. Sci. U. S. A.*, vol. 90, no. 22, pp. 10648–10652, 1993.

[6] V. V. Demidov, M. V. Yavnilovich, B. P. Belotserkovskii, M. D. Frank-Kamenetskii, and P. E. Nielsen, “Kinetics and mechanism of polyamide ('peptide’) nucleic acid binding to duplex DNA,” *Proc. Natl. Acad. Sci. U. S. A.*, vol. 92, no. 7, pp. 2637–2641, 1995.

[7] M. Egholm, L. Christensen, K. L. Dueholm, O. Buchardtt, J. Coull, and P. E. Nielsen, “EfficientpH-independentsequence-specificDNA,” vol. 23, no. 2, pp. 1–6, 2008.

[8] P. E. Nielsen, M. Egholm, and O. Buchardt, “Evidence for (PNA)2/DNA triplex structure upon binding of PNA to dsDNA by strand displacement,” *J. Mol. Recognit.*, vol. 7, no. 3, pp. 165–170, 1994.

[9] T. Vilaivan, C. Khongdeesameor, P. Harnyuttanakorn, M. S. Westwell, and G. Lowe, “Synthesis and properties of chiral peptide nucleic acids with a N-aminoethyl-D-proline backbone,” *Bioorganic Med. Chem. Lett.*, vol. 10, no. 22, pp. 2541–2545, 2000.

[10] P. Travascio, Y. Li, and D. Sen, “DNA-enhanced peroxidase activity of a DNA aptamer-hemin complex,” *Chem. Biol.*, vol. 5, no. 9, pp. 505–517, 1998.

[11] A. Gupta, A. Mishra, and N. Puri, “Peptide nucleic acids: Advanced tools for biomedical applications,” *J. Biotechnol.*, vol. 259, no. May, pp. 148–159, 2017.

[12] J. Amato *et al.*, “Targeting G-Quadruplex structure in the human c-Kit promoter with short PNA sequences,” *Bioconjug. Chem.*, vol. 22, no. 4,

pp. 654–663, 2011.
[13] R. Gambari, J. Gasparello, and A. Finotti, “Peptide nucleic acid-based targeting of microRNAs: possible therapeutic applications for glioblastoma,” *J. Cancer Metastasis Treat.*, vol. 2019, 2019.
[14] R. L. Juliano, “The delivery of therapeutic oligonucleotides,” *Nucleic Acids Res.*, vol. 44, no. 14, pp. 6518–6548, 2016.
[15] F. Amato *et al.*, “Exploitation of a very small peptide nucleic acid as a new inhibitor of miR-509-3p involved in the regulation of cystic fibrosis disease-gene expression,” *Biomed Res. Int.*, vol. 2014, 2014.
[16] V. Viart *et al.*, “Transcription factors and miRNAs that regulate fetal to adult CFTR expression change are new targets for cystic fibrosis,” *Eur. Respir. J.*, vol. 45, no. 1, pp. 116–128, 2015.
[17] F. Zarrilli *et al.*, “Peptide nucleic acids as miRNA target protectors for the treatment of cystic fibrosis,” *Molecules*, vol. 22, no. 7, pp. 1–16, 2017.
[18] Y. Tsujimoto and C. M. Croce, “Analysis of the structure, transcripts, and protein products of bcl-2, the gene involved in human follicular lymphoma,” *Proc. Natl. Acad. Sci. U. S. A.*, vol. 83, no. 14, pp. 5214–5218, 1986.
[19] I. Marschitz, I. Tinhofer, A. Hittmair, A. Egle, M. Kos, and R. Greil, “Analysis of Bcl-2 protein expression in chronic lymphocytic leukemia: A comparison of three semiquantitation techniques,” *Am. J. Clin. Pathol.*, vol. 113, no. 2, pp. 219–229, 2000.
[20] T. J. McDonnell, J. T. Hsieh, and M. L. Campbell, “Expression of the Protooncogene bcl-2 in the Prostate and Its Association with Emergence of Androgen-independent Prostate Cancer,” *Cancer Res.*, vol. 52, no. 24, pp. 6940–6944, 1992.
[21] J. Dai, D. Chen, R. A. Jones, L. H. Hurley, and D. Yang, “NMR solution structure of the major G-quadruplex structure formed in the human BCL2 promoter region,” *Nucleic Acids Res.*, vol. 34, no. 18, pp. 5133–5144, 2006.
[22] M. del Toro *et al.*, “Targeting the G-quadruplex-forming region near the P1 promoter in the human BCL-2 gene with the cationic porphyrin TMPyP4 and with the complementary C-rich strand,” *Biochimie*, vol. 91, no. 7, pp. 894–902, 2009.
[23] C. T. Lin, T. Y. Tseng, Z. F. Wang, and T. C. Chang, “Structural conversion of intramolecular and intermolecular G-quadruplexes of bcl2mid: The effect of potassium concentration and ion exchange,” *J. Phys. Chem. B*, vol. 115, no. 10, pp. 2360–2370, 2011.
[24] N. Borbone *et al.*, “D(CGGTGGT) forms an octameric parallel G-quadruplex via stacking of unusual G(:C):G(:C):G(:C):G(:C) octads,” *Nucleic Acids Res.*, vol. 39, no. 17, pp. 7848–7857, 2011.

Appendix

List of Publications:

1. Nici F., Oliviero G., Falanga A.P., D'Errico S., Marzano M., Musumeci D., Montesarchio D., Noppen S., Pannecouque C., Piccialli G., Borbone N. **Anti-HIV activity of new higher order G-quadruplex aptamers obtained from tetra-end-linked oligonucleotides.** Organic & Biomolecular Chemistry (2018), 16, 2349.

2. Falanga A.P., Cerullo V., Marzano M., Feola S., Oliviero G., Piccialli G., Borbone N. **Peptide Nucleic Acid-Functionalized Adenoviral Vectors Targeting G‑Quadruplexes in the P1 Promoter of Bcl‑2 Proto-Oncogene: A New Tool for Gene Modulation in Anticancer Therapy.** Bioconjugate Chem (2019), 30, 572−582.

3. Marzano M., Falanga A.P., D'Errico S., Pinto B., Roviello G.N., Piccialli G., Oliviero G., Borbone N. **New G-Quadruplex-Forming Oligodeoxynucleotides Incorporating a Bifunctional Double-Ended Linker (DEL): Effects of DEL Size and ODNs Orientation on the Topology, Stability, and Molecularity of DEL-G-Quadruplexes.** Molecules (2019), 24, 654.

4. D'Errico S., Basso E., Falanga A.P., Marzano M., Pozzan T., Piccialli V., Piccialli G., Oliviero G., Borbone N. **New Linear Precursors of cIDPR Derivatives as Stable Analogs of cADPR: A Potent Second Messenger with $Ca2^{+}$-Modulating Activity Isolated from Sea Urchin Eggs.** Mar. Drugs (2019), 17, 476.

5. Falanga A.P., Marzano M., Terracciano M., D'Errico S. **5'-Chloro-5'-deoxy-2',3'-O-isopropylidene-6-fluoro nebularine.** *Molbank* 2019, *2019*(4), M1097.

6. Marzano M., Falanga A.P., Marasco D., Borbone N., D'Errico S., Piccialli G., Roviello G. N., Oliviero G. **Evaluation of an Analogue of the Marine ε-PLL Peptide as a Ligand of G-quadruplex DNA Structures.** Mar. Drugs (2019), 18, 49.

List of Posters and Communications:

1. Falanga A.P., Borbone N., D'Errico S., Pnto B., Marzano M., Cerullo V., Piccialli G., Oliviero G. **PNA-functionalized adenoviral vectors as new tool for gene modulation in anti-cancer treatment.** Società Chimica Italiana, Gruppo Interdivisionale di Biotecnologie (G.r.B). 1° WORKSHOP: I chimici per le biotecnologie, Bologna (Italy), February 23, 2018. **ORAL COMMUNICATION.**

2. Marzano M., Oliviero G., Borbone N., Falanga A.P., Pinto B., D'Errico S., Piccialli G. **Doubler-End-Linked- Oligonucleotide: the rules and effects of the linker size on the topology and stability of G-Quadruplexes.** Convegno Nazionale della Società Chimica Italiana Gruppo Giovani, Rimini (Italy), November 19-21, 2018. **ORAL COMMUNICATION**.

3. Marzano M., Borbone N., Dardano P., Falanga A.P., Rea I., D'Errico S., Terracciano M., De Stefano L., Piccialli G., Oliviero G. **Thioflavin T: an efficient ligand used to control the multimerization of a new symmetric G-rich Oligonucleotides incorporating a 3'-3' inversion of polarity site.** XLIV "A. Corbella" Internation Summer School on Organic Synthesis-ISOS 2019, Gargnano (BS, Italy), June 9-13, 2019. **ORAL COMMUNICATION.**

4. Marzano M., Borbone N., Dardano P., Falanga A.P., Rea I., D'Errico S., Terracciano M., De Stefano L., Piccialli G., Oliviero G. **A new symmetric G-rich Oligonucleotides incorporating a 3'-3' inversion of polarity site as an interesting model for ligand binding studies.** XXXIX Convegno Nazionale della Divisione di Chimica Organica della SCI-CDC0 2019, Turin (Italy), September 8-12, 2019. **ORAL COMMUNICATION.**

5. Marzano M., Oliviero G., Borbone N., Pinto B., D'Errico S., Piccialli G. **DNA G-Quadruplex: From nucleic acids involved in gene control expression to highly ordered supramolecular structures.** XLII Summer School "A. Corbella"-ISOS 2017, Gargnano (BS, Italy), June 18-23, 2017. **POSTER COMMUNICATION.**

6. Marzano M., Oliviero G., Borbone N., Falanga A.P., Pinto B., D'Errico S., Piccialli G. **New G-quadruplex-forming oligodeoxynucleotides incorporating a bifunctional Double-**

Ended-Linker (DEL): effects of DEL size and ONDs orientation on the topology, stability and molecularity of DEL-G-quadruplexes. International Summer School on Natural Products (ISSNP), Naples (Italy), July 1-5, 2017. **POSTER COMMUNICATION.**

7. Marzano M., Nici F., Oliviero G., D'Errico S., Pinto B., Falanga A.P., Musumeci D., Montesarchio D., Balzarini J., Piccialli G., Borbone N. **Studies on G-rich Tetra-End-Linked Oligonucleotides Forming Dimeric G-Quadruplex Structures with in Vitro anti-HIV Activity.** 9th International Symposium on Nano & Supramolecular Chemistry, Naples (Italy), September 4-7, 2017**. POSTER COMMUNICATION.**

8. D'Errico S., Oliviero G., Borbone N., Catalanotti B., Costantino V., Piccialli G., Marzano M. **"Northen" Ribose and pyrophosphate modified cADPR analogues: A novel class of potential Ca^{2+} mobilizers.** XVI CONVEGNO-SCUOLA SULLA CHIMICA DEI CARBOIDRATI, Certosa di Pontignano (SI, Italy), June 17-20, 2018. **POSTER COMMUNICATION.**

Organic & Biomolecular Chemistry

PAPER

View Article Online
View Journal | View Issue

Cite this: *Org. Biomol. Chem.*, 2018, **16**, 2349

Anti-HIV activity of new higher order G-quadruplex aptamers obtained from tetra-end-linked oligonucleotides†

F. Nici, [a] G. Oliviero, [b] A. P. Falanga,[a] S. D'Errico, [a] M. Marzano,[a] D. Musumeci,[c] D. Montesarchio, [c] S. Noppen,[d] C. Pannecouque, [d] G. Piccialli [a] and N. Borbone *[a]

Received 20th September 2017,
Accepted 8th March 2018

DOI: 10.1039/c7ob02346d

rsc.li/obc

By combining the ability of short G-rich oligodeoxyribonucleotides (ODNs) containing the sequence 5′CGGA3′ to form higher order G-quadruplex (G4) complexes with the tetra-end-linked (TEL) concept to produce aptamers targeting the HIV envelope glycoprotein 120 (gp120), three new TEL-ODNs (**1–3**) having the sequence 5′CGGAGG3′ were synthesized with the aim of studying the effect of G4 dimerization on their anti-HIV activity. Furthermore, in order to investigate the effect of the groups at the 5′ position, the 5′ ends of **1–3** were left uncapped (**1**) or capped with either the lipophilic dimethoxytrityl (DMT) (**2**) or the hydrophilic glucosyl-4-phosphate (**3**) moieties. The here reported results demonstrate that only the DMT-substituted TEL-ODN **2** is effective in protecting human MT-4 cell cultures from HIV infection (76% max protection), notwithstanding all the three new aptamers proved to be capable of forming stable higher order dimeric G4s when annealed in K^+-containing buffer, thus suggesting that the recognition of a hydrophobic pocket on the target glycoprotein by the aptamers represents a main structural feature for triggering their anti-HIV activity.

Introduction

DNA G-quadruplexes (G4s) are peculiar secondary structures of DNA which form *in vitro* when suitable G-rich oligodeoxyribonucleotides (ODNs) are annealed in the presence of selected monovalent or divalent cations.[1] In recent years, the visualization of DNA[2,3] and RNA[4] G4s in human cells demonstrated that these non-canonical nucleic acid structures are not just "*in vitro* oddities", but play important cellular roles in both physiological and pathological conditions.[5,6] In this frame, the identification of many G4-forming sequences in the regulatory regions of viral genomes,[7] along with the discovery that many G4-forming aptamers bind with high affinity to important viral proteins,[7] has triggered the search for novel antiviral agents based on ligands of viral G4s[8,9] or on G4-forming aptamers targeting viral proteins.[10–13] One of the most studied viral targets is the envelope glycoprotein 120 (gp120) exposed on the surface of HIV spikes. The interaction of gp120 with the CD4 glycoprotein and with a chemokine receptor, both on the surface of host cells, represents the first event of HIV infection.[14–16] This makes gp120 a suitable target for pharmacological intervention. Several G4-forming chemically modified DNA aptamers targeting gp120 have been proposed so far, and many of them can protect, at least *in vitro*, human cells from HIV infection at sub-micromolar concentration.[17,18] Furthermore, the observation that gp120 is the primary target of Zintevir®, a G4-forming DNA aptamer originally developed as an inhibitor of HIV-1 integrase (which completed Phase I clinical trials),[19] suggests that the interaction with gp120 is not limited to the inhibitors of viral entry, but may involve also drugs designed to target other HIV proteins (*e.g.* HIV integrase and reverse transcriptase). With the aim of overcoming the unfavorable entropic factor associated with tetramolecular and bimolecular G4-forming aptamers targeting gp120, and of increasing their stability towards enzymatic degradation, we have recently developed a series of new monomolecular analogues of the so-called Hotoda sequence (5′TGGGAG3′) by exploiting the Tetra-End-Linker (TEL) strategy first proposed in 2004.[20] Briefly, this consists of linking together the four ODN strands through a non-nucleotidic moiety. By exploring

[a]*Department of Pharmacy, University of Naples Federico II, Via Domenico Montesano 49, 80131 Napoli, Italy. E-mail: nicola.borbone@unina.it; Tel: +39-081 678521*
[b]*Department of Molecular Medicine and Medical Biotechnologies, University of Naples Federico II, Napoli, Italy*
[c]*Department of Chemical Sciences, University of Naples Federico II, Napoli, Italy*
[d]*KU Leuven, Department of Microbiology and Immunology, Laboratory of Virology and Chemotherapy, Rega Institute for Medical Research, Herestraat 49, B-3000 Leuven, Belgium*

†Electronic supplementary information (ESI) available. See DOI: 10.1039/c7ob02346d

different TEL lengths and strand orientations,[21] and also replacing or removing some of the nucleobases in the DNA sequence,[22,23] we produced a small library of TEL-ODNs capable of protecting human CD4$^+$ CEM cell cultures from HIV infection (EC_{50} values in the range of 0.039–0.74 μM). The combined analysis of the docking results and biological assays indicated that the self-assembly of TEL-aptamers into the corresponding G4s was essential for their anti-HIV activity. The same data also evidenced that some phosphate groups of the TEL residue and the last two nucleobases of the DNA sequences were responsible for tuning the biological activity of the studied aptamers. In previous papers, we also demonstrated that ODN strands having the sequences $^{5'}$CGGXGGT$^{3'}$ (with X = A, C, G or T)[24,25] or $^{5'}$CGGT$^{3'}$–$^{3'}$GGC$^{5'}$ [26] are able to self-assemble into dimers, or polymers in the latter case, of tetramolecular G4s by means of non-covalent 5′–5′ end-stacking *via* the formation of unusual G(:C):G(:C):G(:C):G(:C) octads. These higher order secondary structures of DNA display noteworthy thermal stability and reproducible folding, suggesting them as privileged scaffolds for the development of new biologically relevant aptamers or diagnostic/sensing tools. Since there is a quite large consensus that structuration into a higher order G4 organization is a prerequisite for obtaining selective binding aptamers,[27,28] we have envisaged that associating the TEL strategy to these highly self-structuring G-rich sequences could be highly beneficial to obtain more efficient and specific bioactive agents. In this paper, we report on the synthesis and structural characterization of three new TEL G4-forming aptamers based on the ODN sequence $^{5'}$CGGAGG$^{3'}$ (**1–3**, Fig. 1A). In **1–3** each arm of the TEL moiety was linked to the 3′-terminal deoxyguanosine of the ODN chain, whereas the 5′-terminal deoxycytidines had their 5′-hydroxyl groups unprotected (**1**) or capped with either the dimethoxytrityl (DMT) group (**2**) or the glucosyl-4-phosphate group (pGlc) (**3**). The $^{5'}$CGGAGG$^{3'}$ sequence was chosen with the aim of studying the effect of G4 dimerization on the anti-HIV activity of gp120-targeting aptamers. This 6-mer combines several favourable features: (i) it contains two GG repeats required for the formation of stable G4 species; (ii) it includes the $^{5'}$CGGA$^{3'}$ sequence allowing for the 5′–5′ end-stacking dimerization;[24,25] and (iii) it presents the same GG-TEL moiety of TEL-aptamer **II**,[22] one of the most active anti-HIV TEL-ODNs discovered in our laboratories (EC_{50} = 0.041 μM). The effect of the presence of 5′-terminal lipophilic (DMT groups in **2**) or hydrophilic (pGlc residues in **3**) moieties in **2** and **3** was explored on the basis of previous reports, showing that the installation of bulky aromatic groups at the 5′-end of the Hotoda sequence markedly affected the *in vitro* anti-HIV activity of the resulting aptamers.[29–31]

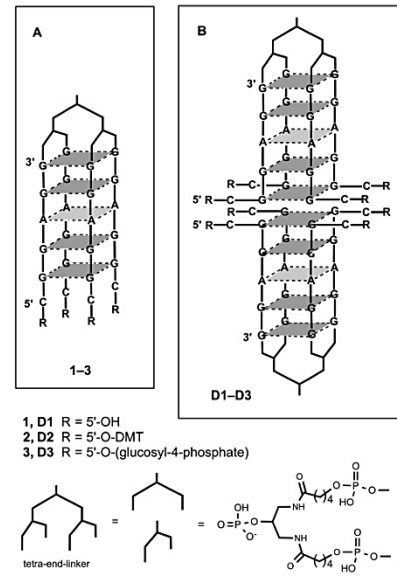

Fig. 1 Schematic representation of the here investigated TEL-ODNs. Panel (A) TEL-G4 monomers (**1–3**); panel (B) TEL-G4 dimers (**D1–D3**).

Results

Synthesis and purification of TEL-ODNs 1–3

The syntheses of TEL-ODNs **1–3** were performed using a solid-phase automated DNA synthesizer according to a previously described procedure.[32] To obtain the final product **2**, a DMT-on protocol, not including the final DMT deblocking step, was adopted. In the case of TEL-ODN **3**, an additional coupling step was inserted at the end of the synthesis, using a DMT-protected glucose phosphoramidite derivative obtained through a previously reported protocol.[33,34] After the automated synthesis, the ODNs were detached from the support and deprotected by treatment with concentrated aqueous ammonia. The crude products were then analysed, purified by HPLC and desalted. The G4s were formed by dissolving the TEL-ODNs **1–3** in a 1 M K$^+$-containing aqueous buffer, as described in the ESI.†

Polyacrylamide gel electrophoresis (PAGE) analysis

To investigate the structural features of the G4 assemblies formed by **1–3**, several analytical techniques were adopted in a combined approach. First, a native polyacrylamide gel electrophoresis (PAGE) analysis was carried out to check the molecularity of the complexes formed by **1–3** after their annealing in 1 M potassium buffer. Fig. 2 shows the PAGE analysis of: (i) $^{5'}$TGGGGT$^{3'}$ (lane 2), used as a tetramolecular G4 size marker due to its well-known ability to form $(^{5'}TGGGGT^{3'})_4$ complexes;[35,36] (ii) $^{5'}$CGGAGGT$^{3'}$ (lane 3), used as a size marker for a dimeric G4 being stably structured as an octa-stranded $(^{5'}CGGAGGT^{3'})_8$ complex;[25] (iii) TEL-$[^{3'}GGAGGC^{5'}]_4$ (**1**, lane 4);

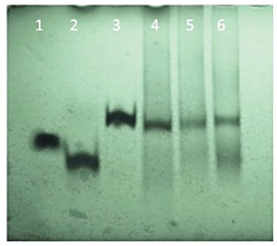

Fig. 2 Non-denaturing PAGE analysis for the sequences $^{5'}$TGGGGT$^{3'}$ (lane 2), $^{5'}$CGGAGGT$^{3'}$ (lane 3), TEL-[$^{3'}$GGAGGC$^{5'}$]$_4$ (**1**, lane 4), TEL-[$^{3'}$GGAGGC$^{5'\text{-DMT}}$]$_4$ (**2**, lane 5), TEL-[$^{3'}$GGAGGC$^{5'\text{-pGlc}}$]$_4$ (**3**, lane 6) annealed in 1 M K^+-containing buffer. Lane 1 = running marker (Coomassie blue).

(iv) TEL-[$^{3'}$GGAGGC$^{5'\text{-DMT}}$]$_4$ (**2**, lane 5); and (v) TEL-[$^{3'}$GGAGGC$^{5'\text{-pGlc}}$]$_4$ (**3**, lane 6). The migration profiles of **1** and **2** (lane 4 and 5, respectively) resemble the one of ($^{5'}$CGGAGGT$^{3'}$)$_8$ (lane 3), suggesting that these sequences can form higher order assemblies under the tested conditions. On the other hand, the migration profile of **3** (lane 6) accounted for the presence in solution of both the dimer **D3** and the TEL-G4 monomer **3**, showing a major band migrating like an octa-stranded G4, along with a faster, less defined band, having a mobility similar to that of ($^{5'}$TGGGGT$^{3'}$)$_4$. The striking similarity between the electrophoretic mobility of the **D1** band of TEL-ODN **1**, devoid of 5′-modifications, and those of the corresponding band of TEL-[$^{3'}$GGAGGC$^{5'\text{-DMT}}$]$_4$ (**D2**) and TEL-[$^{3'}$GGAGGC$^{5'\text{-pGlc}}$]$_4$ (**D3**) indicated that neither the DMT groups nor the glucosyl moieties significantly affected the migration properties of **2**/**D2** and **3**/**D3** in the polyacrylamide gel.

HPLC-size exclusion chromatography (HPLC-SEC)

To further corroborate the PAGE results and to estimate the amount of the dimeric TEL-G4s **D1–D3** relative to the corresponding monomeric species **1–3**, we performed an HPLC Size Exclusion Chromatography study (HPLC-SEC). The retention times of the eluted peaks were compared with those of peaks corresponding to the monomeric and dimeric G4 size markers (Fig. S2 in the ESI†). The obtained HPLC profiles confirmed the formation of two main distinct assemblies for all the three new TEL-ODNs corresponding to the dimeric TEL-G4s **D1–D3** (eluted around min. 19) and to the monomeric TEL-G4s **1–3** (eluted around min. 20). The relative amount of dimeric TEL-G4s *vs.* the corresponding monomeric assemblies was assessed by comparison of the area of the corresponding HPLC peaks for each TEL-ODN sample (see tables in Fig. S2†). The installation of the DMT or pGlc moieties at the 5′-terminal deoxycytidines of **1** resulted in the marked reduction of the amount of the dimeric species **D2** (−10%) and **D3** (−23%), respectively, relative to the monomeric TEL-G4s **2** and **3**.

CD and CD thermal analysis

Circular dichroism is a well-established technique used to provide important information about the conformational and structural properties of DNA. The different interactions between the guanosines within parallel or antiparallel G4 conformations and the circularly polarized light generate different CD profiles that are routinely used as distinctive signatures of the different G4 topologies.[28,37,38] To gain an insight into the conformational features of **1**, **2** and **3**, CD and CD melting experiments were carried out.

The CD spectra of all these systems recorded in 1 M K^+ buffer (Fig. 3A) showed a large positive band at about 264 nm and a small negative band at about 220 nm, indicative of the presence of head-to-tail stacked G-tetrads, as found in parallel G4s. Interestingly, an additional negative band at about 290 nm is visible for all the studied species. Since the latter band was previously associated with the formation of the head-to-head or tail-to-tail stacking interactions allowing for the dimerization of tetramolecular parallel G4s,[24,25] its presence in the CD spectra of **1–3** is in agreement with the dimerization of **1–3** G4s to afford, respectively, **D1**, **D2** and **D3** (Fig. 1B).

To evaluate the thermal stability of the obtained G4s, CD thermal denaturation–renaturation experiments were performed by monitoring the CD value (mdeg) at 264 nm in the temperature range of 5–90 °C. Because of the incomplete unfolding even at 90 °C, the resulting denaturation curves (Fig. 3B) did not allow the determination of the melting temperatures, but only the estimation of $T_{\frac{1}{2}}$, which was *ca.* 65 °C for all the three TEL-ODNs. The small hysteresis observed for all the investigated systems suggested the occurrence of aggregation processes, attributable to the formation of higher order G4s. In fact, to interpret these data, it is important to highlight that TEL-ODNs are neither expected to show typical sigmoidal melting profiles nor hysteresis in denaturation–renaturation curves because of the presence of the TEL moiety, that prevents the four covalently linked G-rich strands from completely dissociating and speeds up the reannealing process. Therefore, it seems plausible to explain the observed CD melting behaviour in terms of transition from **D1–D3** G4 dimers to **1–3** G4 monomers.

NMR analysis

The formation of G4 assemblies for **1–3** in K^+-containing buffer was also confirmed by water-suppressed ^{1}H-NMR spectroscopy (Fig. 4). In fact, the exchange-protected H1 imino proton signals of guanosines participating in G-tetrad formation were observed in the 10.5–11.5 ppm NMR region of **1–3**. The parallel arrangement of all strands participating in the G4 formation was confirmed by the number of the observed imino proton signals: one signal each for G2, G3 and G5 tetrads and two signals for the G6 tetrad because of the partial loss of symmetry induced by the bonding to the TEL arms. Furthermore, the presence of intense signals at *ca.* 9.2 ppm, attributable to the exchange-protected amino proton

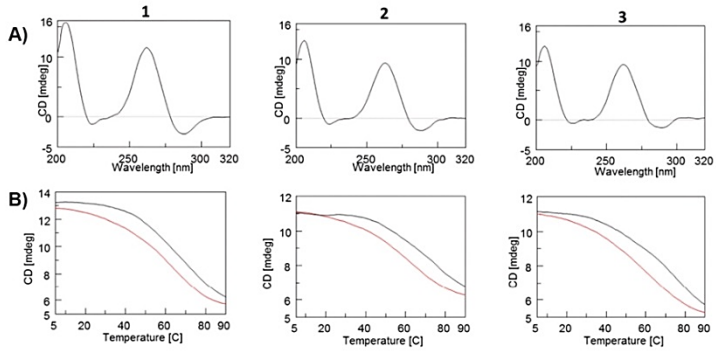

Fig. 3 (A) CD spectra and (B) CD melting (black) and annealing (red) curves of **1–3** registered in 1 M K^+ buffer.

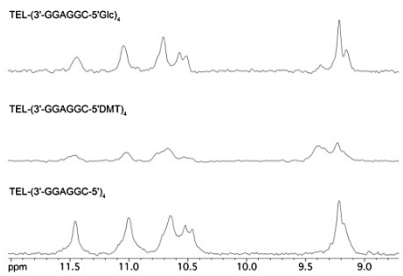

Fig. 4 Imino and amino proton regions of ^{1}H NMR spectra of **1–3** registered in 1 M K^+ buffer.

signals of A4, disclosed the presence of a stable A-tetrad in all the three TEL-ODNs. The relative intensity of imino and amino protons involved in G and A tetrads as compared with that of not-exchangeable protons allowed us to estimate the influence of 5′-capping DMT and glucose moieties on the amount of G4 assemblies formed by TEL-ODN **2** and **3**, respectively (Fig. S1 in the ESI†). From the NMR data it emerged that the insertion of a glucose–phosphate group on the primary OH groups of 5′ terminal deoxycytidines did not significantly alter the amount and symmetry of the resulting G4 stem, whereas the capping with the DMT groups resulted in a lower amount of G4 **2** and in extended loss of symmetry of the G4 stem (Fig. 4). Unfortunately, due to the almost perfect symmetry of the two halves of the dimeric complexes **D1–D3** and to the insufficient signal resolution to perform more in-depth 2D NMR investigations, it was not possible to obtain information on the relative amount of the dimeric G4 complexes **D1–D3** relative to the corresponding monomeric G4s (**1–3**) by NMR experiments.

Anti-HIV activity

To assess the influence of G4 dimerization and 5′-capping of **1** with either the lipophilic DMT (**2**) or the hydrophilic pGlc (**3**) moieties on the anti-HIV activity, we tested the inhibitory effect of **1–3** on HIV-1-induced cytopathicity in MT-4 cells.[39] The resulting EC_{50} values are listed in Table 1, along with the cytotoxicities (CC_{50} values) in uninfected MT-4 cells. In addition, the maximal protection against HIV-1-induced cytopathicity was measured, reported as max % protection in Table 1.

Of the set of tested ODNs, the 5′-DMT capped derivative **2** was the sole compound blocking the HIV-induced cytopathogenic effect with an EC_{50} value of 0.54 μM and a maximal protection between 70 and 76%. The CC_{50} value for this compound in MT-4 cells was 3.3 μM, resulting in a selectivity index (ratio CC_{50}/EC_{50}) of 6.

The congeners **1** and **3** only reached maximal protections of 24 and 33%, respectively, at the highest tested concentration of 5 μM.

Table 1 Anti-HIV and cytotoxicity studies on TEL-aptamers **1–3**

Compound	$EC_{50}^{a,c}$ (μM)	$CC_{50}^{b,c}$ (μM)	Max % protection
1	>5	>5	4–24%
2	0.54 ± 0.04	3.3 ± 1.3	70–76%
3	>5	>5	8–33%

[a] EC_{50}: compound concentration required to achieve 50% protection of MT-4 cells against HIV-1(III_B)-induced cytopathicity. [b] CC_{50}: compound concentration required to reduce the viability of mock-infected cells by 50%. [c] All data represent mean values (standard deviations for at least two separate experiments).

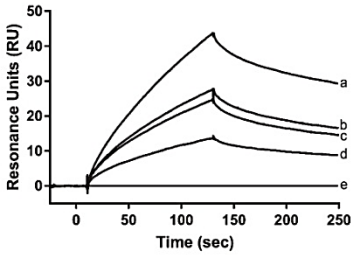

Fig. 5 SPR sensorgram showing the inhibition of gp120-heparin binding by **1–3**. Biotinylated heparin was captured on a streptavidin sensor chip. The sensorgram shows the response (RU) during association (0–120 s) and dissociation (2 min) of 2 μg mL^{-1} gp120 (a) or buffer (e). Gp120 was premixed with 0.5 μM **3** (b), **1** (c) or **2** (d) to test the inhibitory effect on gp120–heparin binding.

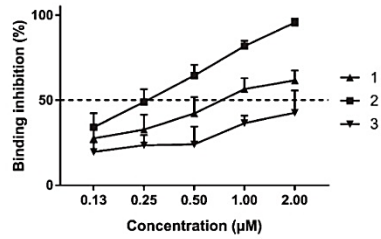

Fig. 6 Dose-dependent inhibition of gp120–heparin binding measured by SPR. Gp120 was premixed with 2-fold serial dilutions of **1–3** and injected over the heparin chip. Binding levels at the end of the association phase were converted in percentages of inhibition relative to gp120 binding without aptamers. Mean (+SEM) of three independent experiments is shown.

Binding affinity study using SPR

HIV-infection starts with the attachment of the virus to glycosaminoglycans of the host cell. To mimic the viral attachment, a Surface Plasmon Resonance (SPR) based approach was used to measure the binding between gp120 and immobilized glycosaminoglycans. Therefore, heparin was biotinylated at the reducing end and captured on a streptavidin sensor chip mimicking the host cell membrane. Gp120 at 2 μg mL^{-1} showed specific binding on heparin (Fig. 5, curve a). Next, gp120 was pre-incubated with the different G-quadruplex-forming aptamers and injected over the chip. A reduced binding was observed indicating that the aptamers are able to block the gp120–heparin interaction. TEL-$[^{3'}GGAGGC^{5'\text{-}DMT}]_4$ (**2**) bearing the hydrophobic DMT moieties showed the highest inhibitory activity (Fig. 5, curve d) followed by TEL-$[^{3'}GGAGGC^{5'}]_4$ (**1**) (Fig. 5, curve c) and TEL-$[^{3'}GGAGGC^{5'\text{-}pGlc}]_4$ (**3**) (Fig. 5, curve b) at 0.5 μM. **2** already reached 50% binding inhibition at 0.25 μM concentration (Fig. 6) and completely blocked the gp120–heparin binding at a 2 μM concentration. **3** was about 10 times less active with an IC_{50} of 2 μM. The IC_{50} of **1** was between 0.5 μM and 1 μM indicating a 2- to 4-fold lower binding inhibitory activity as compared to **2**. Overall, these data indicate that the observed *in vitro* anti-HIV activity of the TEL-ODN compounds could be explained by their ability to specifically block the interaction between gp120 and the polysulfated polysaccharides on the host cell membranes. The installation of the hydrophobic DMT groups in the TEL-G4 structure resulted in the most potent aptamer.

Discussion

The search for new antiviral agents is of paramount importance in the battle against pathogenic viruses. In the past few decades, nucleic acid-based aptamers emerged as potent antiviral therapeutics, indicating aptamer technology as a promising avenue for clinical applications.[17,40] In our previous studies, we reported on the ability of suitable G4 forming TEL-ODNs to bind the HIV glycoprotein 120 (gp120), thus protecting $CD4^+$ human T-lymphocyte CEM cells from HIV infection at sub-micromolar concentrations. Using molecular docking simulations and Surface Plasmon Resonance (SPR)[21,22] or fluorescence-quenching[23] binding affinity data we demonstrated that neither the TEL nor the hydrophobic capping groups at the 5′-ends of G4s, but the formation of a stable G4 is responsible for the anti-HIV activity of TEL-G4s. In other studies,[24,25] we reported on the ability of G-rich G4-forming ODNs starting with the $^{5'}CGGX^{3'}$ sequence to form stable higher order G4 structures by the dimerization of tetramolecular parallel G4s. In this context, we envisaged that the construction of supramolecular G4 complexes might be exploited in the design of new antiviral G4-forming aptamers devoid of bulky aromatic groups at their 5′ ends, whose presence was considered a prerequisite to enhance the rate and stability of G4 formation.[30] Specifically, we here synthesized, characterized and tested for their biological activity three new TEL G4-forming aptamers (**1–3**) in which the four arms of the Tetra-End-Linker were attached to the 3′ end of four $^{5'}CGGAGG^{3'}$ ODN strands. The $^{5'}CGGAGG^{3'}$ sequence was selected because it satisfies the above cited SAR requirements and possesses the $^{5'}CGGA^{3'}$ motif potentially able to induce TEL-G4 dimerization. Moreover, to assess the effect of the presence of 5′ terminal capping groups on the structural properties and antiviral activity of the studied TEL-G4 systems, the 5′-ends of **2** and **3** were conjugated with the hydrophobic DMT group or with the hydrophilic glucosyl–phosphate residue (pGlc), respectively, and the results were compared with those obtained for the 5′-unmodified **1**. The formation of monomeric and dimeric TEL-G4 assemblies was assessed for each sequence by combining PAGE, CD, HPLC Size Exclusion Chromatography (HPLC-SEC) and NMR data. The CD spectra

of **1–3** annealed in 1 M K^+ buffer were in agreement with the formation of higher order G4 dimeric structures (**D1–D3**) obtained by end-to-end stacking interactions between the corresponding parallel G4 stems (**1–3**) (Fig. 1). The CD indications were strongly supported by the PAGE and HPLC-SEC results, which showed that TEL-ODNs **1–3** exist in K^+-containing buffer as a mixture of monomeric and dimeric species, likely corresponding to the monomeric and dimeric G4 complexes. The combined analysis of PAGE and HPLC-SEC studies indicated that the amount of dimeric species relative to the monomeric ones was higher than 70% for **1** and **2** and around 60% for **3**. The NMR data fully confirmed the formation of parallel G4 species for all the three aptamers, although a significant reduction of the stiffness and symmetry of the G4 stem was observed in the case of the 5′-*O*-DMT-capped TEL-ODN **2**. To assess the effects of TEL-G4 dimerization on the anti-HIV activity of **1** and the influence of the presence of lipophilic (**2**) or hydrophilic (**3**) 5′-capping groups on the structural and biological features of **2** and **3**, we determined the EC_{50} and CC_{50} of **1–3** against HIV-1 in MT-4 cells. Based on the biological results reported in Table 1 the following considerations can be drawn: (1) among the here studied TEL-ODN **1–3**, only **2**, *i.e.* the oligomer capped with the DMT groups at its 5′ ends, proved to be effective in protecting human MT-4 T-lymphocyte cells from HIV-1 infection; (2) TEL-G4 **1** devoid of capping groups at its 5′ ends, although able to fold into the most stable G4 dimer **D1** (Fig. 1), did not show significant anti-HIV activity; and (3) the antiviral assays confirmed that the bulky aromatic groups at the 5′ ends of G4 aptamers targeting the HIV gp120 are essential structural motifs for their biological activity, whereas hydrophilic glucosyl–phosphate moieties inserted in the same position proved to be highly detrimental. Moreover, the here reported SPR results indicate that the 5′-bulky aromatic DMT groups enhance the binding affinity of **2** towards gp120 (10 times higher than **3** and 2–4 times higher than **1**), likely by interacting with a hydrophobic pocket on the viral glycoprotein. These findings could suggest a possible, direct and active role of these conjugating groups in G4 structure bioactivity, whereas the previous experimental results mainly pointed to their major role as mere enhancers of the rate of G4 formation and stability.[30]

Conclusions

In conclusion, by using CD, PAGE, NMR and SPR data we demonstrated that TEL-G4-forming ODNs having the sequence $^{5'}$CGGAGG$^{3'}$ (**1–3**) can form higher order dimers of G4 structures (**D1–D3**) using the same 5′–5′ end-to-end stacking interface previously reported for $^{5'}$CGGXGGT$^{3'}$ sequences.[24,26] Taking into account that both the dimerization process and the 5′ OH capping with different groups could influence the anti-HIV activity of new G4-forming aptamers targeting the HIV gp120, three new putative G4-forming TEL-aptamers of the sequence $^{5'}$CGGAGG$^{3'}$ were synthesized: the ODN with free 5′ OH groups (**1**), and its analogues 5′-conjugated with DMT (**2**) or glucosyl–phosphate (**3**) moieties. We observed that all these new TEL-ODNs are able to fold into dimeric G4 complexes, but neither the unconjugated **1** nor the glucosyl-conjugated **3** were capable of protecting human MT-4 cell cultures from HIV infection. Only TEL-ODN **2**, conjugated with the lipophilic aromatic DMT groups, showed significant anti-HIV activity at sub-micromolar concentrations, thus suggesting that the anti-HIV activity of these aptamers can be essentially connected with the specific recognition of a hydrophobic pocket on viral gp120.

Conflicts of interest

There are no conflicts to declare.

Notes and references

1 J. T. Davis, *Angew. Chem., Int. Ed.*, 2004, **43**, 668–698.
2 G. Biffi, D. Tannahill, J. McCafferty and S. Balasubramanian, *Nat. Chem.*, 2013, **5**, 182–186.
3 R. Rodriguez, K. M. Miller, J. V. Forment, C. R. Bradshaw, M. Nikan, S. Britton, T. Oelschlaegel, B. Xhemalce, S. Balasubramanian and S. P. Jackson, *Nat. Chem. Biol.*, 2012, **8**, 301–310.
4 G. Biffi, M. Di Antonio, D. Tannahill and S. Balasubramanian, *Nat. Chem.*, 2014, **6**, 75–80.
5 S. Balasubramanian, L. H. Hurley and S. Neidle, *Nat. Rev. Drug Discovery*, 2011, **10**, 261–275.
6 N. Maizels and L. T. Gray, *PLoS Genet.*, 2013, **9**, e1003468.
7 M. Métifiot, S. Amrane, S. Litvak and M. L. Andréola, *Nucleic Acids Res.*, 2014, **42**, 12352–12366.
8 L. H. Hurley, R. T. Wheelhouse, D. Sun, S. M. Kerwin, M. Salazar, O. Y. Fedoroff, F. X. Han, H. Han, E. Izbicka and D. D. Von Hoff, *Pharmacol. Ther*, 2000, **85**, 141–158.
9 R. Perrone, E. Butovskaya, D. Daelemans, G. Palu, C. Pannecouque and S. N. Richter, *J. Antimicrob. Chemother.*, 2014, **69**, 3248–3258.
10 V. T. Mukundan, A. T. Phan and N. Q. Do, *Nucleic Acids Res.*, 2011, **39**, 8984–8991.
11 C. Marchand, K. Maddali, M. Metifiot and Y. Pommier, *Curr. Top. Med. Chem.*, 2009, **9**, 1016–1037.
12 N. Jing, C. Marchand, J. Liu, R. Mitra, M. E. Hogan and Y. Pommier, *J. Biol. Chem.*, 2000, **275**, 21460–21467.
13 N. J. Jing and M. E. Hogan, *J. Biol. Chem.*, 1998, **273**, 34992–34999.
14 C. Teixeira, J. R. B. Gomes, P. Gomes and F. Maurel, *Eur. J. Med. Chem.*, 2011, **46**, 979–992.
15 R. Wyatt, *Science*, 1998, **280**, 1884–1888.
16 P. D. Kwong, R. Wyatt, J. Robinson, R. W. Sweet, J. Sodroski and W. A. Hendrickson, *Nature*, 1998, **393**, 648–659.
17 D. Musumeci, C. Riccardi and D. Montesarchio, *Molecules*, 2015, **20**, 17511–17532.

18 C. Platella, C. Riccardi, D. Montesarchio, G. N. Roviello and D. Musumeci, *Biochim. Biophys. Acta*, 2017, **1861**, 1429–1447.
19 J. A. Esté, C. Cabrera, D. Schols, P. Cherepanov, A. Gutierrez, M. Witvrouw, C. Pannecouque, Z. Debyser, R. F. Rando, B. Clotet, J. Desmyter and E. De Clercq, *Mol. Pharmacol.*, 1998, **53**, 340–345.
20 G. Oliviero, N. Borbone, A. Galeone, M. Varra, G. Piccialli and L. Mayol, *Tetrahedron Lett.*, 2004, **45**, 4869–4872.
21 G. Oliviero, J. Amato, N. Borbone, S. D'Errico, A. Galeone, L. Mayol, S. Haider, O. Olubiyi, B. Hoorelbeke, J. Balzarini and G. Piccialli, *Chem. Commun.*, 2010, **46**, 8971–8973.
22 V. D'Atri, G. Oliviero, J. Amato, N. Borbone, S. D'Errico, L. Mayol, V. Piccialli, S. Haider, B. Hoorelbeke, J. Balzarini and G. Piccialli, *Chem. Commun.*, 2012, **48**, 9516–9518.
23 G. Oliviero, M. Stornaiuolo, V. D'Atri, F. Nici, A. M. Yousif, S. D'Errico, G. Piccialli, L. Mayol, E. Novellino, L. Marinelli, P. Grieco, A. Carotenuto, S. Noppen, S. Liekens, J. Balzarini and N. Borbone, *Anal. Chem.*, 2016, **88**, 2327–2334.
24 N. Borbone, J. Amato, G. Oliviero, V. D'Atri, V. Gabelica, E. De Pauw, G. Piccialli and L. Mayol, *Nucleic Acids Res.*, 2011, **39**, 7848–7857.
25 V. D'Atri, N. Borbone, J. Amato, V. Gabelica, S. D'Errico, G. Piccialli, L. Mayol and G. Oliviero, *Biochimie*, 2014, **99**, 119–128.
26 G. Oliviero, S. D'Errico, B. Pinto, F. Nici, P. Dardano, I. Rea, L. De Stefano, L. Mayol, G. Piccialli and N. Borbone, *ChemistryOpen*, 2017, **6**, 599–605.
27 A. T. Phan, N. Q. Do, K. W. Lim, M. H. Teo and B. Heddi, *Nucleic Acids Res.*, 2011, **39**, 9448–9457.
28 N. Smargiasso, F. Rosu, W. Hsia, P. Colson, E. S. Baker, M. T. Bowers, E. De Pauw and V. Gabelica, *J. Am. Chem. Soc.*, 2008, **130**, 10208–10216.
29 H. Hotoda, M. Koizumi, R. Koga, M. Kaneko, K. Momota, T. Ohmine, H. Furukawa, T. Agatsuma, T. Nishigaki, J. Sone, S. Tsutsumi, T. Kosaka, K. Abe, S. Kimura and K. Shimada, *J. Med. Chem.*, 1998, **41**, 3655–3663.
30 J. D'Onofrio, L. Petraccone, E. Erra, L. Martino, G. Di Fabio, L. De Napoli, C. Giancola and D. Montesarchio, *Bioconjugate Chem.*, 2007, **18**, 1194–1204.
31 J. D'Onofrio, L. Petraccone, L. Martino, G. Di Fabio, A. Iadonisi, J. Balzarini, C. Giancola and D. Montesarchio, *Bioconjugate Chem.*, 2008, **19**, 607–616.
32 J. Amato, G. Oliviero, N. Borbone, A. Galeone, M. Varra, G. Piccialli, L. Mayol and G. Oliviero, *Biopolymers*, 2006, **81**, 194–201.
33 M. Adinolfi, L. De Napoli, G. Di Fabio, A. Iadonisi, D. Montesarchio and G. Piccialli, *Tetrahedron*, 2002, **58**, 6697–6704.
34 M. Adinolfi, L. De Napoli, G. Di Fabio, A. Iadonisi and D. Montesarchio, *Org. Biomol. Chem.*, 2004, **2**, 1879–1886.
35 F. Aboul-ela, A. I. H. Murchie, D. G. Norman and D. M. J. Lilley, *J. Mol. Biol.*, 1994, **243**, 458–471.
36 G. Laughlan, A. I. Murchie, D. G. Norman, M. H. Moore, P. C. Moody, D. M. Lilley and B. Luisi, *Science*, 1994, **265**, 520–524.
37 M. Vorlíčková, I. Kejnovská, J. Sagi, D. Renčiuk, K. Bednárová, J. Motlová and J. Kypr, *Methods*, 2012, **57**, 64–75.
38 A. I. Karsisiotis, N. M. Hessari, E. Novellino, G. P. Spada, A. Randazzo and M. Webba da Silva, *Angew. Chem., Int. Ed.*, 2011, **50**, 10645–10648.
39 C. Pannecouque, D. Daelemans and E. De Clercq, *Nat. Protoc.*, 2008, **3**, 427–434.
40 K. T. Shum, J. Zhou and J. J. Rossi, *Pharmaceuticals*, 2013, **6**, 1507–1542.

Bioconjugate Chemistry

Article

Cite This: *Bioconjugate Chem.* 2019, 30, 572−582

pubs.acs.org/bc

Peptide Nucleic Acid-Functionalized Adenoviral Vectors Targeting G-Quadruplexes in the P1 Promoter of Bcl-2 Proto-Oncogene: A New Tool for Gene Modulation in Anticancer Therapy

Andrea Patrizia Falanga,[†] Vincenzo Cerullo,[‡,§,∥] Maria Marzano,[†] Sara Feola,[§] Giorgia Oliviero,*[,∥] Gennaro Piccialli,[†] and Nicola Borbone*[,†]

[†]Department of Pharmacy, University of Naples Federico II, Via Domenico Montesano 49, 80131 Naples, Italy

[‡]Drug Research Program (DRP) and [§]Laboratory of Immunovirotherapy (IVTLab), University of Helsinki, Viikinkaari 5E, 00790 Helsinki, Finland

[∥]Department of Molecular Medicine and Medical Biotechnologies, University of Naples Federico II, Via Sergio Pansini 5, 80131 Naples, Italy

Supporting Information

ABSTRACT: The B-cell lymphoma 2 (Bcl-2) gene encodes for an antiapoptotic protein associated with the onset of many human tumors. Several oligonucleotides (ONs) and ON analogues are under study as potential tools to counteract the Bcl-2 expression. Among these are Peptide Nucleic Acids (PNAs). The absence of charges on PNA backbones allows the formation of PNA/DNA complexes provided with higher stability than the corresponding natural DNA/DNA counterparts. To date, the use of PNAs in antigene or antisense strategies is strongly limited by their inability to efficiently cross the cellular membranes. With the aim of downregulating the expression of Bcl-2, we propose here a novel antigene approach which uses oncolytic adenoviral vectors (OAds) as a new cancer cell-targeted PNA delivery system. The ability of oncolytic Ad5D24 vectors to selectively infect and kill cancer cells was exploited to transfect with high efficiency and selectivity a short cytosine-rich PNA complementary to the longest loop of the main G-quadruplex formed by the 23-base-long bcl2midG4 sequence located 52−30 bp upstream of the P1 promoter of Bcl-2 gene. Physico-chemical and biological investigations confirmed the ability of the PNA-conjugated Ad5D24 vectors to load and transfect their PNA cargo into human A549 and MDA-MB-436 cancer cell lines, as well as the synergistic (OAd+PNA) cytotoxic effect against the same cell lines. This approach holds promise for safer chemotherapy because of reduced toxicity to healthy tissues and organs.

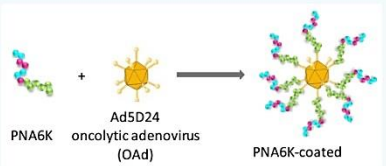

INTRODUCTION

The human B-cell lymphoma 2 (Bcl-2) gene product is a mitochondrial protein involved in the control of programmed cell death. Functioning as inhibitor of apoptosis, the Bcl-2 overexpression has been found in a wide range of human malignancies, including breast, cervical, nonsmall cell lung, and prostate cancers.[1−3] Moreover, part of the oncogenic potential of the Bcl-2 gene is due to its involvement in the onset of resistance toward the chemotherapy-induced apoptosis.[4] Several therapeutic approaches targeting the Bcl-2 gene expression are being explored and encouraging results have been obtained by using peptides and peptidomimetics, small-molecule inhibitors (SMIs) (BH3Is, ABT 263; ABT 737; ABT 199), porphyrins, and antisense oligonucleotides (e.g., G3139, also known as oblimersen, which reached phase II clinical trials).[5−7] However, these strategies suffer from many shortcomings, as the short *in vivo* half-life of used molecules, poor intracellular delivery, acquired resistance against SMIs, mutagenicity, and off-target effects.[8]

A valid alternative to overcome some of these limitations can be the use of peptide nucleic acids (PNAs). PNAs are DNA and RNA mimics in which the sugar phosphate backbone is replaced by N-(2-aminoethyl) glycine units.[9] PNAs have the ability to interact with complementary single-stranded RNA and DNA, obeying to the Watson−Crick hydrogen bonding rules, with higher affinity than that of its natural counterparts.[10] The low electrostatic repulsion resulting from the absence of phosphate moieties allows PNAs to form very stable complexes with the target DNA and RNA. The favorable biophysical properties, together with the high chemical and enzymatic stability and low toxicity, make PNAs one of the most valuable tools for biomedical applications, in both diagnostics[11] and therapeutics (e.g., by exploitation of antigene,[12,13] antisense,[14] and anti-miRNA[15,16] strategies).

Received: September 25, 2018
Revised: December 29, 2018
Published: January 8, 2019

DOI: 10.1021/acs.bioconjchem.8b00674
Bioconjugate Chem. 2019, 30, 572−582

In this context, in 2011 we demonstrated that short cytosine-rich (C-rich) PNA sequences can act either as "G-quadruplex binding agents" or as "G-quadruplex openers" according to the PNA sequence and length and to the composition of the aqueous buffer used.[12] G-quadruplexes (G4s) are noncanonical secondary structures of DNA and RNA which form when suitable guanine-rich (G-rich) strands are annealed in the presence of coordinating cations (usually monovalent).[17−19] It has been demonstrated that the formation of G4 motifs in the close proximity of gene promoters can inhibit the recruitment and scanning of the RNA polymerase complex, thus resulting in the downregulation of gene transcription.[8] Specifically, two promoters, namely, P1 and P2, have been identified in the human Bcl-2 gene and several transcription factors have been reported to modulate the Bcl-2 expression through their binding to the GC-rich region close the 5′-end of the P1 promoter (Sp1,[20] WT1,[21] E2F,[22] NGF[23]). Using modified sequences,[24] it has been demonstrated that the 39-bp-long GC-rich region located 58 to 19 bp upstream of the P1 promoter has the ability to fold into three different G4 structures *in vitro*. Among them, the G4 formed by the 23-mer sequence named bcl2midG4 (Figure 1) is characterized by a

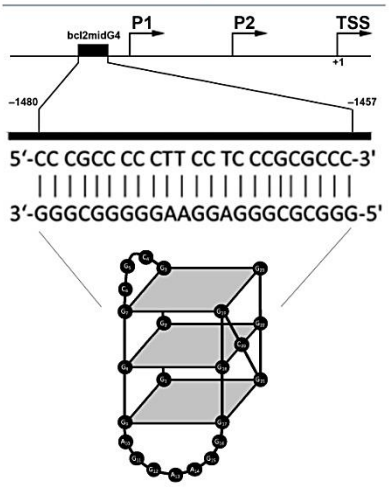

Figure 1. Schematic representations of the Bcl-2 promoter region, bcl2midG4 sequence and of the main G4 formed by the bcl2midG4 DNA sequence.

peculiar monomolecular hybrid type topology involving two lateral loops (three and seven bases long) and one single base propeller loop.[7] Thus, the targeting of the bcl2midG4 G-quadruplex (bcl2midG4-G4) using small complementary PNA probes could represent a new selective weapon against cancer cells overexpressing the Bcl-2 protein. Accordingly, we report here the results of our study aimed at the synthesis and biophysical characterization of two new PNA-derivatives, **PNAK** and **PNA6K**, whose seven-bases-long PNA sequence is fully complementary to the longer lateral loop of the bcl2midG4 quadruplex (Table 1).

Table 1. Sequences of DNAs and PNAs Used in This Study

Sample	Sequence
G-rich bcl2midG4	d(5′GGGCGCGGGAGGAAGGGGGCGGG3′)
C-rich bcl2midG4	d(5′CCCGCGCCCTCCTTCCCCCGCCC3′)
PNAK	H-ccttcct-K-NH_2 (N to C)
PNA6K	H-ccttcct-KKKKKK-NH_2 (N to C)

The interaction between the PNAs and the bcl2midG4 duplex (bcl2midG4-ds) was also investigated in order to determine the selectivity of the binding. One of the main factors that have so far limited the development of PNA-based drugs is the PNA poor cell permeability.[25] Several strategies have been developed in order to overcome biological barriers, such as the use of liposomes,[26,27] dendrimers,[28,29] and nanoparticles.[30−33] Here, for the first time we propose the use of oncolytic adenoviruses (OAds) as PNA drug delivery system to take advantage of the OAds ability to selectively infect and kill cancer cells, as well as to deliver in the latter any molecule adsorbed on the OAd capsid.[34,35] Accordingly, to improve the electrostatic attraction with the negatively charged surface of OAd capsid, we prolonged the positively charged lysine (K) tail of **PNAK** (required for water solubility) from one to six lysines, thus obtaining **PNA6K**. The biological activity of **PNA6K**, OAd-**PNA6K** complex, and the uncoated OAd was assessed by MTS cytotoxicity assay and Western blot analyses against A549 and MDA-MB 436 human cancer cell lines, which were used as models for Bcl-2 protein over-expression.[36,37]

RESULTS

Circular Dichroism (CD). As also reported in the literature, the CD spectrum of G-rich bcl2midG4 annealed in K^+-containing buffer is characterized by two positive CD bands at 263 and 293 nm and one negative band at 240 nm (Figure 2A, solid line), a CD signature characteristic of 3 + 1 hybrid type G4s.[38−40] To confirm the interaction between **PNAK** (Figure 2A, dotted line) and bcl2midG4-G4, we compared the CD profile of bcl2midG4-G4 alone (solid line) with the one obtained after its incubation with **PNAK** (Figure 2A, dashed line) and with the CD profile corresponding to the arithmetic sum of the individual components (Figure 2A, dot-dashed line). The CD spectrum of bcl2midG4-G4/**PNAK** mixture was clearly different from the arithmetic sum of the two separate components, thus confirming that the interaction between the bcl2midG4-G4 and **PNAK** occurred. In particular, the positive CD hump at 293 nm was replaced by a broad shoulder and the remaining positive and negative signals resulted red-shifted by about 2 nm. In parallel, we studied the interactions between **PNAK** and the bcl2midG4 duplex (bcl2midG4-ds) (Figure 2B). In this case, the spectrum of bcl2midG4-ds/**PNAK** (Figure 2B, dashed line) overlapped almost perfectly with the arithmetic sum of the individual components (Figure 2B, dot-dashed line), thus indicating that no hybridization occurred in this condition.

To obtain further information about the interaction between bcl2midG4-G4 or bcl2midG4-ds and **PNAK**, we recorded the CD spectra at different temperatures during the melting and the annealing procedures (Figure 3 and Figure S1), as well as the CD melting profiles of bcl2midG4-ds before and after its

DOI: 10.1021/acs.bioconjchem.8b00674
Bioconjugate Chem. 2019, 30, 572−582

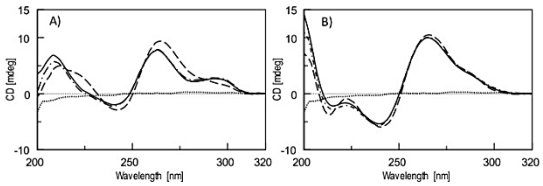

C)

Sample	λ min	λ max
bcl2midG4-G4	240	208, 263, 293
bcl2midG4-G4/**PNAK**	242	212, 265
bcl2midG4-ds	215, 240	265
bcl2midG4-ds/**PNAK**	213, 240	266

Figure 2. (A) CD spectra of bcl2midG4-G4 (solid line) and bcl2midG4-G4 incubated with **PNAK** (dashed line). (B) CD spectra of bcl2midG4-ds (black solid line) and bcl2midG4-ds incubated with **PNAK** (dashed line). In each panel the CD profiles of the arithmetic sum of DNA and **PNAK** and of **PNAK** alone are reported as dot-dashed and dotted lines, respectively. All samples were dissolved in 60 mM K^+-containing buffer and the spectra were normalized at 320 nm. (C) λ values for CD minima and maxima of each sample.

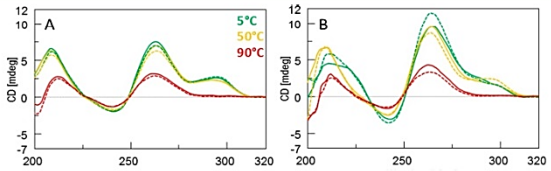

Figure 3. CD profiles of bcl2midG4-G4 (A) and bcl2midG4-G4/**PNAK** (B) recorded at 5 °C (green), 50 °C (yellow) and 90 °C. Heating: solid line; cooling: dashed line.

incubation with 5 equiv of **PNAK** (Figure S2). For the samples involving bcl2midG4-ds, we did not observe any significant difference between spectra obtained either before or after incubation with **PNAK**, or between spectra obtained from the same sample but recorded either during the melting or the annealing runs. These data confirmed that **PNAK** does not bind to the bcl2midG4 duplex. Conversely, two main significant differences were observed for the same analyses involving the bcl2midG4-G4. First, the CD spectrum of bcl2midG4-G4/**PNAK** recorded at 50 °C during the cooling run (Figure 3B, orange dotted line) was almost superimposable with that of bcl2midG4-G4 alone recorded at the same temperature (Figure 3A, orange solid line), being characterized by the minimum at 240 nm and the two maxima at 263 and 293 nm, whereas in all other spectra of bcl2midG4-G4/**PNAK** acquired at temperatures ≤40 °C the hump at 293 nm was not present (Figures 3B and S1). Second, the comparison of the CD spectra recorded at 5 °C before the melting and after the cooling procedure (Figure 3B, green solid and dotted lines, respectively) and the comparison of the heating and cooling CD melting curves of bcl2midG4-G4/**PNAK** mixture (Figure S2B) indicated a significant increasing of the positive dichroic signal at 265 nm. Taken together, the CD results indicated that the **PNAK** is able to form more than one complex with the bcl2midG4-G4 at temperatures lower than 50 °C.

Polyacrylamide Gel Electrophoresis (PAGE). The molecular size of the complexes formed in the different conditions was examined by nondenaturing polyacrylamide gel electrophoresis (PAGE). In the case of the **G-rich bcl2midG4** strand alone annealed in 60 mM K^+ buffer, we observed two main bands corresponding to the monomeric and dimeric G-quadruplexes (Figure 4, lane 3) in agreement with what reported by Lin et al.[38] The fastest band migrating like the 10 bp reference of the DNA ladder (Figure 4, lane 7) was assigned to the 3 + 1 monomeric bcl2midG4-G4, whereas the slowest band, migrating like the $(CGGAGGT)_8$ dimeric G4 size marker (Figure 4, lane 2),[41] was assigned to a dimeric G4. The PAGE mobility of the sample obtained by incubating bcl2midG4-G4 with 5 equiv **PNAK** is shown in Figure 4, lane 4. We observed the reduction of the intensity of the monomeric bcl2midG4-G4 band and the appearance of a new, intense band attributable to a DNA/**PNAK** complex having mobility intermediate between 30 and 40 base pairs. We also observed the band attributable to the dimeric G4 alone and an intense smearing attributable to even higher molecular weight complexes. The comparison of the PAGE mobility of bcl2midG4-ds before and after its incubation with **PNAK** (showed in Figure 4, lanes 5 and 6, respectively) confirmed the CD data pointing at the absence of any interaction between **PNAK** and the double stranded bcl2midG4 sequence. Taken together, the PAGE study confirmed the ability of **PNAK** to

DOI: 10.1021/acs.bioconjchem.8b00674
Bioconjugate Chem. 2019, 30, 572−582

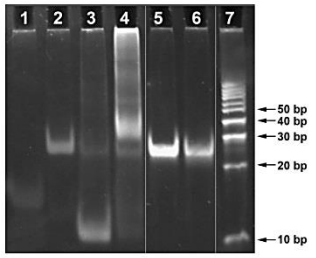

Figure 4. PAGE of bcl2midG4 G4 and duplex incubated with **PNAK** in potassium solution. Lane 1, $[d(TGGGGT)]_4$ G4 marker; lane 2, $[d(CGGAGGT)]_8$ dimeric G4 marker; lane 3, bcl2midG4-G4 annealed in K^+; lane 4, bcl2midG4-G4 incubated with **PNAK**; lane 5, bcl2midG4-ds; lane 6, bcl2midG4-ds incubated with **PNAK**; lane 7, DNA duplex ladder (10−100 bp).

bind selectively the bcl2midG4-G4 over the bcl2midG4-ds, and also evidenced that the incubation with **PNAK** triggers the formation of higher order complexes, attributable to multimeric bcl2midG4 quadruplexes complexed with the short complementary PNA strand.

Size-Exclusion Chromatography (SEC). Considering the indications obtained by the PAGE studies and to shed light on the molecular weight distribution of the complexes formed after the incubation with **PNAK**, we performed an HPLC size exclusion chromatography (SEC) study. Generally, HPLC-SEC profiles show a distribution of peaks in which lower MW species have higher retention times. In Figure 5 are reported the HPLC-SEC profiles obtained at room temperature on a ReproSil 2000 SEC column of (i) the pre-annealed bcl2midG4-G4 alone (A), and (ii) bcl2midG4-G4 incubated with 5 equiv of **PNAK** (B) and **PNAK** alone (C).

Based on SEC principles and considering the PAGE results, the peak at the highest retention time in the HPLC-SEC profile of bcl2midG4-G4 alone (Figure 5A; Rt = 12.16 min) was assigned to the monomeric G4 structure, while the preceding peak (Rt = 11.74 min) was attributed to a dimeric G-quadruplex formed by **G-rich bcl2midG4**. For bcl2midG4-G4/**PNAK** 1:5 mixture (Figure 5B), the HPLC-SEC profile showed the peaks of the unbound species (**PNAK** excess at Rt = 19.16; monomeric and dimeric bcl2midG4 G-quadruplexes at Rt = 12.08 and 11.42 min, respectively) together with a sharp intense peak at Rt = 11.25 min attributable to a **PNAK**-bound dimeric bcl2midG4 G-quadruplex. The remaining retained peak at Rt = 10.03 min and the envelope peak centered at Rt = 9.13 min confirmed the PAGE indications about the presence in solution of supramolecular assemblies of

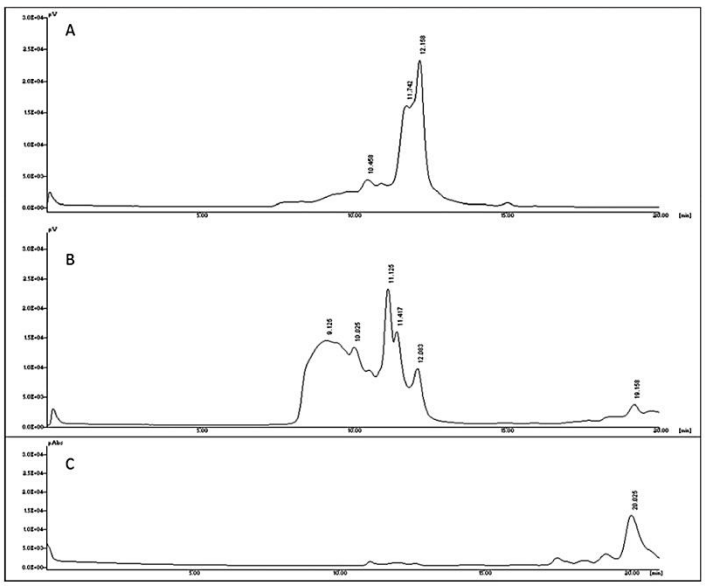

Figure 5. HPLC-SEC profile of bcl2midG4-G4 (A), bcl2midG4-G4/**PNAK** (B), and **PNAK** (C).

DOI: 10.1021/acs.bioconjchem.8b00674
Bioconjugate Chem. 2019, 30, 572−582

A

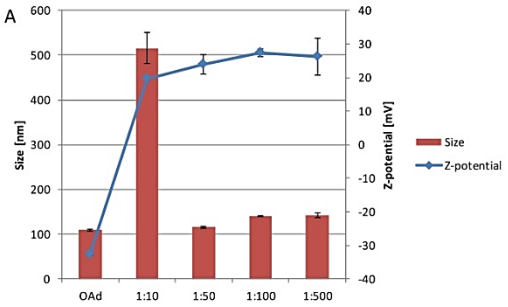

B

Preps [OAd-PNA6K]	Size [nm] ± SD	PDI	Z-Potential [mV] ± SD
Ad5D24	109.03 ± 1.95	0.12	-32.67 ± 0.21
Ad5D24-**PNA6K** [1:10]	515.50 ± 34.24	0.47	19.67 ± 0.42
Ad5D24-**PNA6K** [1:50]	116.07 ± 2.32	0.03	23.90 ± 2.89
Ad5D24-**PNA6K** [1:100]	140.23 ± 2.05	0.18	27.33 ± 1.10
Ad5D24-**PNA6K** [1:500]	142.47 ± 4.55	0.20	26.13 ± 5.51

Figure 6. Hydrodynamic diameter (nm ± SD) and zeta potential (mV ± SD) values of virus-PNA complexes obtained by incubating AdSD24 OAds with **PNA6K** at increasing virus/PNA ratios.

bcl2midG4, either bound or unbound to one or more **PNAK** molecules, whose formation was triggered by the incubation with **PNAK**. Conversely, the addition of **PNAK** to the bcl2midG4 duplex neither induced significant variation in the retention time of the bcl2midG4-ds peak (Figure S3B; Rt = 11.78 min), nor determined the appearance of any new peak besides the peak of the unbound **PNAK** (Rt = 19.38 min).

Ad5D24-PNA6K Complex Formation. Once we demonstrated the ability of **PNAK** to selectively bind the G4s formed by the **G-rich bcl2midG4** sequence, we developed a novel delivery system for the on-demand administration of PNA-based drugs to tumor cells by exploiting the capability of OAds (Ad5D24 strain) to enter and selectively lyse cancer cells with respect to healthy tissues, as well as to transport into the infected cells any suitable cargo adsorbed on the virus surface.[42] The human adenocarcinomic alveolar basal epithelial A549 and the triple negative breast cancer MDA-MB 436 cell lines were selected as cellular models because of their high expression of the Bcl-2 gene product. At first, A549 and MDA-MB 436 cells were incubated with **PNAK** at several concentrations and their viability was assessed by MTS assay at days 1, 3, and 5 from the incubation (Figure S4). The absence of any effect on cells viability, even at the highest **PNAK** concentration (100 μM) and at the longest incubation time (day 5), confirmed the requirement of an efficient delivery strategy to transport **PNAK** within the cancer cells. As previously reported, positively charged molecules can be efficiently adsorbed on the negatively charged surface of OAds via electrostatic interactions.[34,43] In line with previously reports, in order to maximize the amount of **PNAK** on OAd vectors, we enhanced the positive charge of **PNAK** by prolonging the C-terminal lysine tail from one to six lysines, thus obtaining **PNA6K** with an increased positive net charge. Then, **PNA6K**-coated OAds were prepared following the protocol reported in Materials and Methods. The analysis of the CD melting curve of bcl2midG4-G4 incubated with **PNA6K** in K^+-containing buffer (Figure S5) confirmed the ability of **PNA6K** to bind the bcl2midG4-G4, as indicated by the presence of two clear melting transitions at 24 and 76 °C, the first of which corresponding to the dissociation of **PNA6K** strand from bcl2midG4-G4 and the second one to the melting of the G4. We used several OAd/**PNA6K** ratios and monitored the size and charge of the resulting complexes by using dynamic light scattering (DLS) and zeta potential measurements (Figure 6). As summarized in Figure 6 Table B, the net charge of OAd vectors raised from −32.67 ± 0.21 to +26.13 ± 5.51, respectively, for naked OAd and OAd-**PNA6K** [1:500] complexes, whereas the corresponding hydrodynamic diameter raised from 109.03 ± 1.95 to 142.47 ± 4.55 nm. These results suggest that the addition of the positively charged PNA masks the negative charge of OAds not affecting the colloidal stability, except for the 1:10 OAd/PNA ratio at which significant aggregation phenomena occurred as evidenced by the highest values of particles size (515.50 ± 34.24 nm) and polydispersion index (PDI = 0.47). Above 1:10 ratio, the positive net charge reached a plateau-like kinetics as we measured *z*-

DOI: 10.1021/acs.bioconjchem.8b00674
Bioconjugate Chem. 2019, 30, 572−582

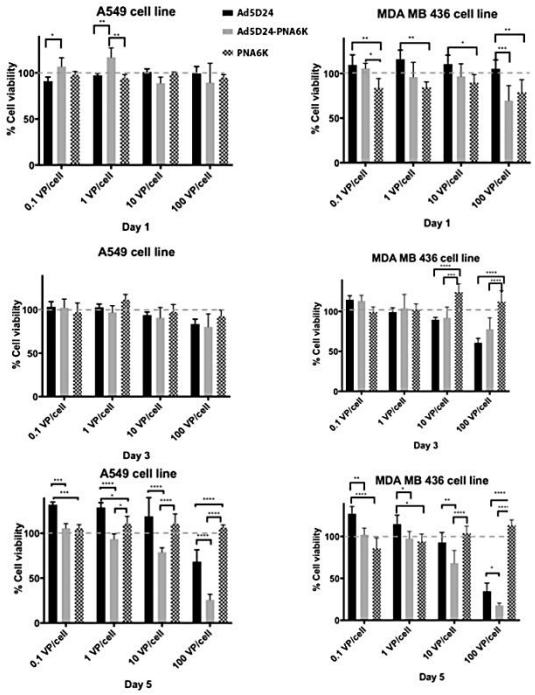

Figure 7. MTS assay on A549 and MDA-MB 436 cells after 1, 3, and 5 days of incubation with Ad5D24 or **PNA6K** alone, or with Ad5D24-**PNA6K** preparations. The cell viability is expressed as percentage with respect to the nontreated control cells. Significance was assessed using the two-way ANOVA, $^{*}P < 0.05$, $^{**}P \leq 0.01$, $^{***}P < 0.01$, $^{****}P = 0.0001$.

potentials of 19.67 ± 0.42, 23.90 ± 2.89, 27.33 ± 1.10 and 26.13 ± 5.51, respectively, for 1:10, 1:50, 1:100, and 1:500 ratios (Figure 6A). On the bases of DLS and zeta potential calculations, we selected the 1:100 OAd/PNA as the optimal ratio for the subsequent cell viability assays.

Cell Viability Studies on A549 and MDA-MB-436 Cancer Cell Lines. To assess the efficiency of the new OAd-based PNA delivery system in transporting **PNA6K** within tumor cells and inducing cell death likely by inhibition of the expression of the antiapoptotic Bcl2 protein, we determined by *in vitro* MTS assay the cell viability of A549 and MDA-MB-436 cell cultures 1, 3, and 5 days after their incubation with either the Ad5D24 OAd alone—using 0.1, 1, 10, and 100 viral particles (VP) per cell—or with the corresponding Ad5D24-**PNA6K** [1:100] preparations. At each time point and for each VP/cell preparation, we also measured the cell viability of cells incubated with PNA6K alone at concentrations corresponding to those used for the Ad5D24-**PNA6K** preparations (Figure 7). The mitochondrial activity of treated cells was compared to that of untreated control cells and the cell viability was expressed as percentage relative to untreated control cells (Figure 7). As anticipated, we did not observe any significant reduction in the cell viability of cells treated with PNA6K alone, even after 5 days from the treatment at the highest concentration for both the tested cell lines. As far as the cells treated with the OAd alone, no significant oncolytic effect was evidenced up to day 3, except for 100 VP/cell preparations for which an 84% and 61% reduction in cell viability was observed, respectively, for A549 and MD-MB-436 cell lines. Up to day 3, in all cases we did not observe any enhancement in the oncolytic activity of Ad5D24-**PNA6K** preparations relative to Ad5D24 preparations alone. Vice versa, the MTS assays performed at day 5 evidenced a striking enhancement in the oncolytic effect of Ad5D24-**PNA6K** preparations relative to the OAd alone at all VP/cell ratios and on both cell lines. The enhancement in the cell killing effect was more evident on A549 cells, which proved more resistant against the oncolytic activity of Ad5D24. The viability of A549 and MDA-MB-436

DOI: 10.1021/acs.bioconjchem.8b00674
Bioconjugate Chem. 2019, 30, 572−582

cells incubated with Ad5D24-**PNA6K** at 100 VP/cell recorded at day 5 was 26% and 18%, respectively. The cell viability at day 5 of the same cells treated with the PNA-uncoated Ad5D24 at 100 VP/cell raised to 68% and 35%, respectively.

Western Blot Analyses. To further confirm that the lower cell viability observed at day 5 for cells treated with the Ad5D24-**PNA6K** preparations compared to cells treated with naked Ad5D24 viruses was actually due to the specific downregulation of the Bcl-2 protein, we performed Western blot analyses (Figure S6). A549 and MDA-MB-436 cells were incubated with Ad5D24 viruses alone, **PNA6K** alone or with Ad5D24/**PNA6K** preparations, and the expression of the Bcl-2 protein was evaluated at day 5 from the incubation as described in the Materials and Methods. The Western blot analyses confirmed that **PNA6K** is actually able to downregulate the expression of the Bcl-2 protein in both tested cell lines, and that its conjugation with the Ad5D24 oncolytic adenovirus greatly enhances the downregulation of the target gene. Using the ImageJ software tool, we estimated that the incubation of MDA-MB-436 cells with the naked virus or with **PNA6K** alone reduced the expression of the Bcl-2 protein by 23.7% or 21.4%, respectively, compared to the nontreated control cells. More interestingly, when the same cells were treated with the Ad5D24-**PNA6K** preparation, the expression of the Bcl-2 protein drastically fell to 55.9% (see the chart in Figure S6). Unfortunately, we could not obtain the corresponding data for the Western blot analysis of A549 cells because the image processing gave unreliable results.

■ DISCUSSION

In previous papers, our and other research groups demonstrated that tailored short PNA sequences can be successfully used to downregulate the expression of specific proto-oncogenes by either directly targeting complementary DNA sequences in their promoters[43−45] or, indirectly, by targeting RNA sequences involved in proto-oncogenes regulation (e.g., mRNAs, miRNAs).[15,16,46,47] However, the translation from proof-of-concept studies toward the development of druggable PNA molecules has been so far limited by the poor capacity of PNAs to cross the plasma membranes of target cells. The main aim of this paper was to assess whether the ability of OAds to specifically recognize and infect cancer cells could be exploited to move into the infected cells short PNA sequences designed to downregulate the expression of the antiapoptotic Bcl-2 protein, thus exerting synergistic antitumor activity on cancer cell lines expressing high level of the Bcl-2 gene product.

In 2006, L. H. Hurley et al. demonstrated that the 39-mer G-rich DNA region localized −58 to −19 bp upstream the translation start site (TSS) of the Bcl-2 P1 promoter (named Pu39WT) is able to form at least three different intramolecular G4s in vitro, the most stable of which is characterized by a 3 + 1 hybrid parallel/antiparallel topology comprising three G-tetrads connected by loops of one, seven, and three bases.[24,48] The unusual length of the seven bases long second loop and its projection outside the G4 core (see Figure 8 in ref 23) triggered our decision to synthesize the complementary 7-mer **PNAK** molecule (Table 1) with the aim of inducing the formation of a bcl2midG4-G4/**PNAK** complex, stable in physiological buffer and temperature, which, being not recognized by DNA helicases, in turn inhibits the binding of transcriptional factors on the Bcl-2 promoter. Before assessing the *in vitro* trafficking efficiency of the OAd-PNA complexes in A549 and MDA-MB 436 cell lines, we assessed by CD, PAGE, and HPLC-SEC studies the ability of **PNAK** to bind the bcl2midG4-G4. Furthermore, to assess the binding selectivity of **PNAK** toward bcl2midG4-G4 vs bcl2midG4-ds, we performed the same chemical-physical analysis also for the interaction of **PNAK** with the bcl2midG4-ds. The formation of a bcl2midG4-G4/**PNAK** complex was confirmed by all three analytical techniques. In fact, following the addition of 5 equiv of **PNAK** to the prefolded bcl2midG4-G4 we observed: (i) the disappearance of the hump at 293 nm together with a 2 nm red-shift of the remaining CD bands (positive at 265 nm and negative at 252 nm) (Figure 2A); (ii) the appearance of a new intense slower band in the PAGE run of the same sample (see the comparison of lanes 3 and 4 in Figure 4); (iii) the comparison of a new, less retained peak (Rt = 11.13 min) in the HPLC-SEC profile (Figure 5). Conversely, we did not observe any significant variation in the corresponding CD, PAGE, and HPLC-SEC analyses when the same amount of **PNAK** was added to the bcl2midG4 duplex (Figure 2B, Figure 4 lanes 5 and 6, Figure S2 and S3, respectively). Although the synthesized PNA probe was designed to selectively bind the second lateral loop of the monomeric 3 + 1 G4 depicted in Figure 1, both PAGE and HPLC-SEC data suggested the formation of higher molecular weight complexes, the main one involving a G4 dimer of the bcl2midG4-G4. Besides the stoichiometry of bcl2midG4-G4/**PNAK** complexes, the comparison of the CD spectra recorded at increasing temperatures indicated that (i) **PNAK** is able to bind the G4s formed by the **G-rich bcl2midG4** sequence without disrupting their G4 scaffold, and (ii) the thermal expulsion of the PNA strand occurs at temperatures higher than the physiological body temperature (within 40−50 °C; see CD curves in Figure S1), thus supporting our hypothesis about the development of novel anti-Bcl-2 anticancer agents based on the G4-binding 7-mer ccttcct PNA sequence. To maximize the electrostatic interactions of the PNA cargo with the OAd vectors and improving the coating yield of the OAd-PNA delivery system, we prolonged the C-terminal lysine tail of **PNAK** from one to six lysines, thus obtaining the PNA probe **PNA6K** that was used for the drug delivery *in vitro* studies. We used DLS and *z*-potential measurements to find the OAd:PNA ratio which allowed the maximal OAds coating without inducing significant aggregation phenomena. As reported earlier, both particles size and *z*-values reached a plateau at the Ad5D24:**PNA6K** ratio of 1:100 (Figure 6A), which was then selected for the *in vitro* cell viability studies. The viability of human A549 and MDA-MB 436 cell lines incubated with Ad5D24, Ad5D24-**PNA6K**, or **PNA6K** was assessed by MTS assay after 1, 3, and 5 days from the treatment. Five different VP/cell ratios (0, 0.1, 1, 10, and 100) were used for both cells at each time point. The results summarized in Figure 7 clearly evidenced that no significant cytotoxic effect was noticed at day 3 from the incubation for both cell lines at all treatments, with the exception of MDA-MB 436 cells treated with Ad5D24 alone at 100 VP/cell. This behavior was not surprising considering that OAds require at least 3 days to enter, replicate, and lyse the infected cells[49,50] and that the purported bioactivity of **PNA6K** requires the downregulation of the expression of the antiapoptotic Bcl-2 protein. Very different and encouraging results were instead obtained from the MTS assays performed 5 days after the treatments. At day 5 the cell viability of cells treated with Ad5D24-**PNA6K** was significantly lower than that of cells treated with naked Ad5D24 at all tested VP/cell treatments, and cell viability values lower than those

DOI: 10.1021/acs.bioconjchem.8b00674
Bioconjugate Chem. 2019, 30, 572−582

obtained for the untreated control cells were observed for both cell lines at 10 and 100 VP/cell. Finally, Western blot analyses performed on both cell lines at day 5 from the treatments demonstrated that the enhancement of the anticancer activity showed by the Ad5D24-**PNA6K** complex, compared to the cytotoxic activity of the oncolytic virus alone, was actually due to the downregulation of the Bcl-2 oncogene. Overall, the combined synergistic toxic effect of the Ad5D24-**PNA6K** complex was higher on MDA-MB 436 than on A549 cells, but the relative enhancement of the cytotoxic activity due to conjugation of the OAd with **PNA6K** was higher on the A549 cell line than on MDA-MB 436. The latter observation is noteworthy considering the higher resistance of A549 cells toward the oncolytic activity of Ad5D24. Finally, it is important to remark that the cell viability of cells treated with **PNA6K** alone was always very similar to that of untreated control cells, even at the latest time point and at the highest **PNA6K** concentration, thus confirming that **PNA6K** requires an efficient delivery platform to efficiently cross the cellular membranes.

■ CONCLUSIONS

In this work we have proposed for the first time the use of oncolytic adenoviruses as an innovative drug delivery platform for PNAs targeting the promoters of human proto-oncogenes. The electrostatic conjugation of positively charged PNAs to the negatively charged capsid of oncolytic adenoviruses allows the selective delivery of PNAs in cancer cells, not affecting healthy tissues which do not overexpress the CAR receptor recognized by the OAds.[51,52] In particular, by using CD, PAGE, and HPLC-SEC techniques we demonstrated that **PNAK** selectively binds the G4 formed by the **G-rich bcl2midG4** DNA sequence, whereas it does not interact with the corresponding duplex. Next, using DLS and ζ-potential measurements we demonstrated that the **PNA6K** analogue, characterized by the presence of a longer six-lysine tail, binds the negatively charged capsid of Ad5D24 OAd forming the Ad5D24-**PNA6K** delivery system. MTS assay readings performed 5 days after the exposure of human breast A546 and lung MD-MBA 436 cancer cell lines to the 1:100 Ad5D24-**PNA6K** system confirmed the delivery of the PNA cargo in the infected cells and the onset of a synergistic cytotoxic effect due the oncolytic activity of the virus and to the downregulation of the antiapoptotic Bcl-2 gene, which in turn was confirmed by Western blot analyses. We believe that the approach reported here could open the way to the development of site-specific and safer chemotherapy because of reduced toxicity to healthy tissues and organs.

■ MATERIALS AND METHODS

DNA Synthesis and Analysis. The ON sequence bcl2midG4 and its complementary C-rich sequence (Table 1) were synthesized by solid phase β-cyanoethyl phosphoramidite chemistry using a Perseptive Biosystem Expedite 8909 automated DNA synthesizer. The syntheses were performed on a CPG Universal Support (35 mg, 1.4 μmol) using 1 μmol scale standard protocol, with the DMT-OFF option. After the syntheses, the oligomers were detached from the support and deprotected by treatment with concentrated aqueous ammonia at 55 °C for 12 h. The combined filtrates and washings were concentrated under reduced pressure, redissolved in H_2O, and analyzed and purified by HPLC on a Nucleogen anion exchange column (Macherey-Nagel, 1000−8/46) using buffer A, 20 mM NaH_2PO_4 aqueous solution, pH 7.0, containing 20% (v/v) CH_3CN; buffer B, 1 M NaCl, 20 mM NaH_2PO_4 aqueous solution, pH 7.0, containing 20% (v/v) CH_3CN. A linear gradient from 0% to 100% B in 30 min and the flow rate of 1.2 mL/min were used. The ONs were collected and successively desalted by Sep-Pak cartridges (C18). The isolated ONs resulted to be >99% pure (NMR). The ON concentration was determined spectrophotometrically at λ = 260 nm and 90 °C, using the molar extinction coefficient ε = 231.3 for **G-rich bcl2midG4** and ε = 175.4 cm^{-1} mM^{-1} for **C-rich bcl2midG4**, as determined using the Sigma-Aldrich OligoEvaluator web tool (www.oligoevaluator.com).

PNA Synthesis and Analysis. **PNAK** and **PNA6K** (Table 1) were synthesized using the 9-fluorenylmethoxycarbonyl (Fmoc) solid-phase strategy. Briefly, 50 mg of 4-methylbenzhydrylamine (MBHA) resin (0.5 mmol/g), after swelling in CH_2Cl_2 for 30 min and dimethylformamide (DMF) washings, was treated with a solution of 20% piperidine in DMF for 10 min. After washings in DMF (5×), one or six couplings with Fmoc-L-Lys(MMt)-OH (MMT = monomethoxytrityl) for **PNAK** and **PNA6K** were performed, respectively, using the following conditions: 5 equiv Fmoc-Lys monomer in *N*-methyl-2-pyrrolidone (NMP) 0.2 M, 5 equiv 3-oxid hexafluorophosphate (HATU) in DMF 0.2 M; 5 equiv *N*,*N*-diisopropylethylamine (DIPEA)/7.5 equiv lutidine for 40 min at room temperature (RT). PNA monomers were then reacted using the following conditions: 10 equiv monomer building block in NMP 0.2 M, 10 equiv HATU in DMF 0.2 M and 10 equiv DIPEA/15 equiv lutidine, 40 min at RT. After each coupling step, the capping with Ac_2O in the presence of pyridine was performed for 20 min at RT and the Fmoc group was removed by two treatments with a 5% 1,8-diazabicyclo[5,4,0]undec-7-ene (DBU) in DMF solution (5 min). At the end of the synthetic cycle, the PNAs were cleaved from the solid support by treatment with trifluoroacetic acid (TFA)/anisole/ethanedithiol (9:1:1; v/v/v) for 4 h and the products were precipitated with cold diethyl ether. The precipitates were recovered by centrifugation, washed twice with diethyl ether, dissolved in water, and finally lyophilized. The PNAs were obtained with a 48−50% overall yield (95% medium yield for each coupling estimated by Fmoc spectrophotometric measurements). The crude samples were purified by semipreparative HPLC analyses and purifications were carried out on a Jasco (Easton, MD, USA) PU-2089 Plus pump equipped with a Jasco UV-2075 Plus UV detector using a 10 × 250 mm C-18 reverse-phase column (particle size 5 μm) eluted with a linear gradient of CH_3CN containing 0.1% (v/v) trifluoroacetic acid (TFA) in H_2O containing 0.1% (v/v) TFA (from 0% to 100% in 45 min, flow 1.2 mL/min). The collected fractions were lyophilized. The amount of each PNA sample dissolved in pure water was estimated by quantitative UV with a Jasco V-530 spectrophotometer (λ = 220−310 nm, 400 nm/min scanning speed, 2.0 nm bandwidth) using the following molar extinction coefficients ε = 52.8 cm^{-1} mM^{-1} for both **PNAK** and **PNA6K**. The final pure products were characterized by ESI-MS. **PNAK**: ESI-MS (m/z) calcd. for $[M + H]^+$ 1948.84, found 1948.8; calcd. for $[M + 2H]^{2+}$ 974.93, found 975.0; calcd. for $[M + 3H]^{3+}$ 650.29, found 650.3 (Figure S7). **PNA6K**: ESI-MS (m/z) calcd. for $[M + 2H]^{2+}$ 1295.16, found 1295.1; calcd. for $[M + 3H]^{+3}$ 863.78, found 863.7 (Figure S8).

DOI: 10.1021/acs.bioconjchem.8b00674
Bioconjugate Chem. 2019, 30, 572−582

Preparation of bcl2midG4 Duplex, Quadruplex, and Their Incubation with PNAK. All DNA samples were prepared at 20 μM concentration in 60 mM potassium buffer obtained by diluting the 1 M buffered solution (100 mM KH_2PO_4, 900 mM KCl, pH = 7.0). For bcl2midG4-G4 preparation, 10 nmol of **G-rich bcl2midG4** were lyophilized and dissolved in 0.5 mL of 60 mM potassium buffer to achieve the 20 μM concentration. For bcl2midG4-ds preparation, a solution of **C-rich bcl2midG4** at 1 mM concentration in 60 mM potassium buffer was used. The bcl2midG4-ds was obtained by dissolving 10 nmol of lyophilized **G-rich bcl2midG4** with 10 μL of the 1 mM **C-rich bcl2midG4** stock solution. The resulting solution was finally diluted to 0.5 mL with the 60 mM potassium buffer. The solutions containing either the bcl2midG4-G4 or bcl2midG4-ds were heated at 90 °C for 5 min, then slowly cooled to RT over 12 h (annealing procedure) and equilibrated at 4 °C for at least 4 h before **PNAK** addition at 1:5 DNA/PNA ratio. Mixtures were incubated at 4 °C for 24 h before data acquisition.

Circular Dichroism (CD). CD spectra were recorded on a Jasco 1500 spectropolarimeter equipped with a Jasco PTC-348-WI temperature controller in the 200−320 nm range at 5, 50, and 90 °C, using 0.1 cm path-length cuvette in 60 mM potassium buffer at the concentration of 20 μM. All CD spectra were averaged over 5 scans, which were recorded at 200 nm min^{-1} scan rate, 4 s response time, 2 nm bandwidth. The buffer baseline was subtracted from each spectrum and the spectra were normalized to have zero ellipticity at 360 nm. Thermal denaturation experiments were also carried out in the temperature range 5−90 °C by monitoring the CD values at 263 nm for bcl2midG4-G4, 265 nm for bcl2midG4-G4/**PNAK** and bcl2midG4-G4/**PNA6K**, 265 nm for bcl2midG4-ds, and 266 nm for bcl2midG4-ds/**PNAK** at a heating rate of 0.5 C°/min.

Nondenaturing Polyacrylamide Gel Electrophoresis (PAGE). Nondenaturing gel electrophoreses were performed using 18% polyacrylamide gels, which were run in 1 × Tris-Borate-EDTA (TBE) buffer supplemented with 30 mM KCl, pH 7.0 for 1 h at 4 °C. All samples were loaded at 20 μM ON concentration. Two microliters of each sample were added to 8 μL of loading buffer (glycerol/1 × TBE + 30 mM KCl 1:9) before gel loading. Electrophoresis was performed at constant voltage of 120 V at a temperature close to 5 °C. The gels were stained with Sybr green (Sigma-Aldrich) and visualized using the Bio-Rad Laboratories Gel Doc XR apparatus.

HPLC-Size Exclusion Chromatography (SEC) Analyses. HPLC-SEC analyses were performed using a ReproSil 2000 SEC column operating in the MW range of 2,000−70,000 Da (Dr. Maisch GmbH, 300 × 8 mm, 5 μm) eluted with 60 mM potassium buffer, flow rate 0.6 mL min^{-1}, detector at 260 nm. The analyses were performed at RT using a Jasco PU-2089 Plus quaternary gradient pump equipped with a Jasco UV-2075 Plus UV/vis detector.

OAds Preparation and Complexation with PNA6K. Ad5D24 OAds were generated, propagated, and characterized using standard protocols.[53] OAd-**PNA6K** complexes were prepared by mixing Ad5D24 OAds and **PNA6K** at 1:10, 1:50, 1:100, and 1:500 ratios as per the following protocol: (i) for each microliter of viral preparation used, the corresponding number of microliters of protein was calculated; (ii) for each microgram of viral protein, 10, 50, 100, or 500 μg of **PNA6K** was added adjusting the volume to 100 μL with sterile Milli-Q water (purchased by VWR); (iii) after vortexing, the mixtures were incubated at RT for 15 min; and (iv) vortexed again just before being used. New OAd-**PNA6K** complexes were prepared before each experiment using fresh reagents.

Zeta Potential and Dynamic Light Scattering (DLS) Analysis. OAd-**PNA6K** complexes were vortexed and diluted to a final volume of 700 mL with sterile Milli-Q water adjusted to pH 7.4 before being transferred to a polystyrene disposable cuvette for DLS analysis. Afterward, the samples were recovered from the cuvette and transferred to a DTS1070 disposable capillary cell (Malvern, Worcestershire, UK) for zeta potential measurements, which were performed at 25 °C using a Malvern Zetasizer Nano ZS system.

Cell Culture and Viability Assay. Human lung carcinoma cell line A549 and human breast cancer cell line MDA-MB-436 were purchased from the American Type Culture Collection (ATCC; Manassas, VA, USA). Both cell lines were grown in adhesion in Dulbecco's modified Eagle's medium (DMEM, Gibco). The medium was supplemented with 10% heat-inactivated fetal bovine serum FBS (Gibco), penicillin (50 U mL^{-1}), streptomycin (500 μg mL^{-1}), and glutamine (4 mmol L^{-1}) in a humidified atmosphere of 95% air and 5% CO_2 at 37 °C. Adherent cells were seeded in 96-multiwell plates at a density of 5 × 10^3 cells/well. The 1:100 ratio (w/w) of OAd-**PNA6K** was chosen to assess the cell viability. After 24 h from the seeding, cells were treated with 50 μL of 0.1, 1, 10, and 100 VP/cell in cell culture medium for 1, 3, and 5 days, and then the MTS assay was performed according to the manufacturer's protocol (CellTiter 96 AQueous One Solution Cell Proliferation Assay; Promega, Nacka, Sweden). Spectrophotometric data were acquired with a Varioskan Flash Multimode Reader (Thermo Scientific, Carlsbad, CA, USA). The cytotoxicity was evaluated as the percentage of treated cell viability compared to untreated cells. Experiments were run in quadruplicate.

Western Blot Analyses. MDA-MB436 and A549 cells were incubated with Ad5D24, **PNA6K**, and Ad5D24-**PNA6K** for 5 days at 1:100 Ad5D24/**PNA6K** ratio and at the concentration of 100 VP/cell. The extracts of the treated cells were isolated by using RIPA Buffer (SIGMA) supplemented with protease inhibitors (Thermo Fisher Scientific). The concentration of the isolated proteins was determined by using Bradford Protein Assay Reagent (BioRad). 25 μg of the protein were separated on 4−20% Mini PROTEAN TGX Precast Gels (BioRad) and transferred to PVDF membranes (BioRad). Membranes where then incubated with the primary antibodies against Bcl-2 (Abcam) or β-actin (Santa-Cruz) and the appropriate secondary antibodies. The Bcl-2 protein (26 kDa) was analyzed and β-actin (43 kDa) was used as loading marker. The ImageJ[54] tool was used to measure the mean gray value of the bands. Mean gray value of each sample was normalized with the corresponding actin control. Finally, each result was normalized with the nontreated control. Percentages of normalized mean gray values were plotted on graph.

Statistical Analyses and Correlation Models. The statistical analysis was performed using the GraphPad Prism 6 software (GraphPad Software, Inc., La Jolla, CA, USA). Data were expressed as mean ± standard deviation (SD). Results repeats were compared by a two-way analysis of variance (ANOVA), and a P-value <0.05 was considered statistically significant.

DOI: 10.1021/acs.bioconjchem.8b00674
Bioconjugate Chem. 2019, 30, 572−582

■ ASSOCIATED CONTENT

Supporting Information

The Supporting Information is available free of charge on the ACS Publications website at DOI: 10.1021/acs.bioconjchem.8b00674.

Additional CD spectra recorded at 5−90 °C of the bcl2midG4-G4 and bcl2midG4-ds alone or incubated with **PNAK**; HPLC-SEC profiles of bcl2midG4-ds alone or incubated with **PNAK**; MTS assays of control cells treated with **PNAK** alone; mass spectra of **PNAK** and **PNA6K**; CD melting curve of bcl2midG4-G4 incubated with **PNA6K**; Western blot analyses on treated and untreated A549 and MDA-MB-436 cells (PDF)

■ AUTHOR INFORMATION

Corresponding Author

*E-mail: golivier@unina.it. Phone +39-081-679896.

ORCID

Giorgia Oliviero: 0000-0003-0765-2127

Nicola Borbone: 0000-0003-0216-9814

Notes

The authors declare no competing financial interest.

■ ACKNOWLEDGMENTS

This work is supported with FOE funds to SYSBIO Italian Centre of Systems Biology, from the Italian Ministry of Education, Universities and Research (MIUR, http://www.istruzione.it − within the Italian Roadmap for ESFRI Research Infrastructures), and with POR funds (project onc3-003145) by Regione Campania (DG 10 staff 93 no. 354, 05/06/2017). The authors are grateful to Dr. Cristian Capasso for technical advice and to Dr. Luisa Cuorvo for graphical editing.

■ REFERENCES

(1) Tsujimoto, Y., and Croce, C. M. (1986) Analysis of the structure, transcripts, and protein products of Bcl-2, the gene involved in human follicular lymphoma. *Proc. Natl. Acad. Sci. U. S. A. 83*, 5214−5218.

(2) Marschitz, I., Tinhofer, I., Hittmair, A., Egle, A., Kos, M., and Greil, R. (2000) Analysis of Bcl-2 protein expression in chronic lymphocytic leukemia. A comparison of three semiquantitation techniques. *Am. J. Clin. Pathol. 113*, 219−229.

(3) McDonnell, T. J., Hsieh, J. T., and Campbell, M. L. (1992) Expression of the protooncogene Bcl-2 in the prostate and its association with emergence of androgen-independent prostate cancer. *Cancer Res. 52*, 6940−6944.

(4) Miyashita, T., and Reed, J. C. (1992) Lymphoid cells to cell death and DNA fragmentation induced by glucocorticoids and multiple chemotherapeutic drugs. *Cancer Res. 52*, 5407−5454.

(5) Degterev, A., Lugovskoy, A., Cardone, M., Mulley, B., Wagner, G., Mitchison, T., and Yuan, J. (2001) Identification of small-molecule inhibitors of interaction between the BH3 domain and Bcl-xL. *Nat. Cell Biol. 3*, 173−182.

(6) Badros, A. Z., Goloubeva, O., Rapoport, A. P., Ratterree, B., Gahres, N., Meisenberg, B., Takebe, N., Heyman, M., Zwiebel, J., Streicher, H., et al. (2005) Phase II study of G3139, a Bcl-2 antisense oligonucleotide, in combination with dexamethasone and thalidomide in relapsed multiple myeloma patients. *J. Clin. Oncol. 23*, 4089−4099.

(7) del Toro, M., Bucek, P., Aviñó, A., Jaumot, J., González, C., Eritja, R., and Gargallo, R. (2009) Targeting the G-quadruplex-forming region near the P1 promoter in the human Bcl-2 gene with the cationic porphyrin TMPyP4 and with the complementary C-rich strand. *Biochimie 91*, 894−902.

(8) Sengupta, P., Chattopadhyay, S., and Chatterjee, S. (2017) G-quadruplex surveillance in Bcl-2 gene: a promising therapeutic intervention in cancer treatment. *Drug Discovery Today 22*, 1165−1186.

(9) Sharma, C., and Kumar, S. (2017) Versatility of peptide nucleic acids (PNAs): role in chemical biology, drug discovery and origins of life. *Chem. Biol. Drug Des. 89*, 16−37.

(10) de Koning, M. C., van der Marel, G. A., and Overhand, M. (2003) Synthetic developments towards PNA−peptide conjugates. *Curr. Opin. Chem. Biol. 7*, 734−740.

(11) Gupta, A., Mishra, A., and Puri, N. (2017) Peptide nucleic acids: advanced tools for biomedical applications. *J. Biotechnol. 259*, 148−159.

(12) Amato, J., Pagano, B., Borbone, N., Oliviero, G., Gabelica, V., De Pauw, E., Derrico, S., Piccialli, V., Varra, M., Giancola, C., et al. (2011) Targeting G-quadruplex structure in the human c-Kit promoter with Short PNA sequences. *Bioconjugate Chem. 22*, 654−663.

(13) Amato, J., Stellato, M. I., Pizzo, E., Petraccone, L., Oliviero, G., Borbone, N., Piccialli, G., Orecchia, A., Bellei, B., Castiglia, D., et al. (2013) PNA as a potential modulator of COL7A1 gene expression in dominant dystrophic epidermolysis bullosa: a physico-chemical study. *Mol. BioSyst. 9*, 3166−3174.

(14) Janson, C. G., and During, M. J. (2007) Peptide nucleic acids, morpholinos and related antisense biomolecules. *Medcal Intelligence Unit*, Springer, Boston, US.

(15) Amato, F., Tomaiuolo, R., Borbone, N., Elce, A., Amato, J., D'Errico, S., De Rosa, G., Mayol, L., Picciali, G., Oliviero, G., et al. (2014) Design, synthesis and biochemical investigation, by in vitro luciferase reporter system, of peptide nucleic acids as new inhibitors of miR-509−3p involved in the regulation of cystic fibrosis disease-gene expression. *MedChemComm 5*, 68−71.

(16) Amato, F., Tomaiuolo, R., Nici, F., Borbone, N., Elce, A., Catalanotti, B., D'Errico, S., Morgillo, C. M., De Rosa, G., Mayol, L., et al. (2014) Exploitation of a very small peptide nucleic acid as a new inhibitor of miR-509−3p involved in the regulation of cystic fibrosis disease-gene expression. *BioMed Res. Int. 2014*, 1.

(17) Davis, J. T. (2004) G-quartets 40 years later: from 5′-GMP to molecular biology and supramolecular chemistry. *Angew. Chem., Int. Ed. 43*, 668−698.

(18) Bryan, T. M., and Baumann, P. (2011) G-quadruplexes: from guanine gels to chemotherapeutics. *Mol. Biotechnol. 49*, 198−208.

(19) Nici, F., Oliviero, G., Falanga, A. P., D'Errico, S., Marzano, M., Musumeci, D., Montesarchio, D., Noppen, S., Pannecouque, C., Piccialli, G., et al. (2018) Anti-HIV activity of new higher order G-quadruplex aptamers obtained from tetra-end-linked oligonucleotides. *Org. Biomol. Chem. 16*, 2349−2355.

(20) Seto, M., Jaeger, U., Hockett, R. D., Graninger, W., Bennett, S., Goldman, P., and Korsmeyer, S. J. (1988) Alternative promoters and exons, somatic mutation and deregulation of the Bcl-2-Ig fusion gene in lymphoma. *EMBO J. 7*, 123−131.

(21) Heckman, C., Mochon, E., Arcinas, M., and Boxer, L. M. (1997) The WT1 protein is a negative regulator of the normal Bcl-2 allele in t(14;18) lymphomas. *J. Biol. Chem. 272*, 19609−19614.

(22) Gomez-Manzano, C., Mitlianga, P., Fueyo, J., Lee, H. Y., Hu, M., Spurgers, K. B., Glass, T. L., Koul, D., Liu, T. J., McDonnel, T. J., et al. (2001) Transfer of E2F-1 to human glioma cells results in transcriptional up-regulation of Bcl-2. *Cancer Res. 61*, 6693−6697.

(23) Liu, Y., Boxer, L. M., and Latchman, D. S. (1999) Activation of the Bcl-2 promoter by nerve growth factor is mediated by the P42/P44 MAPK cascade. *Nucleic Acids Res. 27*, 2086−2090.

(24) Dai, J., Chen, D., Jones, R. A., Hurley, L. H., and Yang, D. (2006) NMR solution structure of the major G-quadruplex structure formed in the human Bcl2 promoter region. *Nucleic Acids Res. 34*, 5133−5144.

(25) Koppelhus, U., and Nielsen, P. E. (2003) Cellular delivery of peptide nucleic acid (PNA). *Adv. Drug Delivery Rev. 55*, 267−280.

(26) Allen, T. M., and Cullis, P. R. (2013) Liposomal drug delivery systems: from concept to clinical applications. *Adv. Drug Delivery Rev. 65*, 36−48.
(27) Maruyama, K. (2011) Intracellular targeting delivery of liposomal drugs to solid tumors based on EPR effects. *Adv. Drug Delivery Rev. 63*, 161−169.
(28) Gillies, E. R., and Fréchet, J. M. (2005) Dendrimers and dendritic polymers in drug delivery. *Drug Discovery Today 10*, 35−43.
(29) Sharma, A. K., Gothwal, A., Kesharwani, P., Alsaab, H., Lyer, A. K., and Gupta, U. (2017) Dendrimer nanoarchitectures for cancer diagnosis and anticancer drug delivery. *Drug Discovery Today 22*, 314−326.
(30) Doane, T. L., and Burda, C. (2012) The unique role of nanoparticles in nanomedicine: imaging, drug delivery and therapy. *Chem. Soc. Rev. 41*, 2885−2911.
(31) Falanga, A., Melone, P., Cagliani, R., Borbone, N., D'Errico, S., Piccialli, G., Netti, P., and Guarnieri, D. (2018) Design, synthesis and characterization of novel co-polymers decorated with peptides for the selective nanoparticle transport across the cerebral endothelium. *Molecules 23*, 1655.
(32) Fotticchia, I., Guarnieri, D., Fotticchia, T., Falanga, A. P., Vecchione, R., Giancola, C., and Netti, P. A. (2016) Energetics of ligand-receptor binding affinity on endothelial cells: an in vitro model. *Colloids Surf., B 144*, 250−256.
(33) Guarnieri, D., Biondi, M., Yu, H., Belli, V., Falanga, A. P., Cantisani, M., Galdiero, S., and Netti, P. A. (2015) Tumor-activated prodrug (TAP)-conjugated nanoparticles with cleavable domains for safe doxorubicin delivery. *Biotechnol. Bioeng. 112*, 601−611.
(34) Capasso, C., Hirvinen, M., Garofalo, M., Romaniuk, D., Kuryk, L., Sarvela, T., Vitale, A., Antopolsky, M., Magarkar, A., Viitala, T., et al. (2016) Oncolytic adenoviruses coated with MHC-I tumor epitopes increase the antitumor immunity and efficacy against melanoma. *Oncoimmunology 5*, 1−11.
(35) Capasso, C., Garofalo, M., Hirvinen, M., and Cerullo, V. (2014) The evolution of adenoviral vectors through genetic and chemical surface modifications. *Viruses 6*, 832−855.
(36) Haldar, S., Negrini, M., Monne, M., Sabbioni, S., and Croce, C. M. (1994) Down-regulation of Bcl-2 by P53 in breast cancer cells. *Cancer 54*, 2095−2098.
(37) Xiong, S., Zheng, Y., Jiang, P., Liu, R., Liu, X., and Chu, Y. (2011) MicroRNA-7 inhibits the growth of human non-small cell lung cancer A549 cells through targeting BcL-2. *Int. J. Biol. Sci. 7*, 805−814.
(38) Lin, C. T., Tseng, T. Y., Wang, Z. F., and Chang, T. C. (2011) Structural conversion of intramolecular and intermolecular G-quadruplexes of bcl2mid: the effect of potassium concentration and ion exchange. *J. Phys. Chem. B 115*, 2360−2370.
(39) Bugaut, A., and Balasubramanian, S. (2008) A sequence-independent study of the influence of short loop lengths on the stability and topology of intramolecular DNA G-quadraplexes. *Biochemistry 47*, 689−697.
(40) Lam, E. Y. N., Beraldi, D., Tannahill, D., and Balasubramanian, S. (2013) G-quadruplex structures are stable and detectable in human genomic DNA. *Nat. Commun. 4*, 1796−1798.
(41) Borbone, N., Amato, J., Oliviero, G., D'Atri, V., Gabelica, V., De Pauw, E., Piccialli, G., and Mayol, L. (2011) d(CGGTGGT) forms an octameric parallel G-quadruplex via stacking of unusual G(:C):G(:C):G(:C):G(:C) octads. *Nucleic Acids Res. 39*, 7848−7857.
(42) Cerullo, V., Diaconu, I., Romano, V., Hirvinen, M., Ugolini, M., Escutenaire, S., Holm, S. L., Kipar, A., Kanerva, A., and Hemminki, A. (2012) An Oncolytic Adenovirus Enhanced for Toll-like Receptor 9 Stimulation Increases Antitumor Immune Responses and Tumor Clearance. *Mol. Ther. 20*, 2076−2086.
(43) Fasbender, A., Zabner, J., Chillón, M., Moninger, T. O., Puga, A. P., Davidson, B. L., and Welsh, M. J. (1997) Complexes of adenovirus with polycationic polymers and cationic lipids increase the efficiency of gene transfer in vitro and in vivo. *J. Biol. Chem. 272*, 6479−6489.
(44) Onyshchenko, M. I., Gaynutdinov, T. I., Englund, E. A., Appella, D. H., Neumann, R. D., and Panyutin, I. G. (2009) Stabilization of G-quadruplex in the Bcl2 promoter region in double-stranded DNA by invading short PNAs. *Nucleic Acids Res. 37*, 7570−7580.
(45) Cogoi, S., Codognotto, A., Rapozzi, V., Meeuwenoord, N., van der Marel, G., and Xodo, L. E. (2005) Transcription inhibition of oncogenic KRAS by a mutation-selective peptide nucleic acid conjugated to the PKKKRKV nuclear localization signal peptide. *Biochemistry 44*, 10510−10519.
(46) Zarrilli, F., Amato, F., Morgillo, C. M., Pinto, B., Santarpia, G., Borbone, N., D'Errico, S., Catalanotti, B., Piccialli, G., Castaldo, G., et al. (2017) Peptide nucleic acids as miRNA target protectors for the treatment of cystic fibrosis. *Molecules 22*, 1144.
(47) Cheng, C. J., Bahal, R., Babar, I. A., Pincus, Z., Barrera, F., Liu, C., Svoronos, A., Braddock, D. T., Glazer, P. M., Engelman, D. M., et al. (2015) MicroRNA silencing for cancer therapy targeted to the tumour microenvironment. *Nature 518*, 107−110.
(48) Dexheimer, T. S., Sun, D., and Hurley, L. H. (2006) Deconvoluting the structural and drug-recognition complexity of the G-quadruplex-forming region upstream of the Bcl-2 P1 promoter. *J. Am. Chem. Soc. 128*, 5404−5415.
(49) Heise, C., Hermiston, T., Johnson, L., Brooks, G., Sampson-Johannes, A., Williams, A., Hawkins, L., and Kirn, D. (2000) An adenovirus E1A mutant that demonstrates potent and selective systemic anti-tumoral efficacy. *Nat. Med. 6*, 1134−1139.
(50) Bischoff, J. R., Kirn, D. H., Williams, A., Heise, C., Horn, S., Muna, M., Ng, L., Nye, J. A., Sampson-Johannes, A., Fattaey, A., et al. (1996) An adenovirus mutant that replicates selectively in P53-deficient human tumor cells. *Science 274*, 373−376.
(51) Ribas, A., Dummer, R., Puzanov, I., van der Walde, A., Andtbacka, R. H. I., Michielin, O., Olszanski, A. J., Malvehy, J., Cebon, J., Fernandez, E., et al. (2017) Oncolytic virotherapy promotes intratumoral T cell infiltration and improves anti-PD-1 immunotherapy. *Cell 170*, 1109−1119.
(52) Kit, D. (2018) Anti-cancer viruses take off universe's coolest lab set to open up quantum world. *Nature 557*, 151−152.
(53) Challberg, M. D., and Kelly, T. J. (1979) Adenovirus DNA replication in vitro. *Proc. Natl. Acad. Sci. U. S. A. 76*, 655−659.
(54) Schneider, C. A., Rasband, W. S., and Eliceiri, K. W. (2012) NIH Image to ImageJ: 25 years of image analysis. *Nat. Methods 9*, 671−675.

DOI: 10.1021/acs.bioconjchem.8b00674
Bioconjugate Chem. 2019, 30, 572−582

molecules

MDPI

Article

New G-Quadruplex-Forming Oligodeoxynucleotides Incorporating a Bifunctional Double-Ended Linker (DEL): Effects of DEL Size and ODNs Orientation on the Topology, Stability, and Molecularity of DEL-G-Quadruplexes

Maria Marzano [1], Andrea Patrizia Falanga [1], Stefano D'Errico [1], Brunella Pinto [2], Giovanni Nicola Roviello [3], Gennaro Piccialli [1], Giorgia Oliviero [4,*] and Nicola Borbone [1]

1 Dipartimento di Farmacia, Università degli Studi di Napoli Federico II, via Domenico Montesano 49, 80131 Napoli, Italy; maria.marzano@unina.it (M.M.); andreapatrizia.falanga@unina.it (A.P.F.); stefano.derrico@unina.it (S.D.); picciall@unina.it (G.P.); nicola.borbone@unina.it (N.B.)

2 Dipartimento di Chimica, Università degli Studi di Milano, via Camillo Golgi 19, 20133 Milano, Italy; brunella.pinto87@gmail.com

3 Istituto di Biostrutture e Bioimmagini, CNR, Via Tommaso De Amicis 95, 80145 Napoli, Italy; giroviel@unina.it

4 Dipartimento di Medicina Molecolare e Biotecnologie Mediche, Università degli Studi di Napoli Federico II, via Sergio Pansini 5, 80131 Napoli, Italy

* Correspondence: golivier@unina.it; Tel.: +39-081-679896

Received: 23 January 2019; Accepted: 6 February 2019; Published: 12 February 2019

Abstract: G-quadruplexes (G4s) are unusual secondary structures of DNA occurring in guanosine-rich oligodeoxynucleotide (ODN) strands that are extensively studied for their relevance to the biological processes in which they are involved. In this study, we report the synthesis of a new kind of G4-forming molecule named double-ended-linker ODN (DEL-ODN), in which two TG_4T strands are attached to the two ends of symmetric, non-nucleotide linkers. Four DEL-ODNs differing for the incorporation of either a short or long linker and the directionality of the TG_4T strands were synthesized, and their ability to form G4 structures and/or multimeric species was investigated by PAGE, HPLC–size-exclusion chromatography (HPLC–SEC), circular dichroism (CD), and NMR studies in comparison with the previously reported monomeric tetra-ended-linker (TEL) analogues and with the corresponding tetramolecular species $(TG_4T)_4$. The structural characterization of DEL-ODNs confirmed the formation of stable, bimolecular DEL-G4s for all DEL-ODNs, as well as of additional DEL-G4 multimers with higher molecular weights, thus suggesting a way towards the obtainment of thermally stable DNA nanostructures based on reticulated DEL-G4s.

Keywords: G-quadruplexes; double-ended linkers; DEL-ODNs; TEL-ODNs; supramolecular G-quadruplexes; NMR; CD; size-exclusion chromatography

1. Introduction

Among the noncanonical secondary structures adopted by nucleic acids, the G-quadruplexes (G4s) are one of the most extensively studied. G4s occur in guanosine-rich oligonucleotides (GRO) and are characterized by the presence of two or more stacked G-tetrads, planar arrangements of four guanosines held together by a cyclic array of eight Hoogsteen's hydrogen bonds [1–3]. The π–π interaction generated among the stacked G-tetrads greatly stabilizes the G4s and the presence of cations, such as potassium or sodium, further contributes to the stability of G4 structures. Structural

studies have demonstrated that GROs can form highly polymorphic G4 scaffolds that can differ by the number of the strands (one, two, or four) and by their mutual orientation, which lead to parallel, antiparallel, or mixed assemblies [4,5]. The wide polymorphism of G4s also arises from the length and the base composition of GROs, from the glycoside conformation of the guanosines involved in each tetrad, and from the cation species used to stabilize the complex [6–8]. G4 structures are involved in several relevant biological processes, such as the expression of many protooncogenes and the maintenance of telomeres length [9–15]. Furthermore, several aptamers, including the thrombin-binding aptamer [16–20] and anti-HIV-1 aptamers [21–26], adopt a G4 scaffold in their biologically active conformation. Recently, G4s emerged as interesting self-assembling scaffolds to be used in supramolecular chemistry applications and in nanotechnology for the development of new sensing probes or new materials. In addition, the G4 scaffold possesses a greater conductivity than the DNA double helix, thus suggesting its use also in bioelectronics [27–30]. It is well documented that the duplex DNA motif can be used to build supramolecular structures of various shapes and sizes by a bottom-up process named DNA origami, which is controlled by the sequence and length of the DNA strands [31–33]. Otherwise, supramolecular structures based on G4 building blocks are essentially confined to G4 hybrid structures, such as duplex–quadruplex repetitions and the so-called G-wires. G-wires are rod-shaped G4 superstructures in which the G4 motif can reach the length of thousands of nanometres along the axis perpendicular to the G-tetrad planes [34–37]. G-wires can be formed by the cooperative assembly of slipped G-rich ODN strands (interlocked G4s) or by the multimerization of G4 building blocks held together by end-to-end π–π stacking interactions [38–43].

In light of the noteworthy chemical–physical properties of the G4s, the discovery and the characterization of new supramolecular G4 assemblies represent a very interesting challenge, and the formation of the G4 scaffold and its structuring in a linear and/or reticulated topology have to be finely controlled. In fact, the main disadvantage in the design of G4-based supramolecular assemblies is the low control over the structuring and aggregation process. For these reasons, many efforts have been devoted to the design of G4-forming oligonucleotides bearing structural modifications that could allow the obtainment of new, supramolecular assemblies in a controlled fashion and that should go beyond the simple, linear rods. For example, GROs attached to the ends of branched linkers have been described, and their propensity to form monomeric or polymeric G4 structures has been investigated [44–46]. Several studies on branched GROs, carried out by our research group and by others, have shown that the presence of a tetra-ended linker (TEL), on which the GRO chains grow up, can positively influence the stability of the resulting G4 structures [47–50]. In particular, we demonstrated that the so-called TEL-G4s are provided with higher thermal stability and more favourable kinetic and thermodynamic parameters compared to the corresponding tetramolecular counterparts. Furthermore, we demonstrated that the TEL analogues of the G4-forming, anti-HIV aptamer having the sequence $^{5'}$TGGGAG$^{3'}$ can be successfully used in place of the corresponding tetramolecular quadruplex to bind, with increased efficiency, the HIV-1 glycoprotein gp120, thus resulting in a clear enhancement of the antiviral activity of the aptamer [24–26].

Continuing our studies on branched GROs, we report here on the synthesis and structural characterization of a new class of G4-forming oligonucleotides named double-ended-linker oligodeoxynucleotides (DEL-ODNs). The structures of DEL-ODNs, in which two TG_4T strands are attached by either their 3′ end (**D1L,S**, Scheme 1) or 5′ end (**D2L,S)** to a symmetric, long (L) [51] or short (S) bifunctional linker, are shown in Scheme 1. As the oligonucleotide (ON) sequence, we chose TG_4T because it forms a stable tetramolecular G-quadruplex that has been structurally characterized in detail [52,53]. Moreover, the use of the TG_4T sequence allowed us to compare the structural properties of the here-reported DEL-G4s with those of the tetramolecular $(TG_4T)_4$ and the monomolecular TEL-$(TG_4T)_4$ (**TEL1L,S** and **TEL2L,S**, Scheme 1) corresponding G4s. The formation and properties of DEL-G4s formed by DEL-$(TG_4T)_2$ were investigated by circular dichroism (CD),

native polyacrylamide gel electrophoresis (PAGE), HPLC size-exclusion chromatography (HPLC–SEC), and ^{1}H-NMR experiments.

The results reported here demonstrate that all the synthesized DEL-$(TG_4T)_2$ fold into thermally stable, parallel quadruplexes (DEL-G4s, Figure 1), regardless of the polarity of the two ON strands and the length of the linker. Furthermore, we anticipate here that **D2L** showed a remarkable propensity to form DEL-G4 multimers with higher molecular weights, which were isolated and investigated.

2. Results and Discussion

*2.1. Synthesis and Purification of DEL-$(TG_4T)_2$ (**D1L,S** and **D2L,S**)*

For the synthesis of **D1L,S** and **D2L,S** (Scheme 1), we used the solid-phase phosphoramidite chemistry protocols previously optimized by us for the synthesis of TEL-ODNs [47–49]. The synthetic strategy uses the commercially available controlled pore glass (CPG)-sulphone-resin **1** (Scheme 1) and the phosphoramidite linkers **4** and **5** (Scheme 1), having symmetrical dimethoxytrityl (DMT)-protected ends and differing for the length of the alkyl arms to obtain the bifunctional supports **2**. Starting from **2**, **D1L,S** and **D2L,S** were obtained using 3′ or 5′ nucleotide phosphoramidite building blocks, respectively. After detachment from the solid support, the crude ON material was purified by HPLC and analyzed by analytical techniques. Support **1** was also used to obtain the tetrabranched support **3**, from which **TEL1L,S** and **TEL2L,S** were obtained following the previously reported strategy [47–49].

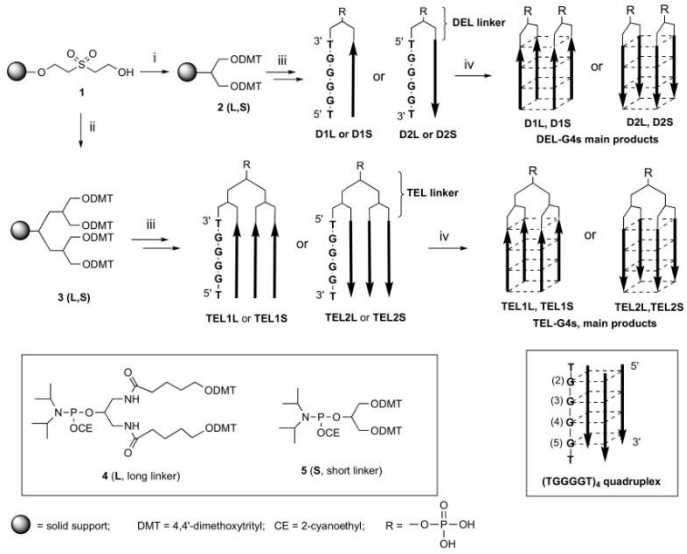

Scheme 1. General synthetic route for compounds **D1L,S**, **D2L,S** and **TEL1L,S**, **TEL2L,S**. (i) Coupling with the phosphoramidite linker **4** or **5**; (ii) two sequential couplings with the phosphoramidite linker **4** or **5**; (iii) solid-phase DNA synthesis by phosphoramidite chemistry; iv) annealing procedure in Na^+- or K^+-containing buffer.

2.2. CD and CD Thermal Analyses

CD spectroscopy is a well-established technique that provides essential information on the formation and topology of G4s. The greater part of published reports indicates that parallel G4s exhibit a maximum at around 265 nm and a minimum at around 240 nm, whereas the antiparallel ones display a maximum at around 295 nm and a minimum at around 260 nm [54–57]. All G4s analysed in this study were obtained by (i) dissolving **D1L,S** and **D2L,S** in 100 mM Na^+- or K^+-containing buffer at 1.0 mM ON concentration, (ii) heating the solutions at 95 °C for 5 min and finally (iii) by rapidly cooling them at 4 °C. All samples were stored at 4° C for 24 h before analyses. In Figure 1, we report the CD profiles recorded at 5 °C of **D1L,S** and **D2L,S** dissolved in 100 mM K^+ buffer. We observed similar profiles for the four DEL-ON species, with a well-defined positive maximum centred at 263 nm and a negative minimum centred at 240 nm. These data indicate that in K^+ buffer **D1L,S** and **D2L,S** prevalently form parallel-oriented G4 structures independently of the orientation of the ON strands and the length of the linker. This behaviour was already observed for the TEL-$(TG_4T)_4$ G-quadruplexes, which showed CD profiles almost superimposable with those reported in Figure 1 [49,50]. The CD spectra of **D1L,S** and **D2L,S** recorded at 5° in 100 mM Na^+ buffer (Supplementary Materials, Figure S1), essentially matched those obtained in K^+ buffer. Taken together, the CD data of all DEL-$(TG_4T)_2$ analogues account for the formation of parallel, bimolecular DEL-G4s, both in Na^+- and K^+-containing buffer (Figure 1). This hypothesis was also confirmed by the PAGE and HPLC–SEC analyses (see below) that confirmed the bimolecularity of the main complex formed by all DEL-G4s. Furthermore, to evaluate the influence of DEL moiety on the stability of the resulting DEL-G4s, CD thermal denaturation experiments were performed to monitor the $CD_{263\,nm}$ value in the temperature range 5–80 °C at a heating rate of 0.5 °C/min. In 100 mM K^+ buffer, all DEL-G4s were stable up to 80 °C, as indicated by the irrelevant variation of the $CD_{263\,nm}$ values up to this temperature. On the contrary, in the presence of 100 mM Na^+ buffer, the increase in temperature led to a significant reduction of the $CD_{263\,nm}$ value and reliable melting temperatures ($T_{\frac{1}{2}}$, Table 1) were calculated from the resulting sigmoidal melting curves (Figure S2). These data indicated that DEL-G4s formed by **D1L** and **D1S** have almost the same $T_{\frac{1}{2}}$ values (55 and 54 °C, respectively) as their tetramolecular counterpart $(TG_4T)_4$ (58 °C) recorded in the same conditions. On the other hand, the $T_{\frac{1}{2}}$ values of DEL-G4s formed by **D2L** and **D2S** (64 °C for both) were about 10 °C higher than those of **D1L** and **D1S**, indicating that the attachment of the DEL moiety at the 5′ end of the TG_4T strand results in DEL-G4s provided with higher thermal stability. Furthermore, the invariance of $T_{\frac{1}{2}}$ values between DEL-G4s incorporating either the long or short DEL disclosed that the length of the DEL arms does not affect the thermal stability of the resulting DEL-G4s.

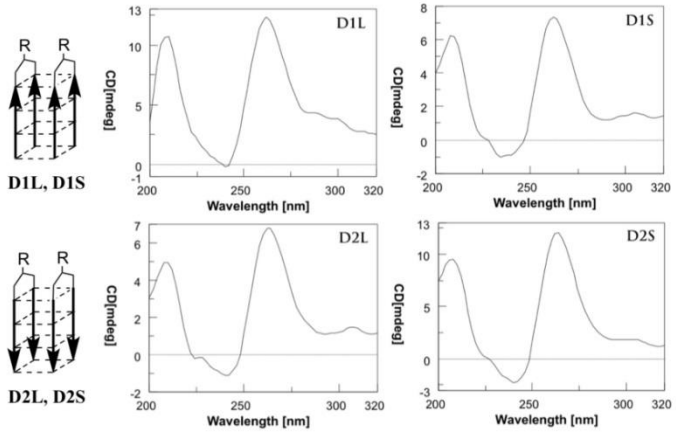

Figure 1. Circular dichroism spectra recorded at 5 °C of **D1L,S** and **D2L,S** annealed in 100 mM K^+ buffer.

Table 1. Melting temperatures ($T_{\frac{1}{2}}$ values in °C) of DEL-$(TG_4T)_2$ and TG_4T ODNs annealed in 100 mM K^+- or Na^+-containing buffer (λ = 263 nm, 0.5 °C/min heating rate).

ODN	$T_{\frac{1}{2}}$ (K^+)	$T_{\frac{1}{2}}$ (Na^+)
D1L	>80	55
D1S	>80	54
D2L	>80	64
D2S	>80	64
TG_4T	>80	58

2.3. Electrophoretic Gel Mobility Studies

To obtain information about the propensity of DEL-ODNs to fold into DEL-G4s and also on the molecularity of DEL-G4s, we performed PAGE analyses of **D1L,S** and **D2L,S**. Figure 2A displays the electrophoretic gel mobility of each complex in comparison with that of the tetramolecular G4 formed by TG_4T. All DEL-$(TG_4T)_2$ ODNs showed a very similar PAGE running behaviour, characterized by an intense, well-defined band which migrated slightly slower than the band of the $(TG_4T)_4$ G-quadruplex and by a consistent smearing phenomenon (Figure 2A). This behaviour suggests that all DEL-ODNs formed mainly the bimolecular G4 complexes depicted in Scheme 1 and that the presence of traces of higher MW complexes cannot be ruled out. The slight reduction in the mobility of the main band can be attributed to the presence of the two DEL linkers in each DEL-G4 complex. In the PAGE reported in Figure 2B, the mobility of the complexes formed by DEL-ODNs was compared to that of TEL-ODNs depicted in Scheme 1. DEL and TEL complexes produced bands having almost the same mobility and both produced excessive smearing. The smearing is considerably marked for **D1L** and **D2L** and additional slower bands are visible. Conversely, the DEL-ODNs which were built using the short linker (**D1S** and **D2S**) migrated as better-defined bands and with a reduced smearing phenomenon. Taken together, the PAGE analyses indicated that: (i) all the here-presented DEL-ODNs fold primarily into the target bimolecular parallel DEL-G4s depicted in Scheme 1; (ii) the consistent smearing observed for

all DEL and TEL complexes can be attributed to the presence of additional supramolecular structures (likely based on parallel G4 scaffolds, in agreement with CD and NMR evidence); (iii) **D1L** and **D2L** incorporating the longer linker have the highest propensity to form supramolecular G4 species.

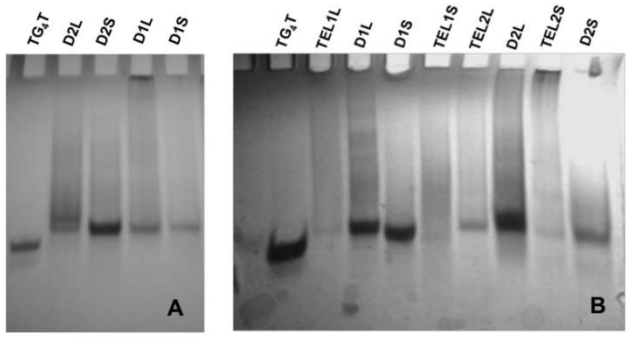

Figure 2. PAGE analyses of complexes formed by DEL-$(TG_4T)_2$ ODNs (**D1L,S** and **D2L,S**) in comparison with the $(TG_4T)_4$ G4 (**A**) and with the complexes formed by TEL-$(TG_4T)_4$ ODNs (**TEL1L,S** and **TEL2L,S**) (**B**). All samples were annealed in 100 mM K^+ buffer.

2.4. Size-Exclusion Chromatography Studies

After annealing in 100 mM K^+ buffer, DEL- and TEL-ODNs were also analysed by HPLC–SEC at room temperature (Figure 3) with the aim of further investigating the molecularity of the resulting complexes. The tetramolecular G4 formed by the TG_4T sequence (see $(TG_4T)_4$ in Scheme 1) and the G4 multimers formed by the $^{5'}CGG^{3'}$-$^{3'}TGGC^{5'}$ sequence (Q_n in Figure 3) [42] were used as size markers for monomeric (Q_1) and multimeric G4 building blocks (Q_{2-n}), respectively. The HPLC–SEC analysis of both size markers indicated that in the used column and conditions the monomeric Q_1 scaffolds (containing 24 or 28 nucleotides, respectively) had retention times (t_R) in the range 14.3–14.5 min, and the Q_n multimers had t_R lower than 13.5 min (corresponding to the Q_2 complex for the Q_n marker). The HPLC–SEC analysis of DEL-ODNs analogues confirmed that they fold primarily into a Q_1 complex (t_R centred at 14.00 min). The slightly reduced t_R observed for DEL-G4s compared to those of the Q_1 size markers can be attributed to the presence of the two DEL moieties in the Q_1-like DEL-G4 complexes. Differently from what observed by PAGE, the HPLC–SEC profiles of all but **D2L** DEL-ODNs did not show additional peaks attributable to higher MW complexes, such as DEL-G4 multimers or other polymeric species. As anticipated, only **D2L** showed an intense shoulder peak at t_R 13.68 min as well as a defined peak eluted at min 12.38, likely attributable to DEL-G4 multimers as those depicted in Figure 4.

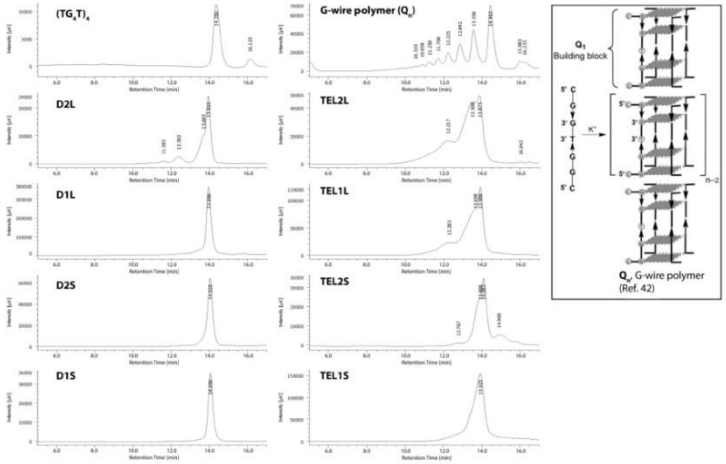

Figure 3. HPLC–SEC chromatograms of the complexes formed by DEL-$(TG_4T)_2$ (**D1L,S**, **D2L,S**) and TEL-$(TG_4T)_4$ (**TEL1L,S** and **TEL2L,S**) in comparison with the $(TG_4T)_4$ G4 (Q_1) and with the Q_n G-wires.

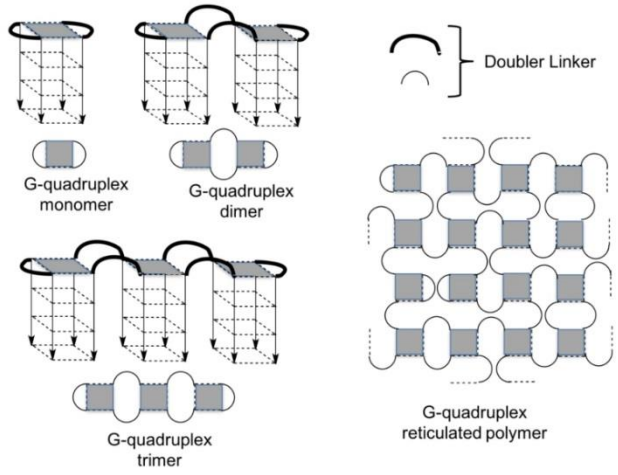

Figure 4. Schematic representation of the parallel G4s obtainable from the self-assembly of DEL-ODNs. The first three complexes, having the least MW, are shown on the left. The hypothetical topology of G4 supramolecular nanostructures based on reticulated parallel DEL-G4s is shown on the right.

The t_R of all peaks corresponding to TEL-G4 monomers (Q_1), obtained by performing the HPLC–SEC separation of the annealed TEL-ODNs (Figure 3, right column), were almost

superimposable with those of the corresponding peaks obtained from the annealed DEL-ODNs. This result indicated that the size of the linker and the polarity of the linkages have a negligible effect on the t_R of the corresponding DEL- and TEL-G4s, thus implying that the two classes of modified G4s have a similar 3D conformation. However, the comparison of the whole HPLC–SEC profiles evidenced a higher propensity of all TEL-ODNs to form higher molecular weight (MW) complexes (in particular for **TEL1L** and **TEL2L**), probably due to more favourable entropic parameters.

2.5. ^{1}H-NMR Studies

The formation of G4s from G-rich oligonucleotides and their analogues is usually confirmed by the observation in the downfield region (10–13 ppm) of water-suppressed ^{1}H-NMR spectra of signals belonging to the exchange-protected N-1 imino protons of guanosines involved in the formation of G-tetrads. When guanosines are involved in the formation of a G-tetrad, their N-1 imino proton is engaged in the formation of a Hoogsteen-type hydrogen bond with the O-6 oxygen atom of flanking guanosine and does not exchange with the protons of bulk water [54,58]. For example, the water-suppressed ^{1}H-NMR spectrum of the highly symmetric $(TG_4T)_4$ quadruplex is characterized by the presence of four sharp imino proton signals, one signal for each of the four G-tetrads (Figure S3) [52,53], whereas four signals are expected for antiparallel and 3+1 mixed G4s [59].

The aromatic and imino protons region of the water-suppressed ^{1}H-NMR spectra recorded at 25, 45 and 85 °C of the studied DEL-ODNs are reported in Figure 5. The presence of strong imino proton signals (10.7–11.8 ppm) in all recorded spectra confirmed that the four new DEL-ODNs fold into DEL-G4s when annealed in K^+-containing buffer. The imino proton regions of the NMR spectra of the four DEL-ODNs were very similar to that of the tetramolecular parallel $(TG_4T)_4$ G4 (Figure S3) and those of the corresponding TEL-G4s [49], both concerning the number and the resonance frequencies of the imino protons peaks. These signals were detectable up to 85 °C, in agreement with the CD melting results reported in Table 1. Only in the case of **D1L** at 25 and 45 °C, we did not observe any well-resolved imino proton signal but only very broad signals resonating at the expected frequencies. This behaviour could be explained with the concomitant presence in solution of small amounts of less stable, rapidly interconverting, bimolecular G4s having different topology (e.g., antiparallel and/or 3+1), as suggested by the presence of a weak positive CD signal at around 290 nm and by the unusually weaker negative CD signal at around 240 nm (Figure 1).

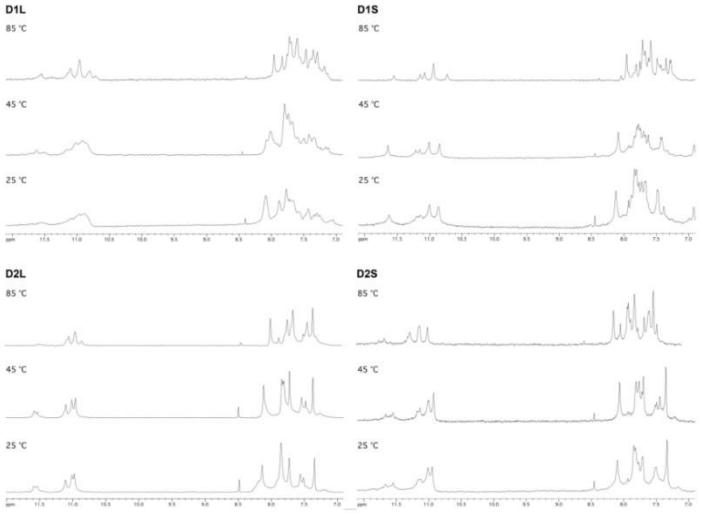

Figure 5. Downfield region of the water-suppressed NMR spectra of **D1L,S** and **D2L,S** annealed in 100 mM K^+ buffer and recorded at 25, 45 and 85 °C.

2.6. Isolation and Analyses of Higher Molecular Weight Species Produced by D2L

To obtain further structural information on the higher MW complexes formed by **D2L**, we collected in a single fraction the least retained peaks of the HPLC–SEC fractionation of **D2L**, as indicated in Figure 6A, and reinjected them on the same column 24 h after storage at 4 °C. The resulting HPLC profile (Figure 6B) presented four partially resolved peaks, which we attributed to the bimolecular DEL-G4 (Q_1, t_R = 13.7 min) and to the DEL-G4 multimers incorporating two (Q_2, t_R = 12.9 min), three (Q_3, t_R = 12.1 min), and four (Q_4, t_R = 11.4 min) G4 scaffolds. To confirm the G4 architecture of the higher MW complexes, we collected them, as indicated in Figure 6B, and recorded their CD spectrum, which resulted almost superimposable to that of the isolated Q_1 species (Figure 7). We attributed the small amount of Q_1 detected in Figure 6B to the partial recovery of this species during the first HPLC–SEC fractionation and not to the dissociation of higher MW DEL-G4 multimers. This hypothesis was corroborated by the HPLC–SEC profile shown in Figure 6C (obtained by injecting the Q1 peak isolated from the first HPLC fractionation of **D2L**), which, not showing any trace of least retained peaks attributable to DEL-G4 complexes belonging to DEL-$Q_{>2}$ types, confirmed that, once isolated, the DEL-Q_n multimers do not interconvert one into the other. The latter observation agrees in full with the formation of G4 multimers based on reticulated G4 building blocks (Figure 4), rather than on end-to-end stacked G4 building blocks (like the Q_n species reported in Figure 3). These results suggest that DEL-G4 multimers comprising more than four G4 scaffolds, similar to the G4 reticulated polymer shown in Figure 4, could also be obtainable by using higher concentrations of DEL-ONs and/or potassium ions and by optimizing the annealing procedure.

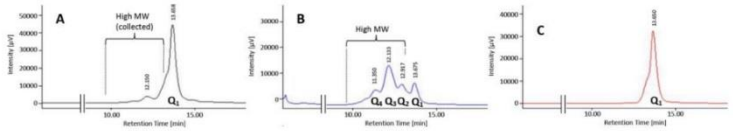

Figure 6. HPLC–SEC chromatograms of: (**A**) complexes formed by **D2L**; (**B**) reinjection of the higher MW species formed by **D2L** collected as shown in panel A; (**C**) reinjection of the purified DEL-Q_1 complex formed by **D2L** collected as shown in panel A.

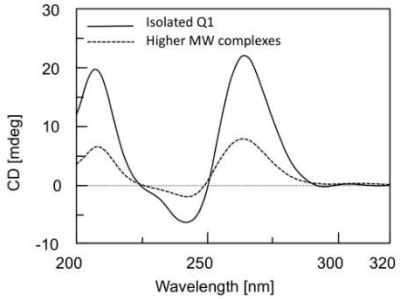

Figure 7. CD spectra of DEL-Q_1 and higher MW species obtained by HPLC–SEC fractionation of **D2L** (100 mM K^+-containing buffer, 5 °C).

3. Materials and Methods

3.1. Reagents and Equipment

Chemicals and solvents were purchased from Sigma-Aldrich (Milan, Italy). Reagents and phosphoramidites for DNA syntheses were purchased from Glen Research (Sterling, VA, USA). The DEL linker **2**, the TEL linker **3** and all the ODNs were assembled on a PerSeptive Biosystems (Framingham, MA, USA) Expedite DNA synthesizer using standard phosphoramidite chemistry. HPLC analyses and purifications were performed with a Jasco (Jasco Europe Srl, Cremella, LC, Italy) PU2089 pump system equipped with an UV detector model 2075 Plus. CPG-resin **1** and the linkers **4** and **5** were purchased from Glen Research. UV spectra were registered using a Jasco V-530 spectrophotometer. CD spectra and thermal denaturation experiments were obtained with a Jasco 1500 CD spectrophotometer equipped with a Jasco PTC-348-WI temperature controller unit. NMR spectra were recorded either on a Varian (Palo Alto, CA, USA) Unity Inova 500 MHz spectrometer equipped with a broadband inverse probe with z-field gradient, or on a Varian Unity INOVA 700 MHz spectrometer equipped with a triple resonance cryoprobe. All NMR spectra were processed using the Varian VNMR and iNMR (http://www.inmr.net) software packages. PAGE bands were visualized on a Bio-Rad Laboratories (Segrate, MI, Italy) Gel Doc™ XR+ image system.

*3.2. Syntheses and Purifications of DEL-ODNs (**D1L,S** and **D2L,S**)*

50 mg of controlled pore glass (CPG) support **1** (0.18 mmol/g) were used for each synthesis in the automated DNA synthesizer following standard phosphoramidite chemistry. 45 mg/mL solutions of phosphoramidite **4** or **5** (both in anhydrous CH_3CN) were used for the synthesis of **2L** or **2S**, respectively. This step was followed by reactions with 3′-phosphoramidite (for **D1L** and **D1S**) or 5′-phosphoramidite (for **D2L** and **D2S**) nucleotide building blocks (six cycles, 45 mg/mL in anhydrous CH_3CN). The coupling yields were consistently higher than 98% (by DMT spectrophotometric

measurements). The solid support was then treated with concentrated aqueous ammonia solution for 7 h at 55 °C. The filtered solution and washings were concentrated under reduced pressure and purified by HPLC with an anion exchange column (Macherey–Nagel, 1000-8/46, 4.4 × 50 mm, 5 µm) eluted with a linear gradient from 0 to 100% B in 30 min; buffer A: 20 mM NaH_2PO_4, pH 7.0 containing 20% CH_3CN; buffer B: 1 M NaCl, 20 mM NaH_2PO_4, pH 7.0, containing 20% CH_3CN; flow rate 1 mL/min. The collected products were desalted by gel filtration on a BioGel P2 column eluted with H_2O/ethanol (9:1, *v*/*v*) to obtain, after lyophilisation, pure **D1L,S** and **D2L,S** (92, 85 and 80, 88 OD_{260} units, respectively). The ON concentrations were determined spectrophotometrically in water at λ = 260 nm and 90 °C using the molar extinction coefficient ε = 28,900 cm^{-1} M^{-1} for DEL-$(TG_4T)_2$ and ε = 57,800 for TEL-$(TG_4T)_4$ calculated for the unstacked ODNs by the nearest-neighbour method.

3.3. Preparation of the G-Quadruplexes (Annealing)

All G4s were formed by dissolving DEL-ODNs, TEL-ODNs, or TG_4T in the K^+ buffer (90 mM KCl, 10 mM KH_2PO_4, pH 7.0) or Na^+ buffer (90 mM NaCl, 10 mM NaH_2PO_4, pH 7.0) and heating to 95 °C for 5 min and then rapidly cooling at 4 °C (annealing). All samples were stored at 4 °C for 24 h before analyses. The solutions were equilibrated at 25 °C for 2 h before performing the experiments.

3.4. PAGE Experiments

Native gel electrophoresis experiments were performed on 12% polyacrylamide gels containing 1× TBE buffer, pH 7.0 with 30 mM KCl, at 4 °C, 120 V for 2 h. Samples were loaded at a final ON concentration of 100 µM; glycerol was added (10% final) to facilitate sample loading in the wells. The bands were finally visualized by UV shadowing or by SYBR Green staining.

3.5. CD Experiments

CD spectra and CD melting profiles were recorded in 0.1 cm optical path quartz cuvettes (100 nm/min scanning speed, 1 s response time). The spectra were recorded in triplicate at 5 °C from 200 to 320 nm. CD samples were prepared in the above reported 0.1 M K^+ or Na^+ buffer at the final single-strand concentration of 20 µM. The buffer baseline was subtracted from each spectrum. The CD melting experiments were performed by monitoring the CD value (mdeg) at 263 nm in the temperature range 5–95 °C at 0.5 °C/min heating rate.

3.6. HPLC–SEC Analyses

HPLC–SEC analyses and purifications were performed using a Phenomenex (Bologna, Italy) Yarra SEC-2000 column (300 × 7.8 mm, 3 µm) eluted with 90 mM KCl and 10 mM KH_2PO_4/CH_3CN (80:20, *v*/*v*), flow rate 0.6 mL/min, UV-detector at 260 nm. The analyses were performed at room temperature.

3.7. NMR Experiments

NMR samples were prepared at 1.8 mM single strand concentration in 200 mL of 100 mM K^+ solution (90 mM KCl, 10 mM KH_2PO_4, pH 7.0, 9:1 H_2O/D_2O). Water suppression was achieved by including a double pulsed-field gradient spin-echo (DPFGSE) module [60,61] in the pulse sequence prior to acquisition. NMR spectra were acquired as 16,384 data points with a recycle delay of 1.0 s at 25, 45, and 85 °C, and the spectra were apodized with a shifted sine bell squared window function.

4. Conclusions

In this study, we reported the synthesis and the structural characterization of a new kind of G4 forming G-rich oligonucleotides, named DEL-ODNs, in which two TG_4T strands are attached either by their 5′ or 3′ end to the two ends of a bifunctional linker. A total of four DEL-$(TG_4T)_2$ ODNs were synthesized using two linkers of different length, and their propensity to form DEL-G4s was investigated by CD, NMR, PAGE and HPLC–SEC analyses. CD and NMR spectroscopies confirmed the

formation of the target bimolecular parallel G4s for all the four DEL-ODNs, regardless of the polarity of the two ON strands and the length of the linker. All four DEL-G4s were provided with extremely high thermal stability, especially in 100 mM K^+-containing solution ($T_{\frac{1}{2}} > 80$ °C). The here-described DEL-G4s were also compared with the corresponding G4s formed by the unmodified TG_4T sequence and by the previously reported TEL-$(TG_4T)_4$ analogues, with the aim of adding useful information on the effect of DEL and TEL linkers on the formation of supramolecular structures based on the parallel $(TG_4T)_4$ G4 scaffold. HPLC–SEC and PAGE analyses, used to obtain information on the molecularity of the complexes, confirmed that all DEL-$(TG_4T)_2$ ODNs formed the target bimolecular DEL-G4s primarily. However, detectable amounts of higher molecular-weight species were detected, especially for **D2L**, which was obtained by linking the 5′ end of two TG_4T strands to the longer linker. Looking at the whole picture, our results indicate that: i) TEL-ODNs have a higher propensity to fold into higher MW G4 complexes than the corresponding DEL-ODNs, likely because of the entropy gain; ii) DEL- and TEL-ODNs incorporating the longer linker have the higher propensity to fold into multimeric G4 complexes; iii) the direction of the TG_4T synthesis on the four TEL arms plays only a marginal role on the molecularity of the resulting TEL-G4s, whereas for DEL-ODNs, clear evidence of the formation of multimeric DEL-G4s was observed just for **D2L**. At the studied concentration of **D2L** and potassium ions, the formation of higher MW G4 complexes comprising up to four parallel G4 scaffolds was confirmed by HPLC–SEC. Taken together, the here-reported results suggest that the synthetic strategy based on DEL and TEL linkers could be further exploited to obtain new supramolecular biomaterials based on the reticulated G4 scaffolds depicted in Figure 4.

Supplementary Materials: The following are available online, Figure S1: CD spectra of samples annealed in 100 mM Na^+-containing buffer, Figure S2: CD melting curves of samples annealed in 100 mM Na+-containing buffer, Figure S3: imino protons region of ^{1}H-NMR spectrum of $(TG_4T)_4$ G-quadruplex.

Author Contributions: Conceptualization, G.O., G.P., and N.B.; methodology, G.O. and G.P.; investigation, M.M., A.P.F., B.P., S.D., G.N.R., and N.B.; visualization, M.M., A.P.F., and N.B.; writing—original draft preparation, G.O., G.P., and N.B.; writing—review and editing, N.B.; supervision, G.O.; project administration, G.O.; funding acquisition, G.O. and G.P.

Funding: This research was funded by Regione Campania POR funds, project onc3-003145 (DG 10 staff 93 n. 354, 05/06/2017).

Conflicts of Interest: The authors declare no conflict of interest.

References

1. Phan, A.T.T.; Kuryavyi, V.; Luu, K.N.; Patel, D.J. Structural Diversity of G-Quadruplex Scaffolds. In *Quadruplex Nucleic Acids*; Neidle, S., Balasubramanian, S., Eds.; Royal Society of Chemistry: Cambridge, UK, 2006; pp. 81–99. ISBN 978-0-85404-374-3.
2. Simonsson, T. G-quadruplex DNA structures variations on a theme. *Biol. Chem.* **2001**, *382*, 621–628. [CrossRef] [PubMed]
3. Parkinson, G.N. Fundamentals of Quadruplex Structures. In *Quadruplex Nucleic Acids*; Neidle, S., Balasubramanian, S., Eds.; Royal Society of Chemistry: Cambridge, UK, 2006; pp. 1–30. ISBN 978-0-85404-374-3.
4. Searle, M.S.; Williams, H.E.L.; Gallagher, C.T.; Grant, R.J.; Stevens, M.F.G. Structure and K^+ ion-dependent stability of a parallel-stranded DNA quadruplex containing a core A-tetrad. *Org. Biomol. Chem.* **2004**, *2*, 810–812. [CrossRef] [PubMed]
5. Guédin, A.; De Cian, A.; Gros, J.; Lacroix, L.; Mergny, J.-L.L. Sequence effects in single-base loops for quadruplexes. *Biochimie* **2008**, *90*, 686–696. [CrossRef] [PubMed]
6. Risitano, A.; Fox, K.R. Influence of loop size on the stability of intramolecular DNA quadruplexes. *Nucleic Acids Res.* **2004**, *32*, 2598–2606. [CrossRef] [PubMed]
7. Rachwal, P.A.; Findlow, I.S.; Werner, J.M.; Brown, T.; Fox, K.R. Intramolecular DNA quadruplexes with different arrangements of short and long loops. *Nucleic Acids Res.* **2007**, *35*, 4214–4222. [CrossRef] [PubMed]
8. Hazel, P.; Huppert, J.; Balasubramanian, S.; Neidle, S. Loop-length-dependent folding of G-quadruplexes. *J. Am. Chem. Soc.* **2004**, *126*, 16405–16415. [CrossRef] [PubMed]

9. Maizels, N. Dynamic roles for G4 DNA in the biology of eukaryotic cells. *Nat. Struct. Mol. Biol.* **2006**, *13*, 1055–1059. [CrossRef] [PubMed]
10. Lipps, H.J.; Rhodes, D. G-quadruplex structures: In vivo evidence and function. *Trends Cell Biol.* **2009**, *19*, 414–422. [CrossRef] [PubMed]
11. Biffi, G.; Tannahill, D.; McCafferty, J.; Balasubramanian, S. Quantitative visualization of DNA G-quadruplex structures in human cells. *Nat. Chem.* **2013**, *5*, 182–186. [CrossRef] [PubMed]
12. Sengupta, P.; Basu, S.; Soni, S.; Pandey, A.; Roy, B.; Oh, M.S.; Chin, K.T.; Paraskar, A.S.; Sarangi, S.; Connor, Y.; et al. Cholesterol-tethered platinum II-based supramolecular nanoparticle increases antitumor efficacy and reduces nephrotoxicity. *Proc. Natl. Acad. Sci.* **2012**, *109*, 11294–11299. [CrossRef]
13. Falanga, A.P.; Cerullo, V.; Marzano, M.; Feola, S.; Oliviero, G.; Piccialli, G.; Borbone, N. PNA-functionalized adenoviral vectors targeting G-quadruplexes in the P1 promoter of Bcl-2 proto-oncogene: A new tool for gene modulation in anti-cancer therapy. *Bioconjug. Chem.* **2019**. Accepted.
14. Xu, Y. Chemistry in human telomere biology: Structure, function and targeting of telomere DNA/RNA. *Chem. Soc. Rev.* **2011**, *40*, 2719–2740. [CrossRef] [PubMed]
15. Patel, D.J.; Phan, A.T.T.; Kuryavyi, V. Human telomere, oncogenic promoter and 5′-UTR G-quadruplexes: Diverse higher order DNA and RNA targets for cancer therapeutics. *Nucleic Acids Res.* **2007**, *35*, 7429–7455. [CrossRef] [PubMed]
16. Avino, A.; Fabrega, C.; Tintore, M.; Eritja, R. Thrombin binding aptamer, more than a simple aptamer: Chemically modified derivatives and biomedical applications. *Curr. Pharm. Des.* **2012**, *18*, 2036–2047. [CrossRef] [PubMed]
17. Aaldering, L.J.; Poongavanam, V.; Langkjær, N.; Murugan, N.A.; Jørgensen, P.T.; Wengel, J.; Veedu, R.N. Development of an Efficient G-Quadruplex-Stabilised Thrombin-Binding Aptamer Containing a Three-Carbon Spacer Molecule. *ChemBioChem* **2017**, *18*, 755–763. [CrossRef] [PubMed]
18. Politi, J.; Rea, I.; Nici, F.; Dardano, P.; Terracciano, M.; Oliviero, G.; Borbone, N.; Piccialli, G.; De Stefano, L. Nanogravimetric and optical characterizations of thrombin interaction with a self-assembled thiolated aptamer. *J. Sensors* **2016**, *2016*. [CrossRef]
19. Scuotto, M.; Persico, M.; Bucci, M.; Vellecco, V.; Borbone, N.; Morelli, E.; Oliviero, G.; Novellino, E.; Piccialli, G.; Cirino, G.; et al. Outstanding effects on antithrombin activity of modified TBA diastereomers containing an optically pure acyclic nucleotide analogue. *Org. Biomol. Chem.* **2014**, *12*, 5235–5242. [CrossRef]
20. Borbone, N.; Bucci, M.; Oliviero, G.; Morelli, E.; Amato, J.; D'Atri, V.; D'Errico, S.; Vellecco, V.; Cirino, G.; Piccialli, G.; et al. Investigating the Role of T 7 and T 12 Residues on the Biological Properties of Thrombin-Binding Aptamer: Enhancement of Anticoagulant Activity by a Single Nucleobase Modi fi cation. *J. Med. Chem.* **2012**, *55*, 10716–10728. [CrossRef]
21. Hotoda, H.; Momota#, K.; Furukawa#, H.; Nakamuta$, T.; Kaneko, M.; Kimura, S.; Shimada, K. Biologically active oligodeoxyribonucleotides—II[1]: Structure activity relationships of anti-HIV-1 pentadecadeoxyribonucleotides bearing 5′-end-modifications. *Nucleosides Nucleotides* **1994**, *13*, 1375–1395. [CrossRef]
22. Wyatt, J.R.; Vickers, T.A.; Roberson, J.L.; Buckheit, R.W.; Klimkait, T.; DeBaets, E.; Davis, P.W.; Rayner, B.; Imbach, J.L.; Ecker, D.J. Combinatorially selected guanosine-quartet structure is a potent inhibitor of human immunodeficiency virus envelope-mediated cell fusion. *Proc. Natl. Acad. Sci.* **1994**, *91*, 1356–1360. [CrossRef]
23. Oliviero, G.; Stornaiuolo, M.; D'Atri, V.; Nici, F.; Yousif, A.M.; D'Errico, S.; Piccialli, G.; Mayol, L.; Novellino, E.; Marinelli, L.; et al. Screening Platform toward New Anti-HIV Aptamers Set on Molecular Docking and Fluorescence Quenching Techniques. *Anal. Chem.* **2016**, *88*, 2327–2334. [CrossRef] [PubMed]
24. Nici, F.; Oliviero, G.; Falanga, A.P.; D'Errico, S.; Marzano, M.; Musumeci, D.; Montesarchio, D.; Noppen, S.; Pannecouque, C.; Piccialli, G.; et al. Anti-HIV activity of new higher order G-quadruplex aptamers obtained from tetra-end-linked oligonucleotides. *Org. Biomol. Chem.* **2018**, *16*, 2349–2355. [CrossRef] [PubMed]
25. D'Atri, V.; Oliviero, G.; Amato, J.; Borbone, N.; D'Errico, S.; Mayol, L.; Piccialli, V.; Haider, S.; Hoorelbeke, B.; Balzarini, J.; et al. New anti-HIV aptamers based on tetra-end-linked DNA G-quadruplexes: Effect of the base sequence on anti-HIV activity. *Chem. Commun.* **2012**, *48*, 9516. [CrossRef] [PubMed]
26. Oliviero, G.; Amato, J.; Borbone, N.; D'Errico, S.; Galeone, A.; Mayol, L.; Haider, S.; Olubiyi, O.; Hoorelbeke, B.; Balzarini, J.; et al. Tetra-end-linked oligonucleotides forming DNA G-quadruplexes: A new class of aptamers showing anti-HIV activity. *Chem. Commun.* **2010**, *46*, 8971. [CrossRef] [PubMed]

27. Livshits, G.I.; Stern, A.; Rotem, D.; Borovok, N.; Eidelshtein, G.; Migliore, A.; Penzo, E.; Wind, S.J.; Di Felice, R.; Skourtis, S.S.; et al. Long-range charge transport in single G-quadruplex DNA molecules. *Nat. Nanotechnol.* **2014**, *9*, 1040–1046. [CrossRef] [PubMed]
28. Liu, S.-P.; Weisbrod, S.H.; Tang, Z.; Marx, A.; Scheer, E.; Erbe, A. Direct measurement of electrical transport through G-quadruplex DNA with mechanically controllable break junction electrodes. *Angew. Chemie Int. Ed.* **2010**, *49*, 3313–3316. [CrossRef] [PubMed]
29. Cohen, H.; Sapir, T.; Borovok, N.; Molotsky, T.; Di Felice, R.; Kotlyar, A.B.; Porath, D. Polarizability of G4-DNA observed by electrostatic force microscopy measurements. *Nano Lett.* **2007**, *7*, 981–986. [CrossRef]
30. Ruttkay-Nedecky, B.; Kudr, J.; Nejdl, L.; Maskova, D.; Kizek, R.; Adam, V. G-quadruplexes as sensing probes. *Molecules* **2013**, *18*, 14760–14779. [CrossRef] [PubMed]
31. Yang, D.; Campolongo, M.J.; Nhi Tran, T.N.; Ruiz, R.C.H.; Kahn, J.S.; Luo, D. Novel DNA materials and their applications. *Wiley Interdiscip. Rev. Nanomed. Nanobiotechnol.* **2010**, *2*, 648–669. [CrossRef] [PubMed]
32. Linko, V.; Dietz, H. The enabled state of DNA nanotechnology. *Curr. Opin. Biotechnol.* **2013**, *24*, 555–561. [CrossRef] [PubMed]
33. Rothemund, P.W.K. Folding DNA to create nanoscale shapes and patterns. *Nature* **2006**, *440*, 297–302. [CrossRef] [PubMed]
34. Marsh, T.C.; Vesenka, J.; Henderson, E. A new DNA nanostructure, the G-wire, imaged by scanning probe microscopy. *Nucleic Acids Res.* **1995**, *23*, 696–700. [CrossRef] [PubMed]
35. Construction and Examination of "G-Wire" DNA. Available online: https://aip.scitation.org/doi/abs/10.1063/1.1520082 (accessed on 11 February 2019).
36. Marsh, T.C.; Henderson, E. G-Wires: Self-Assembly of a Telomeric Oligonucleotide, d(GGGGTTGGGG), into Large Superstructures. *Biochemistry* **1994**, *33*, 10718–10724. [CrossRef] [PubMed]
37. Kotlyar, A.B.; Borovok, N.; Molotsky, T.; Cohen, H.; Shapir, E.; Porath, D. Long, monomolecular guanine-based nanowires. *Adv. Mater.* **2005**, *17*, 1901–1905. [CrossRef]
38. Shi, Y.; Luo, H.Q.; Li, N.B. A highly sensitive resonance Rayleigh scattering method to discriminate a parallel-stranded G-quadruplex from DNA with other topologies and structures. *Chem. Commun.* **2013**, *49*, 6209–6211. [CrossRef] [PubMed]
39. Saintomé, C.; Amrane, S.; Mergny, J.-L.L.; Alberti, P. The exception that confirms the rule: A higher-order telomeric G-quadruplex structure more stable in sodium than in potassium. *Nucleic Acids Res.* **2016**, *44*, 2926–2935. [CrossRef]
40. Smargiasso, N.; Rosu, F.; Hsia, W.; Colson, P.; Baker, E.S.; Bowers, M.T.; De Pauw, E.; Gabelica, V. G-quadruplex DNA assemblies: Loop length, cation identity, and multimer formation. *J. Am. Chem. Soc.* **2008**, *130*, 10208–10216. [CrossRef] [PubMed]
41. Borbone, N.; Amato, J.; Oliviero, G.; D'Atri, V.; Gabelica, V.; De Pauw, E.; Piccialli, G.; Mayol, L. D(CGGTGGT) forms an octameric parallel G-quadruplex via stacking of unusual G(:C):G(:C):G(:C):G(:C) octads. *Nucleic Acids Res.* **2011**, *39*, 7848–7857. [CrossRef] [PubMed]
42. Oliviero, G.; D'Errico, S.; Pinto, B.; Nici, F.; Dardano, P.; Rea, I.; De Stefano, L.; Mayol, L.; Piccialli, G.; Borbone, N. Self-assembly of g-rich oligonucleotides incorporating a 3′-3′ inversion of polarity site: A new route towards G-Wire DNA nanostructures. *ChemistryOpen* **2017**, *6*, 599–605. [CrossRef] [PubMed]
43. D'Atri, V.; Borbone, N.; Amato, J.; Gabelica, V.; D'Errico, S.; Piccialli, G.; Mayol, L.; Oliviero, G.; D'Atri, V.; Borbone, N.; et al. DNA-based nanostructures: The effect of the base sequence on octamer formation from d(XGGYGGT) tetramolecular G-quadruplexes. *Biochimie* **2014**, *99*, 119–128. [CrossRef]
44. Ferreira, R.; Alvira, M.; Aviñó, A.; Gómez-Pinto, I.; González, C.; Gabelica, V.; Eritja, R. Synthesis and structural characterization of stable branched DNA G-quadruplexes using the trebler phosphoramidite. *ChemistryOpen* **2012**, *1*, 106–114. [CrossRef] [PubMed]
45. Murat, P.; Bonnet, R.; Van Der Heyden, A.; Spinelli, N.; Labbé, P.; Monchaud, D.; Teulade-Fichou, M.P.; Dumy, P.; Defrancq, E. Template-Assembled Synthetic G-Quadruplex (TASQ): A Useful System for Investigating the Interactions of Ligands with Constrained Quadruplex Topologies. *Chem.—A Eur. J.* **2010**, *16*, 6106–6114. [CrossRef] [PubMed]
46. Murat, P.; Cressend, D.; Spinelli, N.; Van Der Heyden, A.; Labbé, P.; Dumy, P.; Defrancq, E. A novel conformationally constrained parallel G quadruplex. *ChemBioChem* **2008**, *9*, 2588–2591. [CrossRef] [PubMed]

47. Oliviero, G.; Borbone, N.; Galeone, A.; Varra, M.; Piccialli, G.; Mayol, L. Synthesis and characterization of a bunchy oligonucleotide forming a monomolecular parallel quadruplex structure in solution. *Tetrahedron Lett.* **2004**, *45*, 4869–4872. [CrossRef]
48. Oliviero, G.; Amato, J.; Borbone, N.; Galeone, A.; Varra, M.; Piccialli, G.; Mayol, L. Synthesis and characterization of DNA quadruplexes containing T-tetrads formed by bunch-oligonucleotides. *Biopolymers* **2006**, *81*, 194–201. [CrossRef] [PubMed]
49. Oliviero, G.; Amato, J.; Borbone, N.; Galeone, A.; Petraccone, L.; Varra, M.; Piccialli, G.; Mayol, L. Synthesis and characterization of monomolecular DNA G-quadruplexes formed by tetra-end-linked oligonucleotides. *Bioconjug. Chem.* **2006**, *17*, 889–898. [CrossRef] [PubMed]
50. Oliviero, G.; Borbone, N.; Amato, J.; D'Errico, S.; Galeone, A.; Piccialli, G.; Varra, M.; Mayol, L. Synthesis of quadruplex-forming tetra-end-linked oligonucleotides: Effects of the linker size on quadruplex topology and stability. *Biopolymers* **2009**, *91*, 466–477. [CrossRef] [PubMed]
51. Aviño, A.; Grimau, M.G.; Frieden, M.; Eritja, R. Synthesis and Triple-Helix-Stabilization Properties of Branched Oligonucleotides Carrying 8-Aminoadenine Moieties. *Helv. Chim. Acta* **2004**, *87*, 303–316. [CrossRef]
52. Aboul-ela, F.; Murchie, A.I.H.; Lilley, D.M.J. NMR study of parallel-stranded tetraplex formation by the hexadeoxynucleotide d(TG4T). *Nature* **1992**, *360*, 280–282. [CrossRef]
53. Mergny, J.-L.L.; De Cian, A.; Ghelab, A.; Saccà, B.; Lacroix, L. Kinetics of tetramolecular quadruplexes. *Nucleic Acids Res.* **2005**, *33*, 81–94. [CrossRef]
54. Jin, R.; Gaffney, B.L.; Wang, C.; Jones, R.A.; Breslauer, K.J. Thermodynamics and structure of a DNA tetraplex: a spectroscopic and calorimetric study of the tetramolecular complexes of d(TG3T) and d(TG3T2G3T). *Proc. Natl. Acad. Sci. USA* **1992**, *89*, 8832–8836. [CrossRef] [PubMed]
55. Hardin, C.C.; Perry, A.G.; White, K. Thermodynamic and kinetic characterization of the dissociation and assembly of quadruplex nucleic acids. *Biopolymers* **2000**, *56*, 147–194. [CrossRef]
56. Dapic, V.; Abdomerovic, V.; Marrington, R.; Peberdy, J.; Rodger, A.; Trent, J.O.; Bates, P.J.; Dapić, V.; Abdomerović, V.; Marrington, R.; et al. Biophysical and biological properties of quadruplex oligodeoxyribonucleotides. *Nucleic Acids Res.* **2003**, *31*, 2097–2107. [CrossRef] [PubMed]
57. Petraccone, L.; Erra, E.; Esposito, V.; Randazzo, A.; Mayol, L.; Nasti, L.; Barone, G.; Giancola, C. Stability and Structure of Telomeric DNA Sequences Forming Quadruplexes Containing Four G-Tetrads with Different Topological Arrangements†. *Biochemistry* **2004**, *43*, 4877–4884. [CrossRef] [PubMed]
58. Feigon, J.; Koshlap, K.M.; Smith, F.W. 1H-NMR spectroscopy of DNA triplexes and quadruplexes. *Methods Enzymol.* **1995**, *261*, 225–255. [PubMed]
59. Adrian, M.; Heddi, B.; Phan, A.T. NMR spectroscopy of G-quadruplexes. *Methods (San Diego, Calif)* **2012**, *57*, 11–24. [CrossRef] [PubMed]
60. Hwang, T.L.; Shaka, A.J. Water Suppression That Works. Excitation Sculpting Using Arbitrary Wave-Forms and Pulsed-Field Gradients. *J. Magn. Reson. Ser. A* **1995**, *112*, 275–279. [CrossRef]
61. Dalvit, C. Efficient multiple-solvent suppression for the study of the interactions of organic solvents with biomolecules. *J. Biomol. NMR* **1998**, *11*, 437–444. [CrossRef]

Sample Availability: Samples of the compounds **D1L,S** and **D2L,S** are available from the authors.

marine drugs

MDPI

Article

New Linear Precursors of cIDPR Derivatives as Stable Analogs of cADPR: A Potent Second Messenger with Ca^{2+}-Modulating Activity Isolated from Sea Urchin Eggs

Stefano D'Errico [1,2], Emy Basso [3,4], Andrea Patrizia Falanga [5], Maria Marzano [1], Tullio Pozzan [3,4,6], Vincenzo Piccialli [7], Gennaro Piccialli [1,2], Giorgia Oliviero [5,*] and Nicola Borbone [1,2]

1 Dipartimento di Farmacia, Università degli Studi di Napoli Federico II, via Domenico Montesano 49, Napoli 80131, Italy
2 ISBE Italy/SYSBIO Centro di System Biology, Università di Milano-Bicocca, piazza delle Scienze 2, Milano 20126, Italy
3 Consiglio Nazionale delle Ricerche, Dipartimento di Scienze Biomediche, Istituto di Neuroscienze (Sezione di Padova), viale Giuseppe Colombo 3, Padova 35131, Italy
4 Dipartimento di Scienze Biomediche, Università degli Studi di Padova, via Ugo Bassi 58/b, Padova 35131, Italy
5 Dipartimento di Medicina Molecolare e Biotecnologie Mediche, Università degli Studi di Napoli Federico II, via Sergio Pansini 5, Napoli 80131, Italy
6 Istituto Veneto di Medicina Molecolare, via Orus 2, Padova 35129, Italy
7 Dipartimento di Scienze Chimiche, Università degli Studi di Napoli Federico II, via Cintia, 26, Napoli 80126, Italy
* Correspondence: golivier@unina.it; Tel.: +39-081-679896

Received: 23 July 2019; Accepted: 15 August 2019; Published: 17 August 2019

check for updates

Abstract: Herein, we report on the synthesis of a small set of linear precursors of an inosine analogue of cyclic ADP-ribose (cADPR), a second messenger involved in Ca^{2+} mobilization from ryanodine receptor stores firstly isolated from sea urchin eggs extracts. The synthesized compounds were obtained starting from inosine and are characterized by an N1-alkyl chain replacing the "northern" ribose and a phosphate group attached at the end of the N1-alkyl chain and/or 5′-sugar positions. Preliminary Ca^{2+} mobilization assays, performed on differentiated C2C12 cells, are reported as well.

Keywords: cADPR; ryanodine receptors; neuroblastoma; caffeine; calcium mobilization; phosphorylation; C2C12 cells; IP3

1. Introduction

Ca^{2+}-mediated signaling is the major secondary messenger involved in several essential cell functions. Ca^{2+} ions are generally located in the endoplasmic reticulum (ER) and mitochondria until an extracellular stimulus causes their release into the cytosol [1,2]. This mobilization may lead to a great number of physiological effects such as gene regulation [3], cell proliferation, fertilization [4], muscle contraction [5], and neurotransmitter secretion [6]. Cyclic adenosine diphosphate ribose (cADPR, **1**, Figure 1) is an endogenous cyclic nucleotide that was firstly isolated from sea urchin egg extracts [7], later found also in mammalian cells, such as pancreatic β-cells [8], T-lymphocytes [9], smooth and cardiac muscle cells [10], and cerebellar neurons [11]. cADPR, together with inositol 1,4,5-triphosphate (IP3) and nicotinic acid adenine dinucleotide phosphate (NAADP), is a second messenger involved in cellular Ca^{2+} mobilization [12,13]. It interacts with ryanodine receptors through a mechanism which is

still unclear, causing the Ca^{2+} release from intracellular stores [14]. The 18 membered cyclic structure comes from the catalytic activity of the enzyme ADP-ribosyl cyclase, which in mammalian cells is the multifunctional transmembrane glycoprotein CD38 [15,16]. The latter is able also to catalyze the inverse hydrolytic reaction that produces adenosine diphosphate ribose (ADPR) [17]. The physiological instability of cADPR at the N1-glycosidic bond [17], together with its low ability to cross membranes, likely for the presence of the negative charge at the pyrophosphate moiety [18], have prompted some researchers to develop semi-synthetic and/or synthetic methodologies to obtain novel non-hydrolysable and cell permeant analogues [17,19–23].

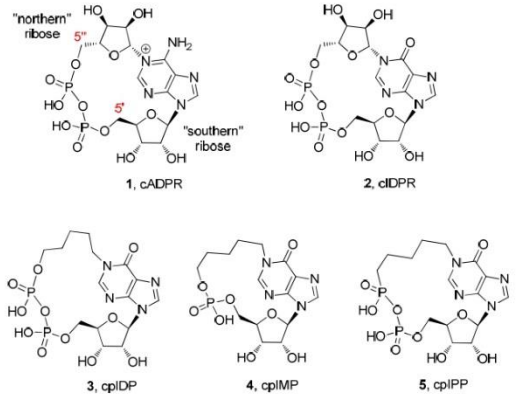

Figure 1. The structures of cyclic adenosine diphosphate ribose (cADRP; **1**) and some of its analogues (**2**–**5**).

Specific structure–activity relationships on different cell lines have been tuned [24,25], featuring modifications mainly involving the "northern" and/or the "southern" ribose. In many cases, the replacement of the northern ribose with ether/alkyl chains was revealed to be the most fruitful modifications for the obtainment of cell permeant analogues, likely by virtue of their reduced molecular polarity [22]. The finding that the isosteric replacement of the adenine base with hypoxanthine generated a more stable analogue (cyclic inosine diphosphate ribose, cIDPR, **2**, Figure 1) with intact Ca^{2+}-mobilizing properties [26], laid the foundations for a more detailed comprehension of the molecular mechanism of action of cADPR, that also took advantage from studies of the biological properties of novel cIDPR analogues [27,28]. However, the poor knowledge of the receptorial cADPR binding pocket [29] makes difficult the rational design of analogues; moreover, the analogues can behave differently depending on the cell line used.

Over the last years, our research group synthesized several cIDPR analogues [30–37]. In particular, the pyrophosphate (cpIDP, **3**, Figure 1) [30] and the monophosphate (cpIMP, **4**, Figure 1) [36] derivatives with a pentyl chain replacing the "northern" ribose showed interesting Ca^{2+}-releasing activities in PC12 cells differentiated in neurons with the use of nerve growth factor (NGF) [18]. Meanwhile, the pyrophosphate derivative with a butyl chain in the place of the "northern" ribose was inactive on the same cell line [37]. In addition, we synthesized the derivative **5** (Figure 1), bearing a phosphono-phosphate anhydride in the place of the pyrophosphate, with the aim of better exploring the role of the pyrophosphate in Ca^{2+}-mobilizing properties of cADPR/cIDPR analogues [37]. Unfortunately, the compound **5** also failed to modify the $[Ca^{2+}]_i$ in PC12 cells. These biological results allowed us to hypothesize two preliminary structure–activity relationships: (1) one phosphate group

appears to be sufficient for the Ca^{2+}-releasing activity in PC12 neuronal cells; (2) the N1-pentyl chain is likely essential for a better conformational accommodation within the putative binding pocket of the intracellular receptor.

The transient receptor potential melastatin 2 (TRPM2) is a non-selective cation channel embedded in plasma membrane and/or lysosomal compartments, that is involved in the response to oxidative stress and inflammation [38–40]. It has been found that ADPR, binding the zebrafish melastatin homology domain 1/2 (MHR1/2) or the human nudix hydrolase 9 homology domain (NUDT9H) of TRPM2, can open the channel favoring the Ca^{2+} ions entry [41]. These findings, together with the discovery that N1-ribose 5′′-monophosphate inosines could act as inhibitors of cADPR hydrolysis [42], are challenging and open the way to the design and synthesis of novel modulators/inhibitors structurally related to cADPR/cIDPR. The latter can be obtained more easily in respect to the cyclic counterparts, thanks to the lack of the last limiting macrocyclization step. In this frame, here, we report on the synthesis and the preliminary evaluation of Ca^{2+}-mobilizing properties of a small set of N1-*ω*-alkyl phosphate 5′-phosphate and N1-*ω*-hydroxyalkyl 5′-phosphate inosines (**11** and **14**, Scheme 1, respectively) obtained by varying the length of the N1 purine alkyl chain from four to six carbon atoms. We also synthesized and tested the two monophosphate derivatives **16** and **18** (Scheme 2). Compound **16** is a useful intermediate for the obtainment of the biologically active cpIDP **4**, whereas compound **18** can be used for the synthesis of cpIPP **5**. These compounds enrich the box of linear precursors of cIDPR analogues, that, until now, have been mainly employed as synthetic intermediates.

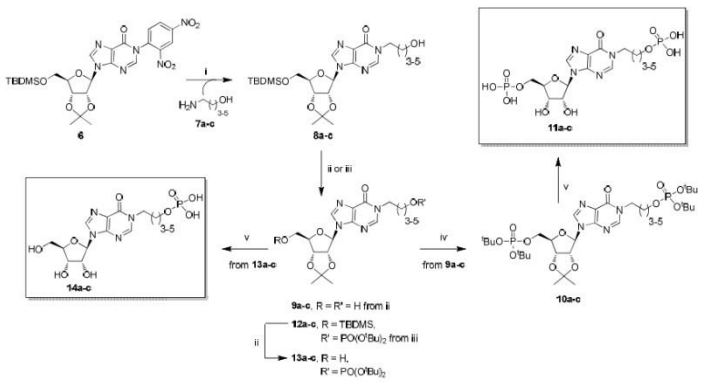

Scheme 1. Reagents and conditions. **(i)** **7a–c**, *N*,*N*-dimethylformamide (DMF), 50 °C, 16 h; **(ii)** tetrabutylammonium fluoride (TBAF), tetrahydrofuran (THF), r.t., 1 h; **(iii)** (a) di-*tert*-butyl *N*,*N*-diisopropylphosphoramidite ($(^tBuO)_2PN(^iPr)_2$), 1-*H*-tetrazole, THF, r.t., 6 h, (b) *tert*-butyl hydroperoxide (^tBuOOH), THF, r.t., 1 h; **(iv)** 50% trifluoroacetic acid (TFA) in H_2O, r.t., 4 h.

2. Results and Discussion

2.1. Chemistry

Compounds **11** and **14** were synthesized starting from the versatile building block **6** (Scheme 1), readily obtained from inosine [36].

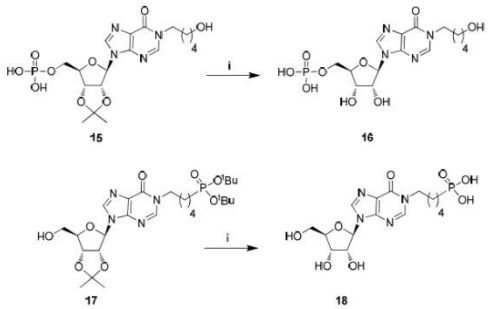

Scheme 2. Reagents and conditions. (**i**) 50% TFA in H_2O, r.t., 4 h.

The strong 2,4-dinitrophenyl electron-withdrawing group makes the C2 purine atom very reactive towards amino-alcohols **7a–c**, affording high yields (70–84%) of N1 ω-hydroxyalkyl inosines (**8a-c**) [43–46], through a mechanism that we have studied in detail [47,48]. In particular, the nucleophilic addition of the amino group to the C2 purine atom leads to the pyrimidine ring opening; then, the same amino group attacks the imidazo 4-carboxamide functionality, reclosing the pyrimidine ring with the 2,4-dinitroaniline displacement. As a next step of the synthesis, the ribose *tert*-butyldimethylsilyl (TBDMS) group was quantitatively removed from derivatives **8a–c** with tetrabutylammonium fluoride (TBAF), yielding the compounds **9a–c**. Then, the phosphorylation of the pendant hydroxy functionalities in **9a–c** was studied. Our research group [37] and others [49,50] demonstrated that the mono-phosphorylation of a nucleoside could be performed in mild and good yielding conditions, exploiting the phosphoramidite chemistry. When compounds **9a–c** were reacted with di-*tert*-butyl *N*,*N*-diisopropylphosphoramidite ($(^tBuO)_2PN(^iPr)_2$) and 1-*H*-tetrazole, followed by *tert*-butyl hydroperoxide (^{t}BuOOH) oxidation of the phosphite to phosphate, compounds **10a–c** (58–62%) were obtained. Recent studies report on the use of the soluble 5-phenyl-1-*H*-tetrazole as activator for the phosphitylation step [49,50]; but, in our hands, it did not furnish satisfying yields of the phosphate-protected nucleotides. The deprotection of both phosphate and 2′,3′-*O*-ribose protecting groups at the final stage of the synthesis was carried out using an aqueous solution of trifluoroacetic acid (TFA). This process proceeded smoothly and could be easily monitored by TLC, allowing the recovery of quantitative yields of the nucleotides **11a–c**. Conversely, to obtain compounds **14a–c**, intermediates **8a–c** were phosphorylated to give the derivatives **12a–c** (57–60% over two steps). Desilylation with TBAF of **12a–c** to afford **13a–c**, followed by the usual acidic treatment, yielded compounds **14a–c** almost quantitatively. For the synthesis of nucleotide **16** (Scheme 2), we started from the intermediate **15**, useful for the synthesis of cpIMP **4** [36]. The acidic treatment on **15** afforded directly the target **16** (99% yield). As verified by reverse-phase HPLC [51], the derivatives **11a–c**, **14a–c**, and **16** were pure. Differently, the aqueous TFA treatment of the protected phosphonate **17** (Scheme 2), the precursor of cpIPP **5** [37], led to a complex mixture from which compound **18** was isolated in 50% yield. This low yield could be, therefore, attributable to the lower acidic resistance of the phosphonate compared with the phosphate moiety.

To evaluate the stability of the synthesized compounds, **11a–c**, **14a–c**, **16**, and **18** were dissolved in a phosphate buffered solution (pH = 7.4) and stored at room temperature. The comparison of the HPLC profiles obtained by injecting samples after 24, 48, and 72 h showed no appreciable decomposition of all tested compounds (data not shown).

2.2. Biology

The compounds **11a–c**, **14a–c**, **16**, and **18** were tested to evaluate their ability to mobilize Ca^{2+} ions from ryanodine receptor expressing stores of C2C12 cells (Figure 2) [52]. At first, to verify that the system worked, differentiated C2C12 cells were loaded with Fura-2 and treated with caffeine. An increase of cytosolic [Ca^{2+}] was observed, as verified by the increase of the 340/380 fluorescence ratio of cytosolic Fura-2. The molecules were tested, probing concentrations from 0.1 up to 20 μM, though no effect was observed on the cytosolic [Ca^{2+}].

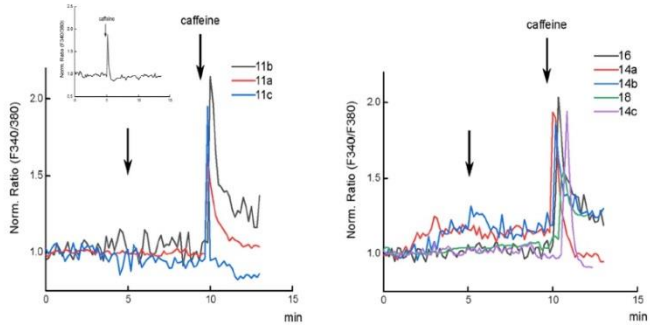

Figure 2. Effect of compounds **11a–c** (left), **14a–c**, **16**, and **18** (right) on cytosolic [Ca^{2+}]. Representative traces of normalized Fura-2 fluorescence ratio for differentiated C2C12 cells. 1 μM of each compound was added, then 10 mM caffeine was added 5 min after the addition of each compound as a control for Ca^{2+} release from ryanodine receptors. The inset in the left panel shows 10 mM caffeine addition to untreated cells.

Compounds **11b** and **16**, at the concentration of 1 μM, appear to enhance the effect of caffeine on the Ca^{2+} release from the stores (see Supplementary Materials, Figure S3). This effect could be ascribed to a stimulus of Ca^{2+} release from the ER, increasing the Ca^{2+} sensitivity of ryanodine receptors [53,54]. The Ca^{2+}-induced Ca^{2+} release (CICR) mediated by ryanodine receptors is a very important mechanism for the amplification of the Ca^{2+} signal in several mammalian cells, such as neurons, astrocytes, and pancreatic β-cells [55]. It could be not excluded that the amplification of the Ca^{2+} signal depends on CICR through other channels located either in the plasma or in intracellular store membranes, as a consequence of reticulum emptying.

3. Materials and Methods

3.1. General Experimental Procedures

All the reagents and solvents for the chemical syntheses were obtained from commercial sources and used without further purification. The ^{1}H- and ^{13}C-NMR experiments were performed using the Varian Mercury Plus 400 MHz and ^{UNITY}INOVA 500 MHz spectrometers and $CDCl_3$, CD_3OD, C_6D_6, and D_2O as solvents. The NMR chemical shifts are reported in parts per million (δ) relative to residual solvents signals: $CHCl_3$ 7.27, CD_2HOD 3.31, C_6D_5H 7.15, HOD 4.80 for ^{1}H-NMR and $CDCl_3$ 77.0, CD_3OD 49.0, C_6D_6 128.1 for ^{13}C NMR. The ^{1}H-decoupled ^{31}P-NMR experiments were carried out on a Varian ^{UNITY}INOVA 500 MHz instrument in $CDCl_3$, D_2O, and C_6D_6 solvents using 85% H_3PO_4 as an external standard (0 ppm). The ^{1}H-NMR chemical shifts were assigned through 2D NMR experiments. Electrospray ionization (ESI) mass spectra were recorded on an AB SCIEX QTRAP 4000 spectrometer. All NMR spectra were processed using the iNMR software package (http://www.inmr.net; release 6.2.1).

Column chromatography was carried out on silica gel-60 with particle size of 0.063–0.200 mm (Merck, Darmstatd, Germany). Analytical TLC analyses were performed using F254 silica gel plates of 0.2 mm thick (Merck, Darmstatd, Germany). The TLC spots were detected under UV light (254 nm). High-performance liquid chromatography (HPLC) was performed on a Jasco UP-2075 Plus pump equipped with a Jasco UV-2075 Plus UV detector using a 4.8 × 150 mm C-18 reverse-phase column (particle size 5 μm) eluted with a linear gradient of CH_3CN in 0.1 M triethylammonium bicarbonate (TEAB) buffer (from 0 to 100% in 60 min, flow 2.0 mL/min). The C2C12 cell line was cultured in DMEM medium (Merck, Darmstatd, Germany) supplemented with 10% fetal bovine serum, 2 mM L-glutamine, and incubated at 37 °C in a controlled atmosphere with 5% CO_2. For Ca^{2+} measurements, the cells were plated on 24 mm glass coverslip treated with 2% gelatin and differentiated by culturing in DMEM supplemented with 5% horse serum and 2 mM L-glutamine for 5–7 days. Statistical analyses (Mann–Whitney non-parametric test) were performed on Origin 2019b software package (www.originlab.com).

3.2. Chemistry

3.2.1. General Procedure for the Preparation of Compounds **8a–c**

In a typical experiment, compound **6** [36] (0.20 g, 0.34 mmol) was dissolved in DMF (1.0 mL) and treated with the amino alcohol **7a** (0.16 mL, 1.7 mmol). The reaction was stirred at 50 °C for 16 h and then evaporated under reduced pressure (TLC monitoring: $CHCl_3$/MeOH; 95:5). The crude containing compound **8a** was purified through a column of silica gel eluted with increasing amounts of MeOH in $CHCl_3$ (up to 2%). The fractions containing the product were collected and evaporated to afford the pure **8a**.

8a: Oil (70% yield). ^{1}H NMR (400 MHz, $CDCl_3$) δ 8.03 (s, 2H, 2-H and 8-H), 6.10 (d, *J* = 2.3 Hz, 1H, 1′-H), 5.07 (dd, *J* = 5.9, 2.4 Hz, 1H, 2′-H), 4.89 (dd, *J* = 5.9, 1.9 Hz, 1H, 3′-H), 4.44–4.40 (m, 1H, 4′-H), 4.18–4.04 (m, 2H, CH_2N), 3.86 (dd, *J* = 11.3, 3.2 Hz, 1H, 5′-H_a), 3.77 (dd, *J* = 11.4, 3.5 Hz, 1H, 5′-H_b), 3.69 (t, *J* = 6.1 Hz, 2H, CH_2O), 2.63 (bs, 1H, OH, exchange with D_2O), 1.91–1.84 (m, 2H, CH_2), 1.65–1.56 (complex signal, 5H, CH_3 and CH_2), 1.38 (s, 3H, CH_3), 0.83 (s, 9H, ^{t}Bu), 0.027 (s, 3H, $SiCH_3$), 0.01 (s, 3H, $SiCH_3$). ^{13}C NMR (100 MHz, $CDCl_3$) δ 156.6, 147.3, 147.0, 138.4, 124.8, 114.2, 91.4, 87.1, 85.4, 81.3, 63.5, 61.8, 46.7, 29.1, 27.2, 26.5, 25.8, 25.3, 18.3, −5.40, −5.60. ESI-MS *m/z* 495 ([M + H]$^+$, $C_{23}H_{39}N_4O_6Si$, requires 495).

8b: Oil (85% yield).^{1}H NMR (400 MHz, $CDCl_3$) δ 8.02 (s, 1H, 2-H), 7.98 (s, 1H, 8-H), 6.09 (d, *J* = 2.0 Hz, 1H, 1′-H), 5.06 (dd, *J* = 5.6, 2.4 Hz, 1H, 2′-H), 4.91–4.85 (m, 1H, 3′-H), 4.43–4.38 (m, 1H, 4′-H), 4.12–3.99 (m, 2H, CH_2N), 3.84 (dd, *J* = 11.2, 2.7 Hz, 1H, 5′-H_a), 3.76 (dd, *J* = 11.3, 3.1 Hz, 1H, 5′-H_b), 3.61 (t, *J* = 5.9 Hz, 2H, CH_2O), 2.52 (bs, 1H, OH, exchange with D_2O), 1.84–1.73 (m, 2H, CH_2), 1.64–1.52 (complex signal, 5H, CH_3 and CH_2), 1.46–1.34 (complex signal, 5H, CH_3 and CH_2), 0.82 (s, 9H, ^{t}Bu), 0.02 (s, 3H, $SiCH_3$), 0.00 (s, 3H, $SiCH_3$). ^{13}C NMR (100 MHz, $CDCl_3$) δ 156.5, 147.2, 146.9, 138.3, 124.8, 114.1, 91.4, 87.0, 85.4, 81.3, 63.5, 62.1, 46.9, 32.0, 29.6, 27.2, 25.8, 25.3, 22.7, 18.3, −5.40, −5.60. ESI-MS *m/z* 509 ([M + H]$^+$, $C_{24}H_{41}N_4O_6Si$, requires 509).

8c: Oil (84% yield).^{1}H NMR (400 MHz, $CDCl_3$) δ 8.02 (s, 1H, 2-H), 7.96 (s, 1H, 8-H), 6.10 (d, *J* = 2.4 Hz, 1H, 1′-H), 5.06 (dd, *J* = 6.0, 2.5 Hz, 1H, 2′-H), 4.88 (dd, *J* = 5.9, 2.1 Hz, 1H, 3′-H), 4.45–4.39 (m, 1H, 4′-H), 4.12–3.96 (m, 2H, CH_2N), 3.85 (dd, *J* = 11.3, 3.2 Hz, 1H, 5′-H_a), 3.76 (dd, *J* = 11.3, 3.5 Hz, 1H, 5′-H_b), 3.61 (t, *J* = 6.5 Hz, 2H, CH_2O), 2.01 (bs, 1H, OH, exchange with D_2O), 1.82–1.71 (m, 2H, CH_2), 1.61 (s, 3H, CH_3), 1.58–1.49 (m, 2H, CH_2), 1.41–1.34 (complex signal, 7H, CH_3 and 2 × CH_2), 0.82 (s, 9H, ^{t}Bu), 0.02 (s, 3H, $SiCH_3$), 0.01 (s, 3H, $SiCH_3$). ^{13}C NMR (100 MHz, $CDCl_3$) δ 156.5, 147.2, 146.9, 138.3, 124.9, 114.2, 91.4, 87.0, 85.4, 81.3, 63.5, 62.5, 46.8, 32.4, 29.8, 27.2, 26.2, 25.3, 25.2, 18.3, −5.40, −5.50. ESI-MS *m/z* 523 ([M + H]$^+$, $C_{25}H_{43}N_4O_6Si$, requires 523).

3.2.2. General Procedure for the Preparation of Compounds **9a–c**

In a typical experiment, to a solution of compound **8a** (0.12 g, 0.24 mmol) in dry THF (1.0 mL), TBAF (0.29 mL of a 1.0 M solution in dry THF, 0.29 mmol) was added dropwise. The reaction mixture was stirred at room temperature for 1 h (TLC monitoring: AcOEt/MeOH; 9:1) and then evaporated under reduced pressure. The residue was purified over a silica gel column eluted with increasing amounts of MeOH in AcOEt (up to 5%) to afford the pure **9a**.

9a: Oil (99% yield). ^{1}H NMR (400 MHz, CD_3OD) δ 8.32 (s, 1H, 2-H), 8.30 (s, 1H, 8-H), 6.15 (d, *J* = 3.0 Hz, 1H, 1′-H), 5.25 (dd, *J* = 6.1, 3.0 Hz, 1H, 2′-H), 5.00 (dd, *J* = 6.1, 2.5 Hz, 1H, 3′-H), 4.36–4.30 (m, 1H, 4′-H), 4.12 (t, *J* = 7.3 Hz, 2H, CH_2N), 3.75 (dd, *J* = 11.9, 2.8 Hz, 1H, 5′-H_a), 3.70 (dd, *J* = 11.9, 4.4 Hz, 1H, 5′-H_b), 3.59 (t, *J* = 6.4 Hz, 2H, CH_2O), 1.89–1.78 (m, 2H, CH_2), 1.63–1.53 (complex signal, 5H, CH_3 and CH_2), 1.36 (s, 3H, CH_3). ^{13}C NMR (100 MHz, CD_3OD) δ 158.1, 149.7, 148.5, 141.3, 125.2, 115.2, 92.3, 88.4, 85.8, 82.8, 63.3, 62.3, 47.8, 30.4, 27.5, 27.3, 25.5. ESI-MS *m/z* 381 ([M + H]$^+$, $C_{17}H_{25}N_4O_6$, requires 381).

9b: Oil (99% yield). ^{1}H NMR (400 MHz, CD_3OD) δ 8.32 (s, 1H, 2-H), 8.31 (s, 1H, 8-H), 6.15 (d, *J* = 3.0 Hz, 1H, 1′-H), 5.24 (dd, *J* = 6.0, 3.0 Hz, 1H, 2′-H), 4.99 (dd, *J* = 6.0, 2.5 Hz, 1H, 3′-H), 4.37–4.31 (m, 1H, 4′-H), 4.09 (t, *J* = 7.3 Hz, 2H, CH_2N), 3.72 (dd, *J* = 12.0, 3.8 Hz, 1H, 5′-H_a), 3.70 (dd, *J* = 12.0, 4.4 Hz, 1H, 5′-H_b), 3.55 (t, *J* = 6.4 Hz, 2H, CH_2O), 1.84–1.74 (m, 2H, CH_2), 1.62–1.53 (complex signal, 5H, CH_3 and CH_2), 1.48–1.38 (m, 2H, CH_2), 1.36 (s, 3H, CH_3). ^{13}C NMR (100 MHz, CD_3OD) δ 158.1, 149.6, 148.5, 141.2, 125.3, 115.2, 92.3, 88.4, 85.8, 82.8, 63.3, 62.5, 47.9, 33.1, 30.4, 27.5, 25.5, 23.9. ESI-MS *m/z* 395 ([M + H]$^+$, $C_{18}H_{27}N_4O_6$, requires 395).

9c: Oil (99% yield). ^{1}H NMR (400 MHz, CD_3OD) δ 8.31 (s, 1H, 2-H), 8.30 (s, 1H, 8-H), 6.15 (d, *J* = 2.9 Hz, 1H, 1′-H), 5.25 (dd, *J* = 6.0, 3.0 Hz, 1H, 2′-H), 5.00 (dd, *J* = 6.0, 2.5 Hz, 1H, 3′-H), 4.37–4.30 (m, 1H, 4′-H), 4.09 (t, *J* = 7.3 Hz, 2H, CH_2N), 3.75 (dd, *J* = 11.9, 3.8 Hz, 1H, 5′-H_a), 3.70 (dd, *J* = 11.9, 4.4 Hz, 1H, 5′-H_b), 3.53 (t, *J* = 6.5 Hz, 2H, CH_2O), 1.83–1.72 (m, 2H, CH_2), 1.58 (s, 3H, CH_3), 1.56–1.49 (m, 2H, CH_2), 1.45–1.38 (m, 4H, 2 × CH_2), 1.36 (s, 3H, CH_3). ^{13}C NMR (100 MHz, CD_3OD) δ 158.1, 149.6, 148.5, 141.2, 125.2, 115.2, 92.3, 88.4, 85.8, 82.8, 63.3, 62.7, 47.9, 33.4, 30.7, 27.5, 27.3, 26.5, 25.5. ESI-MS *m/z* 409 ([M + H]$^+$, $C_{19}H_{29}N_4O_6$, requires 409).

3.2.3. General Procedure for the Preparation of Compounds **10a–c**

In a typical experiment, to a solution of compound **9a** (0.050 g, 0.13 mmol) in dry THF (2.0 mL), 1-*H*-tetrazole (0.065 g, 0.91 mmol) and then $^{i}Pr_2NP(O^{t}Bu)_2$ (0.57 mL, 1.8 mmol) were added under nitrogen atmosphere. The reaction mixture was stirred at room temperature for 6 h (TLC monitoring: AcOEt/MeOH, 9:1) and then ^{t}BuOOH (0.24 mL of a solution 5.5 M in decane, 1.3 mmol) was added at room temperature. After 1 h (TLC monitoring: AcOEt/MeOH, 9:1), the reaction mixture was evaporated under reduced pressure, diluted with AcOEt (10 mL), and washed with brine (10 mL). The organic layer was dried over anhydrous Na_2SO_4, filtered, and evaporated under reduced pressure. The residue was purified over a silica gel column eluted with increasing amounts of MeOH in AcOEt (up to 5%) to afford pure **10a**.

10a: Oil (60% yield over two steps). ^{1}H NMR (400 MHz, $CDCl_3$) δ 8.02 (s, 1H, 2-H), 7.98 (s, 1H, 8-H), 6.11 (d, *J* = 2.7 Hz, 1H, 1′-H), 5.19 (dd, *J* = 6.1, 2.8 Hz, 1H, 2′-H), 5.02 (dd, *J* = 6.1, 2.6 Hz, 1H, 3′-H), 4.50–4.46 (m, 1H, 4′-H), 4.20–4.05 (complex signal, 4H, CH_2OP, 5′-$H_{a,b}$), 4.03–3.95 (m, 2H, CH_2N), 1.95–1.85 (m, 2H, CH_2), 1.78–1.68 (m, 2H, CH_2), 1.63 (s, 3H, CH_3), 1.47 (s, 27H, 3 × $O^{t}Bu$), 1.44 (s, 9H, $O^{t}Bu$), 1.38 (s, 3H, CH_3). ^{13}C NMR (100 MHz, $CDCl_3$) δ 156.4, 147.3, 147.0, 138.5, 125.0, 114.6, 90.6, 84.8 (d, *J* = 8.3 Hz), 84.6, 83.1 (d, *J* = 7.4 Hz), 83.0 (d, *J* = 7.2 Hz), 82.3 (d, *J* = 7.3 Hz), 81.3, 66.0 (d, *J* = 6.1 Hz), 65.9 (d, *J* = 6.5 Hz), 46.3, 29.9, 29.8, 29.7, 27.2, 26.2, 25.3. ^{31}P NMR (202 MHz, $CDCl_3$) δ −9.80 (s). ESI-MS *m/z* 765 ([M + H]$^+$, $C_{33}H_{59}N_4O_{12}P_2$, requires 765).

10b: Oil (58% yield over two steps). ^{1}H NMR (400 MHz, $CDCl_3$) δ 7.97 (s, 1H, 2-H), 7.96 (s, 1H, 8-H), 6.09 (d, *J* = 2.8 Hz, 1H, 1′-H), 5.18 (dd, *J* = 6.2, 2.9 Hz, 1H, 2′-H), 5.01 (dd, *J* = 6.2, 2.8 Hz, 1H, 3′-H),

4.49–4.43 (m, 1H, 4′-H), 4.18–4.10 (m, 2H, 5′-$H_{a,b}$), 4.08–3.97 (m, 2H, CH_2OP), 3.96–3.89 (m, 2H, CH_2N), 1.85–1.75 (m, 2H, CH_2), 1.73–1.65 (m, 2H, CH_2), 1.61 (s, 3H, CH_3), 1.45 (s, 29H, 3 × O^{t}Bu and CH_2), 1.42 (s, 9H, O^{t}Bu), 1.36 (s, 3H, CH_3). ^{13}C NMR (100 MHz, $CDCl_3$) δ 156.4, 147.2, 147.0, 138.5, 125.0, 114.6, 90.6, 84.8 (d, *J* = 8.4), 84.6, 83.1 (d, *J* = 7.4), 83.0 (d, *J* = 7.3), 82.1 (d, *J* = 7.3), 81.3, 66.3 (d, *J* = 6.4), 66.0 (d, *J* = 5.5), 46.8, 29.3, 29.8, 29.7, 29.4, 27.2, 25.3, 22.8. ^{31}P NMR (202 MHz, $CDCl_3$) δ –9.70 (s), –9.80 (s). ESI-MS *m/z* 779 ($[M + H]^+$, $C_{34}H_{61}N_4O_{12}P_2$, requires 779).

10c: Oil (62% yield over two steps). ^{1}H NMR (400 MHz, $CDCl_3$) δ 7.98 (s, 1H, 2-H), 7.97 (s, 1H, 8-H), 6.11 (d, *J* = 2.8 Hz, 1H, 1′-H), 5.20 (dd, *J* = 6.2, 2.8 Hz, 1H, 2′-H), 5.02 (dd, *J* = 6.2, 2.7 Hz, 1H, 3′-H), 4.50–4.46 (m, 1H, 4′-H), 4.19–4.10 (m, 2H, 5′-$H_{a,b}$), 4.08–4.00 (m, 2H, CH_2OP), 3.97–3.90 (m, 2H, CH_2N), 1.83–1.74 (m, 2H, CH_2), 1.70–1.61 (complex signal, 5H, CH_2 and CH_3), 1.47 (s, 31H, 3 × O^{t}Bu and 2 × CH_2), 1.43 (s, 9H, O^{t}Bu), 1.38 (s, 3H, CH_3). ^{13}C NMR (100 MHz, $CDCl_3$) δ 156.4, 147.2, 147.0, 138.5, 125.0, 114.6, 90.6, 84.8 (d, *J* = 8.4), 84.6, 83.1 (d, *J* = 7.4), 83.0 (d, *J* = 7.3), 82.0 (d, *J* = 7.4), 81.3, 66.5 (d, *J* = 6.4), 66.0 (d, *J* = 5.6), 46.9, 30.0, 29.9, 29.8, 29.7, 27.2, 26.2, 25.3, 25.2. ^{31}P NMR (202 MHz, $CDCl_3$) δ –9.70 (s), –9.80 (s). ESI-MS *m/z* 793 ($[M + H]^+$, $C_{35}H_{63}N_4O_{12}P_2$, requires 793).

3.2.4. General Procedure for the Preparation of Compounds **11a–c**

In a typical experiment, compound **10a** (0.020 g, 0.026 mmol) was dissolved in a 1:1 (v/v) solution of TFA in H_2O (1.0 mL) at 0 °C [56]. The reaction mixture was warmed to room temperature, stirred for 4 h (TLC monitoring: ^{i}PrOH/NH_3(aq)/H_2O, 6:3:1) and then lyophilized.

11a: White foam (99% yield). ^{1}H NMR (500 MHz, D_2O) δ 9.08 (s, 1H, 2-H), 8.54 (s, 1H, 8-H), 6.23 (d, *J* = 3.8 Hz, 1H, 1′-H), 4.76–4.72 (m, 1H, 2′-H), 4.52–4.47 (m, 1H, 3′-H), 4.45–4.40 (m, 1H, 4′-H), 4.30–4.24 (m, 1H, 5′-H_a), 4.23–4.13 (complex signal, 3H, CH_2OP, 5′-H_b), 4.01–3.95 (m, 2H, CH_2N), 1.96–1.86 (m, 2H, CH_2), 1.77–1.68 (m, 2H, CH_2). ^{13}C NMR (100 MHz, D_2O) δ 155.1, 150.9, 146.3, 138.5, 118.2, 89.6, 83.9 (d, *J* = 8.5 Hz), 74.7, 69.4, 65.9 (d, *J* = 5.3 Hz), 63.9 (d, *J* = 4.5 Hz), 47.2, 26.5 (d, *J* = 6.8 Hz), 25.0. ^{31}P NMR (202 MHz, D_2O) δ 0.00 (s), −0.08 (s). ESI-MS *m/z* 499 ($[M - H]^-$, $C_{14}H_{21}N_4O_{12}P_2$, requires 499).

11b: White foam (99% yield). ^{1}H NMR (500 MHz, D_2O) δ 9.06 (s, 1H, 2-H), 8.47 (s, 1H, 8-H), 6.17 (d, *J* = 3.7 Hz, 1H, 1′-H), 4.68–4.65 (m, 1H, 2′-H), 5.51–4.47 (m, 1H, 3′-H), 4.37–4.33 (m, 1H, 4′-H), 4.21 (ddd, *J* = 11.9, 4.4, 2.4 Hz, 1H, 5′-H_a), 4.13–4.07 (complex signal, 3H, CH_2OP, 5′-H_b), 3.91–3.86 (m, 2H, CH_2N), 1.80–1.72 (m, 2H, CH_2), 1.67–1.58 (m, 2H, CH_2), 1.42–1.33 (m, 2H, CH_2). ^{13}C NMR (100 MHz, D_2O) δ 154.9, 150.9, 146.1, 138.3, 117.9, 89.5, 83.8 (d, *J* = 8.6 Hz), 74.6, 69.2, 66.2 (d, *J* = 5.2 Hz), 63.7 (d, *J* = 3.8 Hz), 47.4, 28.9 (d, *J* = 6.8 Hz), 27.9, 21.6. ^{31}P NMR (202 MHz, D_2O) δ −0.03 (s), −0.14 (s). ESI-MS *m/z* 513 ($[M - H]^-$, $C_{15}H_{23}N_4O_{12}P_2$, requires 513).

11c: White foam (99% yield). ^{1}H NMR (500 MHz, D_2O) δ 9.05 (s, 1H, 2-H), 8.46 (s, 1H, 8-H), 6.17 (d, *J* = 3.7 Hz, 1H, 1′-H), 4.69–4.65 (m, 1H, 2′-H), 4.44–4.40 (m, 1H, 3′-H), 4.37–4.33 (m, 1H, 4′-H), 4.21 (ddd, *J* = 11.9, 4.0, 2.5 Hz, 1H, 5′-H_a), 4.13–4.06 (complex signal, 3H, CH_2OP, 5′-H_b), 3.90–3.84 (m, 2H, CH_2N), 1.78–1.68 (m, 2H, CH_2), 1.62–1.54 (m, 2H, CH_2), 1.40–1.28 (m, 4H, 2 × CH_2). ^{13}C-NMR (101 MHz; D_2O): δ 156.0, 150.4, 146.8, 138.8, 117.5, 88.9, 84.0 (d, *J* = 8.8 Hz), 74.7, 69.7, 66.3 (d, *J* = 5.5 Hz), 64.0 (d, *J* = 4.6 Hz), 47.6, 29.4 (d, *J* = 6.6 Hz), 28.4, 25.1, 24.4. ^{31}P NMR (202 MHz, D_2O) δ −0.03 (s), −0.14 (s). ESI-MS *m/z* 527 ($[M - H]^-$, $C_{16}H_{25}N_4O_{12}P_2$, requires 527).

3.2.5. General Procedure for the Preparation of Compounds **12a–c**

In a typical experiment, to a solution of compound **8a** (0.050 g, 0.13 mmol) in dry THF (2.0 mL), 1-*H*-tetrazole (0.028 g, 0.40 mmol) and then ^{i}Pr$_2$NP(O^{t}Bu)$_2$ (0.29 mL, 0.91 mmol) were added under nitrogen atmosphere. The reaction mixture was stirred at room temperature for 6 h (TLC monitoring: AcOEt/MeOH, 95:5) and then ^{t}BuOOH (0.24 mL of a solution 5.5 M in decane, 1.3 mmol) was added at room temperature. After 1 h (TLC monitoring: AcOEt/MeOH, 95:5), the reaction mixture was evaporated under reduced pressure, diluted with AcOEt (10 mL), and washed with brine (10 mL). The organic layer was dried over anhydrous Na_2SO_4, filtered, and evaporated under reduced pressure.

The residue was purified over a silica gel column eluted with increasing amounts of AcOEt in CH_2Cl_2 (up to 50%) to afford pure **12a**.

12a: Oil (57% yield over two steps). ^{1}H NMR (400 MHz, C_6D_6) δ 7.80 (s, 1H, 2-H), 7.37 (s, 1H, 8-H), 6.15 (d, *J* = 2.1 Hz, 1H, 1′-H), 5.08 (dd, *J* = 6.2, 2.2 Hz, 1H, 2′-H), 4.93 (dd, *J* = 6.1, 3.0 Hz, 1H, 3′-H), 4.36–4.32 (m, 1H, 4′-H), 3.88–3.80 (m, 2H, CH_2N), 3.65 (dd, *J* = 11.1, 4.7 Hz, 1H, 5′-H_a), 3.60–3.49 (complex signal, 3H, CH_2OP, 5′-H_b), 1.63–1.53 (m, 2H, CH_2), 1.50 (s, 3H, CH_3), 1.41 (s, 18H, 2 × O^{t}Bu), 1.37–1.28 (m, 2H, CH_2), 1.21 (s, 3H, CH_3), 0.87 (s, 9H, ^{t}Bu), −0.04 (s, 3H, $SiCH_3$), −0.06 (s, 3H, $SiCH_3$). ^{13}C NMR (100 MHz, C_6D_6) δ 155.9, 147.0, 138.2, 125.5, 113.6, 90.4, 87.1, 85.1, 81.5, 81.1, 81.0, 65.6 (d, *J* = 6.1 Hz), 63.3, 45.5, 29.8, 29.6, 29.5, 27.0, 25.9, 25.6, 25.1, 18.1, −5.70, −5.80. ^{31}P NMR (202 MHz, C_6D_6) δ −8.50 (s). ESI-MS *m/z* 687 ([M + H]$^+$, $C_{31}H_{56}N_4O_9PSi$, requires 687).

12b: Oil (61% yield over two steps). ^{1}H NMR (400 MHz, C_6D_6) δ 7.81 (s, 1H, 2-H), 7.28 (s, 1H, 8-H), 6.16 (d, *J* = 2.2 Hz, 1H, 1′-H), 5.07 (dd, *J* = 6.2, 2.2 Hz, 1H, 2′-H), 4.92 (dd, *J* = 6.1, 2.9 Hz, 1H, 3′-H), 4.35–4.32 (m, 1H, 4′-H), 3.90–3.84 (m, 2H, CH_2N), 3.65 (dd, *J* = 11.1, 4.7 Hz, 1H, 5′-H_a), 3.52 (dd, *J* = 11.1, 4.4 Hz, 1H, 5′-H_b), 3.50–3.38 (m, 2H, CH_2OP), 1.50 (s, 3H, CH_3), 1.43 (s, 18H, 2 × O^{t}Bu), 1.42–1.32 (m, 4H, 2 × CH_2), 1.21 (s, 3H, CH_3), 1.13–1.04 (m, 2H, CH_2), 0.86 (s, 9H, ^{t}Bu), −0.04 (s, 3H, $SiCH_3$), −0.06 (s, 3H, $SiCH_3$). ^{13}C NMR (100 MHz, C_6D_6) δ 156.8, 147.9, 147.8, 139.1, 126.5, 114.6, 91.4, 88.1, 86.0, 82.4, 81.9 (d, *J* = 6.7 Hz), 66.9 (d, *J* = 6.1 Hz), 64.3, 47.0, 30.6, 30.5, 30.4, 29.9, 28.0, 26.6, 26.1, 23.4, 19.1, −4.70, −4.80. ^{31}P NMR (202 MHz, C_6D_6) δ −8.50 (s). ESI-MS *m/z* 701 ([M + H]$^+$, $C_{32}H_{58}N_4O_9PSi$, requires 701).

12c: Oil (60% yield over two steps). ^{1}H NMR (400 MHz, C_6D_6) δ 7.77 (s, 1H, 2-H), 7.24 (s, 1H, 8-H), 6.16 (d, *J* = 1.8 Hz, 1H, 1′-H), 5.06 (dd, *J* = 6.1, 1.9 Hz, 1H, 2′-H), 4.91 (dd, *J* = 5.9, 2.7 Hz, 1H, 3′-H), 4.36–4.31 (m, 1H, 4′-H), 3.96–3.88 (m, 2H, CH_2N), 3.64 (dd, *J* = 11.0, 4.6 Hz, 1H, 5′-H_a), 3.51 (dd, *J* = 11.1, 4.4 Hz, 1H, 5′-H_b), 3.48–3.36 (m, 2H, CH_2OP), 1.50 (s, 3H, CH_3), 1.45 (s, 18H, 2 × O^{t}Bu), 1.40–1.30 (m, 4H, 2 × CH_2), 1.20 (s, 3H, CH_3), 1.15–1.09 (m, 2H, CH_2), 1.00–0.90 (m, 2H, CH_2), 0.86 (s, 9H, ^{t}Bu), −0.04 (s, 3H, $SiCH_3$), −0.07 (s, 3H, $SiCH_3$). ^{13}C NMR (100 MHz, C_6D_6) δ 156.8, 147.9, 147.8, 126.6, 114.6, 91.4, 88.1, 86.1, 82.4, 81.8 (d, *J* = 6.6 Hz), 67.1 (d, *J* = 6.1 Hz), 64.3, 47.0, 31.0, 30.1, 30.6, 30.5, 30.4, 28.0, 26.8, 26.6, 26.0, 19.0, −4.70, −4.80. ^{31}P NMR (202 MHz, C_6D_6) δ −8.4 (s). ESI-MS *m/z* 715 ([M + H]$^+$, $C_{33}H_{60}N_4O_9PSi$, requires 715).

3.2.6. General Procedure for the Reparation of Compounds **13a–c**

In a typical experiment, to a solution of compound **12a** (0.051 g, 0.074 mmol) in dry THF (1.0 mL), TBAF (0.089 mL of a 1.0 M solution in dry THF, 0.089 mmol) was added dropwise [57]. The reaction mixture was stirred at room temperature for 1 h (TLC monitoring: AcOEt/MeOH; 9:1) and then evaporated under reduced pressure. The residue was purified over a silica gel column eluted with increasing amounts of MeOH in AcOEt (up to 5%) to afford the pure **13a**.

13a: Glassy solid (99% yield). ^{1}H NMR (500 MHz, C_6D_6) δ 8.04 (s, 1H, 2-H), 7.28 (s, 1H, 8-H), 6.15 (d, *J* = 2.2 Hz, 1H, 1′-H), 5.10–5.05 (complex signal, 2H, 2′-H, 3′-H), 4.40–4.36 (m, 1H, 4′-H), 4.07 (d, *J* = 12.0 Hz, 1H, 5′-H_a), 3.87–3.80 (m, 2H, CH_2N), 3.75 (d, *J* = 11.9 Hz, 1H, 5′-H_b), 3.48 (t, *J* = 7.3 Hz, 2H, CH_2OP), 1.55–1.48 (complex signal, 5H, CH_2 and CH_3), 1.40 (s, 18H, 2 × O^{t}Bu), 1.37–1.29 (m, 2H, CH_2), 1.18 (s, 3H, CH_3). ^{13}C NMR (100 MHz, C_6D_6) δ 156.9, 148.1, 147.7, 140.2, 126.3, 114.3, 93.2, 87.8, 85.7, 82.9, 82.2 (d, *J* = 6.7 Hz), 66.6 (d, *J* = 6.0 Hz), 63.7, 46.6, 30.5, 30.4, 28.1 (d, *J* = 7.1 Hz), 27.9, 26.8, 25.9. ^{31}P NMR (202 MHz, C_6D_6) δ −8.70 (s). ESI-MS *m/z* 573 ([M + H]$^+$, $C_{25}H_{42}N_4O_9P$, requires 573).

13b: Amorphous white solid (99% yield). ^{1}H NMR (500 MHz, C_6D_6, 60 °C) δ 7.75 (s, 1H, 2-H), 7.20 (s, 1H, 8-H), 5.92 (d, *J* = 3.3 Hz, 1H, 1′-H), 5.13–5.08 (complex signal, 2H, 2′-H, 3′-H), 4.47–4.44 (m, 1H, 4′-H), 3.89–3.93 (m, 1H, 5′-H_a), 3.89–3.83 (m, 2H, CH_2N), 3.67 (d, *J* = 10.7 Hz, 1H, 5′-H_b), 3.49–3.38 (m, 2H, CH_2OP), 1.49 (s, 3H, CH_3), 1.46–1.38 (complex signal, 20H, CH_2, 2 × O^{t}Bu), 1.37–1.31 (m, 2H, CH_2), 1.18 (s, 3H, CH_3), 1.15–1.07 (m, 2H, CH_2). ^{13}C NMR (100 MHz, C_6D_6, 60 °C) δ 156.8, 148.0, 147.7, 140.2, 126.3, 114.3, 93.2, 87.8, 85.7, 82.9, 82.0, 66.9, 63.8, 47.1, 30.6, 30.5, 30.4, 29.8, 28.2, 25.9, 23.4. ^{31}P NMR (202 MHz, C_6D_6, 60 °C) δ −8.70 (s). ESI-MS *m/z* 587 ([M + H]$^+$, $C_{26}H_{44}N_4O_9P$, requires 587).

13c: Amorphous white solid (99% yield). ^{1}H NMR (500 MHz, C_6D_6, 60 °C) δ 7.70 (s, 1H, 2-H), 7.18 (s, 1H, 8-H), 5.90 (d, *J* = 3.5 Hz, 1H, 1′-H), 5.09–5.04 (complex signal, 2H, 2′-H, 3′-H), 4.39–4.35 (m, 1H, 4′-H), 3.97–3.88 (complex signal, 3H, 5′-H_a, CH_2N), 3.67 (d, *J* = 12.0 Hz, 1H, 5′-H_b), 3.43 (t, *J* = 7.3 Hz, 2H, CH_2OP), 1.49 (s, 3H, CH_3), 1.44 (s, 18H, 2 × O^{t}Bu), 1.40–1.29 (m, 4H, 2 × CH_2), 1.22–1.12 (complex signal, 5H, CH_2, CH_3), 1.03–0.95 (m, 2H, CH_2). ^{13}C NMR (100 MHz, C_6D_6, 60 °C) δ 156.8, 148.0, 147.7, 140.2, 126.3, 114.3, 93.2, 87.8, 85.7, 82.9, 82.0, 66.9, 63.8, 47.1, 30.6, 30.5, 30.4, 29.8, 28.2, 25.9, 23.4. ^{31}P NMR (202 MHz, C_6D_6, 60 °C) δ −8.70 (s). ESI-MS *m*/*z* 601 ([M + H]$^+$, $C_{27}H_{46}N_4O_9P$, requires 601).

3.2.7. General Procedure for the Preparation of Compounds **14a–c**

In a typical experiment, compound **13a** (0.020 g, 0.035 mmol) was dissolved in a 1:1 (v/v) solution of TFA in H_2O (1.0 mL) at 0 °C. The reaction mixture was warmed to room temperature, stirred for 4 h (TLC monitoring: ^{i}PrOH/NH_3(aq)/H_2O, 6:3:1) and then lyophilized.

14a: White foam (99% yield). ^{1}H NMR (500 MHz, D_2O) δ 9.09 (s, 1H, 2-H), 8.51 (s, 1H, 8-H), 6.16 (d, *J* = 4.2 Hz, 1H, 1′-H), 4.72–4.68 (m, 1H, 2′-H), 4.39–4.35 (m, 1H, 3′-H), 4.28–4.24 (m, 1H, 4′-H), 4.17 (t, *J* = 7.2 Hz, 2H, CH_2OP), 4.00–3.95 (m, 2H, CH_2N), 3.92 (dd, *J* = 13.0, 2.0 Hz, 1H, 5′-H_a), 3.82 (d, *J* = 12.8, 3.5 Hz, 1H, 5′-H_b), 1.91–1.83 (m, 2H, CH_2), 1.74–1.66 (m, 2H, CH_2). ^{13}C NMR (175 MHz, D_2O) δ 154.8, 151.0, 146.0, 138.8, 118.1, 89.8, 85.3, 74.1, 69.4, 66.0, 60.4, 47.1, 26.4, 24.9. ^{31}P NMR (202 MHz, D_2O) δ −0.14 (s). ESI-MS *m*/*z* 419 ([M − H]$^-$, $C_{14}H_{20}N_4O_9P$, requires 419).

14b: White foam (99% yield). ^{1}H NMR (500 MHz, D_2O) δ 9.01 (s, 1H, 2-H), 8.50 (s, 1H, 8-H), 6.16 (d, *J* = 4.4 Hz, 1H, 1′-H), 4.75–4.71 (m, 1H, 2′-H), 4.42–4.38 (m, 1H, 3′-H), 4.30–4.26 (m, 1H, 4′-H), 4.15 (t, *J* = 7.2 Hz, 2H, CH_2OP), 4.00–3.92 (complex signal, 3H, CH_2N, 5′-H_a), 3.84 (d, *J* = 12.8, 3.9 Hz, 1H, 5′-H_b), 1.86–1.78 (m, 2H, CH_2), 1.73–1.65 (m, 2H, CH_2), 1.48–1.39 (m, 2H, CH_2). ^{13}C NMR (175 MHz, D_2O) δ 155.2, 150.7, 146.2, 139.0, 118.9, 89.6, 85.3, 74.1, 69.6, 66.3, 60.5, 47.4, 28.9, 27.9, 21.6. ^{31}P NMR (202 MHz, D_2O) δ −0.04 (s). ESI-MS *m*/*z* 433 ([M − H]$^-$, $C_{15}H_{22}N_4O_9P$, requires 433).

14c: White foam (99% yield). ^{1}H NMR (500 MHz, D_2O) δ 8.92 (s, 1H, 2-H), 8.49 (s, 1H, 8-H), 6.16 (d, *J* = 4.4 Hz, 1H, 1′-H), 4.76–4.72 (m, 1H, 2′-H), 4.44–4.39 (m, 1H, 3′-H), 4.31–4.27 (m, 1H, 4′-H), 4.15 (t, *J* = 7.2 Hz, 2H, CH_2OP), 3.97–3.91 (complex signal, 3H, CH_2N, 5′-H_a), 3.84 (d, *J* = 12.8, 3.9 Hz, 1H, 5′-H_b), 1.84–1.76 (m, 2H, CH_2), 1.69–1.61 (m, 2H, CH_2), 1.46–1.34 (m, 4H, 2 × CH_2). ^{13}C NMR (175 MHz, D_2O) δ 155.6, 150.2, 146.3, 139.1, 119.5, 89.4, 85.3, 74.1, 69.5, 66.6, 60.6, 47.5, 29.2, 28.3, 25.0, 24.2. ^{31}P NMR (202 MHz, D_2O) δ 0.04 (s). ESI-MS *m*/*z* 447 ([M − H]$^-$, $C_{16}H_{24}N_4O_9P$, requires 447).

3.2.8. Procedure for the Preparation of Compound **16**

Compound **15** (0.020 g, 0.042 mmol) was dissolved in a 1:1 (v/v) solution of TFA in H_2O (0.5 mL) at 0 °C. The reaction mixture was warmed to room temperature, stirred for 4 h (TLC monitoring: ^{i}PrOH/NH_3(aq)/H_2O, 6:3:1) and then lyophilized. Colorless syrup (99% yield). ^{1}H-NMR (500 MHz; D_2O): δ 8.53 (s, 1H, 8-H), 8.42 (s, 1H, 2-H), 6.15 (d, *J* = 5.9 Hz, 1H, 1′-H), 4.84–4.78 (m, 1H, 2′-H, partially covered by residual solvent signal), 4.54 (dd, *J* = 4.9, 3.7 Hz, 1H, 3′-H), 4.41–4.40 (m, 1H, 4′-H), 4.18 (t, *J* = 7.3 Hz, 2H, CH_2N), 4.12–4.08 (m, 2H, 5′-$H_{a,b}$), 3.63 (t, *J* = 6.5 Hz, 2H, CH_2O), 1.88–1.82 (m, 2H, CH_2), 1.66–1.60 (m, 2H, CH_2), 1.47–1.40 (m, 2H, CH_2). ^{13}C-NMR (101 MHz; D_2O): δ 158.1, 148.9, 147.9, 139.9, 123.4, 87.2, 84.2 (d, *J* = 8.8 Hz), 74.4, 70.4, 64.3 (d, *J* = 4.8 Hz), 61.4, 47.3, 30.8, 28.5, 22.0. ^{31}P NMR (202 MHz, D_2O) δ 1.87 (s). ESI-MS *m*/*z* 433 ([M − H]$^-$, $C_{15}H_{22}N_4O_9P$, requires 433).

3.2.9. Procedure for the Preparation of Compound **18**

Compound **17** (0.040 g, 0.070 mmol) was dissolved in a 1:1 (v/v) solution of TFA in H_2O (0.5 mL) at 0 °C. The reaction mixture was warmed to room temperature, stirred for 4 h (TLC monitoring: ^{i}PrOH/NH_3(aq)/H_2O, 6:3:1), and then lyophilized. The crude was dissolved in TEAB 0.1 M buffer, passed over a PVDF 0.45 µm filter and purified by HPLC (see Section 3.1). The fractions containing the triethylammonium salt of compound **18** were collected and lyophilized. The salt was dissolved

in water and treated with Dowex D50 (H^+ form). Then, the resin was removed by filtration and the solution lyophilized. Colorless syrup (50% yield). ^{1}H-NMR (400 MHz; D_2O): δ 8.41 (s, 1H, 8-H), 8.33 (s, 1H, 2-H), 6.08 (d, *J* = 5.7 Hz, 1H, 1′-H), 4.80 (m, 1H, 2′-H, covered by residual solvent signal), 4.47–4.42 (m, 1H, 3′-H), 4.31–4.26 (m, 1H, 4′-H), 4.15 (t, *J* = 7.2 Hz, 2H, CH_2N), 3.92 (dd, *J* = 12.7, 2.8 Hz, 1H, 5′-H_a), 3.85 (dd, *J* = 12.8, 4.1 Hz, 1H, 5′-H_b), 1.86–1.77 (m, 2H), 1.65–1.53 (m, 4H), 1.48–1.41 (m, 2H). ^{13}C NMR (101 MHz; D_2O): δ 155.3, 150.6, 146.3, 139.2, 119.0, 89.7, 85.5, 74.3, 69.6, 60.6, 47.4, 28.0, 26.4 (*J* = 3.6 Hz), 25.7 (*J* = 121.3 Hz), 21.5 (*J* = 4.8 Hz). ^{31}P NMR (202 MHz; D_2O): δ 31.9. ESI-MS *m/z* 417 ($[M - H]^-$, $C_{15}H_{22}N_4O_8P$, requires 417).

3.3. Biology

Cytosolic Ca^{2+} Imaging

Differentiated C2C12 (days in vitro [DIV] 7) cells were incubated with 1 μM Fura-2/AM, 0.02% pluronic F-127, and 200 μM sulfinpyrazone for 40 minutes at 37 °C in an extracellular-like medium 135 mM NaCl, 5 mM KCl, 0.4 mM KH_2PO_4, 1 mM $MgCl_2$, 1 mM $MgSO_4$, 1 mM $CaCl_2$, 10 mM 4-[2-hydroxyethyl]-1-piperazineethanesulfonic acid, and 10 mM glucose at pH 7.4. Cells were mounted into an open-topped chamber and incubated for 10 minutes on the stage of the microscope, in the same saline without Fura-2/AM. Experiments were performed at 37 °C. Fura-2 fluorescence was visualized on an inverted microscope (Zeiss Axiovert 100, Jena, Germany) mounting a 20× ultraviolet permeable objective (Olympus Biosystems GmbH, Planegg, Germany). Alternating excitation wavelengths of 340 and 380 nm were obtained with a monochromator (polychrome V; TILL Photonics, Kaufbeuren, Germany) controlled by a custom-made software package, Roboscope (developed by Catalin Dacian Ciubotaru, CNR Neuroscience Institute, Padua, Italy). A neutral density filter, UVND 0.6 (Chroma Technology Corp., Bellows Falls, VT, USA), was used in the excitation pathway. The emitted fluorescence was measured at 500–530 nm. Images were acquired every 10 s, with 200 ms exposure time for each wavelength, by a TILL-Imago camera controlled by the same software. Regions of interest, corresponding to the entire soma, were selected for Ca^{2+} imaging. The ratio of the emitted fluorescence intensities (F340/F380) was normalized to the average value measured during the first 2 min of acquisition. The cells were challenged with different concentrations of target compounds diluted in the experimental medium; addition of 10 mM caffeine was used as a control for Ca^{2+} release from ryanodine receptors.

4. Conclusions

Cellular Ca^{2+} mobilization is involved in several physio-pathological processes, and the discovery of molecules that could act as agonist or antagonist of cADPR is an appealing goal for medicinal chemistry. cADPR has a unique structure, but its lability has strongly limited the comprehension of cellular mechanisms regulated by Ca^{2+} mobilization. Synthetic chemistry partially remedied this problem, generating more stable analogues whose preparation is very often laborious and low yielding. In our laboratories, we synthesized many cIDPR derivatives as stable mimics of cADPR, discovering that a pentyl chain replacing the "northern" ribose and one phosphate group could be sufficient to retain the biological activity in PC12 cells differentiated in neurons. In this paper, we probed if the cyclic structure was strictly necessary for the Ca^{2+} release from the intracellular stores, synthesizing a small collection of linear precursors of cIDPR analogues. By varying the length of the N1 purine alkyl chain and the position of the phosphate/phosphonate moieties, we obtained eight derivatives that were tested for the Ca^{2+} mobilizing activity on C2C12 cells that express ryanodine receptors during differentiation [52].

Unfortunately, we have not been able yet to detect any biological effect immediately after the drug addition to the cell culture. We also cannot establish if the lack of activity can be attributed to the absence of cyclic structure, to an inefficacious interaction with the cellular receptor or to a reduced cellular permeability. Furthermore, the reinforcement of the effect of caffeine on the Ca^{2+} release from

the stores by some compounds is intriguing and may be ascribed to a stimulus of Ca^{2+} release from the ER, increasing the Ca^{2+} sensitivity of ryanodine receptors. However, further studies are ongoing in our laboratories to check this assumption and to understand how the reinforcement mentioned above could take place. The most pronounced effect has been found in the linear compounds **14** and **16** characterized by a pentyl chain attached at the N1 position of inosine. These preliminary data reinforce our precedent findings [36,37] on the importance of the five carbon atoms alkyl chain for the design of novel linear and cyclic cADPR/cIDPR analogues to be employed as Ca^{2+} modulators.

Supplementary Materials: The following are available online at http://www.mdpi.com/1660-3397/17/8/476/s1, S1–S23: copies of ^{1}H-NMR and ^{31}P-NMR spectra of compounds **8a–c**, **9a–c**, **10a–c**, **11a–c**, **12a–c**, **13a–c**, **14a–c**, **16**, and **18**; S24–S46: copies of ^{13}C-NMR spectra of compounds **8a–c**, **9a–c**, **10a–c**, **11a–c**, **12a–c**, **13a–c**, **14a–c**, **16**, and **18**; S-47: Figure S3.

Author Contributions: S.D., G.O., G.P., and N.B. conceived and designed the experiments; S.D. performed the synthetic experiments; S.D., N.B., and M.M. performed the spectroscopic experiments and analyzed the data; E.B., A.P.F., and T.P. performed the biological experiments and analyzed the data; S.D., N.B., V.P., and G.O. wrote the paper.

Funding: This research was funded in part by Fondazione Cassa di Risparmio di Padova e Rovigo (Cariparo) - Progetti di Eccellenza 2017 (progetto GliAD) and by Ministero dell'Istruzione, dell'Università e della Ricerca (MIUR) – PRIN2017 (20175C22wm).

Acknowledgments: The authors are grateful to Luisa Cuorvo for her technical assistance.

Conflicts of Interest: The authors declare no conflict of interest.

References

1. Clapham, D.E. Calcium signaling. *Cell* **2007**, *14*, 1047–1068. [CrossRef] [PubMed]
2. Kramer, L. Intracellular Calcium. In *Signal Transduction*; Audet, J., Ed.; Elsevier: London, UK, 2016; pp. 381–439.
3. Barbado, M.; Fablet, K.; Ronjat, M.; De Waard, M. Gene regulation by voltage-dependent calcium channels. *Biochim. Biophys. Acta Mol. Cell Res.* **2009**, *1793*, 1096–1104. [CrossRef] [PubMed]
4. Pinto, M.C.X.; Kihara, A.H.; Goulart, V.A.M.; Tonelli, F.M.P.; Gomes, K.N.; Ulrich, H.; Resende, R.R. Calcium signaling and cell proliferation. *Cell. Signal.* **2015**, *27*, 2139–2149. [CrossRef] [PubMed]
5. Cho, C.H.; Woo, J.S.; Perez, C.F.; Lee, E.H. A focus on extracellular Ca2+ entry into skeletal muscle. *Exp. Mol. Med.* **2017**, *49*, e378. [CrossRef] [PubMed]
6. Neher, E.; Sakaba, T. Multiple roles of calcium ions in the regulation of neurotransmitter release. *Neuron* **2008**, *59*, 861–872. [CrossRef]
7. Clapper, D.L.; Walseth, T.F.; Dargie, P.J.; Lee, H.C. Pyridine nucleotide metabolites stimulate calcium release from sea urchin egg microsomes desensitized to inositol trisphosphate. *J. Biol. Chem.* **1987**, *262*, 9561–9568. [PubMed]
8. Takasawa, S.; Okamoto, H. Pancreatic β-cell death, regeneration and insulin secretion: Roles of poly(ADP-ribose) polymerase and cyclic ADP-ribose. *Int. J. Exp. Diabetes Res.* **2002**, *3*, 79–96. [CrossRef]
9. Guse, A.H.; Da Silva, C.P.; Berg, I.; Skapenko, A.L.; Weber, K.; Heyer, P.; Hohenegger, M.; Ashamu, G.A.; Schulze-Koops, H.; Potter, B.V.L.; et al. Regulation of calcium signalling in T lymphocytes by the second messenger cyclic ADP-ribose. *Nature* **1999**, *398*, 70–73. [CrossRef]
10. Gul, R.; Park, D.R.; Shawl, A.I.; Im, S.Y.; Nam, T.S.; Lee, S.H.; Ko, J.K.; Jang, K.Y.; Kim, D.; Kim, U.H. Nicotinic acid adenine dinucleotide phosphate (NAADP) and cyclic ADP-Ribose (cADPR) mediate Ca2+ signaling in cardiac hypertrophy induced by β-Adrenergic Stimulation. *PLoS ONE* **2016**, *11*, e0149125. [CrossRef]
11. Higashida, H.; Hashii, M.; Yokoyama, S.; Hoshi, N.; Asai, K.; Kato, T. Cyclic ADP-ribose as a potential second messenger for neuronal Ca2+ signaling. *J. Neurochem.* **2001**, *76*, 321–331. [CrossRef]
12. Guse, A.H. Second messenger function and the structure-activity relationship of cyclic adenosine diphosphoribose (cADPR). *FEBS J.* **2005**, *272*, 4590–4597. [CrossRef]
13. Fliegert, R.; Gasser, A.; Guse, A.H. Regulation of calcium signalling by adenine-based second messengers. *Biochem. Soc. Trans.* **2007**, *35*(PT 1), 109–114. [CrossRef]

14. Galione, A.; Cui, Y.; Empson, R.; Iino, S.; Wilson, H.; Terrar, D. Cyclic ADP-Ribose and the Regulation of Calcium-Induced Calcium Release in Eggs and Cardiac Myocytes. *Cell Biochem. Biophys.* **1998**, *28*, 19–30. [CrossRef]
15. Wei, W.; Graeff, R.; Yue, J. Roles and mechanisms of the CD38/cyclic adenosine diphosphate ribose/Ca(2+) signaling pathway. *World J. Biol. Chem.* **2014**, *5*, 58–67. [CrossRef]
16. Okamoto, H.; Takasawa, S.; Sugawara, A. The CD38-Cyclic ADP-Ribose System in Mammals: Historical Background, Pathophysiology and Perspective. *Messenger* **2014**, *3*, 27–34. [CrossRef]
17. Potter, B.V.L.; Walseth, T.F. Medicinal chemistry and pharmacology of cyclic ADP-ribose. *Curr. Mol. Med.* **2004**, *4*, 303–311. [CrossRef]
18. Rosen, D.; Bloor-Young, D.; Squires, J.; Parkesh, R.; Waters, G.; Vasudevan, S.R.; Lewis, A.M.; Churchill, G.C. Synthesis and use of cell-permeant cyclic ADP-ribose. *Biochem. Biophys. Res. Commun.* **2012**, *418*, 353–358. [CrossRef]
19. Guse, A.H.; Cakir-Kiefer, C.; Fukuoka, M.; Shuto, S.; Weber, K.; Bailey, V.C.; Matsuda, A.; Mayr, G.W.; Oppenheimer, N.; Schuber, F.; et al. Novel hydrolysis-resistant analogues of cyclic ADP-ribose: Modification of the "northern" ribose and calcium release activity. *Biochemistry* **2002**, *41*, 6744–6751. [CrossRef]
20. Swarbrick, J.M.; Graeff, R.; Garnham, C.; Thomas, M.P.; Galione, A.; Potter, B.V.L. 'Click cyclic ADP-ribose': A neutral second messenger mimic. *Chem. Commun.* **2014**, *50*, 2458–2461. [CrossRef]
21. Qi, N.; Jung, K.; Wang, M.; Na, L.X.; Yang, Z.J.; Zhang, L.R.; Guse, A.H.; Zhang, L.H. A novel membrane-permeant cADPR antagonist modified in the pyrophosphate bridge. *Chem. Commun.* **2011**, *47*, 9462–9464. [CrossRef]
22. Xu, J.; Yang, Z.; Dammermann, W.; Zhang, L.; Guse, A.H.; Zhang, L.H. Synthesis and agonist activity of cyclic ADP-ribose analogues with substitution of the northern ribose by ether or alkane chains. *J. Med. Chem.* **2006**, *49*, 5501–5512. [CrossRef]
23. Wang, X.; Zhang, X.; Zhang, K.; Hu, J.; Liu, Z.; Jin, H.; Zhang, L.; Zhang, L. Calcium mobilizing behaviors of neutral cyclic ADP-ribose mimics which integrate the modifications of nucleobase, northern ribose and pyrophosphate. *ChemBioChem* **2018**, *19*, 1444–1451. [CrossRef]
24. Guse, A. Biochemistry, Biology, and Pharmacology of Cyclic Adenosine Diphosphoribose (cADPR). *Curr. Med. Chem.* **2004**, *11*, 847–855. [CrossRef]
25. Guse, A.H. Structure-activity relationship of cyclic ADP-ribose, an update. *J. Chin. Pharm. Sci.* **2013**, *22*, 127–136. [CrossRef]
26. Wagner, G.K.; Guse, A.H.; Potter, B.V.L. Rapid synthetic route toward structurally modified derivatives of cyclic adenosine 5'-diphosphate ribose. *J. Org. Chem.* **2005**, *70*, 4810–4819. [CrossRef]
27. Zhang, L.; Yue, J.; Zhang, L.H. Cyclic adenosine 5'-diphosphoribose (cADPR) mimics used as molecular probes in cell signaling. *Chem. Rec.* **2015**, *15*, 511–523. [CrossRef]
28. Shuto, S.; Matsuda, A. Chemistry of Cyclic ADP-Ribose and Its Analogs. *Curr. Med. Chem.* **2004**, *11*, 827–845. [CrossRef]
29. Guse, A.H. The Ca2+-Mobilizing Second Messenger Cyclic ADP-Ribose. In *Calcium: The Molecular Basis of Calcium Action in Biology and Medicine*; Pochet, R., Donato, R., Haiech, J., Heizmann, C.W., Gerke, V., Eds.; Springer: The Netherlands, 2000; pp. 109–128. Available online: https://www.springer.com/gp/book/9780792364214 (accessed on 15 August 2019).
30. Galeone, A.; Mayol, L.; Oliviero, G.; Piccialli, G.; Varra, M. Synthesis of a New N1-Pentyl Analogue of Cyclic Inosine Diphosphate Ribose (cIDPR) as a Stable Potential Mimic of Cyclic ADP Ribose (cADPR). *Eur. J. Org. Chem.* **2002**, *2002*, 4234–4238. [CrossRef]
31. Galeone, A.; Mayol, L.; Oliviero, G.; Piccialli, G.; Varra, M. Synthesis of a novel N-1 carbocyclic, N-9 butyl analogue of cyclic ADP ribose (cADPR). *Tetrahedron* **2002**, *58*, 363–368. [CrossRef]
32. Oliviero, G.; Amato, J.; Varra, M.; Piccialli, G.; Mayol, L. Synthesis of a new N-9 ribityl analogue of cyclic inosine diphosphate ribose (cIDPR) as a mimic of cyclic ADP ribose (cADPR). *Nucleos. Nucleot. Nucl.* **2005**, *24*, 735–738. [CrossRef]
33. Oliviero, G.; Borbone, N.; Amato, J.; D'Errico, S.; Piccialli, G.; Varra, M.; Mayol, L. Synthesis of A New Ribose Modified Analogue of Cyclic Inosine Diphosphate Ribose. *Nucleos. Nucleot. Nucl.* **2007**, *26*, 1321–1324. [CrossRef]

34. Oliviero, G.; D'Errico, S.; Borbone, N.; Amato, J.; Piccialli, V.; Varra, M.; Piccialli, G.; Mayol, L. A solid-phase approach to the synthesis of N-1-alkyl analogues of cyclic inosine-diphosphate-ribose (cIDPR). *Tetrahedron* **2010**, *66*, 1931–1936. [CrossRef]
35. D'Errico, S.; Oliviero, G.; Borbone, N.; Amato, J.; Piccialli, V.; Varra, M.; Mayol, L.; Piccialli, G. Solid-phase synthesis of a new diphosphate 5-aminoimidazole-4-carboxamide riboside (AICAR) derivative and studies toward cyclic AICAR diphosphate ribose. *Molecules* **2011**, *16*, 8110–8118. [CrossRef]
36. Mahal, A.; D'Errico, S.; Borbone, N.; Pinto, B.; Secondo, A.; Costantino, V.; Tedeschi, V.; Oliviero, G.; Piccialli, V.; Piccialli, G. Synthesis of cyclic N 1 -pentylinosine phosphate, a new structurally reduced cADPR analogue with calcium-mobilizing activity on PC12 cells. *Beilstein J. Org. Chem.* **2015**, *11*, 2689–2695. [CrossRef]
37. D'Errico, S.; Borbone, N.; Catalanotti, B.; Secondo, A.; Petrozziello, T.; Piccialli, I.; Pannaccione, A.; Costantino, V.; Mayol, L.; Piccialli, G.; et al. Synthesis and Biological Evaluation of a New Structural Simplified Analogue of cADPR, a Calcium-Mobilizing Secondary Messenger Firstly Isolated from Sea Urchin Eggs. *Mar. Drugs* **2018**, *16*, 89. [CrossRef]
38. Kolisek, M.; Beck, A.; Fleig, A.; Penner, R. Cyclic ADP-ribose and hydrogen peroxide synergize with ADP-ribose in the activation of TRPM2 channels. *Mol. Cell* **2005**, *18*, 61–69. [CrossRef]
39. Swarbrick, J.M.; Riley, A.M.; Mills, S.J.; Potter, B.V.L. Designer small molecules to target calcium signalling. *Biochem. Soc. Trans.* **2015**, *43*, 417–425. [CrossRef]
40. Yu, P.; Liu, Z.; Yu, X.; Ye, P.; Liu, H.; Xue, X.; Yang, L.; Li, Z.; Wu, Y.; Fang, C.; et al. Direct Gating of the TRPM2 Channel by cADPR via Specific Interactions with the ADPR Binding Pocket. *Cell Rep.* **2019**, *27*, 3684–3695. [CrossRef]
41. Watt, J.M.; Rozewitz, M.D.; Guse, A.H.; Fliegert, R.; Potter, B.V.L. Synthesis of Terminal Ribose Analogues of Adenosine 5′-Diphosphate Ribose as Probes for the Transient Receptor Potential Cation Channel TRPM2. *J. Org. Chem.* **2019**, *84*, 6143–6157.
42. Moreau, C.; Liu, Q.; Graeff, R.; Wagner, G.K.; Thomas, M.P.; Swarbrick, J.M.; Shuto, S.; Lee, H.C.; Hao, Q.; Potter, B.V.L. CD38 Structure-Based Inhibitor Design Using the N1-Cyclic Inosine 5′-Diphosphate Ribose Template. *PLoS ONE* **2013**, *8*, e66247. [CrossRef]
43. Oliviero, G.; Amato, J.; Borbone, N.; D'Errico, S.; Piccialli, G.; Mayol, L. Synthesis of N-1 and ribose modified inosine analogues on solid support. *Tetrahedron Lett.* **2007**, *48*, 397–400. [CrossRef]
44. Oliviero, G.; Amato, J.; Borbone, N.; D'Errico, S.; Piccialli, G.; Bucci, E.; Piccialli, V.; Mayol, L. Synthesis of 4-N-alkyl and ribose-modified AICAR analogues on solid support. *Tetrahedron* **2008**, *64*, 6475–6481. [CrossRef]
45. D'Errico, S.; Oliviero, G.; Borbone, N.; Amato, J.; D'Alonzo, D.; Piccialli, V.; Mayol, L.; Piccialli, G. A facile synthesis of 5′-Fluoro-5′-deoxyacadesine (5′-F-AICAR): A novel non-phosphorylable AICAR Analogue. *Molecules* **2012**, *17*, 13036–13044. [CrossRef]
46. D'Errico, S.; Oliviero, G.; Borbone, N.; Piccialli, V.; Piccialli, G. Synthesis of 5-Aminoimidazole-4-Carboxamide Riboside (AICAR) and Its Derivatives Using Inosine as Starting Material. *Curr. Protoc. Nucleic Acid Chem.* **2015**, *63*, 1.35.1–1.35.24.
47. Oliviero, G.; D'Errico, S.; Borbone, N.; Amato, J.; Piccialli, V.; Piccialli, G.; Luciano, M. Facile solid-phase synthesis of AICAR 5-monophosphate (ZMP) and its 4-N-Alkyl derivatives. *Eur. J. Org. Chem.* **2010**, *2010*, 1517–1524. [CrossRef]
48. D'Errico, S.; Oliviero, G.; Borbone, N.; Amato, J.; Piccialli, V.; Varra, M.; Mayol, L.; Piccialli, G. Synthesis of new acadesine (AICA-riboside) analogues having acyclic D-ribityl or 4-hydroxybutyl chains in place of the ribose. *Molecules* **2013**, *18*, 9420–9431. [CrossRef]
49. Ribose, S.; Cyclase, I.A.; Cd, H.; Swarbrick, J.M.; Grae, R.; Zhang, H.; Thomas, M.P.; Hao, Q.; Potter, B.V.L. Cyclic Adenosine 5′-Diphosphate Ribose Analogs without a "Southern" Ribose Inhibit ADP-ribosyl Cyclase—Hydrolase CD38. *J. Med. Chem.* **2014**, *57*, 8517–8529.
50. Swarbrick, J.M.; Potter, B.V.L. Total Synthesis of a Cyclic Adenosine 5′-Diphosphate Ribose Receptor Agonist. *J. Org. Chem.* **2012**, *77*, 4191–4197. [CrossRef]
51. Mangoni, O.; Imperatore, C.; Tomas, C.R.; Costantino, V.; Saggiomo, V.; Mangoni, A. The new carotenoid pigment moraxanthin is associated with toxic microalgae. *Mar. Drugs* **2011**, *9*, 242–255. [CrossRef]
52. Airey, J.A.; Baring, M.D.; Sutko, J.L. Ryanodine receptor protein is expressed during differentiation in the muscle cell lines BC3H1 and C2C12. *Dev. Biol.* **1991**, *148*, 365–374. [CrossRef]

molbank

MDPI

Short Note

5′-Chloro-5′-deoxy-2′,3′-*O*-isopropylidene-6-fluoro nebularine

Andrea Patrizia Falanga [1], Maria Marzano [2], Monica Terracciano [2] and Stefano D'Errico [2,*]

[1] Department of Molecular Medicine and Medical Biotechnology, University of Naples Federico II, via Sergio Pansini, 5, 80131 Napoli, Italy; andreapatrizia.falanga@unina.it

[2] Department of Pharmacy, University of Naples Federico II, via Domenico Montesano, 49, 80131 Napoli, Italy; maria.marzano@unina.it (M.M.); monica.terracciano@unina.it (M.T.)

* Correspondence: stefano.derrico@unina.it; Tel.: +39-081-679981

Received: 20 November 2019; Accepted: 10 December 2019; Published: 13 December 2019

Abstract: In this paper, we report on the synthesis and spectroscopic characterization of the novel nucleoside 5′-chloro-5′-deoxy-2′,3′-*O*-isopropylidene-6-fluoro nebularine, obtained as a side product during the second step of the synthesis of 5′-fluoro-5′-deoxy-5-aminoimidazole-4-carboxamide-β-D-riboside (5′-F-AICAR), a non-phosphorylable analogue of 5-aminoimidazole-4-carboxamide-β-D-riboside (AICAR).

Keywords: AICAR; acadesine; phosphorylation; fluorination; fluorinated nucleosides; nucleoside analogues; modified nucleosides; chlorinated nucleosides; AMPK

1. Introduction

Nucleoside and nucleotide analogues are synthetic modified compounds that have been developed to mimic their physiological counterparts [1]. Considering that several nucleoside and nucleotide analogues have been approved by the Food and Drug Administration (FDA) for the treatment of viral and cancer diseases and others have entered clinical trials [2,3], many research groups have focused their attention on the preparation of novel compounds to expand the pool of molecules with potential biological activities, with the aim of discovering "leads" that are safer and more effective. For example, the replacement of OH groups of sugar moieties with the isosteric F atom has generated life-saving drugs for the treatment of infectious diseases, such as HIV [4], HBV [5], and HCV [6].

The nucleoside AICAR (**1**, Figure 1), besides being an intermediate involved in purine biosynthesis, is an activator of the enzyme adenosine monophosphate-activated protein kinase (AMPK) in the 5′-phosphorylated form [7,8]. This activation leads to a cascade of metabolic events, such as the inhibition of basal and insulin-stimulated glucose uptake, lipogenesis, and glucose oxidation [9]. The AMPK pathway is also implicated in the regulation of cell proliferation, and activation by AICAR could result in pro-apoptotic effects [10]. Given the importance of such a molecule, the synthesis of novel AICAR analogues is an appealing goal to better understand its mechanism of action [11–15]. Considering AICAR's low intestinal absorption and poor penetration of the blood–brain barrier, we synthesized a more lipophilic analogue, where the 5′-OH group was replaced by a fluorine atom (**2**, 5′-F-AICAR) [16].

For the preparation of nucleoside **2**, a key step was the 5′-fluorination of compound **4** (Scheme 1) [16]. In this paper, we report on the synthesis and structural characterization of the novel nucleoside **8** (Scheme 2), obtained by a side reaction during the fluorination step. This nucleoside could represent a valuable intermediate for a modular derivatization of the purine base moiety and the sugar residue.

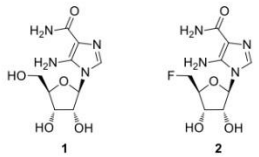

Figure 1. Structures of AICAR (**1**) and 5′-F-AICAR (**2**).

2. Results and Discussion

For the synthesis of 5′-F-AICAR (**2**), we used as the starting material the commercially available 6-chloronebularine (**3**, Scheme 1), which was readily transformed into its 2′,3′-*O*-isopropylidene derivative **4** [17]. After 5′-fluorination, the 6-chloropurine was converted into hypoxanthine and the obtained nucleoside **6** transformed into the derivative **7**. The strong electron-withdrawing 2,4-dinitrophenyl group, introduced at the N1 hypoxanthine position, allowed us to obtain the 5′-F-AICAR **2** through a 1,2-diaminoethane-mediated purine ring degradation [18].

In the second step of the synthesis, the 5′-OH group of nucleoside **4** was replaced by a 5′-F in a one-pot tosylation/fluorination sequence, through the treatment with the tosyl fluoride/tetrabutylammonium fluoride (TsF/TBAF) reagent system with tetrahydrofuran (THF) as solvent, according to Shimizu's procedure [19]. As previously observed by Ashton and Scammells [19], we noted (TLC monitoring in *n*-hexane/AcOEt; 1:1) that the process led not only to the formation of the expected fluorinated product **5a** with Rf = 0.48 (Scheme 1), but also to the formation of the bis-fluorinated product **5b** with Rf = 0.42, as a consequence of the substitution in species **4** of the C6 chlorine atom by a fluoride ion.

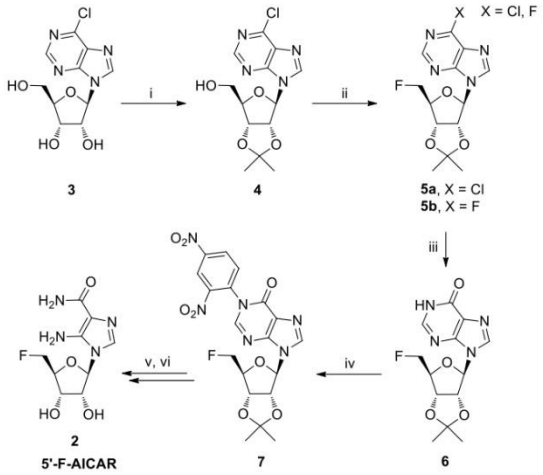

Scheme 1. Reagents and conditions: (i) acetone, 2,2-dimethoxypropane (DMP), *p*-toluensulfonic acid (*p*-TsOH), 2 h, r.t.; (ii) TsF, TBAF, THF, reflux, 18 h; (iii) 0.1 M NaOH, 4 h, r.t.; (iv), K_2CO_3, 1-chloro-2,4-dinitrobenzene, *N*,*N*-dimethylformamide (DMF), 3 h, 80 °C; (v) 1,2-diaminoethane, DMF, 16 h, 50 °C; (vi) 50% trifluoracetic acid (TFA) in H_2O, 4 h.

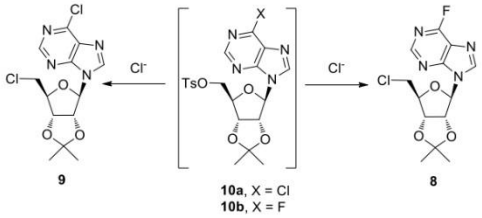

Scheme 2. Proposed mechanisms for the formation of nucleosides **8** and **9**.

The TLC also showed a third spot with Rf = 0.52, whose corresponding product was isolated (10% yield) and analyzed by ^{1}H-NMR. The spectrum evidenced the presence of two compounds in a ratio of 1:8, which were resolved only by means of high-performance liquid chromatography (HPLC). The nucleoside in lower amounts and with Rt = 21.2 min was assigned as the novel 5′-chloro-5′-deoxy-2′,3′-*O*-isopropylidene-6-fluoro nebularine (**8**, Scheme 2). Its structure was established through 1D-, 2D-NMR, and HRESI-MS experiments (see Supplementary Materials). In detail, in the ^{1}H-NMR spectrum the 5′-$H_{a,b}$ protons resonated as two doublets of doublets at 3.81 and 3.70 ppm, whereas in the ^{13}C-NMR spectrum the 5′C carbon resonated at 43.4 ppm. These data were consistent with the presence of a 5′C–Cl bond [20]. In the HMBC spectrum, the 2-H proton at 8.69 ppm correlated with the C6 purine carbon at 159.9 ppm, which appeared as a doublet with J = 261.8 Hz, as a consequence of the coupling with the F atom.

A similar compound, with the 2′- and 3′-ribose hydroxyls protected as acetates, was synthesized by Robins et al. [21] and used to obtain fluorescent probes for detecting the cellular uptake of the drug gemcitabine.

The main component with Rt = 24.2 min was instead identified as the known 5′-chloro-5′-deoxy-2′,3′-*O*-isopropylidene-6-chloro nebularine **9** [20].

A plausible mechanism for the formation of compounds **8** and **9** is described in Scheme 2. The Cl^{-} ions, derived from the partial Cl^{-}/F^{-} exchange at the C6 purine position during the 5′-fluorination step, yielded the nucleosides **8** and **9** by S_N2 displacement of the tosylate groups in the intermediates **10b** and **10a**, respectively.

3. Materials and Methods

All the reagents and solvents for the chemical syntheses were obtained from commercial sources and used without further purification. The ^{1}H-, ^{19}F- and ^{13}C-NMR spectra were acquired on 400/700 MHz instruments (Bruker, Billerica, MA, USA) using $CDCl_3$ as the solvent. The chemical shifts were reported in parts per million (δ) relative to the residual solvent signal (^{1}H: $CHCl_3$ 7.27; ^{13}C: $CDCl_3$ 77.0) and assigned by 2D-NMR experiments. All the NMR spectra were processed using the iNMR software package (Nucleomatica, Molfetta, Italy). The HRESI-MS spectra were recorded in positive mode on a Thermo Orbitrap XL mass spectrometer (ThermoFisher, Waltham, MA, USA). The column chromatography was performed by using silica gel 60, 70–230 mesh (Merck, Darmstadt, Germany). The TLC analyses were performed using 0.2 mm thick F254 silica gel plates (Merck, Darmstadt, Germany). The TLC spots were detected under UV light (254 nm). The high-performance liquid chromatography (HPLC) was performed on a UP-2075 Plus pump equipped with a UV-2075 Plus UV detector (Jasco, Cremella, Italy) using a 5 µm, 250-10 Si column (Purosphere® STAR, Merck, Darmstadt, Germany) eluted with *n*-hexane/AcOEt, 6:4 with a flow rate of 2.0 mL/min.

5′-Chloro-5′-deoxy-2′,3′-O-isopropylidene-6-fluoro nebularine (8). To a stirred solution of 4 (0.28 g, 0.86 mmol) in dry THF (7.5 mL), TsF (0.30 g, 1.7 mmol) and TBAF (2.6 mL of a 1.0 M solution in dry THF, 2.6 mmol) were added and the mixture refluxed for 16 h (TLC monitoring: *n*-hexane/AcOEt; 1:1).

The solvent was removed under reduced pressure and the crude residue purified by silica gel flash chromatography (*n*-hexane/AcOEt, 6:4) to afford, in addition to the two expected compounds 5a and 5b [19], the inseparable mixture of the two nucleosides 8 and 9 with Rf = 0.52 (10% yield). The mixture was purified by HPLC (see above), thus obtaining the pure compound 8. Colorless foam (3.5 mg, 1.2% yield). ^{1}H-NMR (400 MHz; $CDCl_3$): δ 8.69 (s, 1H, 2-H), 8.29 (s, 1H, 8-H), 6.24 (d, *J* = 2.6 Hz, 1H, 1′-H), 5.40 (dd, *J* = 6.4, 2.7 Hz, 1H, 2′-H), 5.13 (dd, *J* = 6.4, 3.1 Hz, 1H, 3′-H), 4.58-4.55 (m, 1H, 4′-H), 3.82 (dd, *J* = 11.6, 6.1 Hz, 1H, 5′-H_a), 3.70 (dd, *J* = 11.6, 4.9 Hz, 1H, 5′-H_b), 1.66 (s, 3H, CH_3), 1.42 (s, 3H, CH_3); ^{19}F-NMR (377 MHz; $CDCl_3$): δ −68.4 (s); ^{13}C-NMR (176 MHz; $CDCl_3$): δ 159.9 (d, *J* = 261.8, 6-C), 154.5 (d, *J* = 11.1, 4-C), 152.2 (d, *J* = 14.3, 2-C), 144.0 (8-C), 121.15 (d, *J* = 29.2, 5-C), 115.1 (C_q acetonide), 91.3 (1′-C), 86.2 (4′-C), 84.2 (2′-C), 82.3 (3′-C), 43.9 (CH_2Cl), 27.1 (CH_3), 25.3 (CH_3); HRESI-MS *m*/*z* 329.0809, ($[M + H]^+$ calcd. for $C_{13}H_{15}ClFN_4O_3$ 329.0817).

Supplementary Materials: The following are available online, Figure S1: copies of ^{1}H- and ^{19}F-NMR spectra of compound **8**; Figure S2: copy of ^{13}C-NMR spectrum of compound **8**; Figure S3: copy of HMBC spectrum of compound **8**; Figure S4: copy of HRESI-MS spectrum of compound **8**.

Author Contributions: S.D. conceived and designed the experiments; A.P.F. performed the synthetic experiments; M.M. performed the spectroscopic experiments; M.T. analyzed the data; S.D. wrote the paper. All authors read and approved the final manuscript.

Funding: This research was funded by "Campania Onco Terapie – Combattere la resistenza tumorale: piattaforma integrata multidisciplinare per un approccio tecnologico innovativo alle oncoterapie" – POR Campania FESR 2014/2020 O.S. 1.2 Az. 1.2.2 Avviso per Manifestazione di interesse per la Realizzazione di Technology Platform nell'ambito della lotta alle patologie oncologiche CUP B61G18000470007".

Acknowledgments: The authors are grateful to Luisa Cuorvo for her technical assistance.

Conflicts of Interest: The authors declare no conflict of interest.

References

1. Burke, M.; Borland, K.; Litosh, V. Base-modified nucleosides as chemotherapeutic agents: Past and future. *Curr. Top. Med. Chem.* **2016**, *16*, 1231–1241. [CrossRef]
2. Berdis, A.J. Inhibiting DNA polymerases as a therapeutic intervention against cancer. *Front. Mol. Biosci.* **2017**, *4*, 78. [CrossRef]
3. De Clercq, E.; Li, G. Approved antiviral drugs over the past 50 years. *Clin. Microbiol. Rev.* **2016**, *29*, 695–747. [CrossRef]
4. Andreatta, K.; Willkom, M.; Martin, R.; Chang, S.; Wei, L.; Liu, H.; Liu, Y.-P.; Graham, H.; Quirk, E.; Martin, H.; et al. Switching to bictegravir/emtricitabine/tenofovir alafenamide maintained HIV-1 RNA suppression in participants with archived antiretroviral resistance including M184V/I. *J. Antimicrob. Chemother.* **2019**, *74*, 3555–3564. [CrossRef]
5. Zhang, J.; Wang, Y.; Peng, Y.; Qin, C.; Liu, Y.; Li, J.; Jiang, J.; Zhou, Y.; Chang, J.; Wang, Q. Novel fluoronucleoside analog NCC inhibits lamivudine-resistant hepatitis B virus in a hepatocyte model. *Brazilian J. Infect. Dis.* **2018**, *22*, 477–486. [CrossRef]
6. Sofia, M.J.; Bao, D.; Chang, W.; Du, J.; Nagarathnam, D.; Rachakonda, S.; Reddy, P.G.; Ross, B.S.; Wang, P.; Zhang, H.R.; et al. Discovery of a β-D-2′-deoxy-2′-α-fluoro-2′-β-C-methyluridine nucleotide prodrug (PSI-7977) for the treatment of hepatitis C virus. *J. Med. Chem.* **2010**, *53*, 7202–7218. [CrossRef]
7. Daignan-Fornier, B.; Pinson, B. 5-Aminoimidazole-4-carboxamide-1-beta-D-ribofuranosyl 5′-monophosphate (AICAR), a highly conserved purine intermediate with multiple effects. *Metabolites* **2012**, *2*, 292–302. [CrossRef]
8. Scudiero, O.; Nigro, E.; Monaco, M.L.; Oliviero, G.; Polito, R.; Borbone, N.; D'Errico, S.; Mayol, L.; Daniele, A.; Piccialli, G. New synthetic AICAR derivatives with enhanced AMPK and ACC activation. *J. Enzyme Inhib. Med. Chem.* **2015**, *6366*, 1–6. [CrossRef] [PubMed]
9. Merrill, G.F.; Kurth, E.J.; Hardie, D.G.; Winder, W.W. AICA riboside increases AMP-activated protein kinase, fatty acid oxidation, and glucose uptake in rat muscle. *Am. J. Physiol. - Endocrinol. Metab.* **1997**, *273*, 1107–1112. [CrossRef] [PubMed]

marine drugs

MDPI

Article

Evaluation of an Analogue of the Marine ε-PLL Peptide as a Ligand of G-quadruplex DNA Structures

Maria Marzano [1], Andrea Patrizia Falanga [1], Daniela Marasco [1,2], Nicola Borbone [1], Stefano D'Errico [1], Gennaro Piccialli [1], Giovanni Nicola Roviello [2,*] and Giorgia Oliviero [3]

1 Department of Pharmacy, University of Naples Federico II, Via Domenico Montesano 49, 80131 Naples, Italy; maria.marzano@unina.it (M.M.); andreapatrizia.falanga@unina.it (A.P.F.); daniela.marasco@unina.it (D.M.); nicola.borbone@unina.it (N.B.); stefano.derrico@unina.it (S.D.); picciall@unina.it (G.P.)

2 Institute of Biostructures and Bioimaging—CNR 1, Via Mezzocannone 16, 80134 Naples, Italy

3 Department of Molecular Medicine and Medical Biotechnologies, University of Napoli Federico II, Via Sergio Pansini 5, 80131 Naples, Italy; golivier@unina.it

* Correspondence: giroviel@unina.it

Received: 7 November 2019; Accepted: 9 January 2020; Published: 11 January 2020

Abstract: ε-poly-L-Lysine (ε-PLL) peptide is a product of the marine bacterium *Bacillus subtilis* with antibacterial and anticancer activity largely used worldwide as a food preservative. ε-PLL and its synthetic analogue α,ε-poly-L-lysine (α,ε-PLL) are also employed in the biomedical field as enhancers of anticancer drugs and for drug and gene delivery applications. Recently, several studies reported the interaction between these non-canonical peptides and DNA targets. Among the most important DNA targets are the DNA secondary structures known as G-quadruplexes (G4s) which play relevant roles in many biological processes and disease-related mechanisms. The search for novel ligands capable of interfering with G4-driven biological processes elicits growing attention in the screening of new classes of G4 binders. In this context, we have here investigated the potential of α,ε-PLL as a G4 ligand. In particular, the effects of the incubation of two different models of G4 DNA, i.e., the parallel G4 formed by the Pu22 (d[TGAGGGTGGGTAGGGTGGGTAA]) sequence, a mutated and shorter analogue of the G4-forming sequence known as Pu27 located in the promoter of the c-myc oncogene, and the hybrid parallel/antiparallel G4 formed by the human Tel22 (d[AGGGTTAGGGTTAGGGTTAGGG]) telomeric sequence, with α,ε-PLL are discussed in the light of circular dichroism (CD), UV, fluorescence, size exclusion chromatography (SEC), and surface plasmon resonance (SPR) evidence. Even though the SPR results indicated that α,ε-PLL is capable of binding with μM affinity to both the G4 models, spectroscopic and SEC investigations disclosed significant differences in the structural properties of the resulting α,ε-PLL/G4 complexes which support the use of α,ε-PLL as a G4 ligand capable of discriminating among different G4 topologies.

Keywords: marine peptide; epsilon-poly-L-lysine; ε-PLL; G-quadruplex DNA; human telomere; c-myc oncogene

1. Introduction

ε-poly-L-Lysine (ε-PLL) is a cationic biopolymer isolated from the marine bacterium *Bacillus subtilis*, responsible for the antibacterial and anticancer activity shown by this microorganism [1]. The same peptide is also produced by the marine bacterial strain PL26 of *Bacillus licheniformis*, isolated from the west coast of India [2]. Due to its well-known antimicrobial properties, ε-PLL is largely used worldwide as a food preservative [3,4], but is also used in many biomedical applications, including the enhancement of some anticancer agents [5], the suppression of the production of the prion protein in neurodegenerative disorders [6], the use in contrast agent probes for Magnetic

Resonance Imaging [7] and the enhancement of gene delivery efficiency [8]. The industrial production of ε-PLL makes use of a mutant of *Streptomyces albulus* [9]. Still, it can be conveniently achieved also using the above mentioned strain PL26 of marine bacterium *Bacillus licheniformis* starting from waste material from biodiesel manufacturing industries [1,2]. On the other side, α-poly-L-lysine (α-PLL) is a synthetic poly(amino acid) successfully used in different biotechnological applications, e.g., in biomass production by microalgae *Chlorella ellipsoidea* [10]. α- and ε-PLL peptides are well soluble in aqueous media, biodegradable, and environmental-friendly [11], and both are good candidates as drug delivery agents due to their polycationic nature [11,12]. Even though dendrimeric α,ε-poly-L-lysines had been previously realized for the compacting and delivery of oligonucleotides [13], a synthetic approach to linear PLLs with sequential α- and ε-peptide bonds (α,ε-PLLs, Figure 1) was firstly reported by Roviello et al. alongside with the initial biological assessment of α,ε-PLLs [13–15]. The interest in poly-L-lysine structures containing both α- and ε- peptide bonds is justified by their superior gene delivery properties when compared to linear or dendritic PLLs based uniquely on ε-peptide bonds [16]. PLLs having a random α- and ε- peptide bond sequence (hyperbranched polylysines) are more resistant to proteolytic action than linear PLL, but undergo a significant degradation after 8 h [17]. On the other side, linear α,ε-PLLs, easily obtainable by standard solid-phase peptide synthesis procedures [15,18,19] and endowed with structural specific nucleic acids binding abilities, do not show any significant degradation after 24 h of incubation in human serum at 37 °C [14].

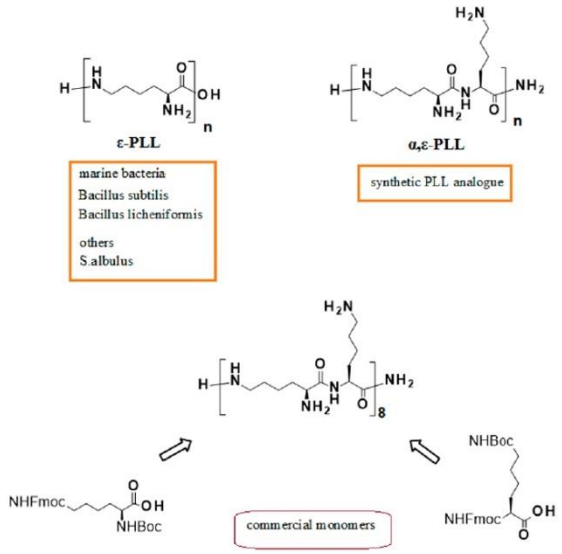

Figure 1. Schematic representation of the natural ε-peptide (ε-PLL) and of our synthetic analogue studied in G-quadruplex (G4)-DNA binding.

Among the DNA secondary structures, the G-quadruplex (G4) family is one of the most intriguing and deeply investigated [20–23]. It has been demonstrated that G4 DNA plays a crucial role in many physiological and disease-related biological mechanisms [24]. Apart from the ubiquitous potassium or sodium cations, positively-charged polyamines and triethylene tetraamine may contribute to the G4 stability and induce biologically-relevant effects [25,26]. In this context, also the polycationic PLL was evaluated for its impact on the formation of G4 structures by the human telomere in cation-deficient media and showed the interesting ability to convert the telomeric G4 from the antiparallel to the parallel topology [27]. However, to our knowledge, no study has yet been published on the interaction of α,ε-PLL with any G4 DNA.

Thus, herein, we report the results of our study on the effects of α,ε-PLL on two different G4 topologies investigated by CD, UV, fluorescence, size exclusion chromatography and SPR techniques. The hybrid-type G4 adopted by the Tel22 telomeric sequence (d[AGGGTTAGGGTTAGGGTTAGGG]), commonly used as the human telomeric DNA model, and the parallel G4 formed by the Pu22 (d[TGAGGGTGGGTAGGGTGGGTAA]) sequence, a shorter and mutated analogue of the G4-forming Pu27 sequence located in the promoter of the human c-myc oncogene, have been employed for this study [28,29]. These two model DNAs can adopt several kinds of topologies under different experimental conditions and are used in this study to evaluate the ability of our lysine-rich peptide to modify, similarly to other oligocation binders [27,30,31], G4 DNA structures.

The results of this study have suggested that α,ε-PLL is a G4 ligand able to bind to both G4 models with μM affinity leading, however, to more evident changes in the secondary structure of parallel G4 structures as described hereinbelow.

2. Results and Discussion

The interest towards the biomedical exploitation of DNA G-quadruplexes and their ligands (of either natural or synthetic origin) prompted us to explore the interaction of α,ε-PLL with two different structural topologies of this class of highly-ordered secondary structures of DNA. In all the spectroscopic studies described below, the contribution to the spectra given by the free peptide was negligible when compared to the intense nucleic acid bands, as also previously reported by Roviello et al. [14]. At first, we studied the interaction of α,ε-PLL with Tel22, that under our experimental conditions showed the characteristic CD bands (~290 nm maximum, ~250–260 nm shoulder, ~240 nm minimum) previously attributed to an equimolar mixture of the hybrid 1 and hybrid 2 G4s [32–35]. Following the addition of α,ε-PLL at the $\frac{1}{2}\frac{[NH_3^+]}{[PO_3^-]}$ ratio (at which ε-PLL caused the largest structural perturbation of telomeric DNA [27]) we observed no change in the CD spectrum of Tel22, reaching the conclusion that α,ε-PLL did not induce any significant structural change on the G4 secondary structure of Tel22 (Figure 2, left). Afterwards, the same study was repeated using the c-myc-derived Pu22 DNA sequence which is known to fold into a parallel G4 as previously demonstrated by NMR [36,37] and X-ray crystallography [38], and confirmed in our study by the CD profile dominated by the negative Cotton effect centered at around 240 nm and the positive one centered at about 265 nm (Figure 2, right) which are typically assigned to parallel G4s [39,40]. Immediately after the addition of α,ε-PLL, we observed a substantial enhancement and broadening of the positive CD band at 260 nm, which indicated that the interaction of α,ε-PLL with Pu22 induced significant changes into the parallel G4 secondary structure. Interestingly, no significant change in CD spectrum of a dsDNA upon peptide addition was detected under the same experimental conditions adopted for G4 DNAs (Figure S1).

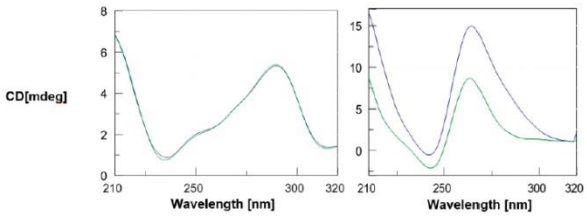

Figure 2. CD spectra of 2.5 μM G4 DNA (Tel22, **left**; Pu22, **right**) + 1.7 μM α,ε-PLL in 10 mM TRIS HCl buffer, 100 mM KCl, pH 7.4 at 15 °C. Arithmetic sum (—); α,ε-PLL/G4 complex (—).

By repeating the acquisition of CD (Figure 3) and UV (Figure 4) spectra at different time points from the addition of α,ε-PLL to the preformed Pu22 G4, we observed a continuous variation of the signals (Figures 3a and 4a) which was particularly evident by plotting the CD value recorded at 261 or 281 (Figure 3b) nm, as well as the UV value at 261 nm (Figure 4b) vs. time.

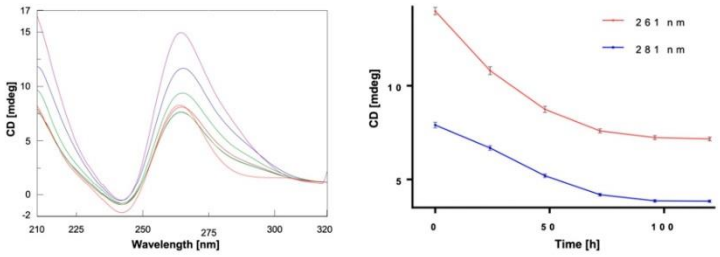

(**a**) (**b**)

Figure 3. (**a**) CD spectra of Pu22 (2.5 μM) recorded before (—) and 0 (—), 24 (—), 48 (—), 72 (—), 96 (—), and 120 (—) h after mixing with α,ε-PLL (1.7 μM) in 10 mM TRIS HCl buffer, 100 mM KCl, pH 7.4 at 15 °C. (**b**) Plots of CD values vs. time at 261 and 281 nm.

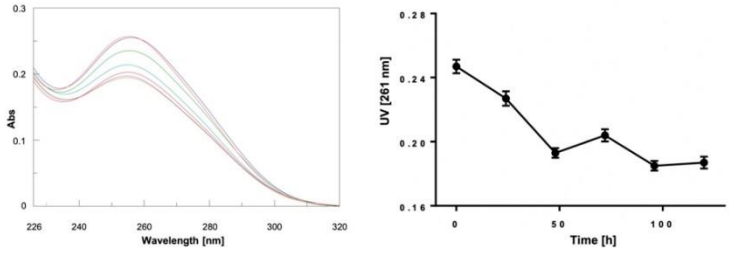

(**a**) (**b**)

Figure 4. (**a**) UV spectra relative to Pu22 (2.5 μM) in 10 mM TRIS HCl buffer, 100 mM KCl, pH 7.4, b = 0.4375 cm, at 15 °C recorded before (—) and 0 (—), 24 (—), 48 (—), 72 (—), 96 (—), and 120 (—) h after mixing with α,ε-PLL (1.7 μM); (**b**) Plot of the UV values at 261 nm vs. time.

From this kinetic study, we concluded that the interaction of α,ε-PLL with the Pu22 G4 leads to the formation of complexes that evolve during the first 96 h after mixing and eventually reach the most stable one when the stabilization of CD signal was achieved (Figure 3). Interestingly, the UV titration experiment clearly showed a hypochromic effect (Figure 4, Figure S2) occurring upon peptide addition to Pu22 that suggests a reinforcement of the stacking between the G-tetrads as an outcome of the binding with the α,ε-PLL.

All the time-dependent spectroscopic changes observed in the above-reported experiments are due to the binding with peptide ligand, as Pu22 G4 alone did not undergo a similar kinetic behavior in the time range explored (data not shown).

Similarly to CD, also fluorescence spectra confirmed a higher structural perturbation for Pu22 G4 DNA with respect to the telomeric one after binding with α,ε-PLL. We observed a slight blue-shift effect associated with increased fluorescence emission in the former case, whereas we did not see any significant effect in the latter case (Figure 5). We also investigated the effects induced by α,ε-PLL on the apparent melting temperatures of the two G4 models.

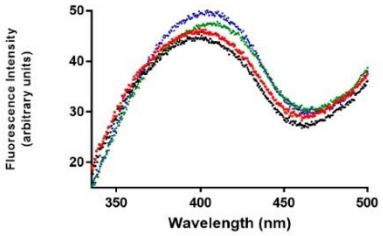

Figure 5. Fluorescence emission spectra of Pu22 (—), Tel22 (—), Pu22 + α,ε-PLL (—) and Tel22 + α,ε-PLL (—): 2.5 μM DNA, α,ε-PLL (1.7 μM) in 10 mM TRIS HCl buffer, 100 mM KCl, pH 7.4 (15 °C).

The CD melting curves of the α,ε-PLL/G4 complexes (Figure 6 and Table 1) disclosed a slight thermal stabilization (ΔT_m ~2 °C) in the case of Pu22, whereas no significant difference was found between the T_m value of Tel22 and that of its complex with α,ε-PLL.

Table 1. Melting temperatures from CD thermal denaturation experiments.

	Tm [°C]	Error	ΔTm [°C]
Tel22	65.7	0.2	–
Tel22 + α,ε-PLL	65.8	0.2	0.1
Pu22	85.6	0.2	–
Pu22 + α,ε-PLL	87.7	0.2	2.1

Overall, the above findings suggest the ability of α,ε-PLL to perturb parallel G4 structures leaving almost unchanged hybrid ones as testified by the spectral consequences seen only for Pu22, whose G4 structure also underwent a slight thermal stabilization. Even though the spectroscopic analyses indicated that the α,ε-PLL peptide is provided with a certain degree of selectivity in G4 structural modification, we decided to ascertain whether it was capable of binding also the Tel22 G4, as we expected on the basis of the electrostatic interactions foreseen for a polycation (α,ε-PLL) interacting with a polyanionic DNA. To this scope, and to quantitatively evaluate the binding affinity of α,ε-PLL for both the studied G4 topologies, we used the surface plasmon resonance (SPR) technique that had proven successful in other literature examples [41]. SPR binding profiles (Figure 7) confirmed that α,ε-PLL was actually capable of binding, in a concentration-depending manner, to both the G4 models, and the fitting of the binding isotherms allowed us to estimate the dissociation constants for the two

complexes, which were quite comparable even though a higher affinity for Pu22 was observed (see Table 2), in the interval time of analysis. Strikingly, the affinity of α,ε-PLL for Pu22 and Tel22 G4 DNA is similar or higher than that found for other previously reported basic peptides acting as G4 DNA ligands (K_D 1–8 μM) [42].

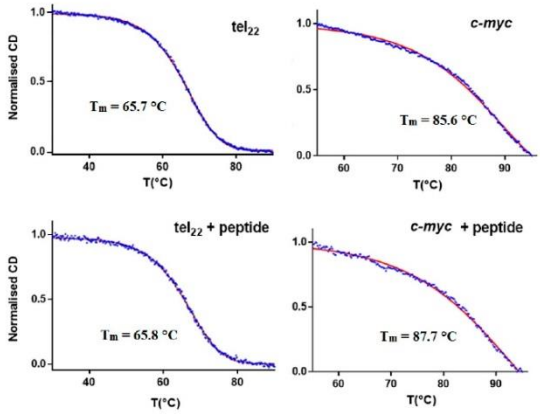

Figure 6. CD melting curves relative to G4 DNA (tel22, **top left**; *c-myc*, **top right**; 2.5 μM) and their complexes with 1.7 μM α,ε-PLL (tel22 + α,ε-PLL, **bottom left**; *c-myc* + α,ε-PLL, **bottom right**) in 10 mM TRIS HCl buffer, 100 mM KCl, pH 7.4.

Overall, the interaction of α,ε-PLL with Pu22 G4 DNA was unambiguously proven by SPR, CD, UV and fluorescence spectroscopies, while Tel22 binding was evidenced only by SPR that revealed, however, a binding affinity for Tel22 (and for Pu22) similar when not higher than that typically found for peptide G4 DNA ligands [42]. It was previously proven that, due to its polycationic nature, α,ε-PLL was able to bind several nucleic targets [14,15] inducing, however, structural rearrangements in its nucleic targets that varied upon their different nature (RNA vs. DNA) and nucleobase sequence [14,15]. This suggested, thus, that other interaction forces besides the obvious ionic ones may determine the overall binding process. In this context, we here paid great attention to the comparison between the effects of α,ε-PLL on a parallel (Pu22) and a hybrid (Tel22) quadruplex structure. More in detail, as shown by CD and fluorescence experiments, only Pu22 underwent a significant secondary structure rearrangement upon peptide binding, an aspect that was explored also in a kinetic study. Nevertheless, the expected electrostatic interactions led α,ε-PLL to bind also Tel22 (as found by SPR) without determining, however, any CD spectral changes in this case and, correspondingly, leaving almost unmodified its secondary structure. Other differences found in the two cases comprise the higher binding affinity of the peptide for Pu22 with respect to Tel22, as evidenced by SPR comparing the K_D values for the two complexes (Table 2, Figure 7), and the slight thermal stabilization of Pu22 (but not of Tel22) found by a CD-melting assay (Table 1).

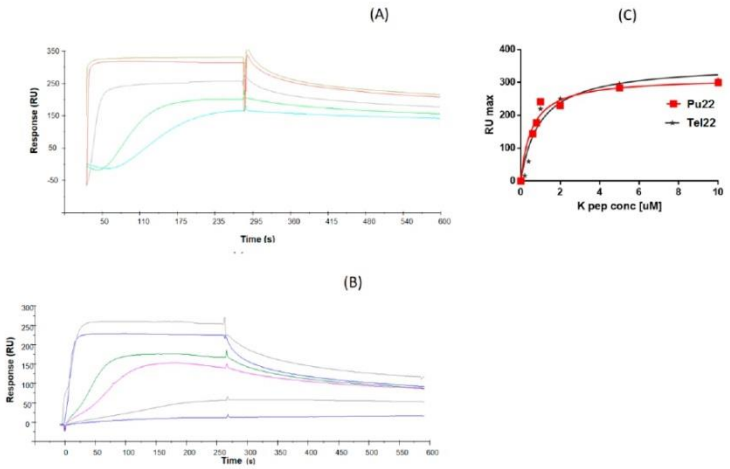

Figure 7. Overlay of surface plasmon resonance (SPR) sensorgrams for the binding of α,ε-PLL to immobilized (**A**) Biot-Pu22 or (**B**) Biot-Tel22. (**C**) Overlay of the corresponding binding isotherms of RU_{max} values vs. α,ε-PLL concentration (0–10 μM concentration range).

Table 2. SPR-based equilibrium dissociation constants (K_D) for the interaction of α,ε-PLL with Pu22 or Tel22 G-quadruplexes. The Graph-Pad Prism software (version 7.00; GraphPad Software, San Diego, CA, USA) was used to fit RUmax for α,ε-PLL concentrations by nonlinear regression analysis.

ODN	K_D (μM)
Pu22	0.56 ± 0.14
Tel22	1.0 ± 0.20

Aiming at further confirming the binding of α,ε-PLL with the two G4 models and also at investigating the effect of the addition of α,ε-PLL on the molecularity of Tel22 and Pu22 G4s, we used the HPLC size exclusion chromatography (HPLC-SEC) technique. In other papers, in fact, we and others demonstrated that the HPLC-SEC could be successfully exploited to assess the molecularity and conformational changes of DNA G4s [43–45]. Accordingly, we recorded the HPLC-SEC profiles of Tel22 and Pu22 G4s before and 96 h after their incubation with α,ε-PLL (Figure 8). As expected, the HPLC-SEC profile of Tel22 alone was populated by a single peak attributable to the mixture of monomeric hybrid 1 and hybrid 2 G4s, which was eluted at min 14.733. After incubation with α,ε-PLL, the appearance of a new less-retained peak eluted at min 13.767 suggested the formation of a higher molecular weight complex in agreement with the SPR data which indicated a concentration-dependent binding between α,ε-PLL and Tel22. Differently from what was observed for Tel22 G4, the HPLC-SEC profile obtained by injecting Pu22 alone was populated by two main peaks, that we assigned to the monomeric parallel G4 (t_R = 14.525 min) and its dimer (t_R = 13.950 min) based on literature reports [38]. On the other hand, the HPLC-SEC profile of Pu22 did not change significantly after the addition of α,ε-PLL, suggesting that the α,ε-PLL/Pu22 binding confirmed by CD, fluorescence and SPR data, did not affect the relative abundance of the monomeric and dimeric G4 forms.

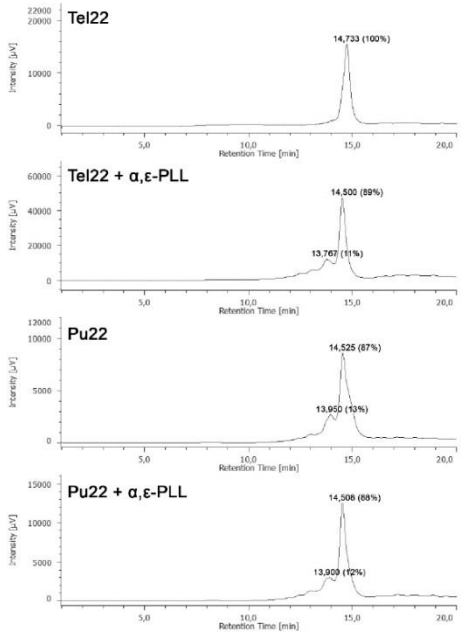

Figure 8. HPLC-size exclusion chromatography (SEC) profiles of Tel22 and Pu22 G4s before and after the addition of α,ε-PLL.

3. Materials and Methods

3.1. α,ε-PLL and DNA

The hexadecapeptide α,ε-PLL (Figure 1) was prepared accordingly to the procedure previously reported by Moccia et al. [15]. Pu22 (d[TGAGGGTGGGTAGGGTGGGTAA]) and Tel22 (d[AGGGTTAGGGTTAGGGTTAGGG]) G4-forming DNAs were purchased from Eurofins Genomics.

3.2. CD and UV Experiments

We obtained the CD spectra in a 210–320 nm wavelength range, on a Jasco J-810 spectropolarimeter equipped with a Jasco PTC-423S/15 Peltier temperature controller (Jasco Europe Srl, Cremella, Italy) in a dual-chamber quartz cell (b = 2 × 0.4375, Hellma 238-QS, Hellma® Analytics, Hellma GmbH & Co. KG, Müllheim, Germany). UV spectra were recorded on a Jasco V-550 spectrophotometer equipped with a Jasco ETC-505T Peltier temperature controller. All spectroscopic experiments were run in duplicate and were repeated three times. Standard deviation values for CD and UV Abs were ≤2%. CD meltings of telomeric and Pu22 G4 DNAs were obtained by recording CD values at 295 and 263 nm, respectively, as function of temperature. All nucleic acids were annealed by heating the solutions at 95 °C for 5 min and letting them cool overnight at room temperature. Melting temperature values were determined as the temperatures relative to minima of the 1st derivative plots of denaturation curves.

3.3. Fluorescence Studies

The experiments were performed at 15 °C using the intrinsic fluorescence of G4 DNAs as reported previously [46], using an excitation wavelength of 270 nm and a fluorescence emission wavelength ranging from 330 to 500 nm on a Jasco FP 8300 spectrofluorometer using a 10 mm path-length quartz cuvette. The acquisition parameters were set as follows: excitation and emission slits at 5 nm; 200 nm/min scan rate; 0.5 nm data interval averaging time at 0.050 s, PMT voltage at "medium".

3.4. Surface Plasmon Resonance (SPR) Experiments

SPR assays were performed at 25 °C on a Biacore 3000 instrument (GE Healthcare, Chicago, IL, US). For immobilization, 5′-biotinylated Tel22 and Pu22 ODNs were injected for 7 min (at 20 μM) on a SA-chip until an immobilization of ~700 RU was achieved, as previously reported [47,48]. The α,ε-PLL analyte was serially diluted in the 10 μM TRIS HCl buffer supplemented with 100 μM KCl (pH 7.4) running buffer, covering a concentration range between 50 and 1000 nM. 90 μL analyte samples were injected at a flow rate of 20 μL/min and the dissociation was followed for 300 s. The reference chip sensorgrams were properly subtracted to sample sensorgrams. After each cycle, the sensor chip surface was regenerated with a 1.0 M NaCl solution for 30 s followed by multiple buffer injections to yield a stable baseline for the following cycles. Experiments were carried out in duplicates. Kinetic parameters were estimated assuming a 1:1 binding model and using version 4.1 Evaluation Software (GE Healthcare).

3.5. HPLC-Size Exclusion Chromatography (SEC) Analyses

HPLC-SEC was performed using a Phenomenex (Bologna, Italy) Yarra SEC-2000 column (300 × 7.8 mm, 3 μm) eluted with 90 mM KCl and 10 mM KH_2PO_4/CH_3CN (80:20, *v*/*v*), flow rate 0.6 mL/min, UV-detector at 260 nm. The analyses were performed at room temperature.

4. Conclusions

Overall, the above-reported findings showed that α,ε-PLL binds the two herein investigated DNA G-quadruplexes with good affinity (as demonstrated by SPR), though clues of changes of the secondary structure and slight thermal stabilization were seen only for the interaction with the Pu22 parallel G4. Following complexation with α,ε-PLL, Pu22 G4 underwent significant alterations of its spectroscopic (CD, UV and fluorescence) properties. In particular, the slight blue-shift in the fluorescence band of peptide/Pu22 complex and the hypochromic UV effect indicated that the interaction with α,ε-PLL increased base stacking within the G4 core. In conclusion, the here presented study provides an interesting insight into G-quadruplex binding of α,ε-PLL, a serum stable [14], marine-inspired peptide that, in spite of its cationic nature, recognizes the structural properties of its targets and uses different binding modes according to their topology.

Supplementary Materials: Additional CD and UV data are available online at http://www.mdpi.com/1660-3397/18/1/49/s1.

Author Contributions: M.M. performed most of the experiments and contributed to the manuscript preparation; G.N.R. performed the study design, synthesized the peptide, performed CD melting experiments and worked on manuscript preparation; D.M. performed SPR experiments and took part in data analysis; G.O. gave an important contribution to the study design, the data interpretation, and manuscript preparation; N.B. and G.P. took part in the study design, manuscript preparation, and data analysis; A.P.F. and S.D. took part in SEC experiments and data analysis. All authors have read and agreed to the published version of the manuscript.

Funding: We are grateful for the support received by Ministero dell'Istruzione, dell'Università e della Ricerca (MIUR) [grant number PON03PE 00060 4] and Regione Campania [POR FESR 2014/2020 "Progetto premio infrastruttura per la medicina di precision in oncologia"].

Conflicts of Interest: The authors declare no conflict of interest.

References

1. El-Sersy, N.A.; Abdelwahab, A.E.; Abouelkhiir, S.S.; Abou-Zeid, D.M.; Sabry, S.A. Antibacterial and anticancer activity of epsilon-poly-L-lysine (epsilon-PL) produced by a marine Bacillus subtilis sp. *J. Basic Microbiol.* **2012**, *52*, 513–522. [CrossRef] [PubMed]
2. Bhattacharya, S.; Dubey, S.; Singh, P.; Shrivastava, A.; Mishra, S. Biodegradable Polymeric Substances Produced by a Marine Bacterium from a Surplus Stream of the Biodiesel Industry. *Bioengineering* **2016**, *3*, 34. [CrossRef] [PubMed]
3. Tanaka, S.; Hayashi, T.; Tateyama, H.; Matsumura, K.; Hyon, S.H.; Hirayama, F. Application of the bactericidal activity of epsilon-poly-L-lysine to the storage of human platelet concentrates. *Transfusion* **2010**, *50*, 932–940. [CrossRef] [PubMed]
4. Lee, N.K.; Paik, H.D. Status, Antimicrobial Mechanism and Regulation of Natural Preservatives in Livestock Food Systems. *Korean J. Food Sci. Anim. Resour.* **2016**, *36*, 547–557. [CrossRef]
5. Bao, W.; Liu, R.; Wang, Y.; Wang, F.; Xia, G.; Zhang, H.; Li, X.; Yin, H.; Chen, B. PLGA-PLL-PEG-Tf-based targeted nanoparticles drug delivery system enhance antitumor efficacy via intrinsic apoptosis pathway. *Int. J. Nanomed.* **2015**, *10*, 557–566. [CrossRef]
6. Titlow, W.B.; Waqas, M.; Lee, J.; Cho, J.Y.; Lee, S.Y.; Kim, D.H.; Ryou, C. Effect of Polylysine on Scrapie Prion Protein Propagation in Spleen during Asymptomatic Stage of Experimental Prion Disease in Mice. *J. Microbiol. Biotechnol.* **2016**, *26*, 1657–1660. [CrossRef]
7. Zu, G.; Liu, M.; Zhang, K.; Hong, S.; Dong, J.; Cao, Y.; Jiang, B.; Luo, L.; Pei, R. Functional Hyperbranched Polylysine as Potential Contrast Agent Probes for Magnetic Resonance Imaging. *Biomacromolecules* **2016**, *17*, 2302–2308. [CrossRef]
8. Du, J.; Tian, C.; Ling, J.; Wang, Y. R8-modified polysarcosine-b-polylysine polypeptide to enhance circulation stability and gene delivery efficiency. *J. Control. Release* **2015**, *213*, e50–e51. [CrossRef]
9. Hamano, Y.; Nicchu, I.; Hoshino, Y.; Kawai, T.; Nakamori, S.; Takagi, H. Development of gene delivery systems for the epsilon-poly-L-lysine producer, Streptomyces albulus. *J. Biosci. Bioeng.* **2005**, *99*, 636–641. [CrossRef]
10. Noh, W.; Kim, J.; Lee, S.J.; Ryu, B.G.; Kang, C.M. Harvesting and contamination control of microalgae Chlorella ellipsoidea using the bio-polymeric flocculant alpha-poly-L-lysine. *Bioresour. Technol.* **2018**, *249*, 206–211. [CrossRef]
11. Shih, I.L.; Van, Y.T.; Shen, M.H. Biomedical applications of chemically and microbiologically synthesized poly(glutamic acid) and poly(lysine). *Mini Rev. Med. Chem.* **2004**, *4*, 179–188. [CrossRef] [PubMed]
12. Ayyappan, J.P.; Sami, H.; Rajalekshmi, D.C.; Sivakumar, S.; Abraham, A. Immunocompatibility and toxicity studies of poly-L-lysine nanocapsules in sprague-dawley rats for drug-delivery applications. *Chem. Biol. Drug Des.* **2014**, *84*, 292–299. [CrossRef] [PubMed]
13. Eom, K.D.; Park, S.M.; Tran, H.D.; Kim, M.S.; Yu, R.N.; Yoo, H. Dendritic alpha,epsilon-poly(L-lysine)s as delivery agents for antisense oligonucleotides. *Pharm. Res.* **2007**, *24*, 1581–1589. [CrossRef] [PubMed]
14. Roviello, G.N.; Musumeci, D.; Roviello, V. Cationic peptides as RNA compaction agents: A study on the polyA compaction activity of a linear alpha,epsilon-oligo-L-lysine. *Int. J. Pharm.* **2015**, *485*, 244–248. [CrossRef] [PubMed]
15. Moccia, M.; Roviello, G.N.; Bucci, E.M.; Pedone, C.; Saviano, M. Synthesis of a l-lysine-based alternate alpha,epsilon-peptide: A novel linear polycation with nucleic acids-binding ability. *Int. J. Pharm.* **2010**, *397*, 179–183. [CrossRef]
16. Kadlecova, Z.; Rajendra, Y.; Matasci, M.; Baldi, L.; Hacker, D.L.; Wurm, F.M.; Klok, H.A. DNA delivery with hyperbranched polylysine: A comparative study with linear and dendritic polylysine. *J. Control. Release* **2013**, *169*, 276–288. [CrossRef]
17. Kadlecova, Z.; Baldi, L.; Hacker, D.; Wurm, F.M.; Klok, H.A. Comparative study on the in vitro cytotoxicity of linear, dendritic, and hyperbranched polylysine analogues. *Biomacromolecules* **2012**, *13*, 3127–3137. [CrossRef]
18. Russo, A.; Aiello, C.; Grieco, P.; Marasco, D. Targeting "Undruggable" Proteins: Design of Synthetic Cyclopeptides. *Curr. Med. Chem.* **2016**, *23*, 748–762. [CrossRef]
19. Roviello, G.N.; Oliviero, G.; Di Napoli, A.; Borbone, N.; Piccialli, G. Synthesis, self-assembly-behavior and biomolecular recognition properties of thyminyl dipeptides. *Arab. J. Chem.* **2020**, *13*, 1966–1974. [CrossRef]

20. D'Atri, V.; Borbone, N.; Amato, J.; Gabelica, V.; D'Errico, S.; Piccialli, G.; Mayol, L.; Oliviero, G. DNA-based nanostructures: The effect of the base sequence on octamer formation from d(XGGYGGT) tetramolecular G-quadruplexes. *Biochimie* **2014**, *99*, 119–128. [CrossRef]
21. Borbone, N.; Amato, J.; Oliviero, G.; D'Atri, V.; Gabelica, V.; De Pauw, E.; Piccialli, G.; Mayol, L. d(CGGTGGT) forms an octameric parallel G-quadruplex via stacking of unusual G(:C):G(:C):G(:C):G(:C) octads. *Nucleic Acids Res.* **2011**, *39*, 7848–7857. [CrossRef] [PubMed]
22. Falanga, A.P.; Cerullo, V.; Marzano, M.; Feola, S.; Oliviero, G.; Piccialli, G.; Borbone, N. Peptide Nucleic Acid-Functionalized Adenoviral Vectors Targeting G-Quadruplexes in the P1 Promoter of Bcl-2 Proto-Oncogene: A New Tool for Gene Modulation in Anticancer Therapy. *Bioconjug. Chem.* **2019**, *30*, 572–582. [CrossRef] [PubMed]
23. Oliviero, G.; Amato, J.; Borbone, N.; Galeone, A.; Varra, M.; Piccialli, G.; Mayol, L. Synthesis and characterization of DNA quadruplexes containing T-tetrads formed by bunch-oligonucleotides. *Biopolymers* **2006**, *81*, 194–201. [CrossRef] [PubMed]
24. Simonsson, T. G-quadruplex DNA structures–variations on a theme. *Biol. Chem.* **2001**, *382*, 621–628. [CrossRef] [PubMed]
25. Kumar, N.; Basundra, R.; Maiti, S. Elevated polyamines induce c-MYC overexpression by perturbing quadruplex-WC duplex equilibrium. *Nucleic Acids Res.* **2009**, *37*, 3321–3331. [CrossRef]
26. Yin, F.; Liu, J.; Peng, X. Triethylene tetraamine: A novel telomerase inhibitor. *Bioorg. Med. Chem. Lett.* **2003**, *13*, 3923–3926. [CrossRef]
27. Zhang, X.F.; Xiang, J.F.; Tian, M.Y.; Yang, Q.F.; Sun, H.X.; Yang, S.; Tang, Y.L. Formation of an intramolecular G-quadruplex of human telomere induced by poly(L-lysine) under salt-deficient conditions. *J. Phys. Chem. B* **2009**, *113*, 7662–7667. [CrossRef]
28. Duchler, M. G-quadruplexes: Targets and tools in anticancer drug design. *J. Drug Target.* **2012**, *20*, 389–400. [CrossRef]
29. Chen, B.-J.; Wu, Y.-L.; Tanaka, Y.; Zhang, W. Small molecules targeting c-Myc oncogene: Promising anti-cancer therapeutics. *Int. J. Biol. Sci.* **2014**, *10*, 1084–1096. [CrossRef]
30. Wen, L.N.; Xie, M.X. Evidence of different G-quadruplex DNA binding with biogenic polyamines probed by electrospray ionization-quadrupole time of flight mass spectrometry, circular dichroism and atomic force microscopy. *Biochimie* **2013**, *95*, 1185–1195. [CrossRef]
31. Keniry, M.A.; Owen, E.A. Insight into the molecular recognition of spermine by DNA quadruplexes from an NMR study of the association of spermine with the thrombin-binding aptamer. *J. Mol. Recognit.* **2013**, *26*, 308–317. [CrossRef] [PubMed]
32. Miller, M.C.; Buscaglia, R.; Chaires, J.B.; Lane, A.N.; Trent, J.O. Hydration is a major determinant of the G-quadruplex stability and conformation of the human telomere 3′ sequence of d(AG3(TTAG3)3). *J. Am. Chem. Soc.* **2010**, *132*, 17105–17107. [CrossRef] [PubMed]
33. Bao, H.L.; Liu, H.S.; Xu, Y. Hybrid-type and two-tetrad antiparallel telomere DNA G-quadruplex structures in living human cells. *Nucleic Acids Res.* **2019**, *47*, 4940–4947. [CrossRef] [PubMed]
34. Ambrus, A.; Chen, D.; Dai, J.; Bialis, T.; Jones, R.A.; Yang, D. Human telomeric sequence forms a hybrid-type intramolecular G-quadruplex structure with mixed parallel/antiparallel strands in potassium solution. *Nucleic Acids Res.* **2006**, *34*, 2723–2735. [CrossRef] [PubMed]
35. Virgilio, A.; Esposito, V.; Mayol, L.; Giancola, C.; Petraccone, L.; Galeone, A. The oxidative damage to the human telomere: Effects of 5-hydroxymethyl-2′-deoxyuridine on telomeric G-quadruplex structures. *Org. Biomol. Chem.* **2015**, *13*, 7421–7429. [CrossRef] [PubMed]
36. Phan, A.T.; Modi, Y.S.; Patel, D.J. Propeller-type parallel-stranded G-quadruplexes in the human c-myc promoter. *J. Am. Chem. Soc.* **2004**, *126*, 8710–8716. [CrossRef]
37. Yang, D.; Hurley, L.H. Structure of the biologically relevant G-quadruplex in the c-MYC promoter. *Nucleosides Nucleotides Nucleic Acids* **2006**, *25*, 951–968. [CrossRef]
38. Stump, S.; Mou, T.C.; Sprang, S.R.; Natale, N.R.; Beall, H.D. Crystal structure of the major quadruplex formed in the promoter region of the human c-MYC oncogene. *PLoS ONE* **2018**, *13*, e0205584. [CrossRef]
39. Ambrus, A.; Chen, D.; Dai, J.; Jones, R.A.; Yang, D. Solution structure of the biologically relevant G-quadruplex element in the human c-MYC promoter. Implications for G-quadruplex stabilization. *Biochemistry* **2005**, *44*, 2048–2058. [CrossRef]

40. Kypr, J.; Kejnovska, I.; Renciuk, D.; Vorlickova, M. Circular dichroism and conformational polymorphism of DNA. *Nucleic Acids Res.* **2009**, *37*, 1713–1725. [CrossRef]
41. Prado, E.; Bonnat, L.; Bonnet, H.; Lavergne, T.; Van der Heyden, A.; Pratviel, G.; Dejeu, J.; Defrancq, E. Influence of the SPR Experimental Conditions on the G-Quadruplex DNA Recognition by Porphyrin Derivatives. *Langmuir* **2018**, *34*, 13057–13064. [CrossRef] [PubMed]
42. Sengupta, P.; Banerjee, N.; Roychowdhury, T.; Dutta, A.; Chattopadhyay, S.; Chatterjee, S. Site-specific amino acid substitution in dodecameric peptides determines the stability and unfolding of c-MYC quadruplex promoting apoptosis in cancer cells. *Nucleic Acids Res.* **2018**, *46*, 9932–9950. [CrossRef] [PubMed]
43. Oliviero, G.; D'Errico, S.; Pinto, B.; Nici, F.; Dardano, P.; Rea, I.; De Stefano, L.; Mayol, L.; Piccialli, G.; Borbone, N. Self-Assembly of G-Rich Oligonucleotides Incorporating a 3′-3′ Inversion of Polarity Site: A New Route Towards G-Wire DNA Nanostructures. *ChemistryOpen* **2017**, *6*, 599–605. [CrossRef] [PubMed]
44. Nici, F.; Oliviero, G.; Falanga, A.P.; D'Errico, S.; Marzano, M.; Musumeci, D.; Montesarchio, D.; Noppen, S.; Pannecouque, C.; Piccialli, G.; et al. Anti-HIV activity of new higher order G-quadruplex aptamers obtained from tetra-end-linked oligonucleotides. *Org. Biomol. Chem.* **2018**, *16*, 2349–2355. [CrossRef] [PubMed]
45. Largy, E.; Mergny, J.L. Shape matters: Size-exclusion HPLC for the study of nucleic acid structural polymorphism. *Nucleic Acids Res.* **2014**, *42*, e149. [CrossRef]
46. Carella, A.; Roviello, V.; Iannitti, R.; Palumbo, R.; La Manna, S.; Marasco, D.; Trifuoggi, M.; Diana, R.; Roviello, G.N. Evaluating the biological properties of synthetic 4-nitrophenyl functionalized benzofuran derivatives with telomeric DNA binding and antiproliferative activities. *Int. J. Biol. Macromol.* **2019**, *121*, 77–88. [CrossRef]
47. Scognamiglio, P.L.; Di Natale, C.; Leone, M.; Poletto, M.; Vitagliano, L.; Tell, G.; Marasco, D. G-quadruplex DNA recognition by nucleophosmin: New insights from protein dissection. *Biochim. Biophys. Acta* **2014**, *1840*, 2050–2059. [CrossRef]
48. Poletto, M.; Malfatti, M.C.; Dorjsuren, D.; Scognamiglio, P.L.; Marasco, D.; Vascotto, C.; Jadhav, A.; Maloney, D.J.; Wilson, D.M., 3rd; Simeonov, A.; et al. Inhibitors of the apurinic/apyrimidinic endonuclease 1 (APE1)/nucleophosmin (NPM1) interaction that display anti-tumor properties. *Mol. Carcinog.* **2016**, *55*, 688–704. [CrossRef]

10. Su, C.C.; Hsieh, K.L.; Liu, P.L.; Yeh, H.C.; Huang, S.P.; Fang, S.H.; Cheng, W.C.; Huang, K.H.; Chiu, F.Y.; Lin, I.L.; et al. AICAR induces apoptosis and inhibits migration and invasion in prostate cancer cells through an AMPK/mTOR-dependent pathway. *Int. J. Mol. Sci.* **2019**, *20*, 1647. [CrossRef] [PubMed]
11. Oliviero, G.; Amato, J.; Borbone, N.; D'Errico, S.; Piccialli, G.; Mayol, L. Synthesis of N-1 and ribose modified inosine analogues on solid support. *Tetrahedron Lett.* **2007**, *48*, 397–400. [CrossRef]
12. Oliviero, G.; Amato, J.; Borbone, N.; D'Errico, S.; Piccialli, G.; Bucci, E.; Piccialli, V.; Mayol, L. Synthesis of 4-*N*-alkyl and ribose-modified AICAR analogues on solid support. *Tetrahedron* **2008**, *64*, 6475–6481. [CrossRef]
13. D'Errico, S.; Oliviero, G.; Borbone, N.; Amato, J.; Piccialli, V.; Varra, M.; Mayol, L.; Piccialli, G. Solid-phase synthesis of a new diphosphate 5-aminoimidazole-4-carboxamide riboside (AICAR) derivative and studies toward cyclic AICAR diphosphate ribose. *Molecules* **2011**, *16*, 8110–8118. [CrossRef]
14. D'Errico, S.; Oliviero, G.; Borbone, N.; Amato, J.; Piccialli, V.; Varra, M.; Mayol, L.; Piccialli, G. Synthesis of new acadesine (AICA-riboside) analogues having acyclic D-ribityl or 4-hydroxybutyl chains in place of the ribose. *Molecules* **2013**, *18*, 9420–9431. [CrossRef] [PubMed]
15. D'Errico, S.; Oliviero, G.; Borbone, N.; Piccialli, V.; Piccialli, G. Synthesis of 5-aminoimidazole-4-carboxamide riboside (AICAR) and its derivatives using inosine as starting material. *Curr. Protoc. Nucleic Acid Chem.* **2015**, *63*, 1.35.1–1.35.24. [CrossRef]
16. D'Errico, S.; Oliviero, G.; Borbone, N.; Amato, J.; D'Alonzo, D.; Piccialli, V.; Mayol, L.; Piccialli, G. A facile synthesis of 5′-fluoro-5′-deoxyacadesine (5′-F-AICAR): A novel non-phosphorylable AICAR analogue. *Molecules* **2012**, *17*, 13036–13044. [CrossRef]
17. Kappler, F.; Hampton, A. Approaches to isozyme-specific inhibitors. 17.1 Attachment of a selectivity-inducing substituent to a multisubstrate adduct. Implications for facilitated design of potent, isozyme-selective inhibitors. *J. Med. Chem.* **1990**, *33*, 2545–2551. [CrossRef]
18. Oliviero, G.; D'Errico, S.; Borbone, N.; Amato, J.; Piccialli, V.; Piccialli, G.; Mayol, L. Facile solid-phase synthesis of AICAR 5′-monophosphate (ZMP) and its 4-*N*-alkyl derivatives. *Eur. J. Org. Chem.* **2010**, *2010*, 1517–1524. [CrossRef]
19. Ashton, T.D.; Scammells, P.J. An improved synthesis of 5′-fluoro-5′-deoxyadenosines. *Bioorg. Med. Chem. Lett.* **2005**, *15*, 3361–3363. [CrossRef]
20. Amiable, C.; Pochet, S. Unprecedented formation of 8(*R*),5′-*O*-cycloribonucleosides through a triflation reaction of purine ribonucleosides. *Tetrahedron* **2015**, *71*, 2525–2529. [CrossRef]
21. Robins, M.J.; Peng, Y.; Damaraju, V.L.; Mowles, D.; Barron, G.; Tackaberry, T.; Young, J.D.; Cass, C.E. Improved syntheses of 5′-*S*-(2-aminoethyl)-6-*N*-(4-nitrobenzyl)-5′-thioadenosine (SAENTA), analogues, and fluorescent probe conjugates: Analysis of cell-surface human equilibrative nucleoside transporter 1 (hENT1) levels for prediction of the antitumor efficacy of gemcitabine. *J. Med. Chem.* **2010**, *53*, 6040–6053. [PubMed]

53. Ríos, E. Calcium-induced release of calcium in muscle: 50 years of work and the emerging consensus. *J. Gen. Physiol.* **2018**, *150*, 521–537. [CrossRef]
54. Dutka, T.L.; Lamboley, C.R.; McKenna, M.J.; Murphy, R.M.; Lamb, G.D. Effects of carnosine on contractile apparatus Ca2+ sensitivity and sarcoplasmic reticulum Ca2+ release in human skeletal muscle fibers. *J. Appl. Physiol.* **2011**, *112*, 728–736. [CrossRef]
55. Wissing, F.; Nerou, E.P.; Taylor, C.W. A novel Ca2+-induced Ca2+ release mechanism mediated by neither inositol trisphosphate nor ryanodine receptors. *Biochem. J.* **2002**, *361*, 605–611. [CrossRef]
56. Guaragna, A.; Roviello, G.N.; D'Errico, S.; Paolella, C.; Palumbo, G.; D'Alonzo, D. Solid phase synthesis of a novel folate-conjugated 5-aminolevulinic acid methyl ester based photosensitizer for selective photodynamic therapy. *Tetrahedron Lett.* **2015**, *56*, 775–778. [CrossRef]
57. D'Errico, S.; Piccialli, V.; Oliviero, G.; Borbone, N.; Amato, J.; D'Atri, V.; Piccialli, G. Probing the reactivity of nebularine N1-oxide. A novel approach to C-6 C-substituted purine nucleosides. *Tetrahedron* **2011**, *67*, 6138–6144. [CrossRef]